Dissertation presented for the degree of Master of Science in the

Department of Chemistry, University of Cape Town

January 2023

Synthesis and Characterisation of Silver(I) Halo-pyridyl Compounds: A Study of the Prominent NCIs that Govern Crystal Packing

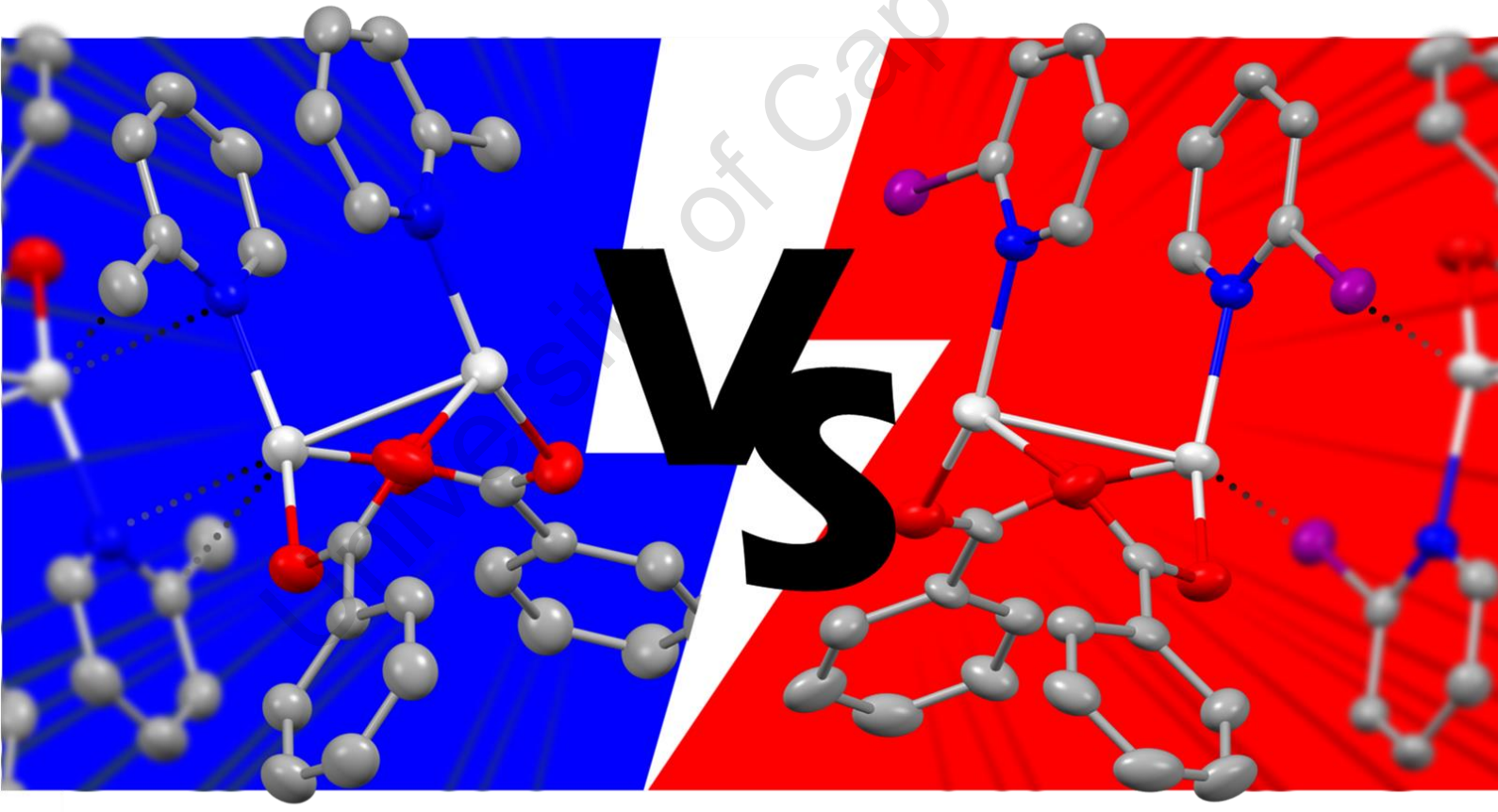

Submitted by Tristan K. Theunissen

Supervisors: Prof. Susan Bourne & Prof. Catharine Esterhuysen

Plagiarism Declaration

I, Tristan Karl Theunissen, know the meaning of plagiarism and declare that all of the work in the dissertation, save for that which is properly acknowledged, is my own.

Acknowledgments

There are many people I would like to thank for their help and support during my two years as an MSc student at the University of Cape Town. First, I would like to thank my supervisor Prof. Susan Bourne for allowing me to conduct research in her lab, taking me to conferences, and always encouraging me in my pursuit of higher education and the acquisition of knowledge. Her advice and expertise have been invaluable to my practical and theoretical chemistry development.

I worked quite closely with Prof. Catharine Esterhuysen at Stellenbosch University for a significant portion of my research. Training and access to her computational group at the Centre for High-Performance Computing (CHPC) and her quantum chemical expertise, as well as long discussions about metallophilic interactions and crystals, were instrumental in the progress of my project, and for that I am thankful.

Dr. Hong Su also deserves special mention for taking the time out of her consistently busy schedule to lend a hand with all my data collecting and assisting me in finding suitable single crystals when I could not.

Prof. Gregory Smith and Stephan de Donker, special thanks are given for their assistance with the synthetic component of my research.

To all the other members of the CSCR lab – a special thank you is needed. If it were not for the assistance of every individual in the CSCR lab, I would not have been able to complete my dissertation.

I could not have undertaken this journey without my dearest friend, Monica van der Walt, whom I'd like to thank for always being a voice of reason when my mind seems to be clouded with self-doubt, and whose love and support helped carry me through many stressful times.

I would like to express my deepest gratitude for one of my closest friends, Jessica Barraclough, whose love and support have been one of the major driving forces behind my completing my MSc. and has always been a huge source of inspiration and determination.

The financial support from the Harry-Crossley Foundation funded by Harry and Doris Crossley is sincerely acknowledged.

Finally, I would like to thank my family, especially my parents and my sister. Without their unconditional love and support, I would not have been able to accomplish any of this.

Dedication

I would like to dedicate this dissertation to our loving family dog, Tinkerbell (nicknamed Tinks). Incidentally, she sadly passed away on 04 March 2022 at sixteen years of age, which is a relatively long time for a little dog. That said, not even an eternity of time spent together would have been enough. Thank you for always making my days brighter and bringing our family closer. For such a little dog, you possibly made one of the biggest impacts on my life. I will forever carry your memory in my heart. I miss you very much.

Tinkerbell Theunissen

2006 – 2022

Abstract

This study aimed to identify which non-covalent interactions (NCIs) would dominate in the solid-state structures of silver(I) halopyridyl compounds. Five novel compounds were synthesised and several metal-involved NCIs were observed. The five compounds which formed a cohesive series are: $[Ag_2(OBn)_2]$, $[Ag_2(2\text{-}Pic)_2(OBn)_2]$, $[Ag_2(3\text{-}Clpy)_2(OBn)_2]$, $[Ag_2(2\text{-}Brpy)_2(OBn)_2]$, and $[Ag_2(2\text{-}Ipy)_2(OBn)_2]$. X-ray diffraction analysis of single crystals constituted the solid-state study portion of the NCIs. Their influence on the crystal structure was carried out using modern computational techniques, such as molecular electrostatic surface potential (MESP), natural bond orbital or NBO analysis, and quantum theory of atoms in molecules (QTAIM).

This dissertation comprises four sections, the first of which introduces background knowledge on particular topics such as crystal engineering, non-covalent interactions, and possible applications that NCIs have within crystal engineering and supramolecular chemistry. The second and third sections discuss specific methods and techniques used to study the NCIs from a crystallographic and computational viewpoint. The final section summarises the contribution of the authors' work to the understanding and body of knowledge of NCIs.

As shown in this dissertation, the 'self-assembled' $[Ag_2(OBn)_2(Xpy)_2]$ compounds are closely related to their strongest non-covalent metal-involved interactions, such as $Ag^I\cdots\pi$, $Ag^I\cdots X$, and $Ag^I\cdots Ag^I$, while also being influenced by weaker interactions', $\pi\cdots\pi$, cooperativity effects. The importance of orbital-based charge-transfers as opposed to being purely electrostatic in the argentophilicity of compounds **I**-**V** has been discussed. In this study, quantitative QTAIM, NBO, and MEPS-based analyses were carried out on the metallophilic ($M^+\cdots M^+$) interactions. The computational studies suggest a greater role of orbital-based interactions in the strength and distance of said interactions. This hypothesis was applied to other NCIs, such as semi-coordination and metal-π NCIs, in which orbital-based charge-transfers are also shown to predominate force stabilising the compounds over pure electrostatic interactions.

Compounds **VI**-**VIII**, although not included within the main series (**I**-**V**) display a variety of similar NCIs, as evident from their single-crystal structures, whose natures or characteristics are formed from the foundations of computations **I**-**V**. Prominent NCIs are $Ag^I\cdots\pi$, $Ag^I\cdots X$, and $Ag^I\cdots Ag^I$, which are also influenced by weaker interactions', $\pi\cdots\pi$, cooperativity effects.

Keywords: Crystallography, Non-covalent interactions, Semi-coordination bonding, Metal-involved NCIs, nucleophilic metal centres, Silver(I) compounds, Argentophilicity, Density functional theory, DFT calculations.

Author Tristan K. Theunissen
Department of Chemistry
University of Cape Town
Western Cape, South Africa
thntri002@myuct.ac.za

Supervisor Professor Susan Bourne
Department of Chemistry
University of Cape Town
Western Cape, South Africa
susan.bourne@uct.ac.za

Co-supervisor Professor Catharine Esterhuysen
Department of Chemistry and Polymer Science
Stellenbosch University
Stellenbosch, South Africa
ce@sun.ac.za

Editor Jessica A. Barraclough
Centre for Film and Media Studies
University of Cape Town
Western Cape, South Africa
jessica.barraclough@gmail.com

List of Abbreviations and Symbols

Å	Angstrom, metric unit of length (10^{-10} m)
a.u.	atomic units, Hartree
OBn	benzoate
BCP	bond critical point
ca.	circa [lat.], around, approximately
calcd.	calculated
conc.	concentrated
CSD	Cambridge Structural Database
DCM	dichloromethane
d	distance
DFT	Density functional theory
e.g.	exempli gratia [lat.], for example
E_g	(HOMO – LUMO) energy gap
Eq	equation
etc.	et cetera [lat.], and so on
EtOH	ethanol
equiv.	equivalent(s)
g	grams, gas
HB	hydrogen bond(s)(ing)
HOBn	benzoic acid
HOMO	Highest Occupied Molecular Orbital
i.e.	id est [lat.], that is
IR	infrared spectroscopy
IUPAC	International Union of Pure and Applied Chemistry
n	any integer
K	Kelvin
L	litre
LA	Lewis acid
LB	Lewis base
LUMO	Lowest Unoccupied Molecular Orbital
m	milli (10^{-3})
M	moles per litre (mol/L)
MeOH	methanol
MEPS	molecular electrostatic potential surface
NBO	natural bond orbital
NCI	non-covalent interaction
P_o	point of extension
Py	pyridine
PXRD	powder x-ray diffraction
QTAIM	Quantum Theory of Atom in Molecules
RCP	ring critical point
rt	room temperature
SCB	semi-coordination bond
SCXRD	single crystal x-ray diffraction

TGA	thermogravimetric analysis
T_d	tetrahedral
UV-VIS	Ultraviolet-visible
vdW	van der Waals
V	volume
X	any halogen atom; fluorine, chlorine, bromine, or iodine
XB	halogen bond(s)(ing)
XBA	halogen bond acceptor
XBD	halogen bond donor
XRD	x-ray diffraction
α	angle between b and c unit cell axes
β	angle between a and c unit cell axes
γ	angle between a and b unit cell axes
λ	Greek letter lambda: wavelength (nm)
ν	Greek letter ny with tilde: wave number (cm^{-1})
π	Greek letter pi: used for double bonds and delocalised electrons
θ	Theta: angle (°)

Table of Contents

Chapter 1
Introduction and Literature Review

1.1 General Introduction

This study focuses on the chemistry of halogen interactions, with the addition of metal-involved interactions, of R_3C-Cl, R_3C-Br, and R_3C-I bonds via semi-coordination to silver(I). The current dissertation also describes the application of the latter non-covalent interactions in crystal engineering and supramolecular chemistry.

The halogens are comprised of a series of five non-metallic elements: fluorine (F), chlorine (Cl), bromine (Br), iodine (I), and astatine (At). These halogens are located on the periodic table to the left of the noble gases making up the 17th group (see Figure 1.1 below). Halogens have seven valence electrons; typically in the configuration $(ns^2)(np^5)$ and thus only require one additional electron to form a full octet. Since these elements are only one electron short of the inert gas configuration, they are electronegative and highly reactive compared to other non-metal groups, making them fundamental to chemistry.

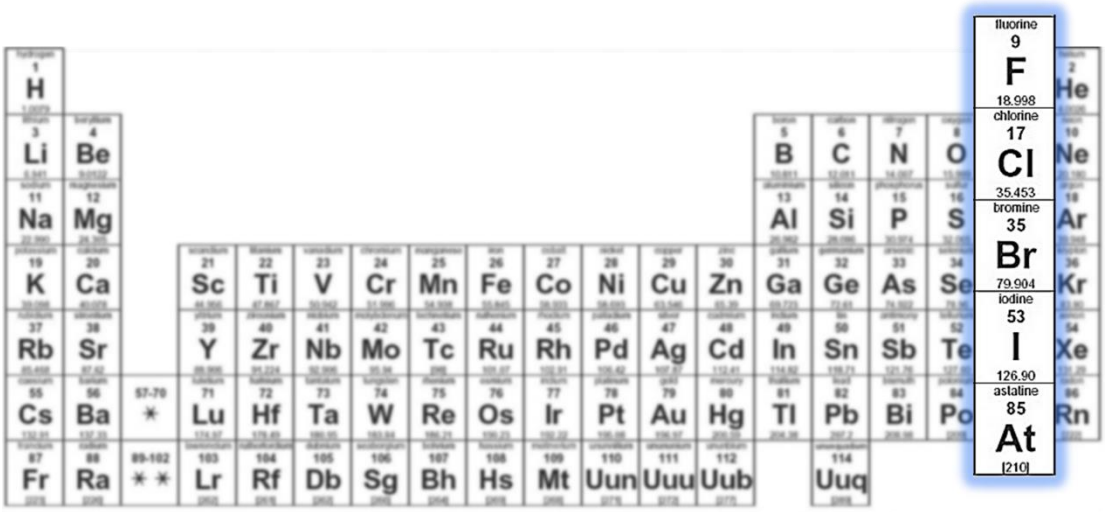

Figure 1.1. Periodic table with group 17 (i.e. the halogens) highlighted.

1.2 Supramolecular chemistry

The establishment of supramolecular chemistry as an 'information science' in which the instructions for the assembly of large complex molecules lie within the individual components has been attributed to three scientists: Charles Pedersen, Jean-Marie Lehn, and Donald Cram. Each of them was awarded the Nobel Prize in Chemistry in 1987 for synthesising cryptands (bi- or polycyclic multidentate ligands for several cations).[1]

The definition for the term 'supramolecular chemistry' is often overly complex; thus, in simple terms, supramolecular chemistry is the chemistry of the non-covalent bond.[2] A more robust definition would describe supramolecular chemistry as being a multidisciplinary field of science concerned with the intermolecular interactions between two (or more) chemical entities, which allows for the formation of more complex molecular assemblies.[3,4] Supramolecular chemistry ultimately aims to study the structures and

functions of the molecular assemblies that have resulted from the aforementioned intermolecular interactions.[4]

Whereas more traditional chemistry emphasises the nature of covalent bonds, supramolecular chemistry focuses on the relatively weaker and reversible non-covalent bonding interactions, such as: hydrogen bonding (H-bonding); dipole-dipole, ion-dipole, and hydrophobic interactions; van der Waals forces; π-π interactions; and dispersion interactions. These classes of interactions tend to vary over a relatively large range of bond energies which can be seen in Figure 1.2 below:

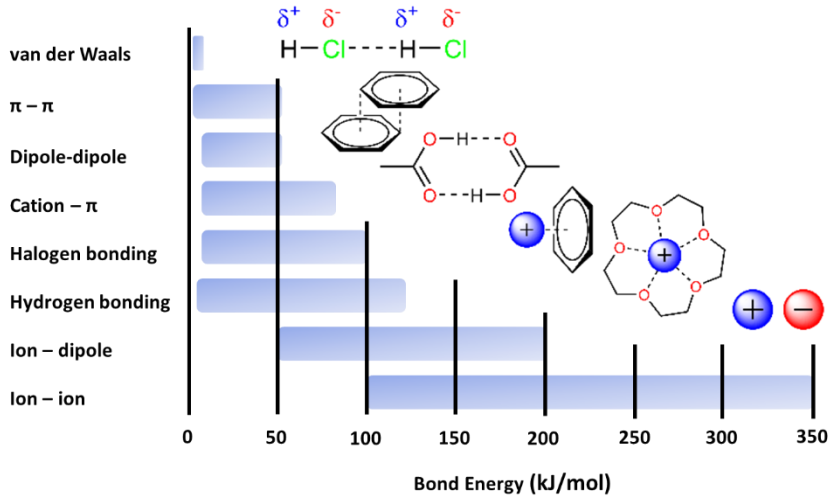

Figure 1.2. Strengths of the most common intermolecular interactions.[4]

1.3 Polymorphism

Compounds can exhibit different crystal forms due to polymorphism.[5] As a result of different packing arrangements or conformations, polymorphs can exhibit significant variation in their physical and chemical properties, which makes them attractive for study within the field of supramolecular chemistry.[6] A polymorph's crystallisation is generally quite sensitive to changes in pressure, temperature, and use of solvent.[7] Several types of polymorphism exist, the most important being conformational polymorphism and packing polymorphism. Different packing polymorphs vary in their three-dimensional (3D) crystal arrangement, but which does not affect the molecules' conformation.[8]

1.4 Crystal engineering

The molecular concept is one of the major cornerstones of chemistry. Chemists first tried to understand molecules as entities on their own, where much of the intrinsic properties of a molecule originate from the types of atoms of which they are comprised. However, the manner in which atoms are connected and interact with one another is of equal importance. Thus, the inter- and intramolecular connections, that hold atoms together can be considered the very essence of (coordination) chemistry.[9] Some examples of inter- and intramolecular interactions are hydrogen, halogen, chalcogen, pnictogen bonding, dipole-dipole, π-interactions, and metallophilic interactions.

As time went on, chemists increasingly moved beyond studies of the singular molecule, instead emphasising the importance of intermolecular associations that form between molecules. These interactions, if stable

enough, would lead to the formation of molecular solids with specific chemical and physical properties.[10] Thus, a new term was described: when two or more molecules collect together via relatively weak interactions as compared to their stronger internal interactions a *molecular crystal* is formed.[11,12] Depending on the way these molecules come together and interact with one another, a particular *molecular crystal* system is generated that is unique to that interaction. It follows that if there is a way to predict and control these intermolecular interactions, then, in principle, the properties of the resulting solids can be dictated. This deduction is what formed the conceptual foundations of crystal engineering.[13]

Crystal engineering thus focuses on the chemical and physical properties of molecular crystals, specifically: how these properties originate via molecule interactions with one another in a crystal packing system.[14]

1.5 Non-covalent Interactions

This section comprises a brief discussion of covalent interactions as compared to non-covalent interactions, as well as the key non-covalent interactions applied in this dissertation.

1.5.1 Differences between covalent and non-covalent

A non-covalent interaction differs from a covalent bond in that it does not involve the sharing of electrons,[15] but rather more dispersed electromagnetic interactions within or between molecules. Non-covalent interactions can be categorised into electrostatic, charge transfer, and/or dispersive interactions.[16,17]

While the nature of said interaction is a highly debated topic, the question remains "what is a chemical bond (interaction) between two atoms?". The IUPAC Golden Book states: “when forces acting between two atoms or groups of atoms lead to the formation of a stable independent molecular entity, a chemical bond is considered to exist between these atoms or groups.”[18] Essentially, if an interaction has a physical consequence on its surroundings, it, therefore, must exist.

Despite IUPAC's clear definition of an ionic and covalent bond, it is preferable to consider the contribution of a certain characteristic of an interaction, i.e. a ‘bond’, instead of just categorising it as purely ionic, covalent, or non-covalent. An interaction should therefore be described by some measurable parameter(s), and in the instance of bond analysis, suitable parameters to measure an interaction with would be energy, ΔE, and distance, *d*.

An interaction can have chemical energy (the energy released during formation) that ranges from a few kJ/mol to hundreds of kJ/mol.[16] There are two types of distance scales when it comes to measuring interactions: a short interaction of less than 2 Å and a long interaction distance between 2-5 Å. While short-range, high-energy interactions are typically assigned an ionic and/or covalent character, there are non-covalent interactions that start with high-energy at a short-range, for example: hydrogen bonds end with low-energy dispersive interactions that approach (or even exceed) the van der Waals (vdW) radius. Therefore, although non-covalent interactions are often referred to as ‘weak’, they are collectively strong enough to create new stable materials that ‘rival’ those with a covalent build.

1.5.2 Halogen atom polarisation

The σ-hole is considered to be the major component that governs halogen interactions. To understand how the σ-hole is formed, one could consider the valence electron configuration of a halogen atom, X, as being: $(ns^2)(np_x^2)(np_y^2)(np_z^1)$, where the z-axis is understood as running along the covalent bond of an alkyl halide, R_3-C—X (see Figure 1.3(a, b) below). A shift in electron density results from the localisation of the single p_z-σ orbital, np_z^1, electron towards the σ-bond region, for example: $R_3C\cdot + \cdot X(:)_2$.[19] Depletion of this density in the outer (non-involved) lobe is sufficient enough to be characterized as an electro-positive potential (δ^+), i.e. the σ-hole. The electro-positive potential is surrounded by an electron-rich ‘belt’ that is formed by the

lone pairs located within the remaining p_x and p_y-π orbitals. These doubly-occupied p_x and p_y orbitals of the halogen atom are orthogonal (90°) to the corresponding σ-bond (see Figure 1.3(a) below). As a consequence of the unequal distribution of electrons, the shape of the halogen's effective radius (R_{vdW}) is shortened in the direction opposite to the σ-bond and lengthened in the direction orthogonal to the σ-bond.[20] Since the electron density is flattened - not spherical - around the halogen atom, the term 'polar flattening' arises (see Figure 1.3(c) below).[21] This so-called polar flattening can explain why halogens act simultaneously as Lewis acids (LA) and/or Lewis bases (LB).

1.5.3 Halogen-involved interactions

As a powerful self-assembly tool,[22,23] halogen bonding has attracted a lot of attention in recent decades. By the IUPAC definition: "a halogen bond occurs when there is evidence of a net attractive interaction between an electrophilic region associated with a halogen atom in a molecular entity and a nucleophilic region in another, or the same, molecular entity."[24]

Halogen bonds (XB) can be represented schematically as $R_3C–X\cdots Y$, where $R_3C–X$ is the halogen bond donor (XBD) and Y is the halogen bond acceptor (XBA). The R-group represented in the $R_3C–X\cdots Y$ scheme is covalently bound to the halogen atom, X, where X = Cl, Br, I. Here, X can be both electrophilic and nucleophilic in nature, however, within a halogen bond, X is typically electrophilic. Furthermore, regards to the XBA, Y is the electron-rich entity (i.e. Lewis base/nucleophile). The distance between X and Y, d(X···Y), is typically shorter than the sum of Bondi's vdW radii in halogen-bonded systems, as is the case with most interactions. The electrophilic region of the halogen atom is commonly referred to as a σ-hole.[25]

Interestingly, X, when covalently bonded to a non-metal substituent R, can behave as a Lewis base/nucleophile (and an electrophile) due to the phenomenon called polar flattening,[21] which was discussed previously above in Section 1.5.2. In this case, X can interact with an electron-deficient species, Y, via its electron belt (nucleophile) in a scheme similar to that of $R_3C–X\cdots Y$ for the halogen bond. This type of interaction, although uncommon, is referred to as a semi-coordination bond (SCB).[26,27] Here, the distance between X and Y, d(X···Y), is typically shorter than the sum of Bondi's vdW radii in the semi-coordinated system.

1.5.4 Main properties of semi-coordination interactions

The main properties of a semi-coordination bond, or interaction include directionality[28] and tunability,[29] which are both closely related to the polarisability of the electron cloud of the halogen atom, X. A semi-coordination bond (SCB) is a directional interaction with an angle $\angle(R_3C–X\cdots Y)$ approaching 90°.[26] This specific angle of 90° is a result of the position of the lone pairs on the halogen atom, X, as shown in Figure 1.3(a) below. Much like XB, an advantage of semi-coordination bonding is tunability. The SCB strength is inversely proportional to the electronegativity of the halogen (X) atom: as electronegativity increases, SCB strength decreases (e.g. SCB of X = Cl << Br < I). Alternatively, as the electron-withdrawing ability of the R-group decreases, the SCB strength increases. Therefore, the strength of a SCB can be adjusted by varying the halide atom or the R-group.

The existence of a semi-coordination bond can be confirmed both with experimental data and theoretical analysis. The experimental methods include, SCXRD, NMR, IR, Raman, XPS, and UV-vis spectroscopies. The theoretical confirmation can be performed via several different computational analyses, such as QTAIM (quantum theory of atoms in molecules), NBO (natural bonding orbital), NCIplot, DORI (density overlap region indicator), ESP (electrostatic potential), and ELF (electron localisation function) methods. Some of these methods, namely SCXRD, QTAIM, NBO, and ESP analysis are discussed further in Chapter 2.

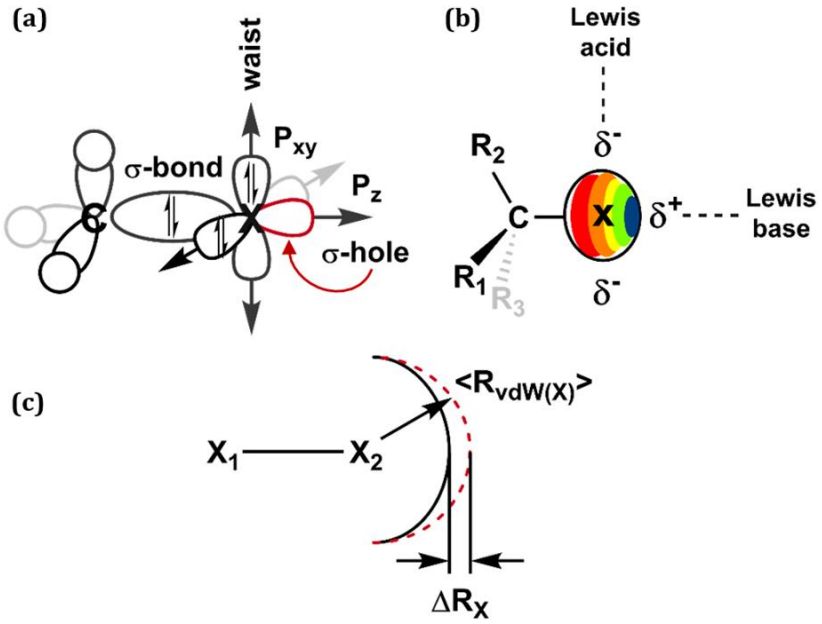

Figure 1.3. Halogen bonding of R_3-C—X: (a) σ-hole formation due to depopulation of the halogen p_z-orbital towards the σ-bond region; flattens the atomic radius opposite the σ-bond, leaving a negative 'belt' comprised of the fully occupied p_{xy}-orbitals; (b) Anisotropic distribution of charge and possible interactions of a typical halogen (X = Cl, Br, I) in a halocarbon toward Lewis acid and bases; (c) Polar flattening ($\Delta R_{(X)}$ taken as an absolute value) is illustrated by the solid black line which represents the real surface, while the hypothetical spherical surface ($<R_{vdW(X)}>$, standard van der Waals radii) is represented by the dashed red line.

1.5.5 Metal-involved interactions

Non-covalent metal-involved interactions may be classified as polar or nonpolar based on the electrophilic or nucleophilic roles assigned to the interacting atoms. Polar interactions are those in which the atoms have clearly defined electro- or nucleophilic roles. There are several types of polar interactions, including NCIs that involve σ-holes (as in hydrogen, halogen, and chalcogen bonding),[30,31] electron belts (in semi-coordination bonding),[32] and π-clouds (in cation–π interactions).[33-35] Furthermore, weak electrostatic interactions between low-valent closed shell (d^{10}) and pseudo-closed shell (d^8) metal ions can be classified as polar metallophilic interactions in heterometallic complexes.[36,37] There are some halogen bonds of intermediate metal-halogen type,[26] as well as metallophilic interactions known for d-block transition metal complexes that are nonpolar (see Figure 1.4 below).[38]

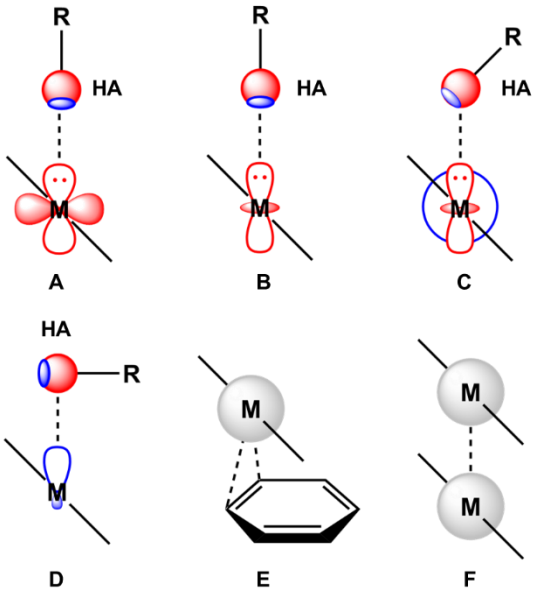

Figure 1.4. Types of non-covalent interactions involving metal centres [M] and halogen atoms (HA). The electrophilic regions are colour-coded as blue, while the nucleophilic regions are coloured red. The above diagrams are described as follows: (a) interaction involving the σ-hole and $d_{x^2-y^2}$[M] or d_{xy}[M] orbital; (b) interaction involving the σ-hole and d_{z^2}[M] orbital; (c) intermediate M···X interaction; (d) interaction involving the electron belt; (e) interaction involving the π-cloud; and (f) metallophilic interaction.

Even though every interaction has its unique nature and properties, it is important to remember that several NCIs often contribute to the arrangement of the structure. This phenomenon is called the cooperative effect, where various NCIs strengthen (or weaken) one another.[39,40] Thus, in metal-involved NCIs that are typically accompanied by stronger interactions, cooperative effects are paramount in stabilising the solid-state system. For example, cooperation of π···π/M^+···π and metallophilic interactions will be shown, as part of this dissertation, to be necessary to stabilize dimeric structures in compounds described in this dissertation. It is possible to achieve various metal-involved contacts, such as M^+···π and M^+···X, by modifying the type of halogen atom substituent even within the same metal compound, which is discussed further in Chapter 4.

1.5.6 Argentophilicity

In gold chemistry, aurophilic interactions became increasingly popular in the 1990's and early 2000's. This was because a variety of structural and other physical characteristics of gold(I) compounds were significantly influenced by these interactions. In spite of frequent reports of aurophilic interactions in molecular compounds, analogous so-called argentophilic interactions have remained relatively unknown. Much debate as to the nature of these interactions is still done to this day, despite silver chemistry being more versatile than gold in terms of coordination numbers and geometries.[41,42]

Many metal-containing compounds containing short intermetallic distances have been observed, which naturally leads to the question of whether or not metal-metal (M-M) bonding is present. M-M bond order is established by the overlapping of d-orbitals, which gives rise to σ, π, and δ bonds. Furthermore, as long as there are fewer electrons in the empty atomic orbitals than in the bonding orbitals, there is no ambiguity as to whether a M-M bond exists.[43] This, however, becomes less when M^+···M^+ units are formed by elements on the far-right side of the d-block, e.g. Cu^I/Ag^I/Au^I, as can be seen in Figure 1.5(a) below. In such cases,

direct M-M bonding is possible by the use of empty ns^0/np^0 orbitals admixing with filled nd^{10} orbitals.[44] Theoretically, outer-shell orbital mixing for $Ag^I\cdots Ag^I$ interaction, with either $5s^0/5p^0$ orbitals and the filled 4 d^{10}-orbital, may produce a net Ag^I-Ag^I bond. However, since many silver(I) compounds are ligated, as is the case for compounds **I-V**, the empty s^0 and p^0 orbitals are occupied with the formation of the metal–ligand coordination bonds. Thus, those specific s^0/p^0 orbital combinations are unable to mix sufficiently to produce said net Ag^I-Ag^I bond (see Figure 1.5(b) below).[44,45] In this dissertation, we have extended this type of M-M inquiry, where the question we are dealing with concerns the attractive interactions between the ligated closed-shell silver(I) atoms. A relatively neglected aspect of this discussion will be emphasized, namely that of the role of orbital interactions in metallophilicity.

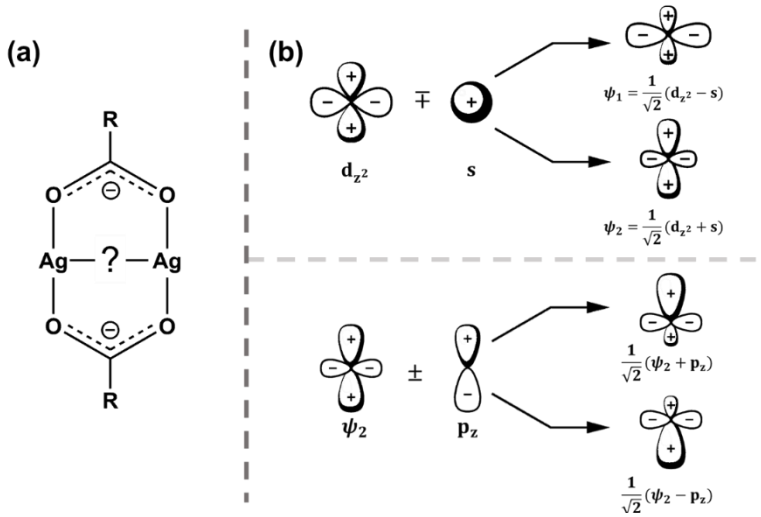

Figure 1.5. (a) Generalized scheme of bonding in a $Ag_2(COOR)_2$ molecular dimer. (b) Sketches illustrating the hybridization of the d_z^2 and s orbitals, which leads to the formation of the ψ_1 and ψ_2 hybrid orbitals. The ψ_2 hybrid can further hybridize by combining with the p_z orbital.[42(c)]

1.6 Crystallography

Many fields, including materials science, chemistry, pharmacology, and molecular biology, rely heavily on crystallographic research. The most comprehensive method for determining molecular structure is X-ray crystallography. Finding a "good crystal", which is often considered the 'rate-limiting' step, is necessary for crystallographic structures to be accurately determined. The subsequent sections described herein will further elaborate on the background theory of X-ray diffraction analysis and its applications in determining the significance of non-covalent interactions within the crystal structure.

1.6.1 Background Theory

Crystals are highly-ordered solid materials whose atoms are arranged periodically.[46,47] These atoms can scatter (or diffract) incoming X-ray waves primarily through their electrons. Scattering occurs when an electron struck by an X-ray emits secondary spherical waves (see Figure 1.6 below). This process is called elastic scattering, where 'elastic' refers to there being no change in the energy of the incoming radiation.[48] As a consequence of the electrons being arranged periodically, many of the secondary spherical waves emitted cancel each other out via destructive interference. However, constructive interference in a few specific directions also occurs, thus allowing for diffraction to be observed. The specific directions wherein

constructive interference will occur (and hence when diffraction is detected) were first proposed by Lawrence Bragg and his father, William Henry Bragg, giving rise to Bragg's Law.[49]

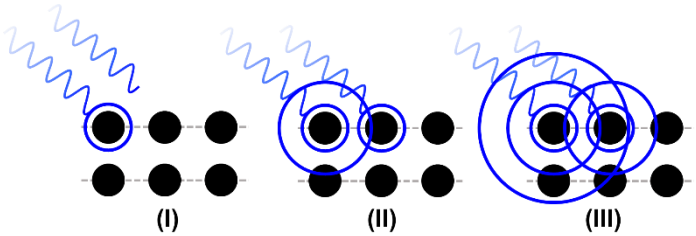

Figure 1.6. X-rays interacting with the atoms in a crystal, demonstrating elastic scattering.

1.6.2 Bragg's Law

Despite Laue's discovery of diffraction,[50] it was the Bragg father–son duo who derived an equation that predicted when diffraction would occur. During Bragg diffraction, X-ray radiation of a wavelength λ comparable to that of the atomic spacing will 'bounce' off the atoms of a crystalline system, and undergo constructive interference. In crystals, waves are scattered from successive layers of atoms separated by lattice planes. The lower X-rays traverse an extra distance of $2d_{hkl}\sin\theta$ (see Figure 1.7 below). Constructive interference occurs when this length is equal to an integer multiple of the wavelength of the radiation.[49]

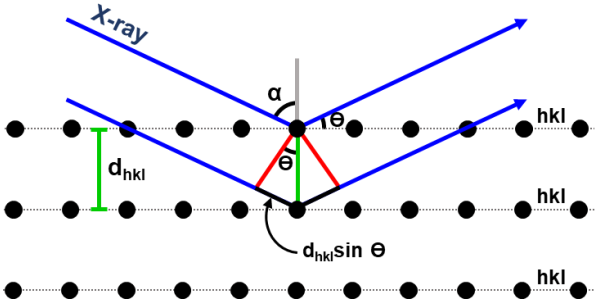

Figure 1.7. X-ray scattering according to Bragg's Law.

While λ represents the wavelength of the X-ray, d_{hkl} is the spacing of the crystal layers (path difference), θ is the incident angle (the angle between the incident ray and the scattering plane), $2d_{hkl}\sin\theta$ is the extra length traversed by the X-ray, and n is a whole integer.

1.6.3 Structure factor

Diffraction beams are observed on a detector as 'spots', forming a pattern indicative of the original diffracting lattice. The spots detected have defined positions and intensities that are dependent on the crystal and form what is known as the reciprocal lattice. What makes the reciprocal lattice different from the original lattice is that it is comprised of reciprocal distances and perpendicular directions. The relationship between the diffraction intensities and the electron density, however, is more complex and requires a Fourier Transform as shown in the structure factor equation below:

$$F_{hkl} = \sum_{j=1}^{N} f_j e^{[2\pi i(hx_j + ky_j + lz_j)]} \quad \text{...Eq. 1}$$

In the above equation, f_j is the temperature-corrected atomic scattering factor.[51]

The crystal's structure can be deduced from the diffraction pattern produced when electrons attached to atoms in a crystal scatter X-rays. There is a greater concentration of electrons in atoms with high atomic numbers than there is in atoms with low atomic numbers. The electron density, ρ, is the sum of the electron concentration and distribution all around the atom. Electron density is measured in units of electrons per cubic angstrom, eÅ^{-3}. Since electron density is a function of position, it can be specified at a point (x, y, z) as $\rho_{(x, y, z)}$.

The electron density can be expressed in terms of the structure factor F_{hkl}:

$$\rho_{(x,y,z)} = \frac{1}{V_c} \sum_{h} \sum_{k} \sum_{l} F_{hkl} e^{-i2\pi(hx+ky+lz)} \quad \text{... Eq. 2}$$

In the above equation, V_c is the volume of the unit cell.[52]

1.6.4 Least-squares refinement

Calculated diffraction patterns can be created once it is thought that the correct crystal structure has been identified. There should be some correspondence between the calculated and observed diffraction patterns if the model structure's atoms are in roughly the correct positions. The calculated structure factor $|F_c|$ and the observed structure factor $|F_o|$ from the experimental data are compared using the least squares refinement. The *residual index* of the *R-factor* is used to describe this comparison, which is defined as:

$$R = \frac{\sum \big| |F_o| - |F_c| \big|}{\sum |F_o|} \quad \text{... Eq. 3}$$

From well-measured experimental data, the *R-factor* for a complete and accurate crystal structure is approximately 0.02-0.07.

Using F^2 values instead of |F| values (a variation on Eq. 3 above) squares the differences and/or incorporates different weighting factors to multiply various reflections based on their standard uncertainties, and incorporates information regarding the relative reliability of various measurements. The following residual factor is frequently utilised for crystal structure determination:

$$wR^2 = \sqrt{\frac{\sum w(F_o^2 - F_c^2)^2}{\sum w(F_o^2)^2}} \quad \text{... Eq. 4}$$

In the above equation, each reflection has its weight function, w, which gives Eq. 4 a more meaningful form from a statistical standpoint than the basic *R factor* described earlier.

1.7 Hirshfeld surface analysis

During the past decade, Hirshfeld surface calculations have become increasingly popular for describing and illustrating the environment of molecules in crystals. As this technique evolved,[53] additional features and tools have been developed to increase its utility for describing and comparing crystal structures.[54] This section aims to summarise some of the basic mathematics used to describe how Hirshfeld surfaces are generated.

Hirshfeld surfaces are an extension of 'Hirshfeld's stockholder partitioning', which breaks down a molecule's electron density into its atomic fragments.[55]

$$w(r) = \left(\rho_A(r) \Big/ \sum_{A \in molecule} \rho_A(r) \right) = \frac{\rho_{atom}(r)}{\rho_{molecule}(r)} \quad \text{... Eq. 5}$$

In the equation above, ρ represents the electron density and (r) indicates the dependence of the function on radius. Spackman and Byrom[53] utilise this idea to divide a crystal's electron density into its molecular fragments.

$$w(r) = \left(\sum_{A \in molecule} \rho_A(r) \Big/ \sum_{A \in crystal} \rho_A(r) \right) = \frac{\rho_{promolecule}(r)}{\rho_{procrystal}(r)} \quad \text{... Eq. 6}$$

By setting the weight function w(r) for each atom in a molecule to 0.5, the space in which the molecule's surface electron density exceeds that of its surroundings (the crystal, and all other molecules) is enclosed by this function's boundary.[53] This is what is meant by the Hirshfeld surface.

A molecule's Hirshfeld surface is represented by many thousands of points from which measurements can be taken and the surface seen.[56] The separation from a point on the Hirshfeld surface to the nearest nucleus inside the surface (the promolecule) is denoted as d_i. Additionally, the surface is mapped with colours that are based on the magnitude of that separation distance (mapping the surface with d_i). Similarly, d_e is the

distance between a point on the Hirshfeld surface and the closest nucleus external to that surface (a neighboring molecule). A two-dimensional (2D) histogram of d_i vs d_e, or a 'fingerprint plot', may subsequently be produced by calculating the d_i and d_e distances for each point on the Hirshfeld surface. To represent the occupancy of a (d_i, d_e) distance, these plots are colour-coded in a range between blue (low frequency) and green (high frequency) with default widths of (0.01 × 0.01 Å^2).[56]

Furthermore, by using the d_{norm} function[57] it is possible to deconstruct the Hirshfeld surface and fingerprint plots, thereby highlighting those (d_i, d_e) distances associated with specific atom···atom contacts (i.e. specific intermolecular distances). To contextualise the distance between the nuclei, the d_{norm} function includes the identity of the atoms that are the subject of the d_i and d_e measurements by including their vdW radii.

$$d_{norm} = \frac{d_i - r_i^{vdW}}{r_i^{vdW}} + \frac{d_e - r_e^{vdW}}{r_e^{vdW}} \quad \text{... Eq. 7}$$

As a result, an intermolecular A···B contact point on the Hirshfeld surface uses the vdW radius of atom A to normalise its d_i measurement, and the vdW radius of atom B to normalise its d_e measurement. To quantify intermolecular contacts, the total percentage area of the Hirshfeld surface that is associated with each specific A···B (and/or B···A) contact can be calculated by adding the points on a molecule's Hirshfeld surface that correspond to that particular atom interacting with another atom.[57]

1.8 An overview of Quantum Mechanics (QM)

In this section, the theoretical background to the quantum mechanical (QM) methods presented in this dissertation is considered. The primary focus is placed on density functional theory (DFT) and the corrections that may be utilised to increase the accuracy of such methods.

1.8.1 QM general approximations

The Schrödinger wave equation[58] provides a statistical description of the energy and position of an electron within space and time. Many approaches within QM are to approximate the time-dependent electronic Schrödinger wave equation, which is given by:

$$\hat{H}_{elec}\Psi_{elec} = E_{elec}\Psi_{elec} \quad \text{... Eq. 8}$$

In the above equation, $\hat{H}$ is the Hamiltonian operator, Ψ is the n-electron wavefunction, and E is the total energy of the system (a molecule).

The Hamiltonian operator $\hat{H}$ is a function composed of the sum of the kinetic and potential energies for an n-particle system, for example: the electron and nucleus for a hydrogen atom. The Hamiltonian operator for a single electron system is defined over three-dimensional (3D) space, and is represented by the equation:

$$\hat{H}_{elec} = \underbrace{\frac{-h^2}{8\pi^2 m_e}\left(\frac{\partial^2}{\partial x^2}+\frac{\partial^2}{\partial y^2}+\frac{\partial^2}{\partial z^2}\right)}_{\textbf{Kinetic energy of the electron}} \underbrace{-\frac{Ze^2}{4\pi\epsilon_0 r}}_{\textbf{Potential energy of the electron}} \quad \text{... Eq. 9}$$

In the above equation: h is Planck's constant, 6.62 x 10^{-34} J·s; m_e is the mass of the electron, 9.1094 × 10^{-31} kg; e is the electron charge, 1.6022 × 10^{-19} C; r is the distance from the nucleus, where $r = \sqrt{x^2 + y^2 + z^2}$; $x, y, \text{and } z$ are its Cartesian components; Z is the charge of the nucleus; and $4\pi\epsilon_0$ is the permittivity of a vacuum.

When taking into account more complex systems that involve multiple electrons, the Hamiltonian operator quickly becomes more difficult. The Hamiltonian operator that describes a many-particle system is given as:

$$\hat{H} = -\frac{\hbar^2}{2m_e}\sum_{i}^{N_e}\nabla_i^2 - \frac{\hbar^2}{2m_p}\sum_{A}^{N_p}\nabla_A^2 - \sum_{i}^{N_e}\sum_{A}^{N_p}\frac{Z_A e^2}{4\pi\varepsilon_0 r_{iA}} + \frac{1}{2}\sum_{\mathbf{i>j}}^{\mathbf{N_e}}\frac{e^2}{4\pi\varepsilon_0 r_{ij}} + \frac{1}{2}\sum_{\mathbf{A>B}}^{\mathbf{N_p}}\frac{Z_A Z_B e^2}{4\pi\varepsilon_0 R_{AB}} \quad \text{... Eq. 10}$$

In the above equation: r_{iA} is the distance between the nuclei and electrons; r_{ij} is the distance between two electrons; and R_{AB} denotes the distance between two nuclei.

A simplification to the molecular $\hat{H}$ can be applied since the masses of the nuclei are relatively much greater than those of electrons: $\{m_p\} >> m_e$. This implies that the electrons move much faster relative to the nuclei, and thus are considered to be moving within a fixed nuclei field. This simplification is known as the Born–Oppenheimer (abbr. BO) approximation and is utilised when taking into account a chemical system that contains more than one electron. The Hamilton operator with the BO approximation applied then becomes:

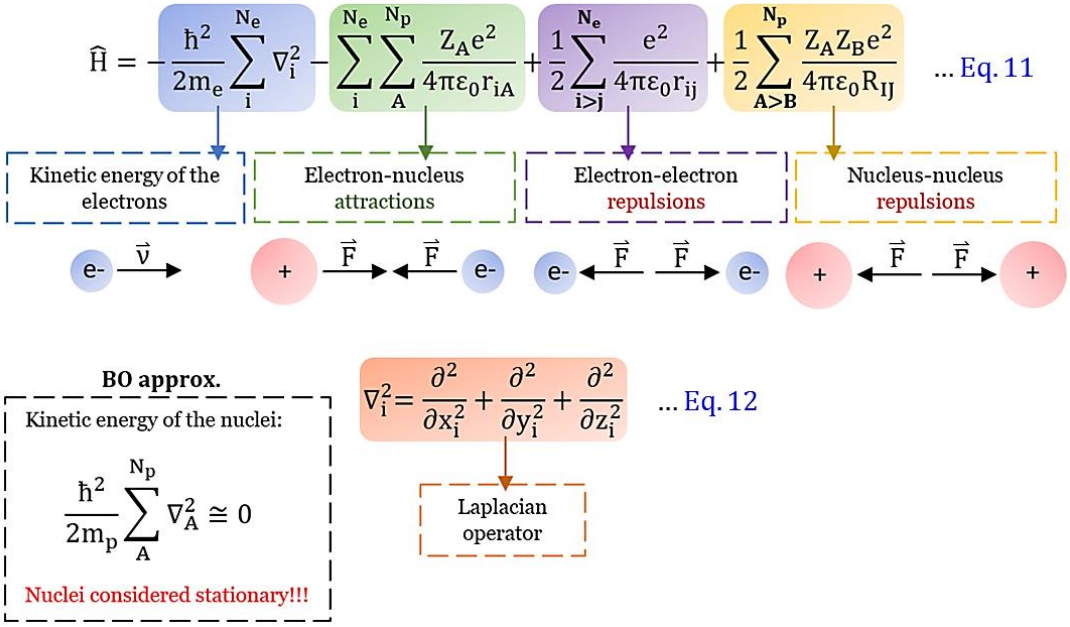

In the above equation: $\hbar$ represents Planck's constant divided by 2π, 1.055 x 10^{-34} J·s; r_i is the position of the i-th electron; R_A is the position of the A-th nucleus; Z is the charge of the nucleus; $4\pi\epsilon_0$ is the permittivity of a vacuum; and ∇_i^2 is the Laplacian operator representative of the i-th particle's position. Note that the factor of ½ is utilised to avoid double counting of the repulsions between electron-electron and nucleus-nucleus interactions.

In the field of quantum chemistry, Hartree atomic units (a.u.) are typically used. This is because SI units for common physical quantities such as meters, kilograms, Coulombs, Joules, and so on are relatively inconvenient when operating at an atomic scale.[59,60] In Table 1.1 below, values of the fundamental physical constants are essentially the same by definition: they are equal to 1.

Table 1.1. Atomic units for QM constants.[61]

Name	Symbol/Definition	Value in a.u.	Value in SI units
Electron mass	m_e	1	9.109 x 10^{-31} kg
Elementary charge	e	1	1.602 x 10^{-19} C
Reduced Planck constant	$\hbar$	1	1.055 x 10^{-34} J·s
Permittivity	$4\pi\varepsilon_0$	1	1.113 x 10^{-10} C^2/J·m
Bohr radius	a_0	1	5.292 x 10^{-11} m

Thus, Eq. (10) is simplified to:

$$\hat{H} = \underbrace{-\frac{1}{2}\sum_{i}^{N_e}\nabla_i^2}_{\hat{T}_e} \underbrace{-\sum_{i}^{N_e}\sum_{A}^{N_p}\frac{Z_A}{r_{iA}}}_{\hat{V}_{en}} \underbrace{+\frac{1}{2}\sum_{i>j}^{N_e}\frac{1}{r_{ij}}}_{\hat{V}_{ee}} \underbrace{+\frac{1}{2}\sum_{A>B}^{N_p}\frac{Z_A Z_B}{R_{AB}}}_{\hat{V}_{nn}} \quad \text{... Eq. 13}$$

$$\therefore \hat{H} = \hat{T}_e + \hat{V}_{en} + \hat{V}_{ee} + \hat{V}_{nn} \quad \text{... Eq. 14}$$

As a result, the time-dependent electronic Schrödinger wave equation is thus given by:

$$\hat{H}_{elec}\Psi_{elec}(r;R) = E_{elec}(R)\Psi_{elec}(r;R) \quad \text{... Eq. 15}$$

In the above equation, r and R denote the electronic and nuclear degrees of freedom, respectively.

In principle, all information about a particular system can be extracted once the wave function is known. It is usually only possible to solve Schrödinger's equation for systems with one particle as calculations of the interactions between the electrons are incredibly difficult due to the many-body problem. To obtain approximate solutions for multiple electron systems, a variety of methods have been developed. In addition to semi-empirical methods, advanced analytical methods have been proposed that are based on different mathematical formalisms (coupled cluster, configuration interaction, many-body perturbation theory).

1.9 Density Functional Theory (DFT)

As mentioned in Section 1.8.1, methods to approximate solutions for larger systems have been developed in response to the fact that the Schrödinger equation can only be solved for a system with one electron. These approaches are typically categorised as wave function theory methods (WFT, HF, or MP2), or methods based on density functional theory (for example, DFT, B3LYP, or M06-2X). Each approach tries to tackle the issue from a different standpoint, where a system's ground state energy is calculated by WFT using the wave function, and where DFT utilises electron density, as their names suggest.

1.9.1 An overview of the mathematics for DFT

The DFT energy model (E^{DFT}) is generally expressed as a sum of the kinetic energy, E_T, electron–nuclear potential energy, E_V, coulombic energy, E_J, and the exchange-correlation energy, E_{XC}. This produces the following equation:

$$E^{DFT} = E_T + E_V + E_J + E_{XC} \quad \text{... Eq. 16}$$

Which, when expanded becomes:

$$E^{DFT} = -\frac{\hbar}{m_e}\sum_i \int \Psi_i^* \nabla^2 \Psi_i d^3r + \int V(r)p(r)d^3r + \frac{1}{2}\iint \frac{p(r)p(r')}{|r-r'|} d^3r d^3r' + E_{ion} \quad \text{... Eq. 17}$$

In the above equation, all of the aforementioned energy components, except E_T, are dependent on the total electron density, $\rho(r)$:

$$\rho(r) = 2\sum_i^{\text{orbitals}} |\Psi_i(r)|^2 \quad \text{... Eq. 18}$$

In the above equation, the single electron wavefunctions Ψ_i (molecular orbital) can be expressed as linear combinations of basis functionals, ϕ:

$$\Psi_i = \sum_\mu^{\text{basis functions}} c_{\mu i}\phi_u \quad \text{... Eq. 19}$$

In Equation (19), the coefficients denoted as $c_{\mu i}$ are the 'unknown' molecular orbital coefficients. This equation is called the linear combination of atomic orbitals (LCAO) approximation.

The utility of DFT arises from the fact that it utilises the electron density directly instead of the many-body wavefunction that is used by other methods like the Hartree-Fock theory. The fact that DFT uses electron density as its basis is what enables speedier calculations, as the electron density is a function of only three variables, i.e. the coordinates: x, y, and z. Many-body wavefunctions like HF would be functions of 3N variables; where N denotes the number of atoms in the system, thus greatly increasing the number of variables in comparison to DFT. Regarding DFT, however, one of the major challenges is to approximate the term (E_{XC} functional) that describes how electrons interact with one another. To describe the dispersion forces that are significant in non-covalent complexes, an exact approximation of electron-electron interactions is necessary. Moreover, long-range electron correlation cannot effectively be taken into account by standard DFT functionals, and thus results for non-covalent complexes are typically rather inaccurate.[62-65]

Despite these shortcomings, DFT has been shown to provide reasonably accurate geometries of molecules (e.g. bond length and angles), and more specifically provides good estimates of bond lengths. Other basic computational properties that are accurately depicted include relative energies, electronic spectra, and molecular orbitals (MOs), as well as the vibrational frequency analysis technique.[66] Overall, given the circumstance of this dissertation, i.e. time constraints, the DFT method is sufficient to yield decently accurate results given that the appropriate alterations (discussed further on) to the functional are made.[67]

1.9.2 The basis set

The quality of the QM calculations depends on both the level of theory used (e.g. the DFT functional) and the size of the basis set (i.e. the number of basis functions included). For dependable results, an accurate functional and large basis set are typically required. This is because in some cases, calculations done with the use of a small basis set may result in an overestimation of the interaction energy through the basis set superposition error (BSSE). To overcome this BSSE, the use of a counterpoise correction factor is required.[68] This is not to say that the use of a small basis set only leads to BSSE - smaller basis sets are generally less accurate because combining more functions gives a better fit of the calculated wavefunction to the true wavefunction.

Basis sets represent one-electron atomic orbitals that can be linearly combined to create molecular orbitals. Moreover, diffuse and polarisation functions (see Figure 1.8 below) can be applied to both hydrogen and heavy metal atoms. To correctly represent bonding between atoms, polarisation functions (such as 'p' or '*') are necessary, whereas diffuse functions (such as 'aug' or '+') are necessary to obtain accurate energies for anionic and weakly bonded systems (i.e. non-covalent interactions). Two examples of popular basis sets that have been used are Pople's 6-31G* and Dunning's aug-cc-pVTZ (as utilised by the current dissertation).

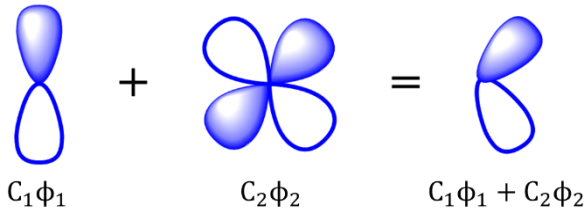

Figure 1.8. A d-polarization function, $C_2\phi_2$, added to a p-orbital, $C_1\phi_1$.[69]

1.9.3 Dispersion correction

Several dispersion-accounting methods have been developed to overcome the fact that the DFT functionals available currently cannot account for long-range electron correlations (i.e. dispersion forces). The dispersion corrected energy ($E_{DFT\text{-}D}$) can be calculated by adding an extra energy term E_D to the DFT calculated energies (E_{DFT}).[70,71] This is given by:

$$E_{DFT-D} = E_{DFT} + E_D \quad \text{... Eq. 20}$$

These methods typically yield an energy term that can be calculated at a relatively low computational cost through empirical deduction. Several DFT functionals, including those for non-covalent complexes,[66] show significant improvement when using corrections to account for dispersion. For the sake of the current dissertation, the D2 method[72] coupled with the B3LYP functional was found to be a suitable method for estimating non-covalent interaction energies.

1.9.4 Molecular electrostatic surface potential (MESP)

Electrostatic potential surfaces have been suggested by Politzer *et al.*[73] as a way to logically predict non-covalent interactions' direction and strength. The molecular electrostatic potential (MESP) describes the attraction or repulsion of a positive charge at a given point in space and is defined as the work required to bring a positive test charge from an infinite distance. MESP maps can be built for atoms (or molecules) by

mapping the determined MESP on the outer surface of the molecular electron density. As a result, information about the molecule's shape, size, and electron distribution can be found within an MESP map.

In the case of the current dissertation, the B3LYP/cc-pVTZ-PP method is used to calculate the MESP and electron density surface, resulting in the construction of ESP maps (see Figure 1.9 below). The electron density surfaces were presented on the maps at an isosurface value of 0.001 a.u., as this value best illustrates the electronic charge of a molecule, as recommended by Bader *et al*.[74] The MESP (in kcal/mol) is typically represented by a colour spectrum that ranges from red (electron-rich), orange, yellow, green, to blue (electron-deficient). To examine non-covalent interactions, the MESP maps have been used to visually examine electron densities at close contact points, to see whether the close contacts are electrostatically driven.

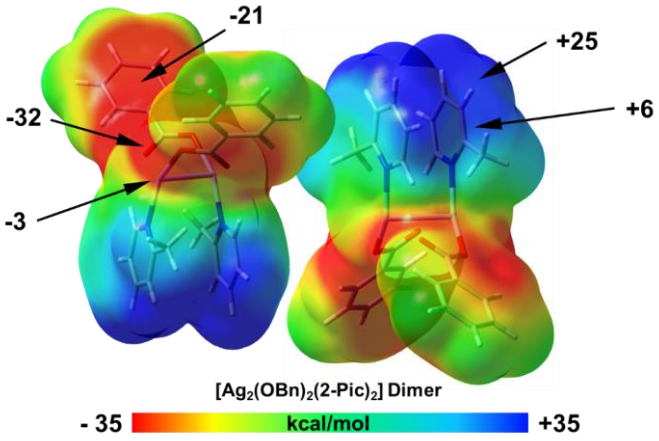

Figure 1.9. Electrostatic potential surface calculated at the B3LYP/cc-pVTZ-PP level on the 0.001 a.u. molecular surfaces of two compounds.

1.9.5 Quantum theory of atoms in molecules, (QTAIM)

Bader's QTAIM[75] is primarily based on the topology of the electron density, $\rho_{(r)}$, where ρ is the electron density and (r) is a spatial variable, i.e. coordinates. Once the topology of the electron density is determined, other properties such as the nature of chemical bonds and non-covalent interactions can be analysed and classified.

The distribution of electron density is affected by the electron-nuclear force, where the highest density is located at the nuclear sites, i.e. nearest the nucleus, and the lowest density is located further away from the nucleus. Bond paths (BPs) are lines of maximum density that connect adjacent atomic regions. Utilising the first, $\nabla\rho_{(r)}$, and second, $\nabla^2\rho_{(r)}$, derivatives at these BPs yield useful structural information such as a measure of the degree of covalency and the strength of an interaction. Furthermore, the first derivative $\nabla\rho_{(r)}$ describes the maxima, minima, or saddle points in space, but then disappears at certain points called critical points (CPs).[76] The characteristics of the CPs, such as the local charge concentration or charge depletion, are then described with the use of the second derivative $\nabla^2\rho_{(r)}$ of the electron density.

$$\nabla\rho_{(r)} = i\frac{\partial\rho}{\partial x} + j\frac{\partial\rho}{\partial y} + k\frac{\partial\rho}{\partial z} \quad \text{... Eq. 21}$$

The second derivative $\nabla\rho_{(r)}$ of the electron density can be ordered into a three-by-three matrix called the Hessian matrix:

$$\nabla\nabla^{T}\rho_{(r)} = \begin{pmatrix} \frac{\partial^2\rho}{\partial x^2} & \frac{\partial^2\rho}{\partial x\,\partial y} & \frac{\partial^2\rho}{\partial x\,\partial z} \\ \frac{\partial^2\rho}{\partial y\,\partial x} & \frac{\partial^2\rho}{\partial y^2} & \frac{\partial^2\rho}{\partial y\,\partial z} \\ \frac{\partial^2\rho}{\partial z\,\partial x} & \frac{\partial^2\rho}{\partial z\,\partial y} & \frac{\partial^2\rho}{\partial z^2} \end{pmatrix} \quad \ldots \text{Eq. } 22$$

Diagonalisation of the Hessian matrix $\nabla\nabla^{T}\rho_{(r)}$ yields three diagonal elements, namely: the eigenvalues λ_1, λ_2, and λ_3, which represent principal curvatures; as well as the corresponding eigenvectors:

$$\nabla^2\rho_{(r)} = \frac{\partial^2\rho}{\partial x^2} + \frac{\partial^2\rho}{\partial y^2} + \frac{\partial^2\rho}{\partial z^2} = \lambda_1 + \lambda_2 + \lambda_3, \text{where } \lambda_1 < \lambda_2 < \lambda_2 \quad \ldots \text{Eq. } 23$$

Eigenvalues of a CP are characterised by a specified ranking of the Hessian of $\rho_{(r)}$ (no. of non-zero eigenvalues) and a signature (i.e. sum of the signs of eigenvalues) classification system. CPs that are 'topologically stable' always have a rank of three, which allows for four different sets of combinations, namely, (3, −3), (3, −1), (3, +1), and (3, +3). Definitions of each notation set are as follows:

- (3, −3), implies that all curvatures are negative and that the ρ is at a local maximum at (r);
- (3, −1), two curvatures are negative and, one is positive. The ρ is at a maximum in one plane and minimum perpendicular to that plane at (r);
- (3, +1), represents two positive curvatures and one negative curve, where ρ is at a minimum in one plane and a maximum perpendicular to that plane;
- (3, +3), all curvatures are positive and ρ is a local minimum at (r).

Each type of critical point within the system described above is identified with a component of the molecular structure: (3, −3) nuclear critical point (NCP); (3, −1) bond critical point (BCP); (3, +1) ring critical point (RCP); and (3, +3) cage critical point (CCP).

Through the local form of the virial theorem, one can determine the total electron energy density, $H_{(r)}$; potential energy density, $V_{(r)}$; and kinetic energy density, $G_{(r)}$, from the relationship that exists between the energetic topological parameters and $\nabla^2\rho_{(r)}$ (see Equations 24 and 25 below). Here, $G_{(r)}$ and $V_{(r)}$ are positive and negative quantities, respectively.

$$\frac{1}{4}\nabla^2\rho_{(r)} = 2G_{(r)} + V_{(r)} \quad \ldots \text{Eq. } 24$$

and

$$H_{(r)} = G_{(r)} + V_{(r)} \quad \text{... Eq. 25}$$

The connection between $V_{(r)}$ and $G_{(r)}$ can be used to investigate the degree of covalency of an interaction. When $|V_{(r)}|/G_{(r)} > 1$, then $\nabla^2\rho_{(r)} < 0$ in the internuclear area, indicating covalent or polar bonding, as well as a shared interatomic interaction. When $|V_{(r)}|/G_{(r)} < 1$, then $\nabla^2\rho_{(r)} > 0$, which indicates closed-shell interactions or ionic bonds and NCIs. In this case, $\rho_{(r)}$ rapidly increases away from the BCP.

The delocalisation index, DI(δ), which indicates the number of electrons shared between atomic basins ϕ_i and ϕ_j, can also be used to estimate covalency.[77] Covalent bonding is characterised by high localisation indices, whereas ionic bonds or NCIs are characterised by low indices.

The QTAIM method has become an invaluable tool for describing various non-covalent interactions. The IUPAC definition of halogen bonding, for instance, includes topological analysis of the electron density.[24] There is a bond path and a (3, –1) critical point between two adjacent atomic basins when halogen bonding occurs.

1.10 Studying silver(I) compounds as systems

The general idea for the current research involved the application of NCIs for the creation of non-covalently bonded compounds. The metal-containing compounds (or systems) in the study had to have donor/acceptor characteristics, i.e. dualism, as this is needed for monomer units to form non-covalently bound dimers. The metal compounds of particular interest, in this case, were those involving silver, since silver compounds have several applications in synthesis,[78] catalysis,[79] and medicine.[80] Similarly, the incorporation of halogen atoms within the metal compounds further introduces NCI anchor points, as halogens are known for forming halogen bonds. This was done as halogen bonds have uses in organic catalysis,[22] supramolecular chemistry,[81-83] drug design,[84] biochemistry,[22] crystal engineering,[22] and liquid crystals.[81] The type of halogen atom within the system alternated between chloro-, bromo-, and iodo-substituents in the hopes of creating different non-covalently bound silver(I) compounds, based on the $[Ag_2(Xpy)_2(OBn)_2]$ (X = I, Br, Cl; py = pyridine; OBn = benzoate) coordination environment. Additionally, the use of similar pyridine derivative ligands (halo-pyridines) enable the creation of isostructural silver(I) compounds, and allows analysis of similarities and differences in the influence of the metal center on the metal-involved NCI.

Three molecules were chosen to act as halogen bond donors (XBDs) in this case. These molecules were: 3-chloropyridine (3-Clpy), 2-bromopyridine (2-Brpy), and 2-iodopyridine (2-Ipy). All pyridine derivatives are further capable of π-interactions. Overall, tuning the types of NCIs of the desired silver(I) compound can be accomplished in two ways: by varying the halide (X = Cl, Br, I) of the substituent and by varying the position of the XBD on said substituent molecule (out of the scope of the current study). There were several attempts to control the crystal growth of the ionic salt, of which two general methods are noted, both of which differ by one solvent. The first was slow evaporation from H_2O and DCM over several days in a darkroom. The second was the same except for the use of acetonitrile instead of DCM. It should be noted the second method seemed to dissolve the precursor compounds slightly better than the DCM method. The molecules described herein can be divided into two categories, namely; electrophiles (see Figure 1.10 below) and nucleophile, where the nucleophile is the $[Ag_2OBn_2]$ complex. An analysis of the Cambridge Structural Database (CSD) identified six compounds similar to synthesized compounds **I**-**V**. These compounds feature a silver-silver dimer and/or exhibit heteroleptic coordination. The following CSD refcodes for the six compounds are given as: BIPKIV[85], ETODAV[86], ETODEZ[86], GONCUK[87], QEWXOI[88], and ZUNNAA[89].

Furthermore, our studies uncovered a polymorph of compound **I** (CSD refcode: BZOAGA)[90], which will be further discussed in Chapter 3.

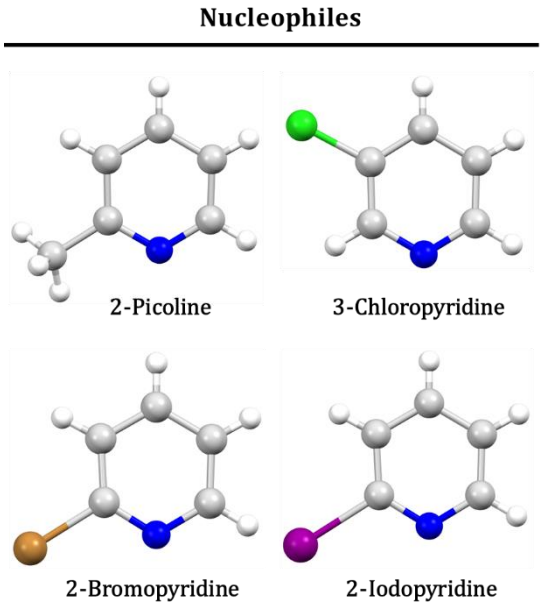

Figure 1.10. Nucleophilic molecules (2-Pic, 3-Clpy, 2-Brpy, and 2-Ipy) are involved in the synthesis of the silver(I) compounds II-V.

Molecules with electrophilic centers, i.e. the silver(I) ions, interact with neighbouring molecules with nucleophilic character, i.e. the halogen's electron belt or a double bond, to yield eight new crystals self-assembled via NCIs. They are: $[Ag_2(OBn)_2]$…(**I**), $[Ag_2(2\text{-Pic})_2(OBn)_2]$…(**II**), $[Ag_2(3\text{-Clpy})_2(OBn)_2]$…(**III**), $[Ag_2(2\text{-Brpy})_2(OBn)_2]$…(**IV**), $[Ag_2(2\text{-Ipy})_2(OBn)_2]$…(**V**), $[Ag(py)_2(OBn)]HOBn$…(**VI**), $[Ag_2(4\text{-Pic})_4](NO_3)(OEt)$…(**VII**), and $[Ag(3\text{-Ipy})_2]NO_3$…(**VIII**). Compounds **I-V** form a coherent series (see in Figure 1.11) and are described further later on in Chapters 3 and 4, while compounds **VI-VIII** did not fit into the series. Their structures are described in Chapter 5.

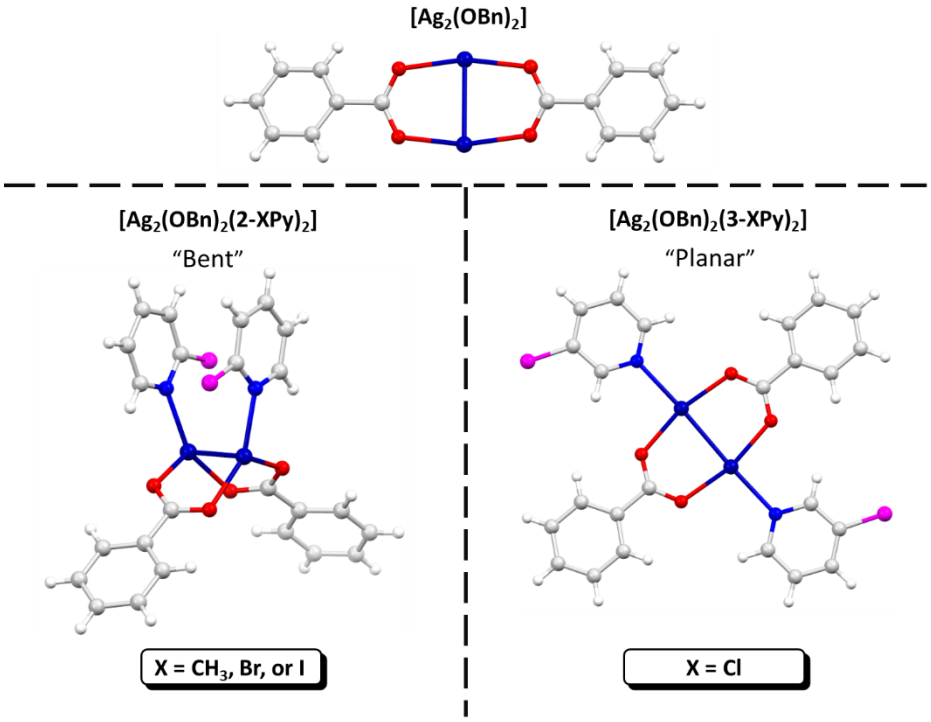

Figure 1.11. Structures of silver(I) compounds studied in this work. Compound **I** is denoted by the formula $[Ag_2(OBn)_2]$. Compounds **II**, **III**, **IV**, and **V**, with magenta atoms (X) representating pyridyl substituents (i.e., CH_3, Cl, Br, and I), are given the general formula $[Ag_2(OBn)_2(X\text{-}Py)_2]$.

1.11 Aims of the study

In contrast to covalent and/or ionic bonds, non-covalent interactions (NCIs) are generally considered to be relatively weak.[91] Despite this, the cooperative or additive effect of several NCIs may enhance the final material's stability.[92] This study aimed to design non-covalently bonded compounds as crystalline materials by using a well-known NCI; halogen bonding.[24] This effort also aimed to improve general understanding of intermolecular interactions by combining several approaches, such as: single-crystal X-ray crystallography, powder X-ray diffraction (PXRD), computational analysis, and thermogravimetric analysis (TGA). With a more in-depth understanding of non-covalent bonding, NCIs may be used in crystal engineering more precisely,[93] particularly within supramolecular chemistry. In the case of the current study, single crystal X-ray diffraction was used as the main experimental analysis method, along with several computational approaches such as QTAIM, EDA, and NBO analysis. The combination of these techniques enables analysis of the nature of the NCIs foregrounded herein.

The major goal of the current dissertation was to create novel silver(I) halopyridyl compounds bonded by NCIs. The additional subgoals were to:

- Study the influence of various halogen bond donors, i.e. Cl, Br, and I;
- Investigate the nature and role of metal-involved interactions (e.g. $M^+\cdots X$, $M^+\cdots\pi$, and $M^+\cdots M^+$) in the silver(I) compounds synthesised;
- Consider the influence of NCIs on the geometry of the compound as well as the structure of the obtained crystals.

Chapter 2

Materials and Methods

The materials and methods utilised in the course of this dissertation are identified in this chapter. The instrumentation, techniques, procedures, and further analyses are all outlined.

2.1 Materials for synthesis

Chemicals were purchased in reagent grade (≥ 99% purity) from Merck and Sigma-Aldrich and used as received unless specified otherwise. Solvents such as dichloromethane (≥ 99% purity), nitric acid (≥ 70% purity), acetonitrile (≥ 99% purity), and Milli-Q® water were also acquired from Merck and Sigma-Aldrich. Other solvents were purified by distillation before use.

2.2 Experimental procedures

The general synthetic procedure used to prepare the silver(I)-halopyridyl complexes are outlined in this section, below. Techniques used for structural elucidation and full characterisation of the synthesised materials are also presented herein.

2.2.1 Synthesis and crystallization of compounds I-VIII

1 mmol sodium benzoate (C_6H_5COONa) and 1 mmol pyridyl ligand were dissolved in 1 mL water after which 3 mL acetonitrile (CH_3CN) was added under stirring for ca. 1 h at room temperature. In another beaker, 1 mmol silver(I) nitrate ($AgNO_3$) was dissolved in 2 mL CH_3CN.[94-96] The sodium benzoate-pyridyl solution and $AgNO_3$ solution were simultaneously added to one another, forming a colourless solution. The obtained solution was left at ambient temperature under dark conditions. After standing for one week, single colourless crystals of $[Ag_2(C_6H_5COO)_2(Xpy)_2]$ were formed in the solution. The crystals were filtered, washed with cold water then stored for analysis. (Note: the alternative method used DCM in place of CH_3CN)[97] The synthesis of the silver(I) halopyridyl compounds is represented by the general equation:

$$2AgNO_3 + 2C_6H_5COONa + 2Xpy \rightarrow [Ag_2(C_6H_5COO)_2(XPy)_2] + 2NaNO_3$$

2.3 Thermal analysis

Thermogravimetric analysis (TGA) was used to evaluate the physical properties of the compounds. This technique determined the change in physical properties (i.e. mass loss) of the sample as a function of temperature. TGA was used to model the number of guest molecules in the crystal structure and to determine the thermal stability of the host framework.

2.3.1 Thermogravimetric analysis (TGA)

Samples were prepared by removing crystals from the mother liquor, blotting them on filter paper, and leaving them to dry. Crystals were gently crushed, sieved, and weighed directly into open aluminium oxide crucibles. Particle size was not measured during the thermal investigation since it was not a parameter relevant to the current scope of the study. A total of 4−10 mg was used in the samples of compounds **I-V**. Unless stated otherwise, experiments were performed over a temperature range of 30−400 °C at a heating rate of 20 °C·min^{-1} under dry N_2 gas with a flow rate of 40 cm^3·min^{-1}. Thermogravimetric analysis was performed using a TA-Q500 thermo-gravimetric analyser, and the TG results were analysed using TA Instruments Universal Analysis 2000 software.

2.4 X-ray diffraction (XRD) analysis

X-ray diffraction (XRD) was utilised to provide detailed information on the crystallographic structures of compounds **I-VIII**. This technique was also applied in order to identify and characterise the bulk crystalline material of all samples, enabling rapid determination of the sample's purity.

2.4.1 Single crystal X-ray diffraction

Good quality single crystals were selected from the mother liquor to perform single-crystal X-ray diffraction (SCXRD). To prevent loss of solvent or decomposition, selected crystals were immediately covered in Paratone-N oil. Suitable single crystals were selected under a microscope and attached to a nylon loop connected to a rigid mount. In the instance where the single crystals were too large, they were cut to obtain the appropriate size, between 30 and 300 μm. This was followed by mounting the nylon loop on the goniometer head under a cold stream of N_2 gas. Crystal data for compounds **I-VIII**: $[Ag_2(OBn)_2]$, $[Ag_2(OBn)_2(2\text{-pic})_2]$, $[Ag_2(OBn)_2(3\text{-Clpy})_2]$, $[Ag_2(OBn)_2(2\text{-Brpy})_2]$, $[Ag_2(OBn)_2(2\text{-Ipy})_2]$, $[Ag(py)_2(OBn)]HOBn$, $[Ag_2(4\text{-Pic})_4]\cdot H_2O(NO_3)(OEt)$, and $[Ag(3\text{-Ipy})_2]NO_3$ were collected with the Bruker DUO APEX II diffractometer equipped with a CCD detector using monochromated Mo K_α radiation (λ = 0.71073 Å). X-rays were generated by a Bruker K780 generator powered at 50 kV and 30 mA. Data collections were carried out at a low temperature of ca. 100 K using a Cryostream cooler (Oxford Cryostems, UK) at a flow rate of 20 $cm^3 \cdot min^{-1}$. APEX II software was used for controlling the data collection and determining the unit cells before data collection. The intensity data were collected using the ϕ and ω scan techniques, scaled and reduced with SAINT-Plus.[98] The correction of the collected intensities for absorption was executed using the SADABS program.[99] XPREP[100] was used to process and prepare input files for SHELXT 2014/5[101] and SHELXL 2018,[102] which were used to solve and refine the structures using the OLEX2 graphical interface.[103] All non-hydrogen atoms were refined isotropically or anisotropically depending on the occurrence of disorder in the structures. Some C−C and C−O bond lengths in disordered molecules were restrained. All C−H hydrogen atoms were placed geometrically and refined with a riding model for their isotropic temperature factors. Diagrams were generated using Mercury (2020 3.0).[104] To display and calculate the percentage volume of voids, this study made use of the Mercury default probe radius (1.2 Å), approximate grid spacing (0.7 Å), and the 'contact surface' method.

2.4.2 Van der Waals (vdW) radii

The distances between atoms that interact non-covalently (at least those that have been measured experimentally) are typically shorter than the total of the equivalent vdW radii in NCIs.[105] Regarding NCIs, Bondi's vdW radii are frequently employed, with examples listed in Table 2.1.[106] As a result, a typical measure for calculating and contrasting the relative strengths of NCIs is the distance reduction ratio (R_{IX}). A shorter contact, for instance, results in a stronger NCI. The distance reduction ratio may be calculated as follows:

$$R_{IX} = \frac{d(I \cdots X)}{R^{I}_{vdW} + R^{X}_{vdW}} \quad \text{... Eq. 26}$$

In the equation above: I represents the electron-deficient atom; X is the electron-rich atom; d(I···X) is the distance between I and X; and R^{I}_{vdW} and R^{X}_{vdW} are the corresponding vdW's radii of I and X.

Table 2.1. Selected values for Bondi's vdW radii.[100]

Atom	vdW	Atom	vdW
H	1.20 Å	**Cl**	1.75 Å
C	1.70 Å	**Br**	1.85 Å
N	1.55 Å	**Ag**	1.72 Å
O	1.52 Å	**I**	1.98 Å

2.4.3 Molecular similarity calculations

The molecular similarity between compounds **I** and BZOAGA was evaluated using the root-mean-square deviation (RMSD) of the atomic positions. The RMSD is calculated with the formula:

$$\mathrm{RMSD} = \sqrt{\frac{1}{N}\sum_{i=1}^{N} d_i^2} \quad \text{... Eq. 27}$$

where N is the number of atoms in the compound and d_i is the distance between atom i in compound **I** and the corresponding atom in BZOAGA. A smaller RMSD value indicates higher similarity between the two molecules being compared.

2.4.4 Powder X-ray diffraction (PXRD)

Measurements were recorded on a Bruker D8 powder X-ray diffractometer using Cu Kα radiation (λ = 1.5418 Å). X-rays were generated by a current flow of 40 mA and an accelerating voltage of 30 kV. Samples were gently ground into a fine powder and placed on a zero-background sample holder, and subsequently scanned over the 2Θ range between 4° to 40°, with a step rate of 0.016°sec^{-1}. A receiving slit of 0.6 mm and primary and secondary slits of 2.5 mm was used. Powder diffraction traces were recorded at 298 K and repeated at intervals of 25 min. The generated powder data were saved as text files and the PXRD graphs were plotted using Microsoft Excel 2018.[107]

The calculated PXRD patterns were generated using the Mercury[104] program package. Calculated PXRD patterns were used to determine the phase purity of the bulk material by acting as a reference when compared to the experimental PXRD patterns.

2.5 Hirshfeld surfaces

The quantification of the various types of intermolecular interactions and their contributions to crystal packing was investigated through Hirshfeld surface (HS) analysis. This was performed through the Crystal Explorer 17 program package.[108] Calculations are based on the information provided by the crystallographic structure (CIF file). HS distribution of a particular complex is shown through d_{norm},[57] d_i, and d_e mapping. Here, d_e and d_i are the distances from a given point on the surface to the nearest atom outside and inside, respectively. The d_{norm} surface shows a brick-red circular area in some places in the HS, which indicates close contact with the neighbouring molecules. The blue regions were related to contacts longer that the sum of the vdWs radii. Two-dimensional (2D) fingerprint (FP) plots provide information about the type of intermolecular contact between atoms, and analyse the differences in these patterns that represent a major intermolecular connection in the entire crystal structure.

2.6 Theoretical Studies

Experimental investigations of non-covalent interactions (NCIs) are not always feasible. That said, the possibility to investigate NCIs may be accessible to scientists by means of theoretical modelling.

Nucleophile/electrophile pairings between molecules within a given system can be identified through electrostatic surface potential (ESP) analysis. Pairings may be further justified by QTAIM analysis, which gives an estimation of the interaction's degree of covalency. Comprehension of the magnitude of the donor-acceptor interactions can also be determined via natural bonding orbital (NBO) analysis.[115] Together, these approaches make it possible to anticipate potential structures of systems of interest and enhance our comprehension of NCIs.

2.6.1 Computational details

DFT calculations were performed using the Gaussian16[109] suite of programs in order to gain more insight into the nature of the various NCIs present within each compound. Structures were optimised from their SCXRD data at the DFT hybrid functional B3LYP (Becke, 3-Parameter, Lee-Yang-Parr)[110] level of theory. The Dunning's correlation consistent basis set, with added AUG diffuse function aug-cc-pVTZ-PP,[111] an ultrafine mesh for numerical integration, and a full geometry optimisation with tight convergence criteria were utilised for all monomeric compounds, **I**-**V**. For the dimeric compounds of **I**-**V**, the cc-pVTZ-PP basis set was used due to computational costs. The basis set superposition error (BSSE)[68] was compensated for by implementing correction factors such as counterpoise dispersion.[112] For a more accurate measurement of the extent of such metal-involved interactions, AIM (atoms in molecules) analysis was performed. The QTAIM software[113,114] was utilized for the topographical analysis of compounds **I**-**V**. Further, natural bond orbital (NBO) analysis was performed using NBO program[115] to investigate the magnitude of the donor-acceptor interactions in the metal-involved interactions. All structures were visualised using the Chemcraft program.[116]

Chapter 3

Results and Discussion

This chapter outlines the main research questions of the current dissertation. First, the choice of systems is outlined, the aims of the study are detailed, and the chapter continues with an analysis of the influence of various non-covalent interactions (NCIs) on the crystal packing of each system.

3.1 Crystallography and structural characterisation

Single crystal X-ray diffraction (SCXRD) is one of the most widely used techniques for determining the structure of molecules. This technique is capable of obtaining useful data regarding the spatial arrangement of atoms as well as useful geometrical parameters like bond lengths and angles. X-ray crystallography can provide valuable information of close-contacts between atoms. In NCIs, the sum of the corresponding vdW radii is typically shorter than the distances between non-covalently interacting atoms that have been measured experimentally using SCXRD.

3.2 Single-crystal X-ray diffraction (SCXRD) analysis of compound I

Figure 3.1 below represents the molecular structure of compound **I**. Relevant bond distances and bond angles are summarised in Table 3.1 below, with standard deviations in parentheses. Structural information of compound **I** is as follows: asymmetric unit (ASU) consists of one silver(I) metal (centre) and one benzoate ligand (OBn). Within the ASU only the O1 atom of the OBn ligand is coordinated to the silver(I), where: d(Ag1···O1) = 2.219(5) Å. The symmetry generated molecular structure shown in Figure 3.1(b) below illustrates two benzoate fragments, each bridging a pair of Ag(I) atoms [d(Ag^{I}···Ag^{I}) = 2.885(14) Å], forming a [$Ag_2C_{14}H_{10}O_4$] binuclear system (symmetry code: −x, −y, −z). The Ag^{I}···Ag^{I} separation is within the conventional bonding distance of metallic silver, 2.889 Å.[117] This close contact is seemingly representative of a d^{10}-d^{10} argentophilic interaction.[36,37] The [$Ag_2C_{14}H_{10}O_4$] structure generated in situ can be considered as a secondary building unit (SBU) with the silver(I) and oxygen atoms being the points of extension, denoted as P_o (see Figure 3.2(a) below). The manner in which both the benzoate ligands coordinate to the metals are the same: delocalised carboxylate (CO_2^-) groups adopt a bidentate μ_2-η^1:η^1 mode to bridge the two silver(I) atoms.[118] Regarding the coordination geometry around the silver(I), each silver(I) atom is coordinated to two carboxylate oxygen atoms, which occupy the equatorial positions (two single Ag—O) as illustrated in Figure 3.1(b) below. The Ag—O coordination bond distances are 2.215(6) Å for $O2^{ii}$ and 2.220(6) Å for O1, which are both smaller than the sum of the Bondi's van der Waal radii (3.42 Å).[105,106]

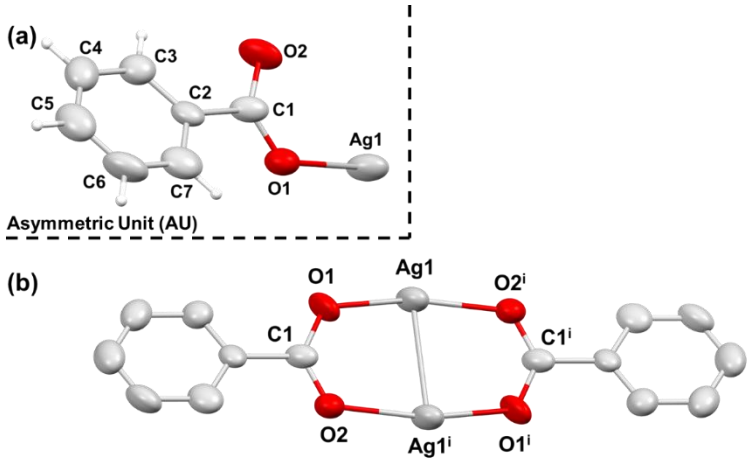

Figure 3.1. Molecular diagrams of compound **I** determined by single crystal X-ray diffraction methods. The structure of the asymmetric unit (a) [$Ag(C_7H_5O_2)$] and of the dimeric [$Ag_2(C_7H_5O_2)_2$] compound (b) is presented. Hydrogen atoms in (b) are omitted for clarity; anisotropic displacement ellipsoids of non-hydrogen atoms are shown at 50% probability. Symmetry code: (i) − x, − y, − z.

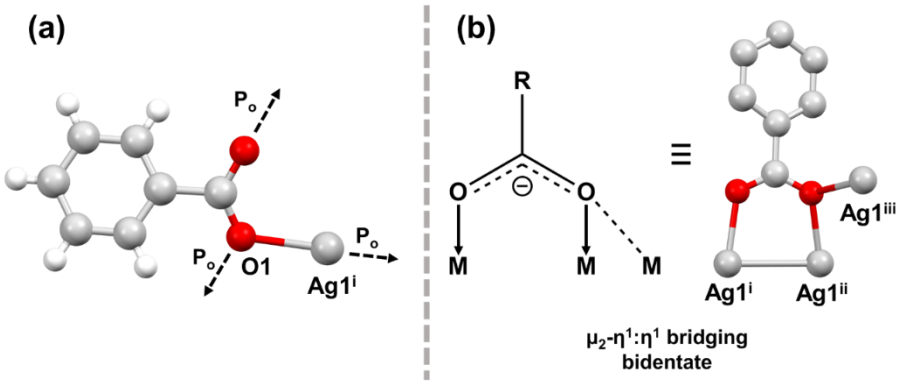

Figure 3.2. (a) The asymmetric unit of compound **I** which highlights the oxygen and silver atoms being points of extension for the secondary building unit. (b) Molecular diagram showing the chelation of the benzoate ligand.

Table 3.1. Selected bond lengths, *d* (Å) and bond angles, ∠ (°) of Ag(I) centres in (**I**).

Bond/Contact	*d*	Bonds	∠
Ag1—O1	2.220(6)	O1—Ag1—O2^{ii}	88.31(19)
Ag1—O2^{i}	2.499(6)	O2^{i}—Ag1—O1	159.5(2)
Ag1—O2^{ii}	2.215(6)	O2^{i}—Ag1—O2^{ii}	108.7(2)
Ag1···Ag1^{i}	2.885(14)	C1—O1—Ag1	122.7(5)
C1—O1	1.268(9)	Ag1^{i}—O2—Ag1^{iii}	105.0(2)
C1—O2	1.256(9)	C1—O1—Ag1^{iii}	118.1(5)
-	-	C1—O1—Ag1^{i}	124.1(5)
-	-	O2—C1—O1	126.9(2)

Symmetry code: (i) 1−x, 2−y, 1−z, (ii) ½ −x, 3/2−y, 1−z, (iii) -1/2+x, 3/2-y, 1-z

3.2.1 Atom connectivity

Molecules of compound **I** are linked to each other through C1-O1···Ag1 semi-coordination bonds, forming two-dimensional (2D) silver(I)/OBn sheets (see Figure 3.3 below). The distance [d(Ag1···O1) = 2.499(6) Å] is shorter than the sum of the Bondi's vdW radii (3.24 Å) [105,106] but is considered too long for a conventional coordination bond. Figure 3.3(c) below depicts the polymeric chain formed by adjacent silver(I) centres of the compound **I**, where the adjacent silver(I) cores are bridged by OBn moieties along the crystallographic b direction and are linked by non-covalent Ag^{I}···π and Ag^{I}···O(carboxyl) interactions.

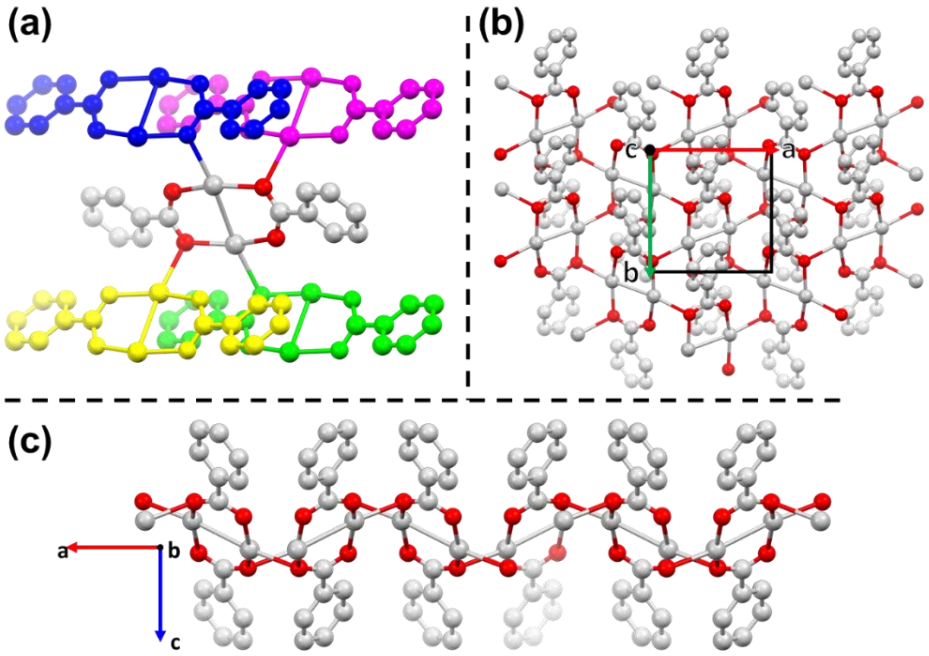

Figure 3.3. Representations of three different viewpoints (a), (b), and (c) of the crystal packing of compound **I**: (a) connectivity of I with adjacent compounds; (b) complex three-dimensional (3D) packing viewed down the c-axis; (c) two-dimensional (2D) polymer chain when viewed down the b-axis. These images together illustrate the intermolecular semi-coordination bonds that construct a three-dimensional (3D) framework. H-atoms are omitted for clarity.

3.2.2 Crystallographic evaluation of short contacts

According to Lindeman, Rathore, and Kochi;[35] the criteria for classifying close contacts as $M^{n+}\cdots\pi$ interactions for silver(I) compounds with aromatic donors are determined by studying three 'essential' structural features. Two examples can be seen in Figure 3.4 below. Firstly, silver(I) atoms generally lie within a relatively narrow range of separation from the coordinated benzene's mean plane, which averages around d_{avg} = 2.41(5) Å. Secondly, no preference is shown by silver(I) toward either coordination type η^1 or η^2. It is important to note that silver(I) generally occupies a narrow arc over the periphery of the coordinated benzene ring, and its deviation Δ from the centroid axis (where the centroid of the ring is defined by atoms C2, C3, C4, C5, C6, C7) can be used to calculate its azimuthal position. The angle β and the distance Δ should be approximately 32(3)° and 1.53(2) Å, respectively. Thirdly, a 'grab' angle α between the coordinate benzene planes lies within three sharply defined regions, 95°, 130°, and 155° (typically within 3°) corresponding roughly to octahedral, tetrahedral, and linear hybridizations of silver.

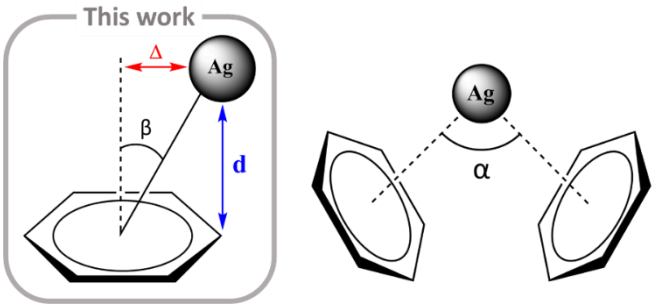

Figure 3.4. Geometric parameters that define $Ag^{I}\cdots\pi$ interactions (based on work by Lindeman, Rathore, and Kochi).[35]

Given the aforementioned criteria, it appears that compound **I** exhibits slight deviations from the relevant criterion (with only the first and second only being applicable) that define Lindeman, Rathore, and Kochi's $Ag^{I}\cdots\pi$ interactions.[35] For instance, the distance parameter, measuring the normal separation of silver(I) from the mean aromatic plane in compound **I** is approximately 0.5(1)Å longer than the expected value (d = 2.41(5)Å), see Table 3.2 below detailed values. These deviations may be akin to the other intermolecular forces present within the crystal system.

Table 3.2. Geometric parameters that define $Ag^{I}\cdots\pi$ interactions in compound **I**.

Compound	Ligand	Metal (precursor)	$Ag^{I}\cdots C_n$/Å (n = 2, 3, 4)	*d*/Å	β/°	Δ/Å
I	benzoate	$AgNO_3$	3.240(5), 2.393(5), 3.343(7)	2.925(2)	28.88	1.612

Another method of identifying $Ag^{I}\cdots\pi$ interactions would be via the mode in which silver(I) compounds associate with particular carbon atoms of the phenyl ring. There are thought to be four types of $Ag^{I}\cdots\pi$ interaction modes, namely m-η^1, p/m-η^2, o/m-η^2, and o/m/p-η^3 (see in Figure 3.5 below).[119] Concerning **type I**, the benzoate ligand can coordinate one silver(I) atom at the meta-position of the phenyl ring (η^1); regarding **type II**, one benzoate ligand coordinates one silver(I) atom at the *meta*- and *para*-position of the phenyl ring (η^2); regarding **type III**, similarly to **type II**, it coordinates one silver(I) atom at two positions on the phenyl ring, but with a slight alteration: instead of coordinating to the *para*-position, the Ag(I) atom interacts with the *meta*- and *ortho*-position (η^2). Regarding **type IV**, one benzoate ligand coordinates one silver(I) atom at the *ortho*-, *meta*-, and *para*-positions of the phenyl ring (η^3).

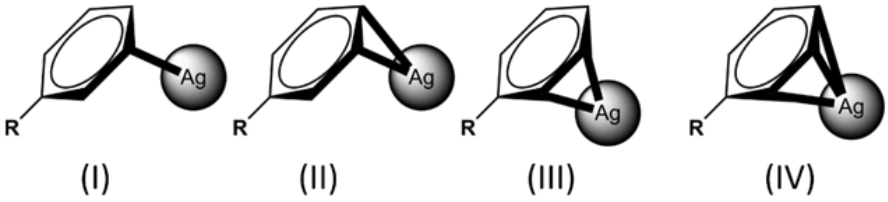

Figure 3.5. Four types of $Ag^{I}\cdots\pi$ interactions, m-η^1 (I), m/p-η^2 (II), o/m-η^2 (III), and o/m/p-η^3 (IV). Here, R = carboxylate group.

The major driving force behind packing appears to be from the formation of an attractive intermolecular $Ag^{I}\cdots\pi$ interaction between the *ortho*- and *meta*-carbons (η^2) of the phenyl group (see in Figure 3.6 below). Such an interaction would be classified as a modified **type IV**, in which the carbon atom closest to the '-R' group replaces the *para*-carbon's position. The uncommon η^3 coordination geometry in compound **I** seems to be consistent with the coordination geometry of some previous Ag·benzoate compounds, with the $Ag^{I}\cdots C_{(aromatic)}$ contacts ranging from 2.939 - 3.240 Å, CSD refcode: BZOAGA.[90] These prominent $Ag^{I}\cdots\pi$ contacts within compound **I** (see Figure 3.7 below) are thought to be the major driving force behind packing within the crystal structure. To better substantiate this, Hirshfeld surface analysis was performed on compound **I**.

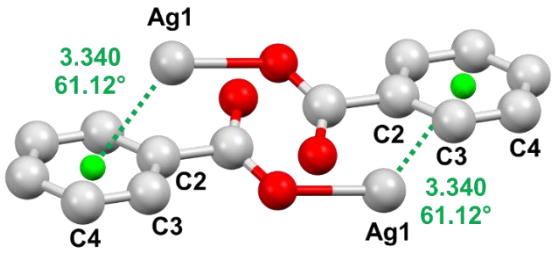

Selected bond lengths (Å)
Ag1—C2 = 3.240(5)
Ag1—C3 = 2.939(5)
Ag1—C4 = 3.343(7)
Selected bond angles (°)
Ag1—(•)—C2 = 73.90
Ag1—(•)—C3 = 61.31
Ag1—(•)—C4 = 78.29

Figure 3.6. Crystal packing of **I** showing the occurrence of double $Ag^{I}\cdots\pi$ interactions. Interactions are generalised by showing the Ag^{I}-centroid (Centroid, Cg are represented as green spheres) distances. It should be noted that interactions take place mainly through carbons 2, 3, and 4. Hydrogen atoms are omitted for clarity. Distance (Å) and angle (°) parameters are shown in green.

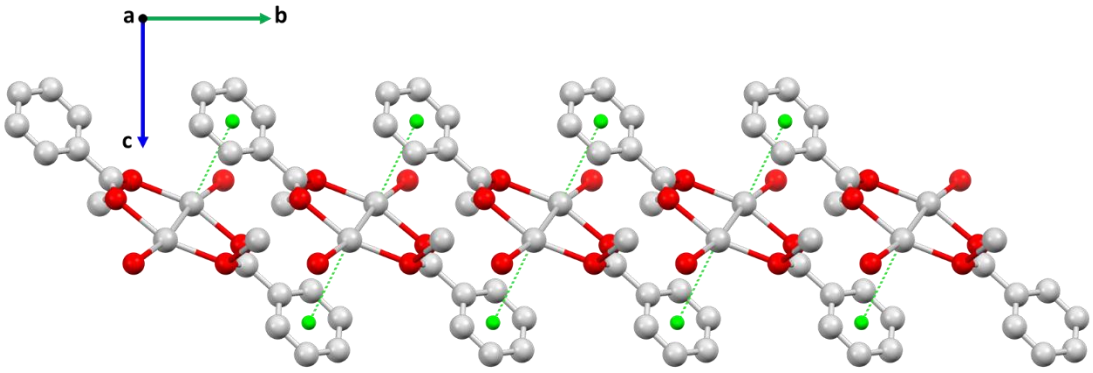

Figure 3.7. Crystal packing diagram of compound **I**. Aromatic hydrogen atoms in compounds have been omitted for clarity. Intermolecular $Ag^{I}\cdots\pi$ interactions are depicted as dashed green lines.

3.2.3 Hirshfeld surface (HS) analysis

Hirshfeld surfaces (HSs) allow for the comparison of analogous structures by providing information about a molecule's immediate environment and non-covalent intermolecular interactions.[54]

HSs of compound **I** are illustrated in Figure 3.8 below, showing surfaces mapped with d_{norm} (-0.5 to 1.4 Å),[57] d_e (1.0 to 2.7 Å), and d_i (1.0 to 2.9 Å) properties. The HS mapped with d_{norm} uses a red, white, and blue colour scheme: contacts with distances equal to the sum of van der Waals (vdW) radii are represented as white-coloured regions, while contacts with distances shorter or longer than the sum of vdW radii are shown in red and blue, respectively. Important quantitative information of the main intermolecular contacts in compound **I** was obtained by plotting 'translated' two-dimensional (2D) fingerprint (FP) plots, as shown in Figure 3.9 below. In this case, one molecule acts as a donor ($d_e > d_i$) and the other as an acceptor ($d_i > d_e$).

The FP plots were selected to be decomposed (see Figure 3.9) as decomposition allows for the separation of contributions from different interaction types, which overlap in the full fingerprint.[54,57] The distance of $Ag^{I}\cdots O$ in this compound [d(Ag1⋯O1) = 2.499(6) Å] is shorter than the sum of the vdW radii (3.24 Å).[105,106] These contacts can be seen as red depressions on the d_{norm} map, and are labelled as (1). This is indicative of the silver(I) atoms interacting with the O-atoms of the carboxylate groups, allowing for the formation of the bidentate μ_2-η^1:η^1 mode.[118] These interactions are also visible in the FP plots as a pair of symmetrical spikes at ($d_e + d_i$) ≅ 2.65 Å, and which constitutes 9.3% of the total HS area of the molecular moiety. The prominent light red coloured (relative to the Ag⋯O interactions) depressions near the silver(I) atom and phenyl ring, labelled as (2) in Figure 3.8, indicate moderate Ag⋯C contacts arising from $Ag^{I}\cdots C_{(aromatic)}$ connectors. The distance of Ag⋯C in this compound [d(Ag1⋯C3) = 2.939(5) Å] is shorter than the sum of the vdW radii (3.42 Å).[105,106] As per Figure 3.9, the relatively broad spikes in the FP plot are attributed to Ag⋯C/C⋯Ag molecular interactions, which comprise 6.2% of the total HS area. Inspection of the other atom contacts showed that various other interatomic contacts are also present, such as O⋯O, C⋯O/O⋯C (4), O⋯H/H⋯O (3), C⋯H/H⋯C (5), and H⋯H (6), which contribute 1.1, 6.7, 12.9, 23.3, and 33.4% to the total HS area, respectively.

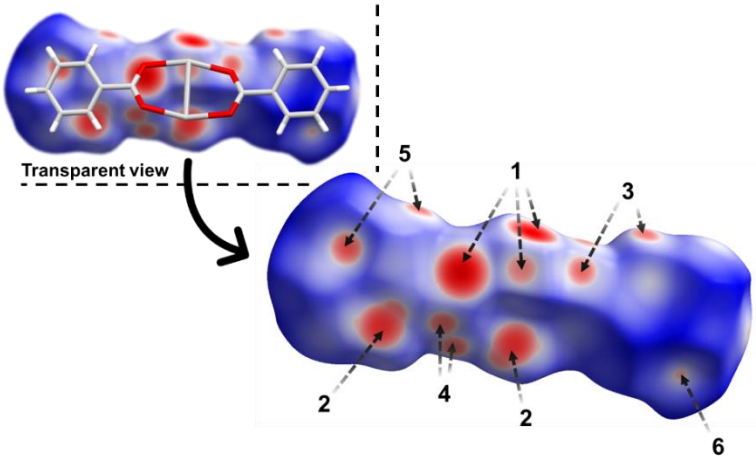

Figure 3.8. Hirshfeld surfaces of compound **I** mapped with d_{norm} function.[58] The labels are discussed in the main text.

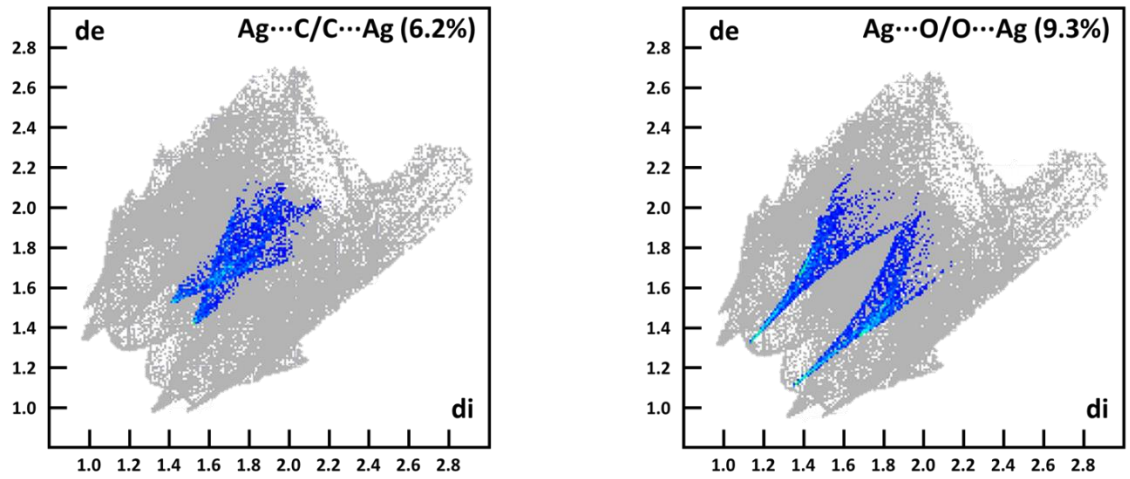

Figure 3.9. Decomposed two-dimensional (2D) fingerprint plots for compound **I**. Close contacts are labelled as follows: (a) Ag···C/C···Ag and (b) Ag···O/Ag···H.

3.2.4 Comparison with BZOAGA polymorph

Relevant selected bond distances and angles for the $[Ag_2(OBn)_2]$ polymorphs are given in Tables 3.3 and 3.4 below. In each structure, referring to compound **I** and BZOAGA,[90] the molecular unit contains two silver(I) ions bound to two benzoate ligands, which chelate the silver(I) metal using their two O atoms. This gives rise to the distinct dimeric Ag_2OBn_2 environments. However, the ASU of compound **I** contains only one silver(I) ion bound to a single benzoate ligand, while BZOAGA seemingly doubles this in its own ASU. For both compounds, the Ag–O1 and Ag–O2 distances are within the range of 2.218–2.239 Å, which is shorter than the sum of the Bondi's van der Waals radii (vdW = 3.24 Å).[105,106] The structures of the two polymorphs both seem to be stabilised by prominent $Ag^{I}\cdots\pi$ interactions, with distances of d(Ag···centroid) = 3.318-3.519 Å and d(Ag···centroid) = 3.340 Å, for BZOAGA and **I**, respectively. The O–Ag–O angles assume values of 88.29(11)° and 97.28° in **I** and BZOAGA, respectively.

Table 3.3. Crystallographic information for the comparison between two silver(I) benzoate polymorphs.

Refcode	BZOAGA	I
Empirical Formula	$C_{14}H_{10}Ag_2O_4$	$C_{14}H_{10}Ag_2O_4$
M_r(g/mol)	457.96	457.96
Temperature (K)	298	100
Crystal size (mm^3)	0.14×0.22×0.17	0.06×0.16×0.60
Crystal system	Orthorhombic	Orthorhombic
Space group	$P2_12_12_1$ (no. 19)	Pbca (no. 61)
a (Å)	6.297(5)	8.943(3)
b (Å)	8.987(6)	6.3030(2)
c (Å)	23.771(15)	23.603(7)
α (°)	90.00	90.00
β (°)	90.00	90.00
γ (°)	90.00	90.00
V ($Å^3$)	1345.2(3)	1330.5(7)
Z	4.0	4.0
Radiation type	Mo Kα	Mo Kα
Calc. density (g/cm^{-3})	2.261	2.286
R^1 (%)	6.7	5.9
$Ag^I\cdots Ag^I$ (Å)	2.90(2)	2.88(5)

Table 3.4. Crystallographic information for the comparison between two silver(I) benzoate polymorphs.

Compound	BZOAGA	I
Bond type	**Bond length (Å)**	
Ag1···Ag1	2.902(3)	2.885(1)
Ag1—O1	2.239(2)	2.219(5)
Ag1—O2	2.221(2)	2.215(6)
	Bond angle (°)	
O1—C1—C2—C7	152.70	154.83(6)
$O1^i$—$C1^i$—$C2^i$—$C7^i$	-158.79	-154.83(6)
O2—C1—C2—C3	155.07	158.44(6)
$O2^i$—$C1^i$—$C2^i$—$C3^i$	-154.61	-158.44(6)

*Note: Original paper for BZOAGA did not give torsion angles, so standard deviations are omitted.

3.2.5 Packing polymorphism

The compound in **I** has previously been reported as CSD refcode: BZOAGA.[90] Single crystal X-ray diffraction studies revealed that compound **I** and BZOAGA have similar binuclear structures but crystallise in different space groups. Thus, these are polymorphs[5] of $[Ag_2(OBn)_2]$: both are orthorhombic, with BZOAGA crystallising in $P2_12_12_1$ and **I** in *Pbca*. Each molecule of the silver(I) compounds possesses two benzoate groups (OBn) that can adopt multiple torsion angles (τ) indicating the orientation of the benzene ring relative to the carboxylate mean plane. To determine if the compounds display conformational or packing polymorphism, the torsion angles were compared. For BZOAGA these are composed of the atoms ∠O1-C1-C2-C7 for τ_1 and ∠O3-C8-C9-C10 for τ_2, and atoms ∠O1-C1-C2-C7 for τ_1^1 and ∠$O1^i$-$C1^i$-$C2^i$-$C7^i$ for τ_1^i in **I**. A comparison of the torsion angles ($\tau_1^1 = \tau_1^i = 154.83$, $\tau_1 = 152.70$, and $\tau_2 = 158.79°$) from each unit presented some slight differences, but after superimposed, said differences are shown to be negligible (see Figure 3.10 below). To quantify the differences between the two forms, we overlaid the two compounds and calculated the root-mean-square deviation ($RMSD_n$, where n is the number matched molecules). The calculated $RMSD_2$ was 0.0765 Å, which supports the claim of a high degree of similarity between the two compounds. One may conclude that these structures, despite the free rotation about the C1-C2 bond of the benzoate groups, do not present as exhibiting conformational polymorphism, but rather, they constitute cases of packing polymorphism. In evidence of the latter claim, the difference in the two packing modes becomes clear through a simple visualisation of the packing patterns (see Figure 3.11 below). Indeed, both structures are organized similarly, but the repetitive arrangements of the $[Ag_2(OBn)_2]$ unit within the unit cell are slightly different.

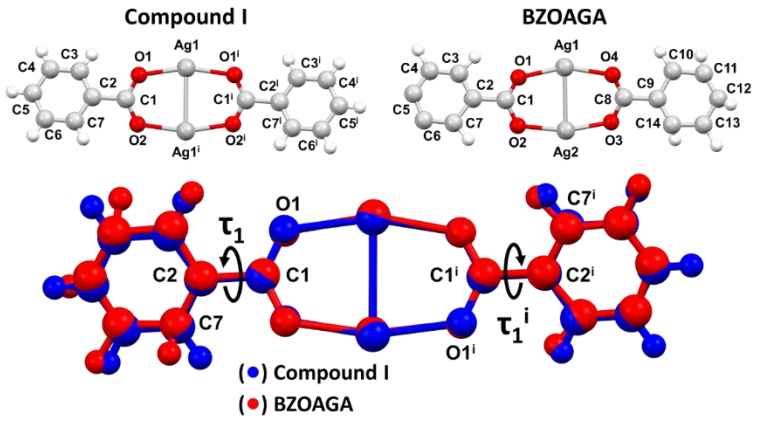

Figure 3.10. Overlay of the two molecular units (unit A from the monoclinic form (red) with unit B from the orthorhombic form (blue)). The flexible torsion angle in the benzoate molecule is numbered and indicated by τ. Symmetry code: (i) − x, − y, − z.

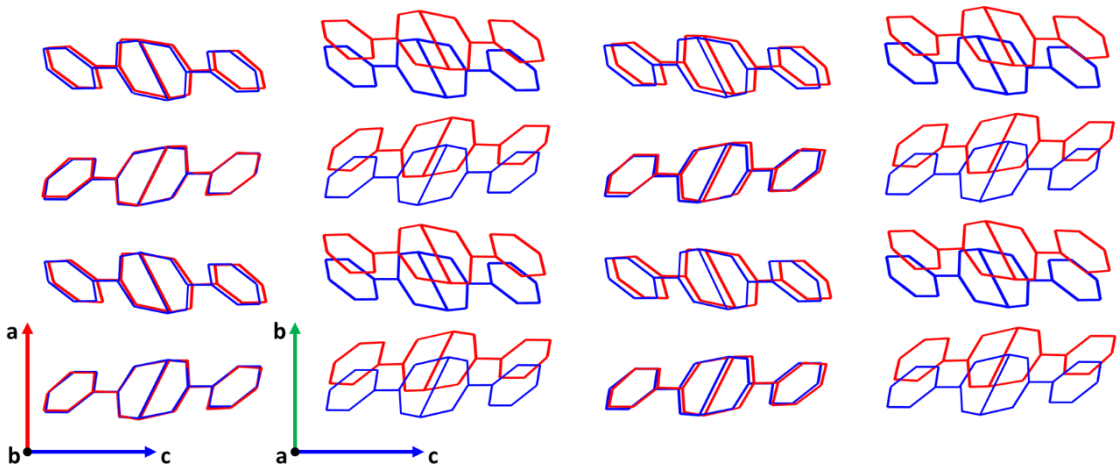

Figure 3.11. Representation of the unit cells of the two polymorphs of $[Ag_2(Bn)_2]$. Compound **I** is represented as blue and BZOAGA as red. H-atoms are omitted for clarity.

3.2.6 Powder X-ray diffraction (PXRD) results

The experimental and calculated PXRD patterns of compound **I** and BZOAGA are depicted in Figure 3.12 below. Although compound **I** and BZOAGA have similar patterns, non-negligible differences can be seen as additional peaks as indicated below. This serves as slight evidence towards the claim that **I** is a polymorph of BZOAGA.

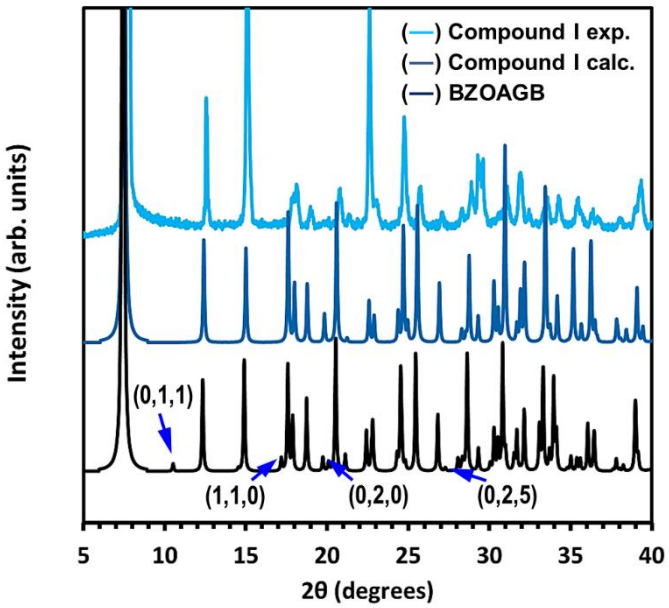

Figure 3.12. Comparison of the experimental powder X-ray diffraction pattern of compound **I** (light blue) and the BZOAGA (dark blue) from single-crystal data.

3.3 X-ray structure determination

X-ray diffraction data of compounds **I**, **II**, **III**, **VI**, and **V** were collected with a Bruker DUO APEX II diffractometer with Mo Kα radiation (λ = 0.71073 Å) at 100 K. The structure was solved using direct methods via SHELXT 2014/5[101] and refined by full-matrix least-squares procedures on F^2 using the program SHELXL 2018.[102] All non-hydrogen atoms were refined anisotropically. Crystallographic data and details of the data collection and structure refinement are summarised in Table 3.5 below.

Table 3.5. Crystallographic information for compounds **I-V**

Compound	**I**	**II**	**III**	**IV**	**V**
Chemical formula	$C_{14}H_{10}Ag_2O_4$	$C_{26}H_{24}Ag_2N_2O_4$	$C_{24}H_{18}Ag_2Cl_2N_2O_4$	$C_{24}H_{18}Ag_2Br_2N_2O_4$	$C_{24}H_{18}Ag_2I_2N_2O_4$
M_r	457.96	644.21	685.05	773.96	867.96
Space group	Pbca (no. 61)	C2/c (no. 15)	C2/c	C2/c	C2/c
Temperature (K)	100	100.10	100	100	100
a (Å)	8.943(3)	21.3081(6)	28.5454(1)	21.6012(1)	22.259(5)
b (Å)	6.3030(2)	9.0100(2)	5.5971(3)	9.0731(4)	9.0046(2)
c (Å)	23.603(7)	12.3688(4)	15.6217(7)	12.8041(6)	13.306(3)
α (°)	90.00	90.00	90.00	90.00	90.00
β (°)	90.00	100.9340(1)	107.1740(1)	108.201(2)	111.39(3)
γ (°)	90.00	90.00	90.00	90.00	90.00
V (Å^3)	1330.5(7)	2331.53(1)	2384.6(2)	2383.92(2)	2483.2(1)
Z	4.0	4.0	4.0	4.0	4.0
$D_{calc.}$ (g cm^{-3})	2.286	1.835	1.908	2.156	2.322
μ (mm^{-1})	2.951	1.716	1.901	5.030	4.097
F(000)	880.0	1280.0	1344.0	1488.0	1632.6
Crystal size (mm)	0.06×0.16×0.60	0.09×0.14×0.34	0.05×0.09×0.12	0.28×0.32×0.33	0.08×0.09×0.23
Radiation type	Mo Kα	Mo Kα	Mo Kα	Mo Kα	Mo Kα
2Θ range for data collection (°)	5.716 to 56.584	4.922 to 61.088	5.394 to 61.158	5.582 to 63.392	3.94 to 61.2
Index ranges	-11 ≤ h ≤ 11, -8 ≤ k ≤ 8, -31 ≤ l ≤ 31	-30 ≤ h ≤ 30, -12 ≤ k ≤ 12, -17 ≤ l ≤ 17	-40 ≤ h ≤ 40, -8 ≤ k ≤ 7, -22 ≤ l ≤ 22	-31 ≤ h ≤ 31, -13 ≤ k ≤ 13, -18 ≤ l ≤ 18	-31 ≤ h ≤ 31, -12 ≤ k ≤ 12, -18 ≤ l ≤ 19
Reflections collected	21850	38781	49008	72364	19162
Independent reflections	1656 [R_{int} = 0.1206, $R_σ$ = 0.0630]	3565 [R_{int} = 0.0404, $R_σ$ = 0.0208]	3647 [R_{int} = 0.0663, $R_σ$ = 0.0331]	3996 [R_{int} = 0.0431, $R_σ$ = 0.0145]	3798 [R_{int} = 0.0401, $R_σ$ = 0.0342]
Data/restraints/parameters	1656/105/79	3565/0/155	3647/0/154	3996/0/154	3798/0/154
Goodness-of-fit on F^2	1.266	1.068	1.027	1.128	1.005
Final R indexes [I>=2σ (I)]	R_1 = 0.0591, wR_2 = 0.1201	R_1 = 0.0229, wR_2 = 0.0413	R_1 = 0.0312, wR_2 = 0.0600	R_1 = 0.0171, wR_2 = 0.0407	R_1 = 0.0240, wR_2 = 0.0399
Final R indexes [all data]	R_1 = 0.0958, wR_2 = 0.1302	R_1 = 0.0305, wR_2 = 0.0434	R_1 = 0.0547, wR_2 = 0.0677	R_1 = 0.0181, wR_2 = 0.0410	R_1 = 0.0366, wR_2 = 0.0429
$Δρ_{max}/Δρ_{min}$ (e Å^{-3})	1.09, -1.10	0.50/-0.42	0.55/-0.82	0.51/-0.66	1.01/-1.10

3.4 Single-crystal X-ray diffraction analysis of compound II

Figure 3.13(a) below represents the molecular structure of compound **II**. Relevant bond distances and bond angles are summarised in Table 3.6 below, with standard deviations in parentheses. The asymmetric unit (ASU) consists of one silver(I) metal (centre), one benzoate ligand (OBn^-), and one 2-picoline (2-Pic) ligand. Within the ASU, only the O1 atom of the OBn ligand and N1 of the 2-Pic ligand coordinate to the silver(I) metal, with d(Ag1···O1) = 2.173(13) Å and d(Ag1···N1) = 2.212(13) Å, respectively. The symmetry generated molecular structure (symmetry code: 1−x, y, 3/2−z) is shown in Figure 3.13(b) below, where two OBn ligands coordinate to two silver(I) ions via the carboxylate oxygen atoms. These oxygen atoms bridge the silver(I) ions in an asymmetric mode, forming the $[Ag_2C_{14}H_{10}O_4]$ binuclear system. Within this system, each silver(I) ion is three-coordinated; with the third (2-Pic) acting as a monodentate chelator and coordinating via the pyridine's nitrogen atom. The $Ag^{I}\cdots Ag^{I}$ separation [d(Ag···Ag) = 2.868(3) Å] is within the conventional bonding distance of metallic silver, 2.889 Å.[117] This close contact suggests a d^{10}-d^{10} argentophilic interaction.[36,37] The manner in which both the benzoate ligands coordinate to the metals is the same: the delocalised carboxylate (CO_2^-) groups adopt a bidentate μ_2-η^1:η^1 mode to bridge the two silver(I) atoms.[118] The Ag—O coordination bond distances are 2.173(13) for O1 and 2.442(13) Å for $O2^i$, which are both shorter than the sum of Bondi's vdW radii ($R_{vdW}(Ag) + R_{vdW}(O)$ = 3.24 Å).[105,106] The AgO_2N coordination environment forms an approximate Y-shape geometry, with a silver(I) at the centre (see Figure 3.13(b)), and with the three subtended angles being 148.41(5), 94.87(7), and 115.76(5)° (see Table. 3.6).

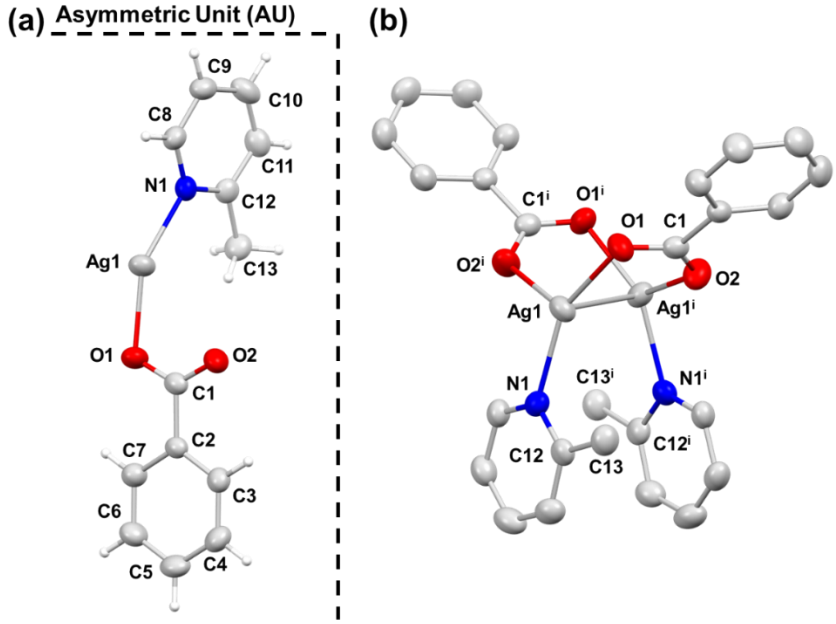

Figure 3.13. Molecular diagrams of compound **II** determined by single crystal X-ray diffraction methods. Illustrated is the structure of the (a) asymmetric unit and of the (b) dimeric $[Ag_2(C_7H_5O_2)_2(C_6H_7N)_2]$ compound with atomic labeling given. Hydrogen atoms are omitted in (b) for clarity; anisotropic displacement ellipsoids of non-hydrogen atoms are given with a 50% probability. Symmetry code: (i) 1−x, y, 3/2−z.

Table 3.6. Selected bond lengths, *d* (Å) and bond angles, ∠ (°) of Ag(I) centers in **II**.

Bond/Contact	*d*	Bonds	∠
Ag1—O1	2.173(13)	O1—Ag1—O2^{i}	165.43(7)
Ag1—O2^{i}	2.442(13)	O1—Ag1—N1	98.49(7)
Ag1—N1	2.212(15)	O2^{i}—Ag1—N1	95.69(7)
Ag1···Ag1^{i}	2.868(3)	C1—O1—Ag1	121.99(17)
C1—O1	1.254(2)	C1—O1—Ag1^{i}	125.81(17)
C1—O2	1.254(2)	O1—C1—O2	126.1(2)

Symmetry code: (i) 1−x, y, 3/2−z.

3.4.1 Crystallographic evaluation of short contacts for compound II

The crystallographic packing of compound **II** seems to be dominated by Ag^{I}···π interactions taking place between the silver(I) transition metal and the pyridyl ring (π-system) of a 2-Pic ligand on an adjacent molecule. The distance between the silver(I) metal and the centroid (Cg) of the aromatic ring of the 2-Pic ligand is given to be d(Ag1···Cg^{i}) = 3.307(3)Å. The angle of the normal to the aromatic ring plane, ∠(Ag1···Cg), with the vector between the centres of the aromatic rings, is 70.55° (see Figure 3.14 below). Interestingly, compound **II** is packed such that the silver(I) ions are directed toward the N1 and C12 atoms of the π-faces of adjacent aromatic rings (see Figure 3.15 below). When analysing these short contacts between the pyridyl ring plane and silver(I), the distance of the nearest aromatic atom (N1), with d(Ag(I)···$N_{aromatic}$) = 3.131(3)Å, is shorter than the sum of Bondi's vdW radii (R_{vdW}(Ag) + R_{vdW}(N) = 3.27 Å). The Ag–C bond distances range from 3.249 to 3.807 Å, which are also shorter than the sum of Bondi's vdW radii (R_{vdW}(Ag) + R_{vdW}(C) = 3.42 Å).[105,106] These sub-van der Waals (vdWs) distances are suggestive of molecular orbital-based (covalent-like) effects, where the transition metal cation/π interactions often exhibit substantial covalent character (η^1-, η^2-, or η^3-interactions), in addition to electrostatic effects.[119]

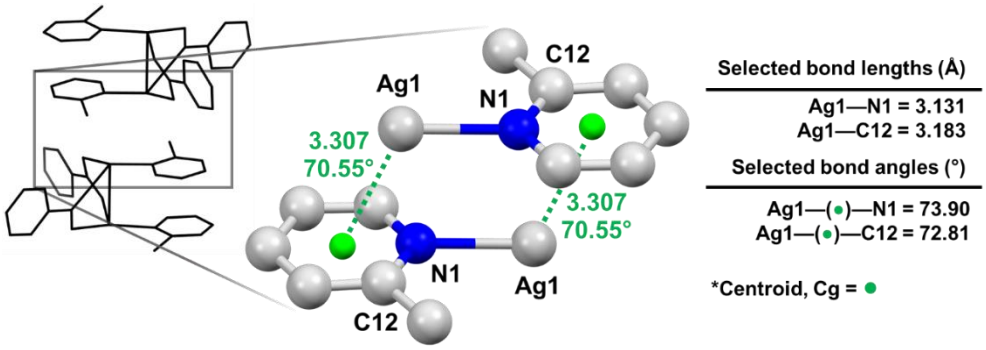

Figure 3.14. Crystal packing of **II** showing the occurrence of double Ag^{I}···π interactions (in green). Interactions are generalised by showing the Ag^{I}/centroid (Centroids, Cg are represented by green spheres) distances. It should be noted that interactions take place mainly through the nitrogen and carbon atoms 1 and 12, respectively. Hydrogen atoms are omitted for clarity. Relevant distance (Å) and angle (°) measurements are shown in green.

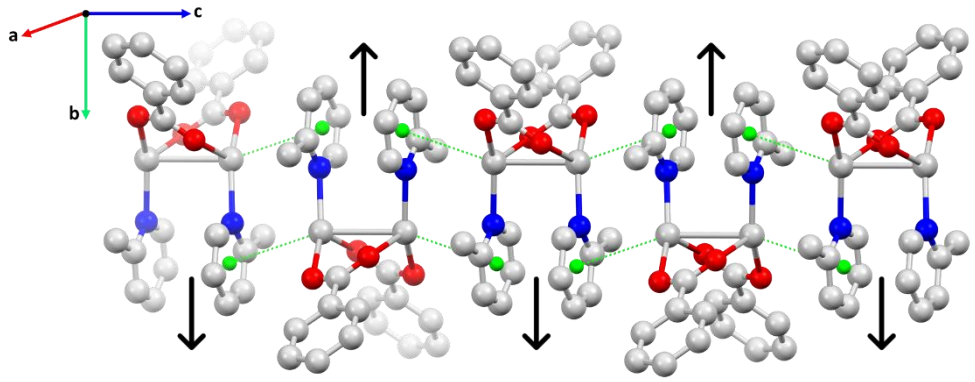

Figure 3.15. Crystal packing of **II** highlighting the non-covalent $Ag^{I}\cdots\pi$ interactions (in green dashed lines). Hydrogen atoms are omitted from this figure for better visualization. (Centroids, Cg are represented by green spheres)

3.4.2 Hirshfeld surface analysis

The three-dimensional (3D) HSs of compound **II** are illustrated in Figure 3.16 below, showing surfaces that are mapped with d_{norm} (-0.1 to 1.3 Å)(a,b),[57] d_e (1.0 to 2.6 Å)(c), and d_i (1.0 to 2.5 Å)(d) properties. Important quantitative information about the main intermolecular contacts in compound **II** was obtained by plotting 'translated' two-dimensional (2D) fingerprint (FP) plots, as shown in Figure 3.17 below. The $Ag^{I}\cdots N_{(aromatic)}$ distance in this compound [d(Ag1···N1) = 3.131(3)Å] is shorter than the sum of Bondi's vdW radii ($R_{vdW}(Ag) + R_{vdW}(N)$ = 3.27 Å).[105,106] These contacts are visible as red depressions on the d_{norm} map (see Figure 3.16(b)) labelled as **1**. This is indicative of the silver(I) atoms interacting with the N-atoms of the pyridyl ligands on adjacent molecules.

These interactions are also visible in the FP plots as a pair of broadened symmetrical spikes at ($d_e + d_i$) ≅ 3.14 Å (see Figure 3.17(a)) and which contribute 1.8% of the total HS area of the molecular moiety. In Figure 3.16(b), larger (relative to the $Ag^{I}\cdots N$ interactions) red-coloured depressions near the Ag1 atom and pyridyl ring, labelled as **2**, indicate moderate Ag···C contacts arising from $Ag^{I}\cdots\pi$ (C12-atom) connectors. The Ag···C distance in this compound [d(Ag1···C12) = 3.183(5) Å] is shorter than the sum of Bondi's vdW radii ($R_{vdW}(Ag) + R_{vdW}(C)$ = 3.42 Å).[105,106] As shown in Figure 3.17(b), the broad spikes in the vicinity of ($d_e + d_i$) ≅ 3.2 Å, and which are observed in the FP plot, are attributed to Ag···C/C···Ag molecular interactions, which comprise 2.7% of the total HS area. These findings indicate a significant presence of $Ag^{I}\cdots\pi$ contacts through the $N\text{-}C_{aromatic}$ atoms in the packing arrangement of the crystal structure. Inspection of the other atom contacts showed that various other interatomic contacts are also present, such as N···N, N···H/H···N, C···O/O···C, O···H/H···O (3), C···H/H···C (4), and H···H, which contribute 0.4, 0.4, 2.4, 13.2, 27.5, and 50.3% to the total HS area, respectively. Most of these contributions occur at separations greater than the sum of the vdW radii.

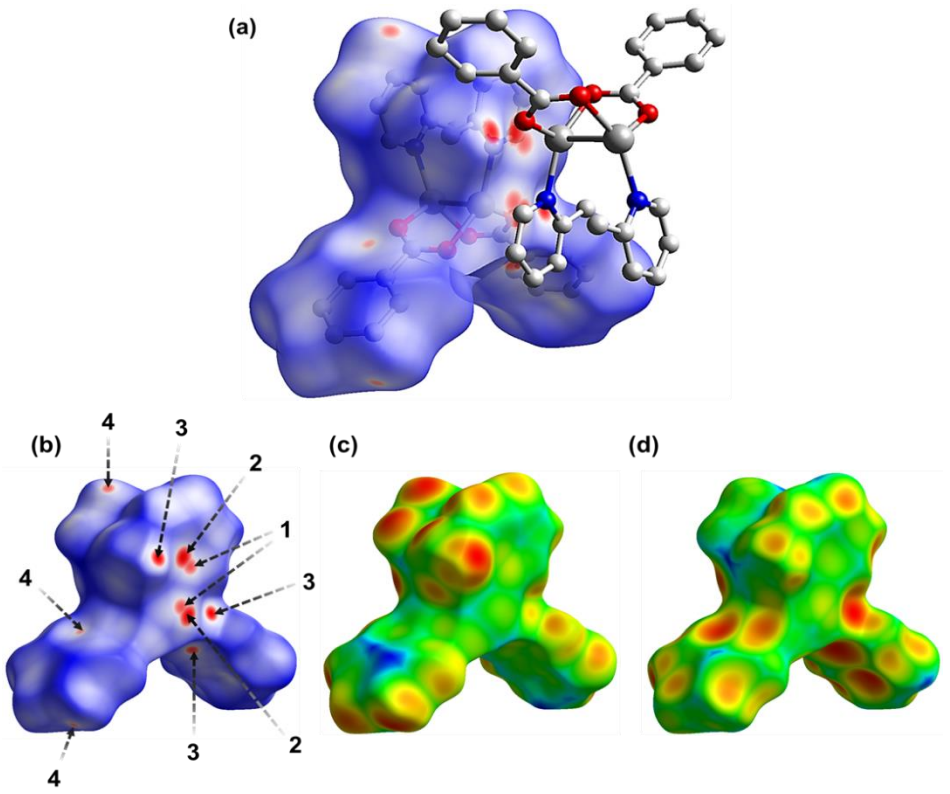

Figure 3.16. (a) A dimer of compound **II** with one molecule surrounded with a d_{norm}[57] decorated HS and the other in a ball and stick presentation. (b) The three-dimensional (3D) HS of II showing the red spots corresponds to the close intermolecular interactions and mapped with d_e (c) and d_i (d).

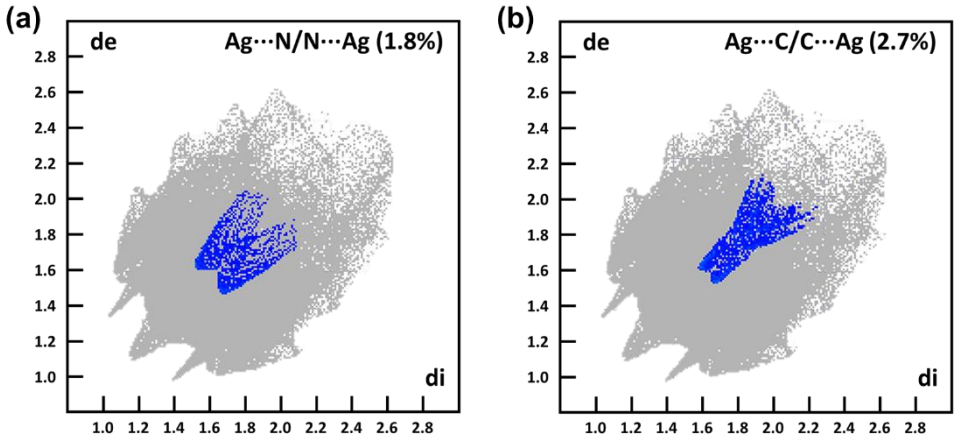

Figure 3.17. Decomposed two-dimensional (2D) FP plots for compound **II**. Close contacts are labelled as follows: (a) Ag···N/N···Ag and (b) Ag···C/Ag···C. For each fingerprint map, the grey area is a representation of the whole plot.

3.4.3 Powder X-ray diffraction analysis

The PXRD pattern of compound **II** is depicted in Figure 3.18 below. The pattern was collected at room temperature and ambient pressure. The bulk material was analysed as is without any further purification. The trace obtained for compound **II** (light blue) is consistent with the calculated pattern (dark blue) from the single-crystal data. The agreement between the experimental data and the calculated pattern proves the phase purity of the bulk material.

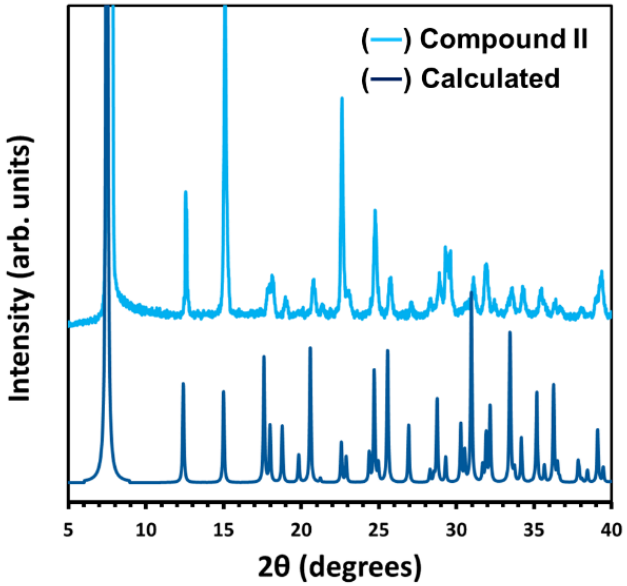

Figure 3.18. Comparison of the experimental powder X-ray diffraction pattern of compound **II** (light blue) and the calculated one (dark blue) from single-crystal data.

3.4.4 Thermogravimetric analysis

The thermal analysis of compound **II** is shown in Figure 3.19 below. The conditions under which compound **II** was studied constituted a temperature range of 20-400 °C, and a heating rate of 10 K·min^{-1} under a nitrogen atmosphere. Compound **II** demonstrates two decomposition stages/steps and is stable up to a temperature of approximately 125 °C. The first experimental weight loss (25.3%) in the range of 65–140 °C takes place with the endothermic removal of the 2-Pic ligand. The calculated weight loss of 27.4% for this stage agrees with the experimental weight loss. The subsequent second stage (250–325 °C) corresponds with the endothermic removal of the OBn ligand, with an experimental weight loss of 31.1% (calcd. weight loss 36.0%). The residual product of the thermal degradation is calculated as silver(I) oxide, ½ Ag_2O (calcd. weight 36.6%, exp. weight 43.6%). The calculated and experimental weight losses for compound **II** are relatively consistent with each other, showing the precision of the proposed structures.

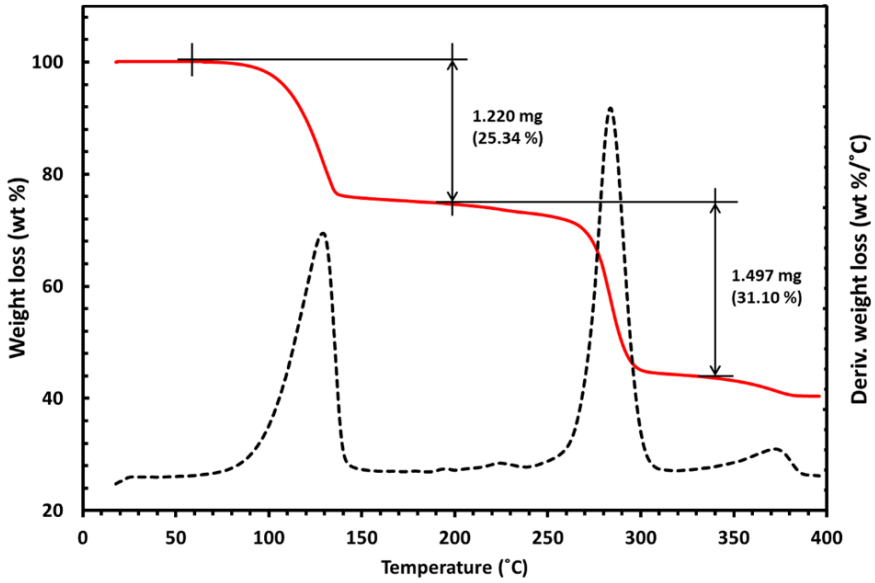

Figure 3.19. Thermogravimetric analysis (TGA) of compound **II**. The curve was recorded with a temperature ramp of 10 K·min^{-1} under a flow of N_2 to track the thermal decomposition of compound **II**.

3.5 Single-crystal X-ray diffraction analysis of compound III

Figure 3.20(a) below represents the molecular structure of compound **III**. Relevant bond distances and angles are summarised in Table 3.7 below, with standard deviations given in parentheses. The asymmetric unit (ASU) consists of one silver(I) metal ion, one benzoate ligand (OBn), and one 3-Chloropyridine (3-Clpy) ligand. In the ASU, only the O1 atom of the OBn ligand and N1 of the 3-Clpy ligand are coordinated to the silver(I) atom, with d(Ag1···O1) = 2.196(19) Å and d(Ag1···N1) = 2.349(2) Å, respectively. The symmetry generated molecular structure (symmetry code: 1−x, −y, 1−z) shown in Figure 3.20(b) represents the dimeric unit, where two OBn ligands coordinate with the silver(I) ions via their carboxylate (CO_2^-) oxygen atoms. These O-atoms bridge the silver(I) ions in an asymmetric mode, forming the $[Ag_2C_{14}H_{10}O_4]$ binuclear system. Within the binuclear compound, each silver(I) ion is three-coordinated, with the third (3-Clpy) acting as a monodentate ligand, coordinating via the pyridine's nitrogen atom. Compound **III**'s $Ag^I \cdots Ag^I$ separation distance [d(Ag···Ag) = 2.790(4) Å] is within the conventional bonding distance of metallic silver, 2.889 Å.[117] This close contact suggests a d^{10}-d^{10} argentophylic interaction.[36,37] Furthermore, the manner in which the OBn ligands coordinate to the silver(I) metals are seemingly identical: the delocalised CO_2^- groups adopt a bidentate μ_2-η^1:η^1 mode that bridges the two silver(I) atoms.[118] The Ag—O coordination bond distances range between 2.196(19) and 2.203(17) Å, which is smaller than the sum of Bondi's vdW radii (R_{vdW}(Ag) + R_{vdW}(O) = 3.24 Å).[105,106] Strangely, the Ag—N distances are slightly longer than those of the Ag—O distances, this is due to filled empty atomic orbitals on the nitrogen atoms. The $[AgO_2N]$ coordination environment forms an approximately T-shaped geometry at Ag1 (see Figure 3.20(b)), with the three subtended angles being 165.43(7), 95.69(7), and 98.49(7)° (see Table. 3.7).

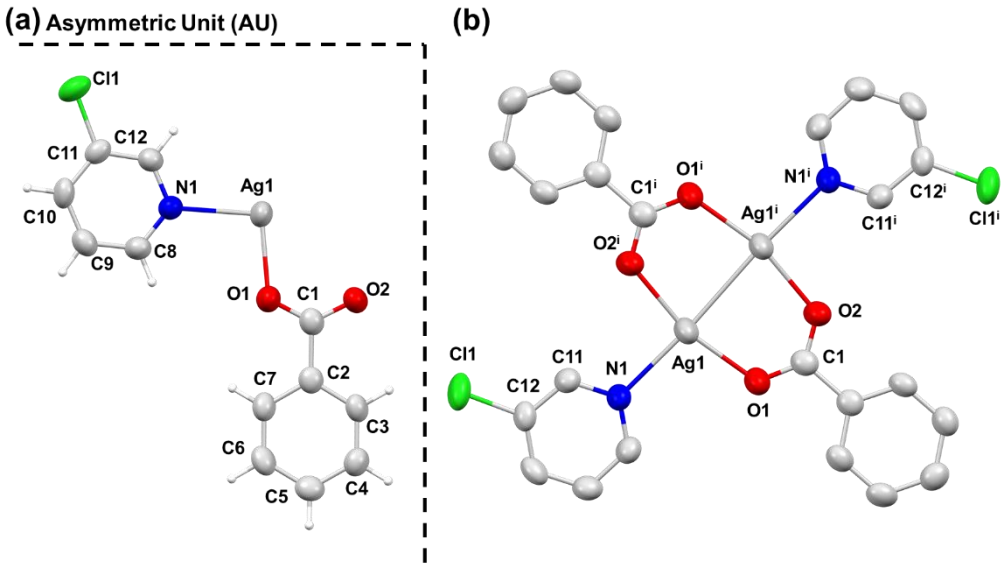

Figure 3.20. Molecular diagrams of compound **III** determined by single crystal X-ray diffraction methods. The structure of the (a) asymmetric unit and the (b) dimeric $[Ag_2(C_7H_5O_2)_2(C_5H_4NCl)_2]$ compound with atomic labelling is given. Hydrogen atoms are omitted in (b) for clarity; anisotropic displacement ellipsoids of non-hydrogen atoms are given with a 50% probability. Symmetry code: (i) 1−x, −y, 1−z.

Table 3.7. Selected bond lengths, *d* (Å) and bond angles, ∠ (°) of Ag(I) centres in **III**.

Bond/Contact	*d*	Bonds	∠
Ag1—O1	2.196(19)	O1—Ag1—O2^{i}	165.43(7)
Ag1—O1^{i}	2.203(17)	O1—Ag1—N1	98.49(7)
Ag1—N1	2.349(2)	O2^{i}—Ag1—N1	95.69(7)
Ag1···Ag1^{i}	2.790(4)	C1—O1—Ag1	121.99(17)
C1—O1	1.255(3)	C1—O1—Ag1^{i}	125.81(17)
C1—O2	1.258(3)	O1—C1—O2	126.1(2)

Symmetry code: (i) 1−x, −y, 1−z.

3.5.1 Crystallographic evaluation of short contacts

The crystallographic packing of compound **III**, much like that of compound **II**, seems to be predominated by Ag^{I}···π interactions. These interactions occur between the silver(I) transition metal and the pyridyl aromatic ring (π-system) portion of 3-Clpy of adjacent molecules. The distance between the silver(I) metal and centroid (Cg) of the aromatic ring of the 3-Clpy is given to be d(Ag1···Cg) = 3.548 Å. Furthermore, the angle of the normal to the aromatic ring plane, ∠(Ag1···Cg), with the vector between the centre of the aromatic ring is given to be 62.30° (see Figure 3.21 below). Interestingly, compound **III** packs such that the two silver(I) ions are directed toward the C8 and C9 double bond (C=C) of the π-face of the adjacent aromatic ring (see Figure 3.22 below). This Ag^{I}···π interaction differs slightly from that of **II**; as the interaction in **III** has both silver(I) ions in contact with the π-face. When analysing the short contacts between the pyridyl ring plane and silver(I) ions, considering the nearest aromatic atom (C9), essentially the most prominent contact, d(Ag^{I}···C$_{aromatic}$) = 3.159(3)Å, which is smaller than the sum of Bondi's vdW radii (R_{vdW}(Ag) + R_{vdW}(C) = 3.42 Å). The second contact's (Ag1^{i}–C9) bond distance is also smaller than the sum of Bondi's vdW radii where d = 3.319 Å.[105,106] As previously mentioned, sub vdWs distances are generally indicative of molecular orbital-based effects, where transition metal cation/π interactions often exhibit large degrees of covalent character (η^{1}-, η^{2}-, or η^{3}-interactions), in addition to electrostatic effects.[116]

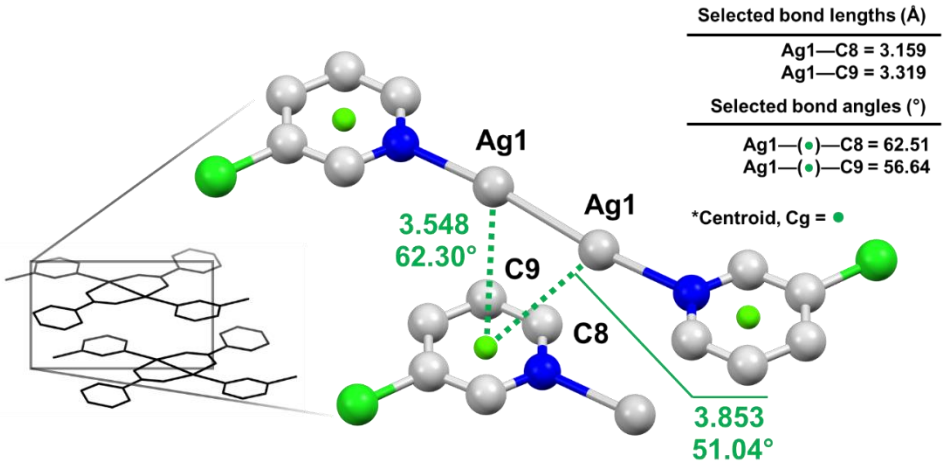

Figure 3.21. Crystal packing of **III** showing the dimer interaction of two molecules via Ag(I)···π interactions (in green). Interactions are generalised by showing the Ag(I)-centroid (Centroid, Cg is shown in green) distances. It should be noted that interactions take place mainly through the nitrogen and carbon atoms 1 and 12, respectively. Hydrogen atoms are omitted for clarity. Distance (Å) and angle (°) parameters are shown in green.

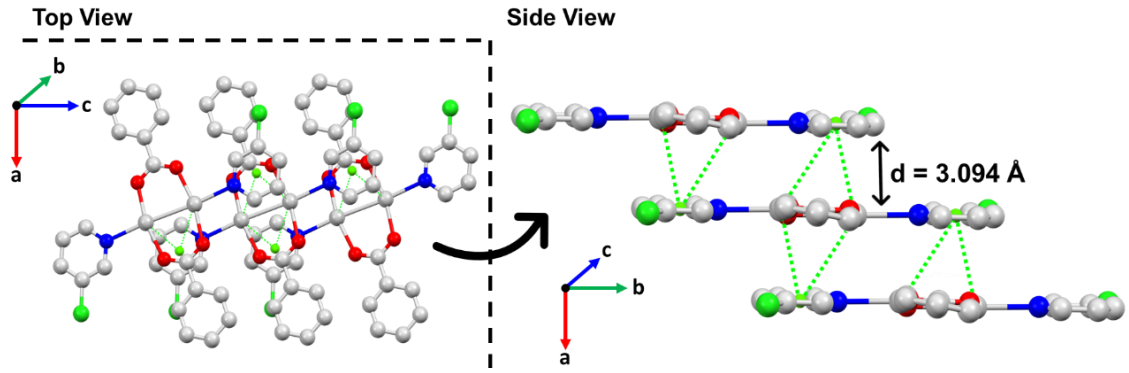

Figure 3.22. Crystal packing of **III** which highlights the "sandwich-stacked" packing mode, proposed to optimize the non-covalent Ag(I)···π interactions (in green). All hydrogen atoms are omitted from this figure for better visualization. (Centroid, Cg is shown in green)

3.5.2 Hirshfeld surface analysis

The three-dimensional (3D) HSs of compound **III** are illustrated in Figure 3.23 below, showing surfaces that are mapped with d_{norm} (-0.1 to 1.4 Å)(a,b),[57] d_e (1.0 to 2.6 Å)(c), and d_i (1.0 to 2.5 Å)(d) properties. Important quantitative information of the main intermolecular contacts in compound **III** was obtained by plotting 'translated' two-dimensional (2D) fingerprint (FP) plots as shown in Figure 3.24 below. Reiterating from the previous paragraph, the distance of the $Ag^{I}\cdots C_{aromatic}$ contacts between the two interacting molecules d(Ag1···C8) = 3.159 Å and d(Ag1···C9) = 3.319 Å are both shorter than the sum of Bondi's vdW radii (R_{vdW}(Ag) + R_{vdW}(C) = 3.42 Å).[105,106] These contacts can be seen as red depressions on the d_{norm} map (see Figure 3.23(b)), and are labelled as **1**. This kind of contact is indicative of $Ag^{I}\cdots\pi$ interactions, where two silver(I) atoms interact with a double bond (C8-C9) of the pyridyl ligand (π-system) of adjacent molecules.

These interactions are also visible in the FP plots as a pair of broadened symmetrical spikes at (d_e + d_i) ≅ 3.10 Å (see Figure 3.24(a)), constituting 3.4% the total HS area of the molecular moiety. In Figure 3.23(b), a pair of fainter red spots within the ring of the benzoate ligand, labelled as **2**, is indicative of a moderate Cg···H contact (π···H-CR interactions) arising from Cg···H10 connectors. The distance of Cg···H in this compound [d(Cg···H10) = 2.595 Å] is shorter than the sum of Bondi's vdW radii (R_{vdW}(C) + R_{vdW}(H) = 2.80 – 2.90 Å).[105,106] Shown in Figure 3.24(b) are broad spikes in the vicinity of (d_e + d_i) ≅ 2.6 Å, which are attributed to C···H/H···C molecular interactions, and which comprise 27.1% of the total HS area. These findings indicate the significance of these contacts in the packing arrangement of the crystal structure. Inspection of the remaining atom contacts showed that various other interatomic contacts are also present, such as C···C (**3**), N···H/H···N, C···O/O···C, O···H/H···O, Cl···H/H···Cl, and H···H, which contribute 1.8, 2.5, 3.3, 8.2, 15.9, and 28.0% to the total HS area, respectively. Most of these contributions occur at separations greater than the sum of the vdW radii.

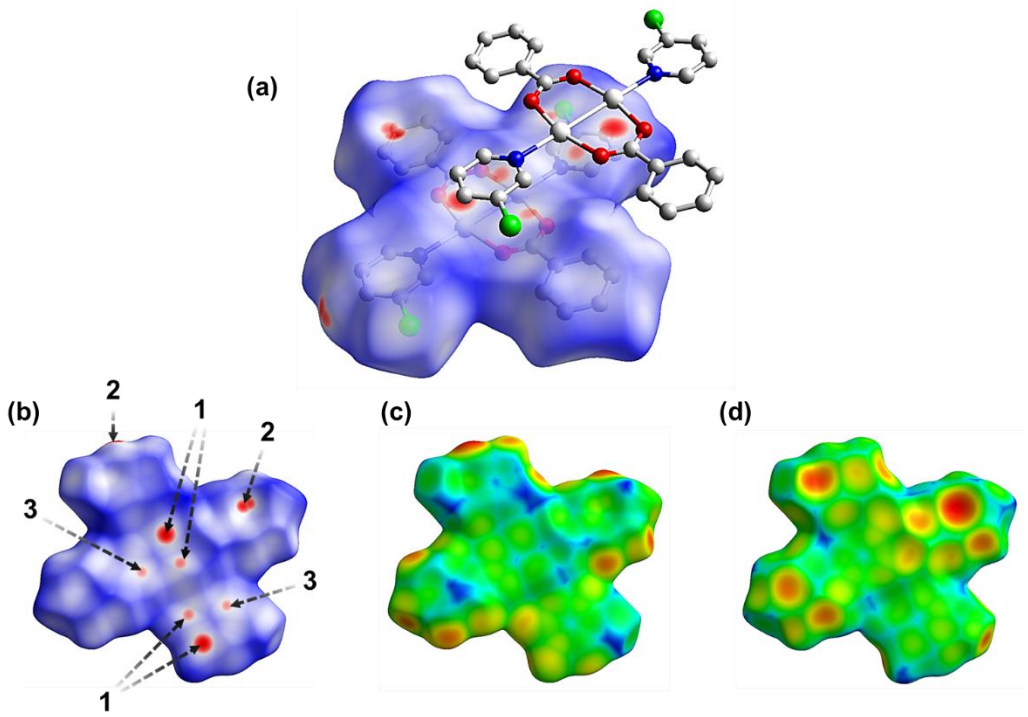

Figure 3.23. (a) A dimer of compound **III** with one molecule surrounded with a d_{norm}[57] decorated HS and the other in a ball and stick presentation. (b) The three-dimensional (3D) HS of **III** showing the red spots corresponds to the close intermolecular interactions. For compound **III** the HS is shown mapped with d_e (c) and d_i (d).

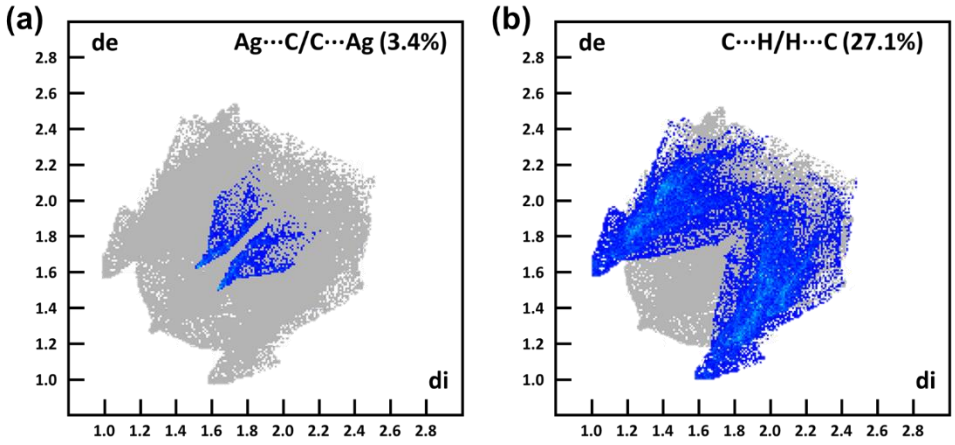

Figure 3.24. Decomposed two-dimensional (2D) FP plots for compound **III**. Close contacts are labelled as follows: (a) Ag···C/C···Ag and (b) C···H/H···C. For each fingerprint map, the grey area is a representation of the whole plot.

3.5.3 Powder X-ray Diffraction analysis

The PXRD pattern of the synthesised compound **III** is depicted in Figure 3.25 and was collected at room temperature and ambient pressure. The bulk material was analysed as is, without any further purification. The trace obtained for compound **III** (light blue) is consistent with the calculated pattern (dark blue) from the single-crystal data. The agreement of the experimental with the calculated pattern proves the phase purity of the bulk material.

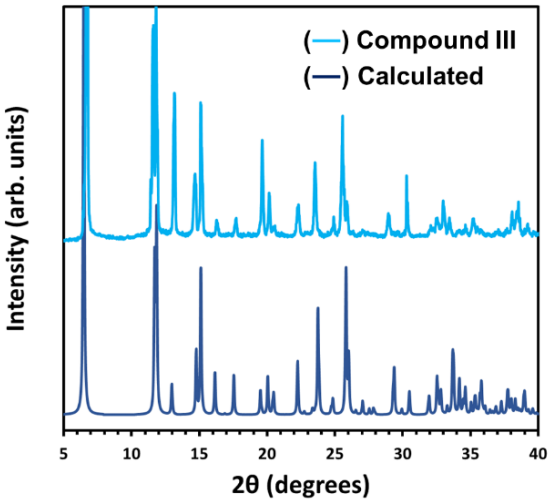

Figure 3.25. Comparison of the experimental powder X-ray diffraction pattern of compound **III** (light blue) and the calculated one (dark blue) from single-crystal data.

3.5.4 Thermogravimetric analysis

The thermal analysis of compound **III** is shown in Figure 3.26 below. The conditions under which compound **III** was studied fell within a temperature range of 20-400 °C, and a heating rate of 10 K·min^{-1} under a nitrogen atmosphere. Compound **III** demonstrates two decomposition stages/steps, and indicates stability up to a temperature of approximately 130 °C. The first experimental weight loss (29.7%) in the range of 75–155 °C takes place with the endothermic removal of the 3-Clpy ligand. The calculated weight loss of 31.5% for this stage agrees with the experimental weight loss. The subsequent second stage (250–325 °C), corresponds with the endothermic removal of the OBn ligand and an experimental weight loss of 33.1% (calcd. weight loss 34.1%). The residual product of the thermal degradation is calculated as silver(I) oxide, ½ Ag_2O (calcd. weight 34.4%, exp. weight 37.2%). The calculated and experimental weight losses for compound **III** are relatively consistent with one another, indicating the precision of the proposed structures.

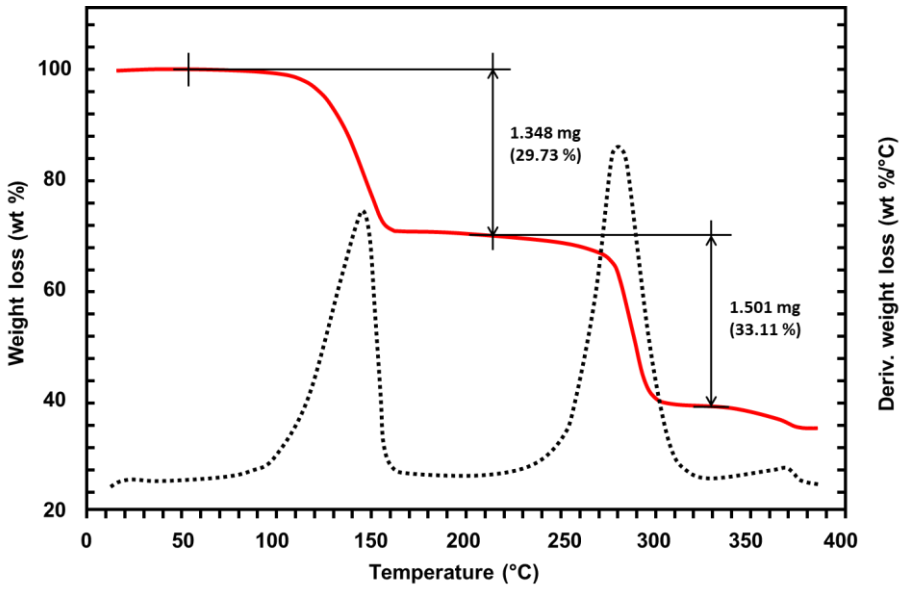

Figure 3.26. Thermogravimetric analysis (TGA) of compound **III**. The curve was recorded with a temperature ramp of 10 K·min^{-1} under a flow of N_2 to track the thermal decomposition of compound **III**.

3.6 Single-crystal X-ray diffraction analysis of compound IV

Figure 3.27(a) below represents the molecular structure of compound **IV**. Relevant bond distances and angles are summarised in Table 3.8 below, with the standard deviations included in parentheses. The asymmetric unit (ASU) consists of one silver(I) metal ion, one benzoate ligand (OBn), and one 2-Bromopyridine (2-Brpy) ligand. Within the ASU, only the O1 atom of the OBn ligand and N1 of the 2-Brpy ligand are coordinated to the silver(I), where d(Ag1···O1) = 2.199(10) Å and d(Ag1···N1) = 2.237(12) Å, respectively. The symmetry generated molecular structure (symetry code: (i) 1−x, +y, ½−z) is shown in Figure 3.27(b), where two OBn ligands coordinate the silver(I) ions via the carboxylate (CO_2^-) oxygen atoms. The O-atoms bridge the silver(I) ions in an asymmetric mode, forming the $[Ag_2C_{14}H_{10}O_4]$ binuclear system. In the binuclear compound, each silver(I) ion is three-coordinated, with the third ligand, 2-Brpy, acting as a monodentate ligand, and coordinating via the pyridine's nitrogen atom. Compound **IV**'s $Ag^I\cdots Ag^I$ separation [d(Ag···Ag) = 2.943(3) Å] is slightly larger than the conventional bonding distance of metallic silver, 2.889 Å,[117] and is the first of the series (**I-IV**) to exist outside this convention. However, this close contact still suggests a d^{10}-d^{10} argentophylic interaction,[36,37] albeit much less prominent in comparison. The manner in which both OBn ligands coordinate to the metals are the same: the delocalised CO_2^- groups adopt a bidentate μ_2-η^1:η^1 mode to bridge the two silver(I) ions.[118] The Ag—O coordination bond distances are 2.199(10) for O1 and 2.435(11) Å for $O1^i$, which are both smaller than the sum of the van der Waal radii (3.42 Å).[105,106] Like previous compounds **II** and **III**, the Ag1—N1 distance is slightly longer than that of the Ag1—O1 distance, which is due to filled atomic orbitals on the nitrogen atoms. The $[AgO_2N]$ coordination environment forms an approximately Y-shaped geometry at Ag1 (see Figure 3.27(b)), with the three subtended angles being 114.64(4), 149.38(4), and 94.80(4)° (see Table. 3.8).

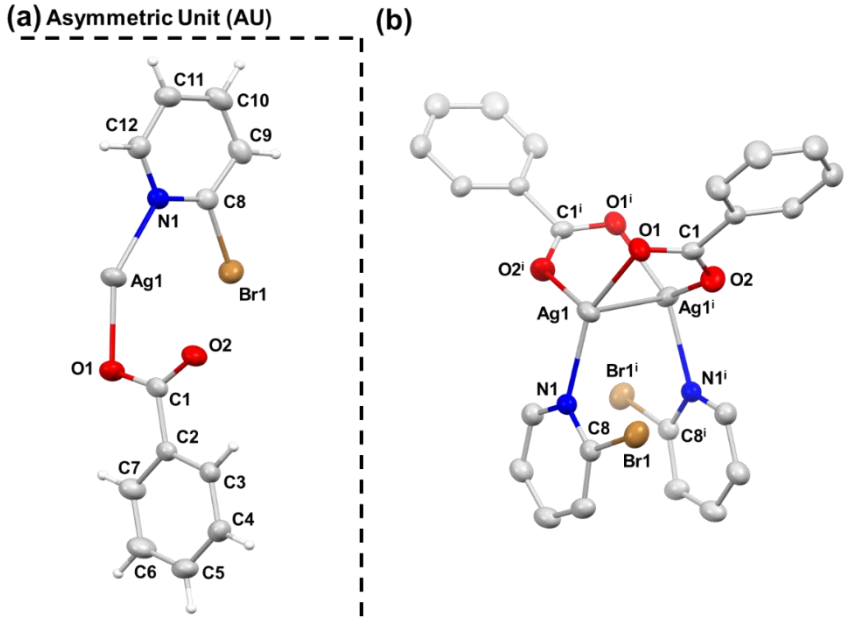

Figure 3.27. Molecular diagrams of compound **IV** determined by single crystal X-ray diffraction methods. The structure of the (a) asymmetric unit and the (b) dimeric $[Ag_2(C_7H_5O_2)_2(C_5H_4NBr)_2]$ compound with atomic labeling given. Hydrogen atoms are omitted in (b) for clarity; anisotropic displacement ellipsoids of non-hydrogen atoms are given with a 50% probability. Symmetry code: (i) 1−x, +y, ½−z.

Table 3.8. Selected bond lengths, *d* (Å) and bond angles, ∠ (°) in **IV**.

Bond/Contact	*d*	Bonds	∠
Ag1—O1	2.199(10)	O1—Ag1—O2^{i}	114.64(4)
Ag1—O1^{i}	2.435(11)	O1—Ag1—N1	149.38(4)
Ag1—N1	2.237(12)	O2^{i}—Ag1—N1	94.80(4)
Ag1···Ag1^{i}	2.943(3)	C1—O1—Ag1	109.79(9)
Ag1···Br1	3.194(4)	C8—Br1—Ag1	80.05(4)
C1—O1	1.266(17)	C1—O1—Ag1^{i}	128.28(9)
C1—O2	1.258(17)	O1—C1—O2	125.65(13)

Symmetry code: (i) 1−x, +y, ½−z.

3.6.1 Crystallographic evaluation of short contacts

The crystallographic packing of compound **IV** seems to be predominated by uncommon Ag^{I}···Br contacts. These contacts are indicative of semi-coordination interactions between the silver(I) transition-metal and the halogenated 2-Brpy ligand. This interaction takes place specifically through the bromine atom of 2-Brpy on adjacent molecules. The distance between the silver(I) metal ion and the bromine substituent is given to be d(Ag1···Br1) = 3.149 Å, which is shorter than the sum of Bondi's vdW radii (R_{vdW}(Ag) + R_{vdW}(Br) = 3.57 Å).[99,100] Furthermore, the M···X—CR_3 angle, ∠(Ag1···Br1-$C8_{py}$), is given to be 80.05° (see Figure 3.28 below), which is approximately 10° off from the expected angle of 90°. Ideally, this angle would position the region of negative electrostatic potential on the said halogen atom to optimally interact with the metal centre.[115] Interestingly, compound **IV** packs such that the silver(I) ions are seemingly directed toward the partial negative (δ^-) belt region of the Br1 atoms (see Figure 3.29 below), acting as an electrophilic site (δ^+) for the halogen lone pair. These sub-vdW distances are generally suggestive of molecular orbital-based (covalent-like) effects. The silver(I)-involving interactions with halogens were not attributed to halogen bonding, most likely due to the silver(I) centre being formally positive; hence, it is considered to be a Lewis acid.

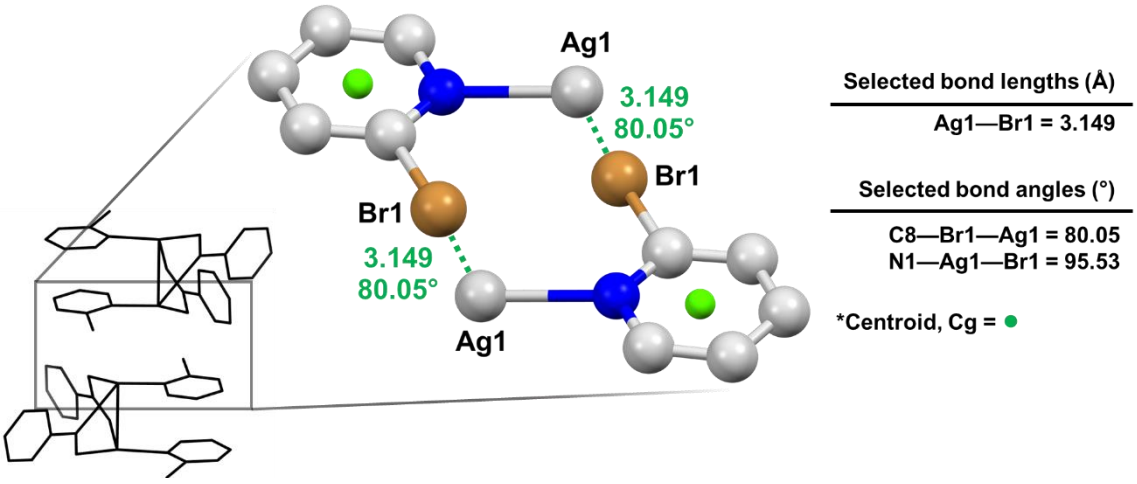

Figure 3.28. Crystal packing of **IV** showing the dimer interaction of two molecules of **IV** via Ag^{I}···Br interactions. Hydrogen atoms are omitted for clarity. Distance (Å) and angle (°) parameters are shown in green.

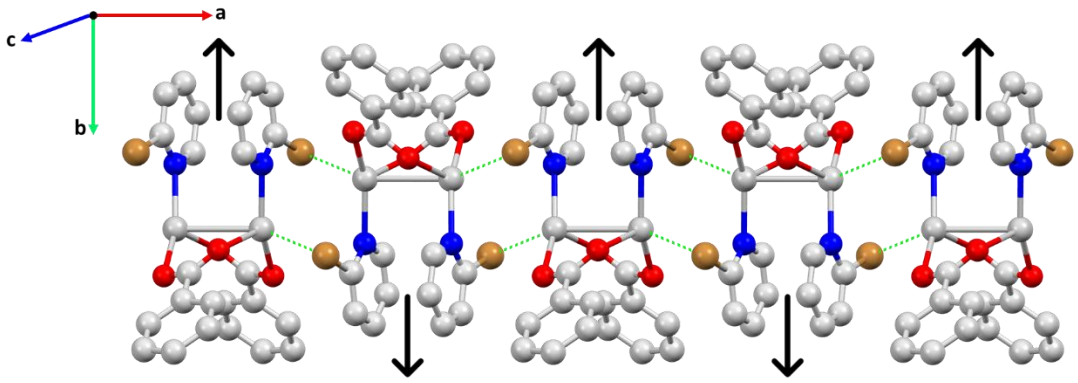

Figure 3.29. Crystal packing of IV highlighting the "head-to-tail" orientations (arrows), proposed to optimise the non-covalent $Ag^{I}\cdots Br$ interactions (in green). All hydrogen atoms are omitted from this figure for better visualisation.

3.6.2 Hirshfeld surface analysis

The three-dimensional (3D) HSs of compound **II** are illustrated in Figure 3.30 below, depicting surfaces mapped with d_{norm} (-0.2 to 1.4 Å)(a,b),[57] d_e (1.0 to 2.7 Å)(c), and d_i (1.0 to 2.7 Å)(d) properties. Important quantitative information of the main intermolecular contacts in compound **IV** was obtained by plotting translated two-dimensional (2D) fingerprint (FP) plots, as shown in Figure 3.31 below. The distance of $Ag^{I}\cdots Br$ in this compound [d(Ag1···Br1) = 3.149 Å] is shorter than the sum of Bondi's vdW radii (R_{vdW}(Ag) + R_{vdW}(Br) = 3.57 Å).[99,100] These contacts can be seen as two large red depressions on the d_{norm} map (Figure 3.30(b)), labelled as **1**. This is indicative of the Ag(I)-atoms interacting with the Br-atoms of the pyridine ligands of the adjacent molecules.

These interactions are also visible in the FP plots as a pair of symmetrical spikes at (d_e + d_i) ≅ 3.10 Å (Figure 3.31(a)), contributing 3.1% of the total HS area of the molecular moiety. In Figure 3.30(b), pairs of fainter red spots within the ring of the benzoate ligand and on the 2-Brpy ligand, labelled as **2**, are indicative of moderate Cg···H contact (π···H-CR interactions) arising from Cg···H10 connectors. The distance of Cg···H in this compound [d(Cg···H10) = 2.768 – 2.802 Å] is shorter than the sum of Bondi's vdW radii (R_{vdW}(C) + R_{vdW}(H) = 2.80 – 2.90 Å).[99,100] As shown in Figure 3.31(b) the broad spikes in the vicinity of (d_e + d_i) ≅ 2.75 Å, observed in the FP plot are attributed to C···H/H···C molecular interactions, which comprise 28.3% of the total HS area. These findings highlight the signifcance of these contacts in the packing arrangement of the crystal structure. Inspection of the remaining atom contacts showed that various other interatomic contacts are also present, such as N···O/O···N, C···O/O···C, Br···C/C···Br (3), Br···H/H···Br, O···H/H···O (4), and H···H, which contribute 1.1, 2.3, 3.6, 9.5, 11.7, and 35.8% to the total HS area, respectively. Most of these contributions occur at separations greater than the sum of the van der Waals radii.

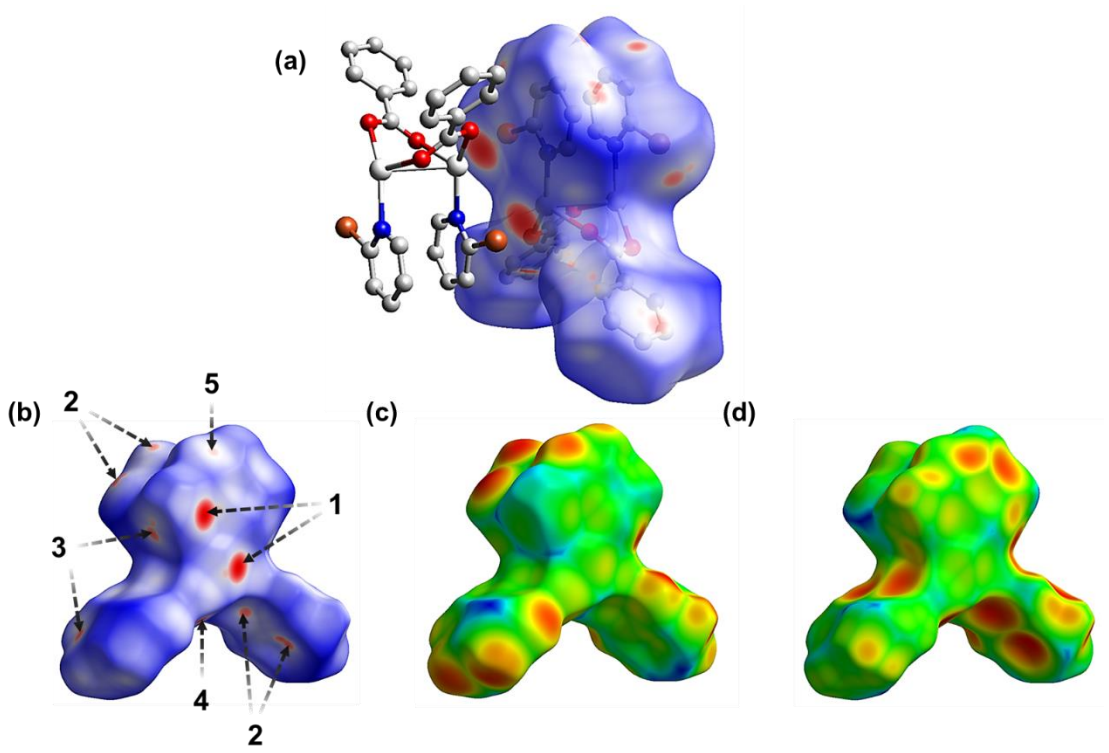

Figure 3.30. (a) A dimer of compound IV with one molecule surrounded with a d_{norm}[57] decorated HS and the other in a ball and stick presentation. (b) The three-dimensional (3D) HS of **IV** showing the red spots corresponds to the close intermolecular interactions. For compound IV the HS is shown mapped with d_e (c) and d_i (d).

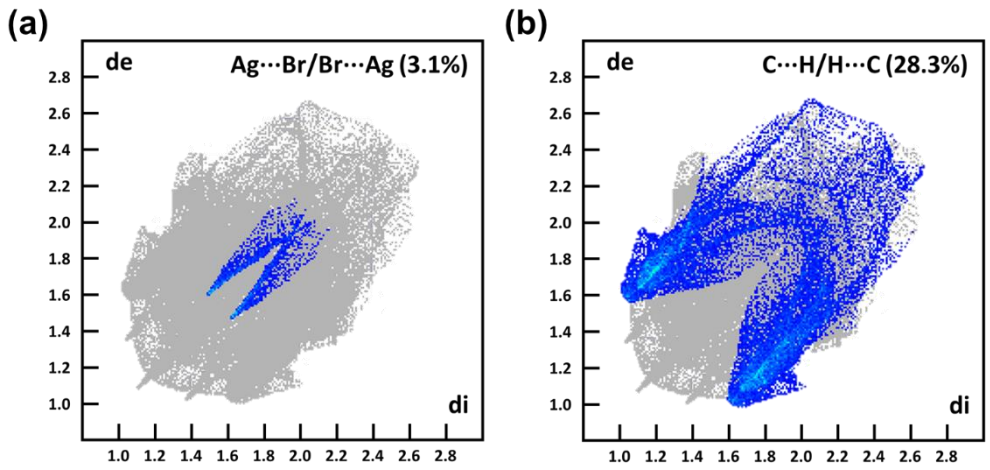

Figure 3.31. Decomposed two-dimensional (2D) FP plots for compound **IV**. Close contacts are labelled as follows: (a) Ag···Br/Br···Ag and (b) C···H/H···C. For each fingerprint map, the grey area is a representation of the whole plot.

3.6.3 Powder X-ray Diffraction analysis

The PXRD pattern of the synthesised compound **IV** is depicted in Figure 3.32 and was collected at room temperature and ambient pressure. The bulk material was analysed as is, without any further purification. The trace obtained for compound **IV** (light blue) is consistent with the calculated pattern (dark blue) from the single-crystal data. The agreement of the experimental with the calculated pattern proves the phase purity of the bulk material.

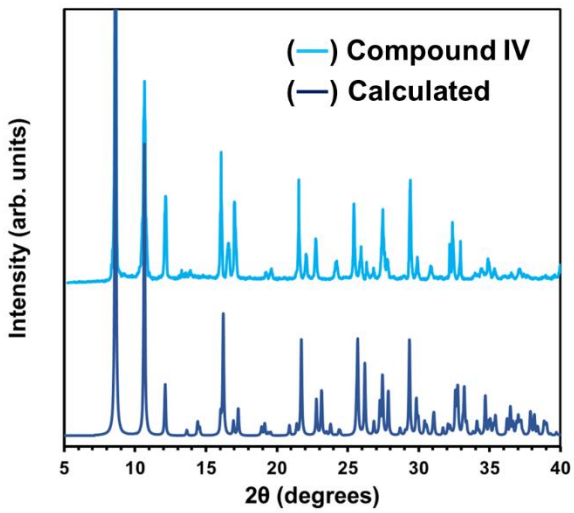

Figure 3.32. Comparison of the experimental powder X-ray diffraction pattern of compound **IV** (light blue) and the calculated one (dark blue) from single-crystal data.

3.6.4 Thermogravimetric analysis

The thermal analysis of compound **IV** is shown in Figure 3.33 below. The conditions under which the compound **IV** was studied ranged between temperatures of 20-400 °C, with a heating rate of 10 K·min^{-1} under a nitrogen atmosphere. Compound **IV** demonstrates two decomposition stages/steps, and indicates stability up to a temperature of approximately 135 °C. The first experimental weight loss (37.7%) in the range of 80–160 °C take place with the endothermic removal of the 2-Brpy ligand. The calculated weight loss of 39.1% for this stage agrees with the experimental weight loss. The second stage (250–325 °C) corresponds to the endothermic removal of the OBn ligand with an experimental weight loss of 28.6% (calcd. weight loss 30.3%). The residual product of the thermal degradation is calculated as silver(I) oxide, ½ Ag_2O (calcd. weight 30.8%, exp. weight 33.7%). The calculated and experimental weight losses for compound **IV** are relatively consistent with each other, showing precision within the proposed structures.

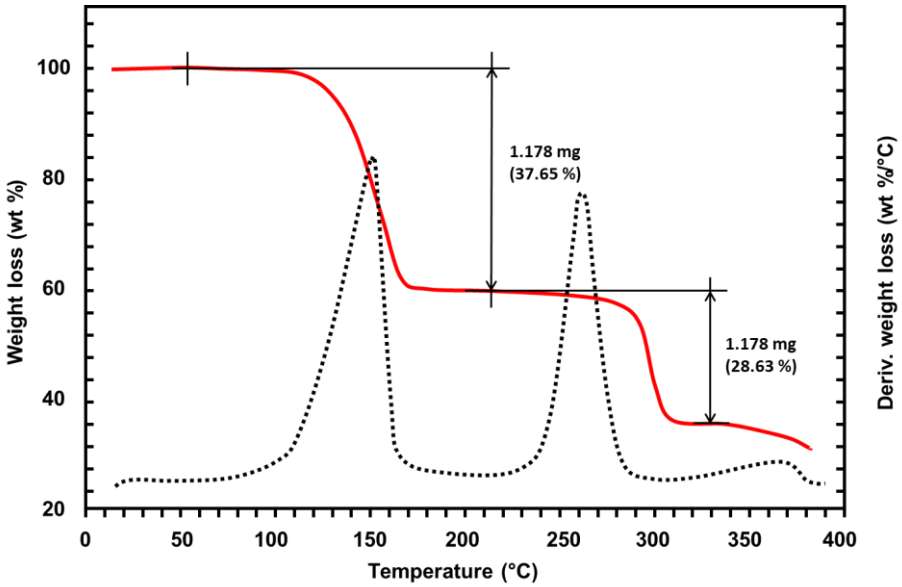

Figure 3.33. Thermogravimetric analysis (TGA) of compound **IV**. The curve was recorded with a temperature ramp of 10 K·min^{-1} under a flow of N_2 in order to track the thermal decomposition of compound **IV**.

3.7 Single-crystal X-ray diffraction analysis of compound V

Figure 3.34(a) below represents the molecular structure of compound **V**. Selected bond distances and angles are summarised in Table 3.9 below, with standard deviations given in parentheses. The asymmetric unit (ASU) consists of one silver(I) ion, one benzoate ligand (OBn), and one 2-Iodopyridine (2-Ipy) ligand. Within the ASU, only the O1 atom of the OBn ligand and N1 of the 2-Ipy ligand are coordinated to the silver(I), where d(Ag1···O1) = 2.216(18) Å and d(Ag1···N1) = 2.272(2) Å, respectively. The dimeric structure is shown in Figure 3.34(b), where the two OBn ligands coordinate to the silver(I) ions via their carboxylate (CO_2^-) oxygen atoms, forming an eight-membered dimetallacycle. This metallacycle allows for a transannular $Ag^I \cdots Ag^I$ contact. Each silver(I) ion within the binuclear system is three-coordinated, with the auxiliary 2-Ipy lingand acting as a monodentate chelator, coordinating via the pyridine's nitrogen atom. Compound **V**'s $Ag^I \cdots Ag^I$ separation [d(Ag···Ag) = 2.975(8) Å] is slightly larger than the conventional bonding distance of metallic silver, 2.889 Å.[117] However, this close contact could still suggest a d^{10}-d^{10} argentophylic interaction.[36,37] The manner in which both OBn ligands coordinate to the metals are essentially the same: the delocalised CO_2^- groups adopt a bidentate μ_2-η^1:η^1 mode to bridge the two silver(I) atoms.[118] The eight-membered ring of the $[Ag_2(RCOO)_2]$ dimer shows a slightly folded geometry, approaching a boat-boat conformation as seen in Figure 3.34(b). The Ag—O coordination bond distances are 2.216(18) for O1 and 2.411(19) Å for $O1^i$, both of which are smaller than the sum of the van der Waal radii (3.42 Å).[105,106] The $[AgO_2N]$ coordination environment forms an approximately Y-shaped geometry at Ag1 (see Figure 3.34(b)), with the three subtended angles being; 119.03(7), 93.79(7), and 145.14(7)° (see Table. 3.9).

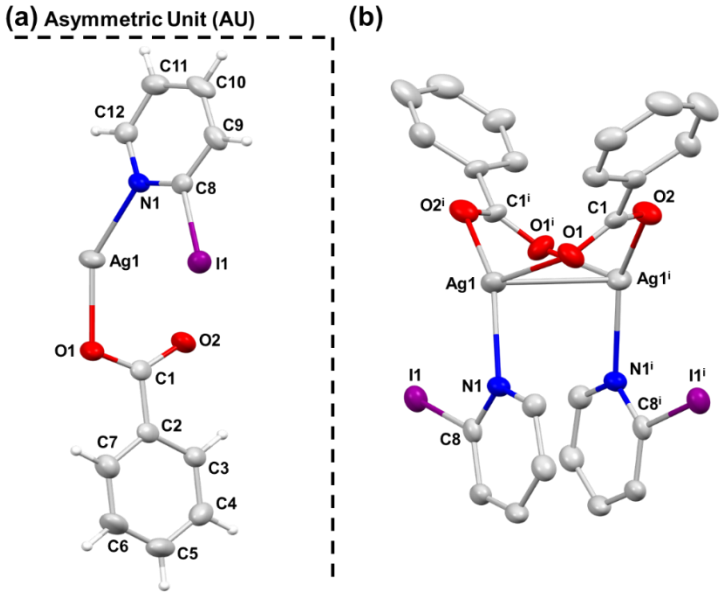

Figure 3.34. Molecular diagrams of compound **V** determined by single crystal X-ray diffraction methods. The structure of the (a) asymmetric unit and of the (b) dimeric $[Ag_2(C_7H_5O_2)_2(C_5H_4NI)_2]$ compound with atomic labelling is given. Hydrogen atoms are omitted in (b) for clarity; anisotropic displacement ellipsoids of non-hydrogen atoms are given with a 50% probability. Symmetry code: (i) 1−x, 1−y, 2−z.

Table 3.9. Selected bond lengths, *d* (Å) and bond angles, ∠ (°) in **V**.

Bond/Contact	*d*	Bonds	∠
Ag1—O1	2.216(18)	O1—Ag1—O2^{i}	119.03(7)
Ag1—O1^{i}	2.411(19)	O1—Ag1—N1	145.14(7)
Ag1—N1	2.272(2)	O2^{i}—Ag1—N1	93.79(7)
Ag1···Ag1^{i}	2.975(8)	C1—O1—Ag1	112.19(16)
Ag1···I1	3.073(10)	C8—I1—Ag1	87.08(7)
C1—O1	1.262(3)	C1—O1—Ag1^{i}	128.19(16)
C1—O2	1.259(3)	O1—C1—O2	125.8(2)

Symmetry code: (i) 1−x, 1−y, 2−z.

3.7.1 Crystallographic evaluation of short contacts

The crystallographic packing of compound **V** seems to be predominated by Ag^{I}···I contacts, which is similar to that of **IV**. These contacts are indicative of semi-coordination interactions between the silver(I) and the halogenated 2-Ipy ligand. This contact takes place specifically through iodine atom on adjacent molecules. The distance between the silver(I) metal and iodine substituent is given to be d(Ag1···I1) = 3.073 Å, which is shorter than the sum of Bondi's vdW radii (R_{vdW}(Ag) + R_{vdW}(I) = 3.70 Å).[105,106] Furthermore, the M···X—R angle, ∠(Ag1···I1-C8$_{py}$), is 87.08 ° (see Figure 3.35 below), which ∼3 ° shy of the expected angle of 90°. This angle would ideally position the region of negative electrostatic potential on the halogen atom to optimally interact with the metal centre.[121] Interestingly compound **V**, much like **IV**, packs such that the Ag(I) ions are seemingly directed toward the partial negative (δ^{-}) belt region of the I1 atoms (see Figure 3.36 below), acting as an electrophilic site (δ^{+}) for the halogen lone pair. These sub-vdW distances are generally suggestive of molecular orbital-based (covalent-like) effects. These silver(I)-involving interactions with halogens were not attributed to halogen bonding, most likely because the silver(I) metal is formally positive; hence, it was considered to be a Lewis acid.

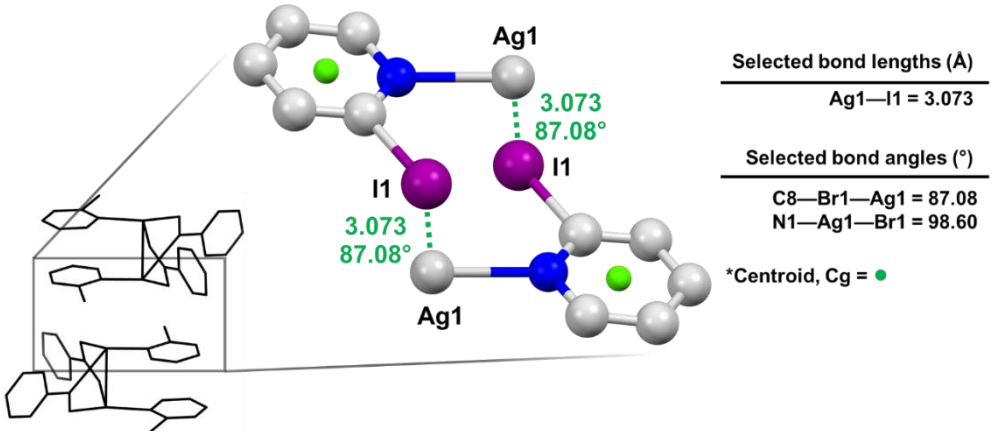

Figure 3.35. Crystal packing of **V** showing the dimer interaction of two molecules of **V** via Ag^{I}···I interactions. Hydrogen atoms are omitted for clarity. Distance (Å) and angle (°) parameters are shown in green.

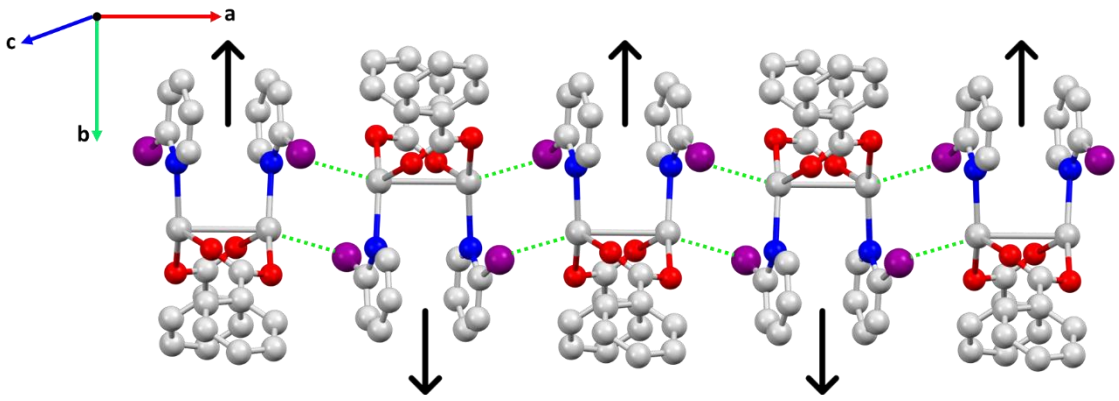

Figure 3.36. Crystal packing of **V** highlighting the "head-to-tail" orientations (arrows), proposed to optimize the non-covalent $Ag^{I}\cdots I$ interactions (in green). All hydrogen atoms are omitted from this figure for better visualization.

3.7.2 Hirshfeld surface analysis

The three-dimensional (3D) HSs of compound **V** are illustrated in Figure 3.37 below, showing surfaces mapped with d_{norm} (-0.34 to 1.5 Å)(a,b),[57] d_e (1.0 to 2.8 Å)(c), and d_i (1.0 to 2.7 Å)(d) properties. Important quantitative information of the main intermolecular contacts in compound **V** was obtained by plotting translated two-dimensional (2D) fingerprint (FP) plots shown in Figure 3.38 below. The distance of $Ag^{I}\cdots I$ in this compound [d(Ag1···I1) = 3.073 Å] is shorter than the sum of Bondi's vdW radii (R_{vdW}(Ag) + R_{vdW}(I) = 3.70 Å).[105,106] These contacts can be seen as two large red depressions on the d_{norm} map (Figure 3.37(b)), labelled as **1**. This is indicative of the silver(I) atoms interacting with the I-atoms of the pyridyl ligands of the adjacent molecules.

These interactions are also visible in the FP plots as a pair of symmetrical spikes at (d_e + d_i) ≅ 3.05 Å (Figure 3.38(a)), constituting 4.1% of the total HS area of the molecular moiety. In Figure 3.37(b), pairs of fainter red spots within the ring of the benzoate ligand and on the 2-Ipy ligand, labelled as **2**, are indicative of moderate I···C contact (I···π interactions) arising from I1···C4,5 connectors. The distances of I···$C_{aromatic}$ in this compound [d(I···C) = 3.488 – 3.593 Å] are shorter than the sum of Bondi's vdW radii (R_{vdW}(I) + R_{vdW}(C) = 3.68 Å).[105,106] As shown in Figure 3.38(b) the broad spikes in the vicinity of (d_e + d_i) ≅ 3.40 Å, observed in the FP plot are attributed to I···C/C···I molecular interactions, which comprise 3.5% of the total HS area. These findings highlight the signifcance of these contacts in the packing arrangement of the crystal structure. Inspection of the remaining atom contacts showed that various other interatomic contacts are also present, such as N···O/O···N, C···O/O···C, I···H/H···I, C···H/H···C (3), O···H/H···O (4), and H···H (5), which contribute 1.3, 2.0, 9.9, 11.6, 28.5 and 35.4% to the total HS area, respectively. Most of these contributions occur at separations greater than the sum of the van der Waals radii.

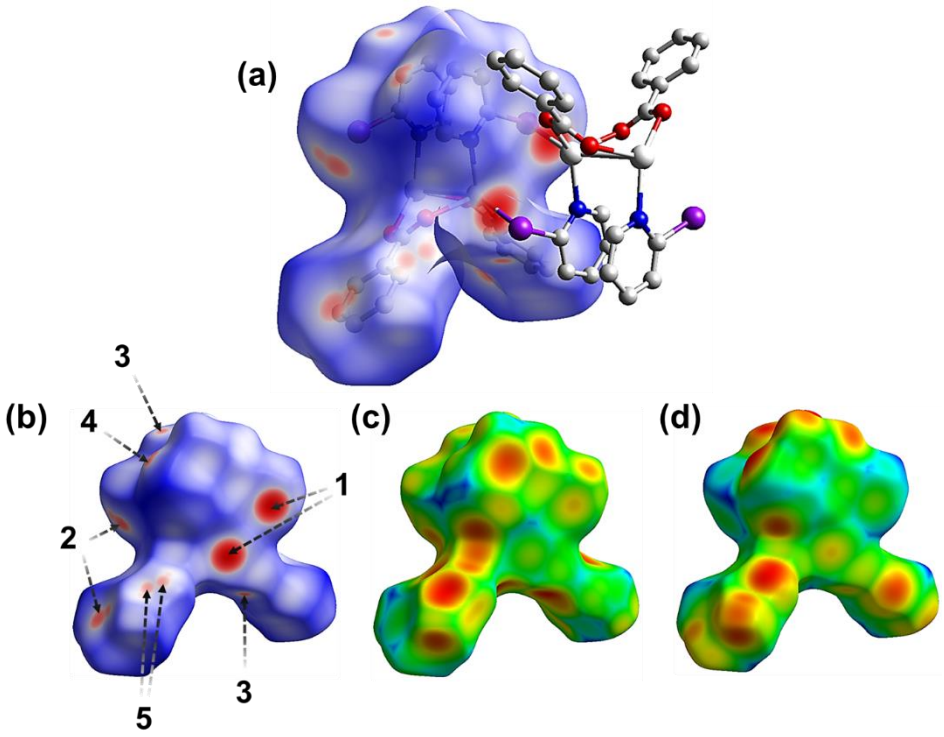

Figure 3.37. (a) A dimer of compound **V** with one molecule surrounded with a d_{norm}[57] decorated HS and the other in a ball and stick presentation. (b) The three-dimensional (3D) HS of **V** showing the red spots corresponds to the close intermolecular interactions. For compound **V** the HS is shown mapped with d_e (c) and d_i (d).

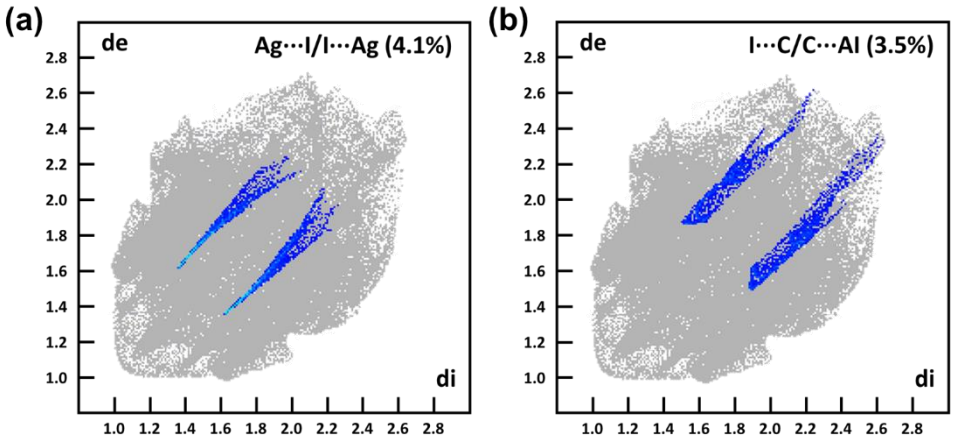

Figure 3.38. Decomposed two-dimensional (2D) FP plots for compound **V**. Close contacts are labelled as follows: (a) Ag···I/I···Ag and (b) I···C/C···I. For each fingerprint map, the grey area is a representation of the whole plot.

3.7.3 Powder X-ray Diffraction analysis

The PXRD pattern of the synthesised compound **V** is depicted in Figure 3.39 below and was collected at room temperature and ambient pressure. The bulk material was analysed as is, without any further purification. The trace obtained for compound **V** (light blue) is consistent with the calculated pattern (dark blue) from the single-crystal data. The agreement of the experimental with the calculated pattern proves the phase purity of the bulk material.

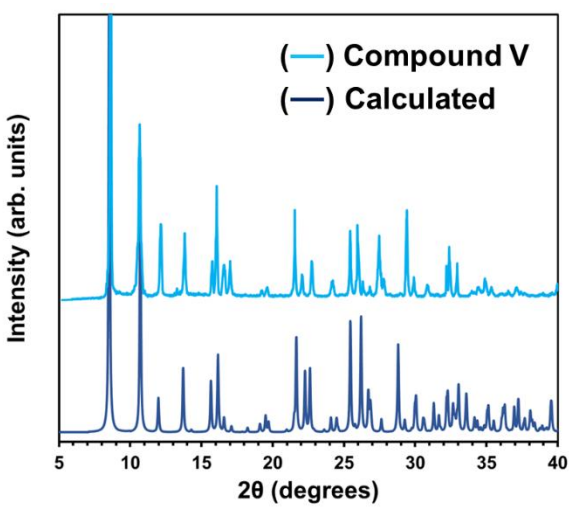

Figure 3.39. Comparison of the experimental powder X-ray diffraction pattern of compound **V** (light blue) and the calculated one (dark blue) from single-crystal data.

3.7.4 Thermogravimetric analysis

The thermal analysis of compound **V** is shown in Figure 3.40 below. The conditions under which the compound **V** was studied ranged between temperatures of 20-400 °C, with a heating rate of 10 K·min^{-1} under a nitrogen atmosphere. Compound **V** demonstrates two decomposition stages/steps, and indicates stability to a temperature of approximately 145 °C. The first experimental weight loss (43.9%) in the range of 90–170 °C take place with the endothermic removal of the 2-Ipy ligand. The calculated weight loss of 45.4% for this stage agrees with the experimental weight loss. The second stage (250–300 °C) corresponds to the endothermic removal of the OBn ligand with an experimental weight loss of 25.1% (calcd. weight loss 27.1%). The residual product of the thermal degradation is calculated as silver(I) oxide, ½ AgO (calcd. weight 27.5%, exp. weight 31.0%). The calculated and experimental weight losses for compound **V** are relatively consistent with each other, indicating the precision of the proposed structures.

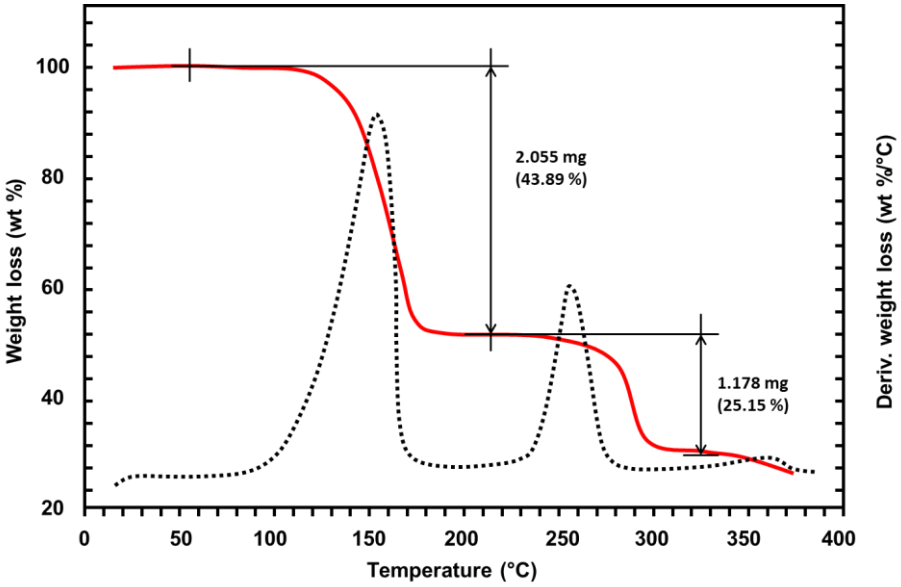

Figure 3.40. Thermogravimetric analysis (TGA) of compound **V**. The curve was recorded with a temperature ramp of 10 K·min^{-1} under a flow of N_2 in order to track the thermal decomposition of compound **V**.

3.8 Conclusion

In this chapter, with the exception of **I**, a variety of isostructural silver(I) compounds (**II**-**V**) have been successfully synthesized and described utilising single-crystal X-ray diffraction (SCXRD), powder X-ray diffraction (XRD), Hirshfeld surface (HS) analysis, and thermogravimetric analysis (TGA).

The TGA results obtained were primarily used as a characterization tool, confirming a two-step thermal removal of the X-py and OBn ligands from the samples, while also providing valuable information about the stability of the material under different thermal conditions (see Supporting Information S2).

Each halogenated pyridyl ligand's interaction (non-covalent interaction, NCI) with its surrounding molecules, which varied from **I** to **V**, could be identified. SCXRD analysis revealed three major types of metal-involved interactions present within the aforementioned series. These have been described herein as: $Ag^{I}\cdots Ag^{I}$, $Ag^{I}\cdots X$, and $Ag^{I}\cdots\pi$ interactions.

Understanding the quantum characteristics of non-covalently bonded compounds can help to explain why different types of non-covalent interactions exist depending on the pyridyl ligand. These aspects will be addressed again in Chapter 4, where the quantum theory of atoms in molecules (QTAIM) and natural bond orbital (NBO) analysis of compounds **I**-**V** will be discussed.

Chapter 4

Computational Studies

4.1 Theoretical study: topological QTAIM analysis

This section presents the results obtained using the quantum theory of atoms in molecules (QTAIM) method during analysis of the non-covalent interactions present within each of the studied compounds **I**-**V**.[114] Based on the calculated electronic densities of the complexes, the topology approach of QTAIM separates the molecule into atomic basins with associated critical points. A bond critical point (BCP) is the region on the bond path (line of maximum density) where two atoms' electronic densities have the highest superposition. The following topological descriptors at the BCPs of interacting atoms were analysed: ρ, the electronic density; $\nabla^2\rho_{(r)}$, the Laplacian of the electronic density; $G_{(r)}$ the kinetic energy density; $V_{(r)}$, the potential energy density; and $H_{(r)}$, the total energy density. These calculations were performed in order to probe the nature and estimate the magnitude of the interactions within the aforementioned compounds.

4.2. QTAIM analysis of $Ag^{I}\cdots Ag^{I}$ interaction in compound I

The bond critical point (BCP) (3, -1) along the $Ag^{I}\cdots Ag^{I}$ bond exhibits a relatively low electron density (ρ_{BCP} ≈ 0.028 a.u.) and a small positive Laplacian value ($\nabla^2\rho_{BCP}$ ≈ 0.074 a.u., see Table 4.1 below), which is a typical characteristic for M···M interactions.[122,123] In order to classify the degree of covalency of the interaction, the ratio |V|/G, which distinguishes pure closed-shell (|V|/G < 1) interactions and pure shared-shell (|V|/G > 2) interactions, was analysed. According to the classification by Bianchi *et al*.,[124] the |V|/G ratio (1.13) of compound **I** corresponds to an intermediate bond character (1 < |V|/G < 2), which lies between electron-shared covalent bonds, classifying the $Ag^{I}\cdots Ag^{I}$ interaction as a transit closed-shell. A second useful measurement for characterising the covalency of M···M interactions can be derived from the H/ρ_{BCP} ratio, otherwise referred to as the bond degree parameter (BD). The measured |H|/ρ ratio (-0.10) gives a negative value which suggests a slight covalent character, where a more negative value would indicate a greater covalent interaction.[125] The interaction energy (E_{int} = ½V) provides an estimate of the strength of the M···M interaction,[126] with E_{int} ≈ -7.63 kcal/mol for compound **I**. The delocalisation index[127] (DI, δ) is a measure of the degree of electron sharing between atoms and has been proposed to be a measure of the bond order;[128] DI = 0.26 for compound **I** showing that the bond features some donor-acceptor behaviour (see Table 4.1). These values all suggest that the $Ag^{I}\cdots Ag^{I}$ contact is a transit closed-shell (weakly-covalent) supported argentophilic interaction.

4.3 QTAIM analysis of carboxylate O,O-bridging in I

The metal–ligand, Ag-O, bonds in compound **I** are also in the region between pure closed-shell (ionic) and pure shared-shell (covalent) interactions. This conclusion is based on the above criteria, where the BCP descriptors related to the O,O'-bridged $Ag^{I}\cdots Ag^{I}$ contact. In other words, the Ag-O bonds are comparable with those of dative bonding (see Table 4.1, Figure 4.1 below),[129] where the Ag-O bonds exhibit relatively low electron density values (ρ_{BCP} ≈ 0.066 and 0.067 a.u.) and large positive Laplacian values ($\nabla^2\rho_{BCP}$ ≈ 0.276 and 0.279 a.u.), as can be seen in Table 4.1 below. The values of the delocalisation index (DI) for the Ag-O bonds are less than 1, indicating that the bonds feature donor-acceptor behaviour. The measured |H|/ρ ratio (-0.17) is negative indicating that they feature some covalency, where a more negative value indicates greater covalent interactions. The values of the interaction energies of the Ag-O bonds are similar, where E_{int} ≈ -29.0 kcal/mol for both Ag-O1 and Ag-O2.

Table 4.1. Selected properties of the electron density at the BCPs according to QTAIM analysis, as well as computed DIs (δ) between appropriate atom pairs.

BCP	$\rho_{(r)}$	$\nabla^2\rho_{(r)}$	$V_{(r)}$	$H_{(r)}$	BD	$\lvert V_{(r)}\rvert/G_{(r)}$	DI(A,B)	E_{int} (kcal/mol)
Ag1-Ag^{i}	0.028	0.074	-0.024	-0.003	-0.10	1.13	0.26	-7.63
Ag1-O1	0.066	0.276	-0.092	-0.011	-0.17	1.14	0.49	-28.8
Ag1-O2	0.067	0.279	-0.093	-0.011	-0.17	1.14	0.49	-29.0

ρ(r), $\nabla^2\rho(r)$, H(r), and V(r), are all given in atomic units (a.u.).

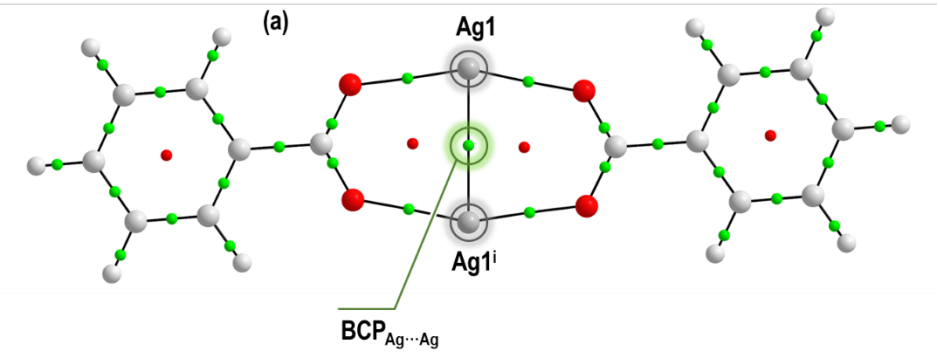

(b) QTAIM results for Ag···Ag BCP in I

BD	|V|/G	DI(δ)	E_{int}[a]
-0.17	1.13	0.26	-7.63

[a] E_{int} is given in kcal/mol

*Bond Critical Point, BCP = ●

Ring Critical Point, RCP = ●

Figure 4.1. a) QTAIM molecular diagram calculated at the B3LYP-D2/aug-cc-PVTZ (Ag) level for the experimental structure of compound **I**. This diagram emphasises the relevance of the bond critical point (BCP; green dots) along the intramolecular Ag···Ag bond path. b) Selected results of QTAIM analysis showing Ag···Ag non-covalent interaction.

4.4 QTAIM analysis of $Ag^{I}\cdots Ag^{I}$ interaction in compound II

The $Ag^{I}\cdots Ag^{I}$ BCP in **II** exhibits a relatively low electron density ($\rho_{BCP} \approx 0.028$ a.u.) and a small positive Laplacian value ($\nabla^2\rho_{BCP} \approx 0.079$ a.u., Table 4.2 below). According to the classification by Bianchi *et al.*,[124] the |V|/G ratio (1.14) of compound **II** corresponds to an intermediate bond character ($1 < |V|/G < 2$), which lies between electron-shared covalent bonds, classifying the $Ag^{I}\cdots Ag^{I}$ interaction as a transit closed-shell. The measured |H|/ρ ratio (-0.11) gives a negative value which suggests a slight covalent character.[125] The interaction energy[126] ($E_{int} = ½V$) for compound **II** is given to be $E_{int} \approx$ -8.10 kcal/mol. The delocalisation index[127] is measured as 0.22 (see Table 4.2). These values are all indicative of a transit closed-shell (weakly-covalent) supported argentophilic ($Ag^{I}\cdots Ag^{I}$) interaction.

4.5 QTAIM analysis of double O,N-bridging in II

Based on the above criteria, the BCP descriptors related to the double-bridged $Ag^{I}\cdots Ag^{I}$ contact, namely the Ag-N and Ag-O bonds, are comparable with those of dative bonding (see Table 4.2, Figure 4.2 below)[129] as they exhibit a range of relatively low electron density values ($\rho_{BCP} \approx 0.040 – 0.076$ a.u.) and large positive Laplacian values ($\nabla^2\rho_{BCP} \approx 0.171 – 0.321$ a.u.), as can be seen in Table 4.2 below. The DI values for both Ag-N and Ag-O are all less than 1, indicating that the bonds feature donor-acceptor behaviour. Measured |H|/ρ ratios (-0.04 to -0.20) give negative values, where a more negative value indicates greater covalent interactions. Closer examination of the |H|/ρ ratios of Ag-O1 (-0.15) and Ag-O2 (-0.04) reveal that the Ag-O2 bond contains a greater ionic character than that of Ag-O1. This is not to say that the Ag-O2 is an ionic bond, but rather nears the criteria for one as compared to Ag-O1. Similarly, the value of the interaction

energy of Ag-O2 (E_{int} ≈ -14.3 kcal/mol) is weaker than that of Ag-O1 (E_{int} ≈ -34.7 kcal/mol). The values of the interaction energies of Ag-O1 and Ag-N1 are similar, where E_{int} ≈ -34.0 kcal/mol, with the interaction energy of the Ag-O1 being slightly higher than that of Ag-N1.

Table 4.2. Selected properties of the electron density at the BCPs according to QTAIM analysis, as well as computed DIs (δ) between appropriate atom pairs.

BCP	$\rho_{(r)}$	$\nabla^2\rho_{(r)}$	$V_{(r)}$	$H_{(r)}$	BD	$\lvert V_{(r)}\rvert/G_{(r)}$	DI(A,B)	E_{int} (kcal/mol)
Ag1-Ag^i	0.028	0.079	-0.026	-0.003	-0.11	1.14	0.22	-8.10
Ag1-O1	0.074	0.321	-0.111	-0.015	-0.20	1.16	NA	-34.7
Ag1-O2	0.040	0.171	-0.046	-0.001	-0.04	1.03	NA	-14.3
Ag1-N2	0.076	0.275	-0.107	-0.019	-0.18	1.22	0.57	-33.5

$\rho(r)$, $\nabla^2\rho(r)$, H(r), and V(r), are all given in atomic units (a.u.).

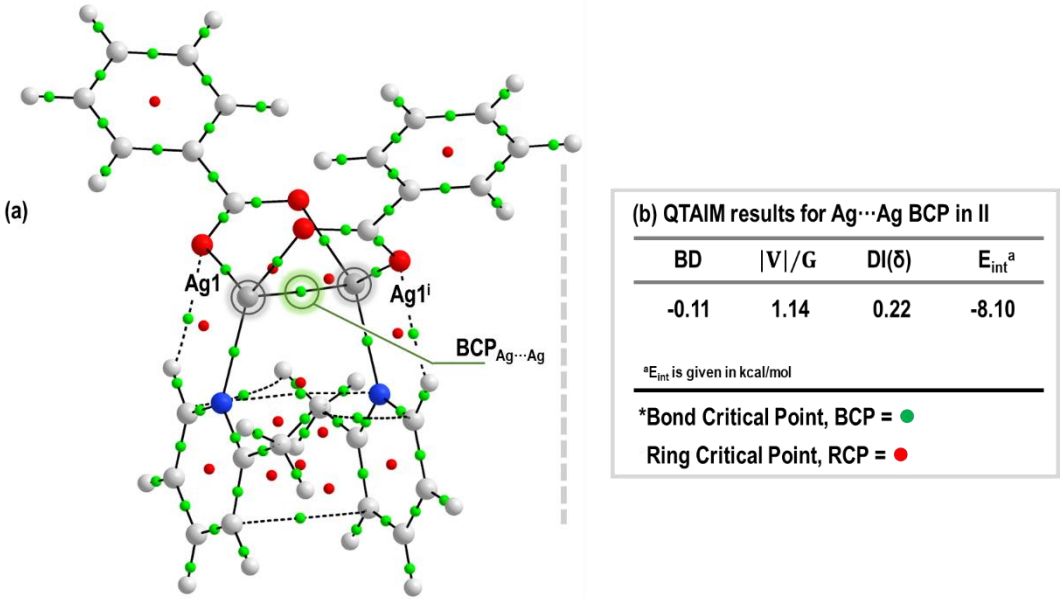

Figure 4.2. a) QTAIM molecular diagram calculated at the B3LYP-D2/aug-cc-PVTZ-PP (Ag) level for the experimental structure of compound **II**. This diagram emphasises the relevance of the bond critical point (BCP; green dots) along the intramolecular Ag···Ag bond path. b) Selected results of QTAIM analysis showing Ag···Ag non-covalent interaction.

4.6 QTAIM analysis of Ag^I···Ag^I interaction in compound III

The Ag^I···Ag^I BCP in **III** exhibits a relatively low electron density (ρ_{BCP} ≈ 0.037 a.u.) and a small positive Laplacian value ($\nabla^2\rho_{BCP}$ ≈ 0.086 a.u., see Table 4.3 below). According to the classification by Bianchi *et al.*,[124] the |V|/G ratio (1.22) of compound **III** corresponds to an intermediate bond character (1 < |V|/G < 2), which lies between electron-shared covalent bonds, classifying the Ag^I···Ag^I interaction as a transit closed-shell. The measured |H|/ρ ratio (-0.16) gives a negative value, indicating a weak covalent interaction.[125] The interaction energy[126] (E_{int} = ½V) for compound **III** is given to be E_{int} = -10.7 kcal/mol. The delocalisation index[127] is calculated as 0.34 (see Table 4.3). These values are all indicative of a transit closed-shell (weakly-covalent) supported argentophilic Ag^I···Ag^I interaction.

4.7 QTAIM analysis of double O,N-bridging in III

The BCP descriptors related to the double-bridged Ag···Ag contact, namely the Ag-N and Ag-O bonds, are comparable with those of dative bonding (see Table 4.3, Figure 4.3 below)[129] with the Ag-N and Ag-O bonds exhibiting a range of relatively low electron density values (ρ_{BCP} ≈ 0.057 – 0.070 a.u.) and large positive Laplacian values ($\nabla^2\rho_{BCP}$ ≈ 0.207 – 0.303 a.u.), as seen in Table 4.3 below. The values of the delocalisation index for both Ag-N and Ag-O are all less than 1, indicating donor-acceptor behaviour. All measured |H|/ρ ratios (-0.18) give negative values. Closer examination of the |H|/ρ ratios of Ag-O1 (-0.18) and Ag-O2 (-0.18) reveal that the Ag-O bonds are similar. Additionally, the values of their interaction energies (E_{int} ≈ -31.8 and -31.0 kcal/mol, respectively) are also similar in magnitude. In contrast to this, the values of the interaction energies between Ag-O1/O2 and Ag-N1 differ slightly, where E_{int} ≈ -31.0 kcal/mol and E_{int} ≈ -22.4 kcal/mol, respectively.

Table 4.3. Selected properties of the electron density at the BCPs according to QTAIM analysis, as well as computed DIs (δ) between appropriate atom pairs.

BCP	$\rho_{(r)}$	$\nabla^2\rho_{(r)}$	$V_{(r)}$	$H_{(r)}$	BD	$\lvert V_{(r)}\rvert/G_{(r)}$	DI (δ)	E_{int} (kcal/mol)
Ag1-Ag^i	0.037	0.086	-0.034	-0.006	-0.16	1.22	0.34	-10.7
Ag1-O1	0.070	0.303	-0.101	-0.013	-0.18	1.15	0.46	-31.8
Ag1-O2	0.068	0.299	-0.099	-0.012	-0.18	1.14	0.45	-31.0
Ag1-N2	0.057	0.207	-0.071	-0.010	-0.18	1.16	0.39	-22.4

ρ(r), $\nabla^2\rho(r)$, H(r), and V(r), are all given in atomic units (a.u.).

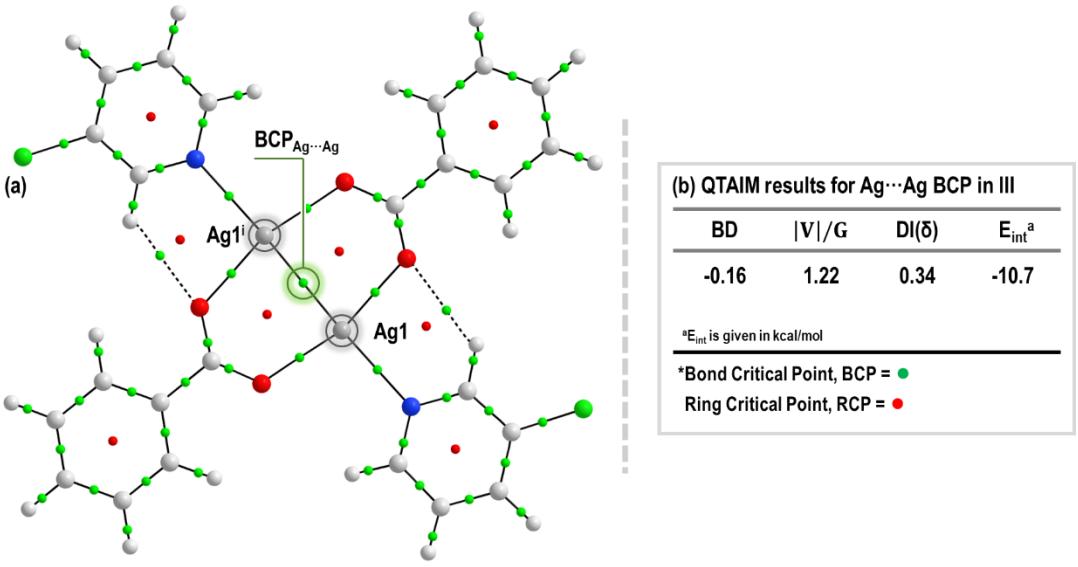

Figure 4.3. a) QTAIM molecular diagram calculated at the B3LYP-D2/aug-cc-PVTZ-PP (Ag) level for the experimental structure of compound **III**. This diagram emphasises the relevance of the bond critical point (BCP; green dots) along the intramolecular Ag···Ag bond path. b) Selected results of QTAIM analysis showing Ag···Ag non-covalent interaction.

4.8 QTAIM analysis of $Ag^{I}\cdots Ag^{I}$ interaction in compound IV

The $Ag^{I}\cdots Ag^{I}$ BCP exhibits a relatively low electron density ($\rho_{BCP} \approx 0.024$ a.u.) and a small positive Laplacian value ($\nabla^2\rho_{BCP} \approx 0.066$ a.u., see Table 4.4 below). According to the classification by Bianchi *et al.*,[124] the |V|/G ratio (1.11) of compound **IV** corresponds to an intermediate bond regime ($1 < |V|/G < 2$), which lies between electron-shared covalent bonds, classifying the $Ag^{I}\cdots Ag^{I}$ interaction as a transit closed-shell. The measured |H|/ρ ratio (-0.08) gives a negative value, indicating a weak covalent interaction.[125] The interaction energy[126] ($E_{int} = \frac{1}{2}V$) for compound **IV** is given to be $E_{int} = -6.42$ kcal/mol. The DI, δ[127] was measured as 0.18 (see Table 4.4 below). These values are indicative of a transit closed-shell supported argentophilic interaction.

4.9 QTAIM analysis of double O,N-bridging in IV

The BCP descriptors related to the Ag···Ag contact, namely the Ag-N and Ag-O bonds, are comparable with those of dative bonding (see Table 4.4, Figure 4.4 below).[129] This is evidently due to the circumstance whereby the Ag-N and Ag-O bonds exhibit a range of relatively low electron density values ($\rho_{BCP} \approx 0.040 – 0.071$ a.u.) and large positive Laplacian values ($\nabla^2\rho_{BCP} \approx 0.173 – 0.300$ a.u.), as seen in Table 4.4 below. The DI values for both Ag-N and Ag-O are less than 1, indicating that the bonds feature donor-acceptor behaviour. Measured |H|/ρ ratios (-0.03 – 0.23) give negative values. Closer examination of the |H|/ρ ratios of Ag-O1 (-0.19) and Ag-O2 (-0.03) reveal that the Ag-O2 bond contains a greater ionic character when compared to that of Ag-O1. Similarly, the value of the interaction energy of Ag-O2 ($E_{int} \approx -14.5$ kcal/mol) is weaker than that of Ag-O1 ($E_{int} \approx -32.1$ kcal/mol). Additionally, the values of the interaction energies of Ag-O1 and Ag-N1 are similar, where $E_{int} \approx -31.0$ kcal/mol, with the interaction energy of the Ag-O1 being slightly higher than that of Ag-N1.

Table 4.4. Selected properties of the electron density at the BCPs according to QTAIM analysis, as well as computed DIs (δ) between appropriate atom pairs.

BCP	$\rho_{(r)}$	$\nabla^2\rho_{(r)}$	$V_{(r)}$	$H_{(r)}$	BD	$\lvert V_{(r)}\rvert/G_{(r)}$	DI(A,B)	E_{int} (kcal/mol)
$Ag1\text{-}Ag^{i}$	0.024	0.066	-0.020	-0.002	-0.08	1.11	0.18	-6.42
Ag1-O1	0.071	0.300	-0.102	-0.014	-0.19	1.15	0.48	-32.1
Ag1-O2	0.040	0.173	-0.046	-0.001	-0.03	1.03	0.29	-14.5
Ag1-N2	0.071	0.262	-0.099	-0.016	-0.23	1.20	0.47	-30.9

ρ(r), $\nabla^2\rho(r)$, H(r), and V(r), are all given in atomic units (a.u.).

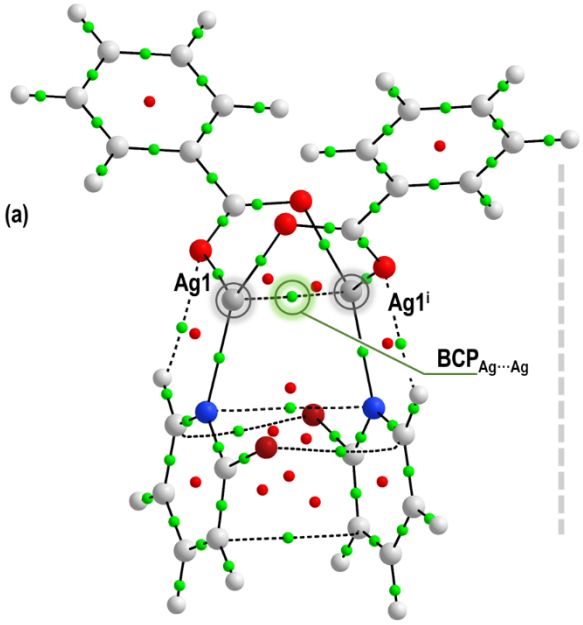

(b) QTAIM results for Ag···Ag BCP in IV

BD	|V|/G	DI(δ)	E_{int}[a]
-0.08	1.11	0.18	-6.42

[a] E_{int} is given in kcal/mol

*Bond Critical Point, BCP = ●
Ring Critical Point, RCP = ●

Figure 4.4. (a) QTAIM molecular diagram calculated at the B3LYP-D2/aug-cc-PVTZ-PP (Ag) level for the experimental structure of compound **IV**. This diagram emphasises the relevance of the bond critical point (BCP; green dots) along the intramolecular Ag···Ag bond path. (b) Selected results of QTAIM analysis showing Ag···Ag non-covalent interaction.

4.10 QTAIM analysis of $Ag^{I}\cdots Ag^{I}$ interaction in compound V

The $Ag^{I}\cdots Ag^{I}$ BCP exhibits a relatively low electron density ($\rho_{BCP} \approx 0.024$ a.u.) and a small positive Laplacian value ($\nabla^2\rho_{BCP} \approx 0.064$ a.u., see Table 4.5 below). According to the classification by Bianchi *et al.*,[124] the |V|/G ratio (1.14) of compound **V** corresponds to an intermediate bond regime ($1 < |V|/G < 2$), which lies between electron-shared covalent bonds, classifying the Ag···Ag interaction as a transit closed-shell. The measured |H|/ρ ratio (-0.11) gives a negative value, indicating a weak covalent interaction.[125] The interaction energy[126] (E_{int} = ½V) for **V** is given to be E_{int} = -8.13 kcal/mol. The DI, δ[127] was measured as 0.18 for compound **IV** (see Table 4.5 below). These values are indicative of a transit closed-shell supported argentophilic interaction.

4.11 QTAIM analysis of double O,N-bridging in V

The BCP descriptors related to the $Ag^{I}\cdots Ag^{I}$ contact, namely the Ag-N and Ag-O bonds, are comparable with those of dative bonding (see Table 4.5, Figure 4.5 below).[129] This is evidently due to the circumstance whereby the Ag-N and Ag-O bonds exhibit a range of relatively low electron density values ($\rho_{BCP} \approx 0.039 – 0.069$ a.u.) and large positive Laplacian values ($\nabla^2\rho_{BCP} \approx 0.164 – 0.325$ a.u.), as seen in Table 4.5 below. The DI values for both Ag-N and Ag-O are less than 1, indicating that the bonds feature donor-acceptor behaviour. Measured |H|/ρ ratios (-0.03 – 0.23) give negative values. Inspection of the |H|/ρ ratios of Ag-O1 (-0.19) and Ag-O2 (-0.03) reveal that Ag-O2 contains a greater ionic character when compared to that of Ag-O1. Similarly, the values of the interaction energies of Ag-O2 ($E_{int} \approx$ -14.5 kcal/mol) is weaker than that of Ag-O1 ($E_{int} \approx$ -32.1 kcal/mol). Values of the interaction energies of Ag-O1 and Ag-N1 are shown to be similar, where $E_{int} \approx$ -31.0 kcal/mol, with the interaction energy of the Ag-O1 being slightly higher than that of Ag-N1.

Table 4.5. Selected properties of the electron density at the BCPs according to QTAIM analysis, as well as computed DIs (δ) between appropriate atom pairs.

BCP	$\rho_{(r)}$	$\nabla^2\rho_{(r)}$	$V_{(r)}$	$H_{(r)}$	BD	$\lvert V_{(r)}\rvert/G_{(r)}$	DI(A,B)	E_{int} (kcal/mol)
Ag1-Ag^i	0.024	0.064	-0.021	-0.003	-0.11	1.14	0.18	-6.58
Ag1-O1	0.067	0.325	-0.088	-0.004	-0.19	1.15	0.48	-32.1
Ag1-O2	0.039	0.164	-0.043	-0.001	-0.03	1.03	0.29	-14.5
Ag1-N2	0.069	0.299	-0.091	-0.008	-0.23	1.20	0.47	-30.9

$\rho(r)$, $\nabla^2\rho(r)$, H(r), and V(r), are all given in atomic units (a.u.).

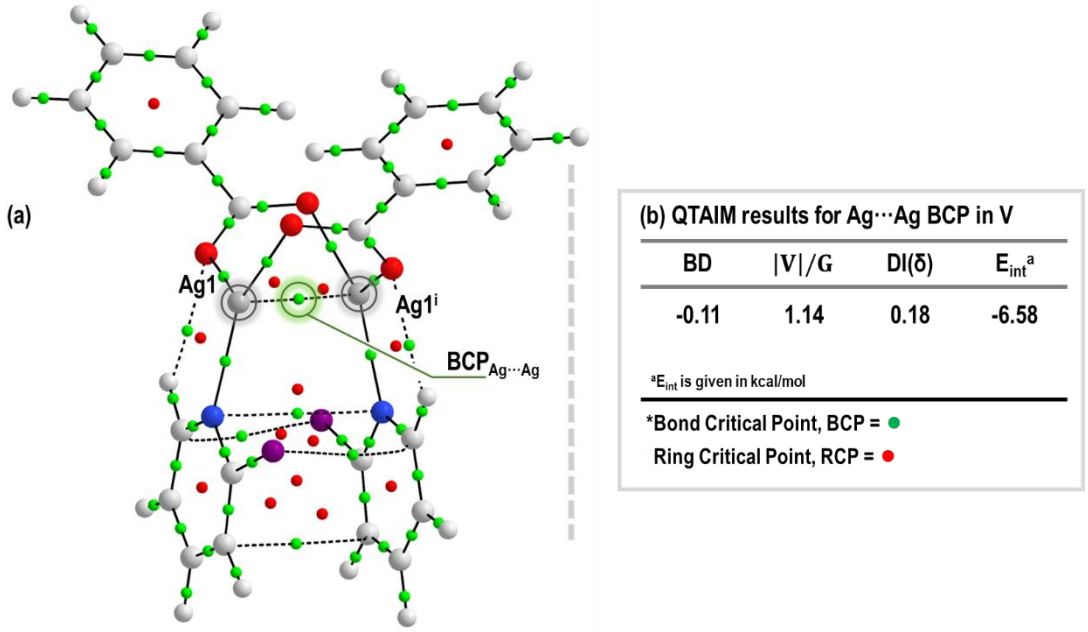

Figure 4.5. (a) QTAIM molecular diagram calculated at the B3LYP-D2/aug-cc-PVTZ-PP (Ag) level for the experimental structure of compound **V**. This diagram emphasises the relevance of the bond critical point (BCP; green dots) along the intramolecular Ag···Ag bond path. (b) selected results of QTAIM analysis showing Ag···Ag non-covalent interaction.

4.12 Support for the identification of semi-coordination interactions ($M^{+}\cdots X$) in compounds IV and V: QTAIM analysis

The ability of silver(I) compounds to interact with halogenated pyridine derivatives has not been thoroughly studied in terms of their semi-coordinated nature until the current study. Identified herein are $Ag^{I}\cdots X$ semi-coordinations of the electrophilic silver(I) centre with an electron belt of X, where X = Br or I. In order to classify the nature of the non-covalent interactions in compounds **IV** and **V**, and quantify their energies from a theoretical standpoint, comprehensive computational analysis at the B3LYP-D2/cc-pVDZ-PP level of theory was performed, as well as a topological analysis of the electron density distribution in the framework of Bader's theory (QTAIM method).[114] For the structure of **IV** and **V** at 100 K, the current researcher conducted the same computational study as described in Section 2.6, analysing the nature and energies of the $Ag^{I}\cdots Ag^{I}$ interactions. Results are summarised in Tables 4.6 and 4.7 below, with the contour line diagrams of the Laplacian distribution $\nabla^2\rho(r)$, bond paths, and selected zero-flux surfaces shown in Figures 4.6 and 4.7 below.

4.12.1 Semi-coordination interactions ($M^{+}\cdots X$) in compound IV

The QTAIM analysis demonstrated the presence of appropriate bond critical points for the semi-coordination interactions listed in Table 4.6 below for compound **IV**. The low magnitude of the electron density (0.018 a.u.), positive values of the Laplacian (0.055 a.u.), and close to zero (0.0003 a.u.) energy density at these BCPs are typical for non-covalent interactions. The current researcher has defined energies for these contacts according to the procedures proposed by Espinosa *et al*.[126] and Vener et al.[132] The estimated energies for these contacts are around -4.1 kcal/mol each. The ratio is |V|/G is less than 1 for both contacts; thus, their nature is predominantly non-covalent.[125]

Table 4.6. Selected properties of the electron density at the BCPs according to QTAIM analysis, as well as computed DIs (δ) between appropriate atom pairs.

BCP	$\rho_{(r)}$	$\nabla^2\rho_{(r)}$	$V_{(r)}$	$H_{(r)}$	BD	$\lvert V_{(r)}\rvert/G_{(r)}$	DI(A,B)	E_{int} (kcal/mol)
Ag1···Br1	0.018	0.055	-0.013	0.0003	0.02	0.97	0.18	-4.07

$\rho(r)$, $\nabla^2\rho(r)$, H(r), and V(r), are all given in atomic units (a.u.).

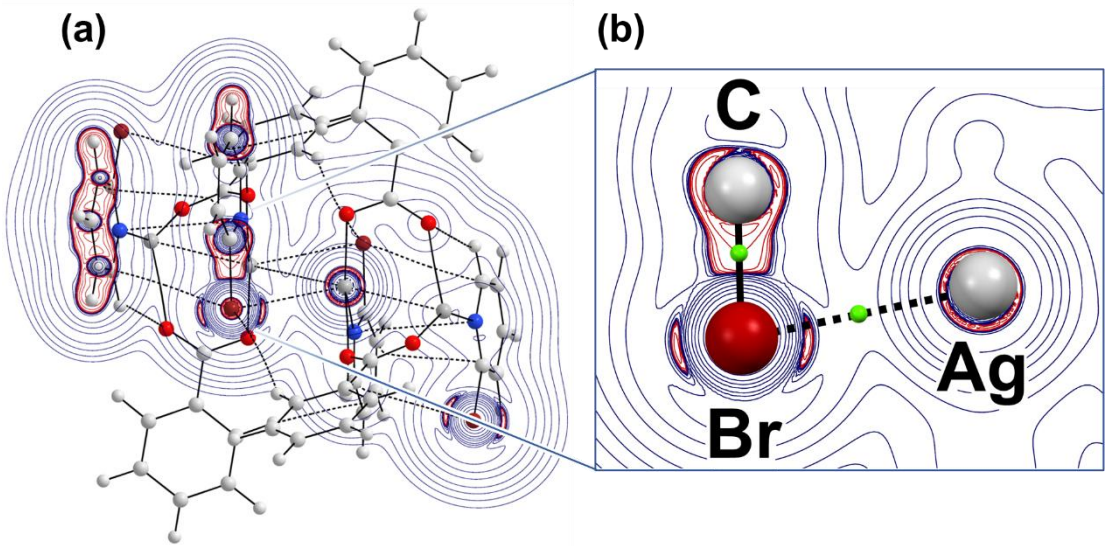

Figure 4.6. (a) The full atomic connectivity graph and $\nabla^2\rho_{(r)}$ contour plot of the mean-squared C—Br···Ag plane of the isolated dimer of compound **IV** (negative values are given by red dashed lines). (b) Fragment of the isolated pair with CPs (3, -1) of $\rho_{(r)}$ shown as green spheres, while the bold dashed curves correspond to bond paths of the R—Br···Ag interactions.

4.12.2 Semi-coordination interactions ($M^+\cdots X$) in compound V

QTAIM analysis demonstrated the presence of appropriate BCPs for the semi-coordination interactions listed in Table 4.7 below for compound **V**. The relatively low magnitude of the electron density (0.026 a.u.), positive values of the Laplacian (0.068 a.u.), and close to zero (-0.002 a.u.) energy density on these BCPs are typical for non-covalent interactions. The estimated energies for these contacts are around -6.6 kcal/mol, each. The ratio is |V|/G less than 1 for both contacts, thus indicating that they have some covalent character.[125]

Table 4.7. Selected properties of the electron density at the BCPs according to QTAIM analysis, as well as computed DIs (δ) between appropriate atom pairs.

BCP	$\rho_{(r)}$	$\nabla^2\rho_{(r)}$	$V_{(r)}$	$H_{(r)}$	BD	$\lvert V_{(r)}\rvert/G_{(r)}$	DI(A,B)	E_{int} (kcal/mol)
Ag1···I1	0.026	0.068	-0.021	-0.002	-0.08	1.10	0.18	-6.59

ρ(r), $\nabla^2\rho(r)$, H(r), and V(r), are all given in atomic units (a.u.).

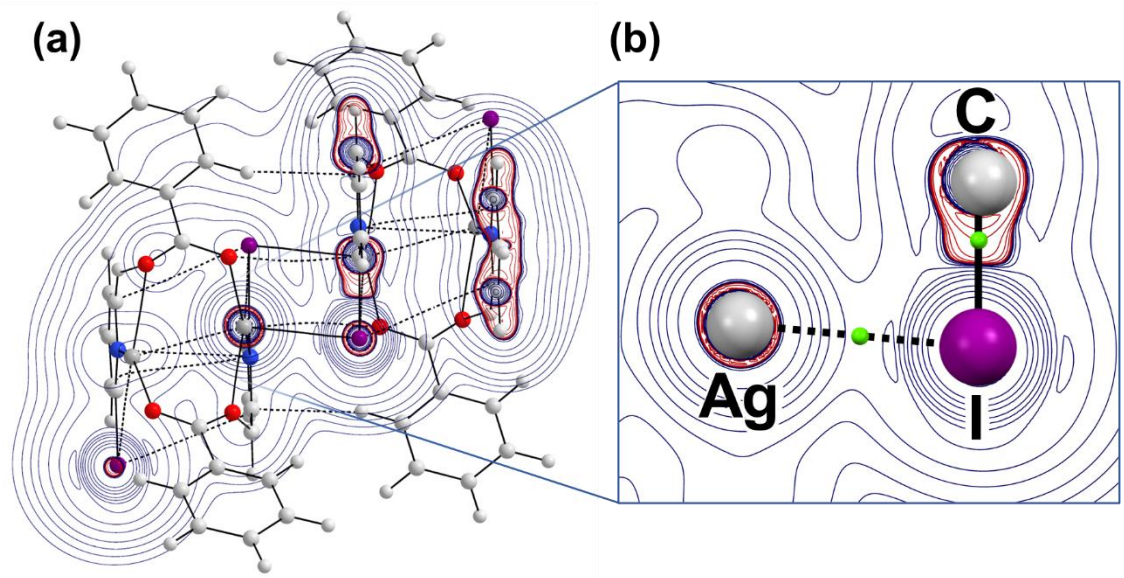

Figure 4.7. (a) The full atomic connectivity graph and $\nabla^2\rho_{(r)}$ contour plot of the mean-squared C—I···Ag plane of the isolated dimer of compound **V** (negative values are given by red dashed lines). (b) Fragment of the isolated pair with CPs (3, -1) of $\rho_{(r)}$ shown as green spheres, while the bold dashed curves correspond to bond paths of the R—I···Ag interactions.

4.13 Summary of theoretical studies of non-covalent interactions: QTAIM results

The dimerisation and/or association of the silver(I) atoms in compounds **I-V**, leading to $Ag^I\cdots Ag^I$ argentophilic interactions, has been shown to be associated with a degree of electron delocalisation (i.e. covalency). The magnitude of the $Ag^I\cdots Ag^I$ (and $Ag^I\cdots X$) interaction energies (E_{int}) was determined by DFT calculations and QTAIM analysis. This was done in order to understand the physical nature of the uncommon $Ag^I\cdots Ag^I$ interactions. A sign of an interaction is the presence of a BCP and BP linking two atoms.[133] Thus, the presence of BPs with associated BCPs interconnecting the silver(I) atoms in all compounds, **I-V**, confirms the existence of the argentophilic interactions.

The strengths of these interactions were estimated by halving the potential energy density (E_{int} = ½V), where a larger value of E_{int} signifies a stronger interaction and *vice versa*. The E_{int} values of the intramolecular $Ag^I\cdots Ag^I$ interactions for each compound is listed in Table 4.8 below. The QTAIM analysis data in Table 4.8 clearly indicates that compound **III**, with E_{int} = -10.7 kcal/mol, has the strongest intramolecular $Ag^I\cdots Ag^I$ interaction as compared to compounds **I**, **II**, **IV**, and **V**. This is presumably due to the difference in geometry, where **III** exhibits a more planar structure, as compared to the 'bent' structures of compounds **II**, **IV**, and **V**. In contrast to the strongest interaction, compounds **IV** and **V** together exhibit the weakest $Ag^I\cdots Ag^I$ interactions, with E_{int} = -6.42 and -6.58 kcal/mol, respectively. A polynomial regression (n^{th} deg. = 2, R^2 = 0.993) can be determined between the interaction energies, E_{int}, as a function of the $Ag^I\cdots Ag^I$ interaction distances displayed in Figure 4.8 below. This graph illustrates the general trend: as $Ag^I\cdots Ag^I$ interaction distance increases, the interaction energy (in kcal/mol) decreases, however, it is not a linear relationship. The E_{int} values range from -6.42 kcal/mol to -10.7 kcal/mol, which are considered to be quite moderate in terms of their strength.[134] Furthermore, the relationships between a number of the QTAIM descriptors of the $Ag^I\cdots Ag^I$ BCPs are shown in Figure 4.9 below. The QTAIM descriptors of the $Ag^I\cdots Ag^I$ BCPs are similar in their nature over the series from **I-V**. They seem to indicate an intermediate bonding regime ($V_{(r)avg}/G_{(r)avg} \approx$

1.15). On the other hand, their degrees of covalency, as measured by DI_{avg}, differ a notable amount from one another. Compound **III** has the highest delocalised electron density at the $Ag^{I}\cdots Ag^{I}$ BCP, while compounds **IV** and **V** have the lowest.

The values of charge density $\rho_{(r)}$ at the BCPs that characterise the $Ag^{I}\cdots Br$ and $Ag^{I}\cdots I$ contacts in compounds **IV** and **V**, respectively, are indicated in Table 4.8 below. As previously stated, it is well known that the density at the BCP is a good indicator of the strength of the interaction. The values of $\rho_{(r)}$ (0.018 a.u.) and Laplacian ($\nabla^2\rho_{(r)}$ = 0.055 a.u.) at the $Ag^{I}\cdots Br$ BCP in **IV** are smaller than those at the $Ag^{I}\cdots I$ BCP in **V** ($\rho_{(r)}$ = 0.026 and $\nabla^2\rho_{(r)}$ = 0.068 a.u.), thus indicating a stronger semi-coordination interaction for $Ag^{I}\cdots I$, in agreement with the polarisability of iodine over bromine (I > Br). Interestingly, the average values of the $Ag^{I}\cdots X$ (E_{avg} = -5.3 kcal/mol) contacts, for compounds **IV** and **V**, and those of their $Ag^{I}\cdots Ag^{I}$ interactions (E_{avg} = -6.5 kcal/mol) are relatively close in energy. Compounds **IV** and **V** exhibiting longer $Ag^{I}\cdots Ag^{I}$ contacts (relative to **I**, **II**, and **III**) may be due to the moderate association between the silver(I) atom of one compound with an iodine/bromine atom of an adjacent compound, i.e. the $Ag^{I}\cdots X$ contact. This association may prevent optimal orbital interaction/charge-transfer between the silver(I) atoms that constitute the dimeric structure, and thus may lead to a longer $Ag^{I}\cdots Ag^{I}$ contact distance. Whether or not this hypothesis is true would require further computational analysis via Energy Decomposition Analysis (EDA). This is, however, outside the scope of the current study.

Table 4.8. Selected properties of the electron density at the BCPs according to QTAIM analysis, as well as computed DIs (δ) between appropriate atom pairs.

$Ag^{I}\cdots Ag^{I}$	**I**	**II**	**III**	**IV**	**V**
Distance (Å)	2.885(10)	2.868(3)	2.790(4)	2.943(3)	2.975(8)
BD	-0.17	-0.11	-0.16	-0.08	-0.11
$\lvert V_{(r)}\rvert/G_{(r)}$	1.13	1.14	1.22	1.11	1.14
DI(A,B)	0.26	0.22	0.34	0.18	0.18
E_{int} (kcal/mol)	-7.63	-8.10	-10.7	-6.42	-6.58
$Ag^{I}\cdots X$ (X = Br,I)					
$\rho_{(r)}$	-	-	-	0.018	0.026
$\nabla^2\rho_{(r)}$	-	-	-	0.055	0.068
$\lvert V_{(r)}\rvert/G_{(r)}$	-	-	-	0.97	1.10
E_{int} (kcal/mol)	-	-	-	-4.07	-6.59

ρ(r), $\nabla^2\rho(r)$, V(r), and G(r), are all given in standard atomic units (a.u.).

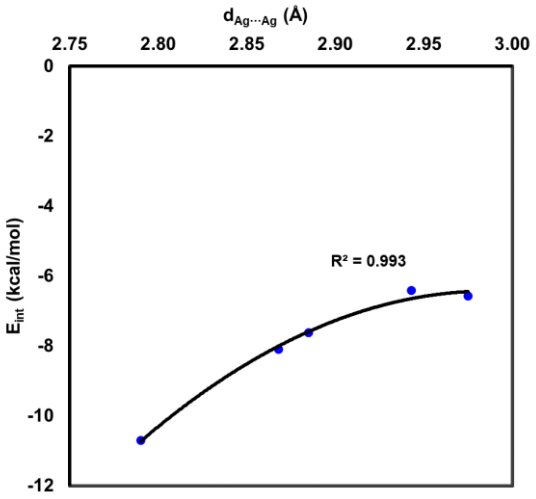

Figure 4.8. Correlation between the QTAIM interaction energy (E_{int}) and experimental Ag···Ag distances (Å) at the BCPs of compounds **I-V**.

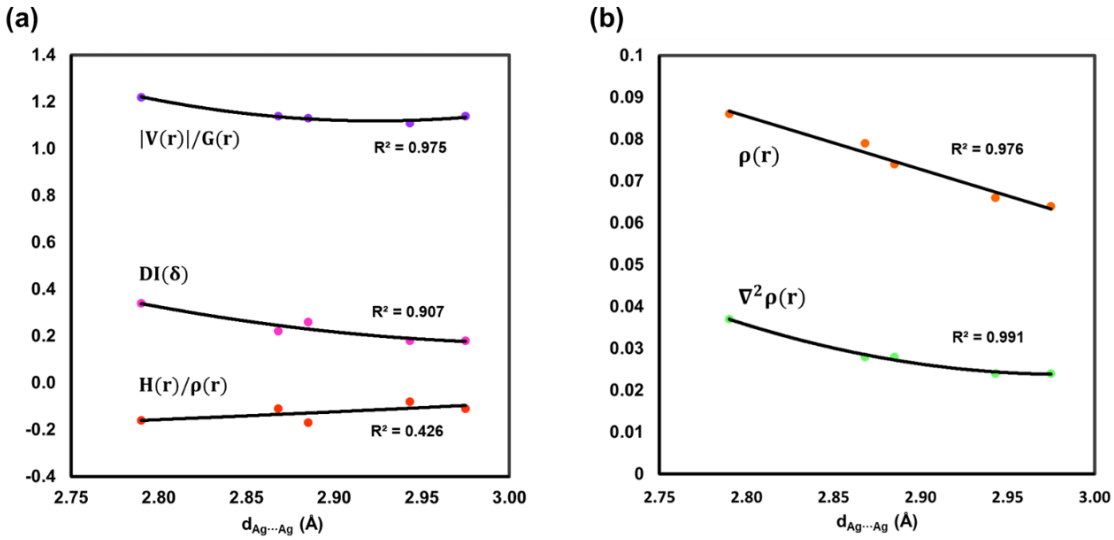

Figure 4.9. (a) Correlation between the interaction energy (E_{int}) and Ag···Ag distance (Å) at the BCPs of compounds **I-V**. (b) Selected QTAIM descriptors (V/G, DI, and BD) showing correlation between degree of covalency of Ag···Ag interactions and Ag···Ag distance in compounds **I-V**.

4.14 Theoretical studies of noncovalent interactions: natural bond orbital analysis

Natural bond orbital (NBO) analysis is a theoretical method used to investigate inter- and intramolecular interactions between any particular pair of localised orbitals. NBO analysis was performed using the NBO 3.0 program available through the Gaussian16 program suite.[115] This method was applied to probe the orbital nature of the argentophilic (and other Ag^{I}-related) interactions present within compounds **I-V**. A larger stabilisation energy $E^{(2)}$ value shows a more intense interaction between filled Lewis-type donor NBOs and empty acceptor non-Lewis-type NBOs.[136-138] The energies of these interactions may be calculated by second-order perturbation theory using the following equation:

$$\Delta E_{ij}^{(2)} = 2\frac{\langle \phi_i | F_{ij} | \phi_j \rangle}{\varepsilon_i - \varepsilon_j} \quad \text{... Eq. 28}$$

In the above, ϕ_i is the filled orbital of the donor (i) and ϕ_j is the empty orbital of the acceptor (j), $F_{(i,j)}$ is the off-diagonal NBO Fock matrix element, and ε_j and ε_i are diagonal elements (orbital energies) of the i^{th} and j^{th} NBO orbitals.[139] In the present study, the stabilisation energies of the intramolecular $Ag^{I}\cdots Ag^{I}$ and intermolecular $Ag^{I}\cdots\pi$ and $Ag^{I}\cdots X$ interactions were investigated by NBO analysis and compared.

Compounds **I-III** contain bonding (BD) electrons within their respective donor aromatic systems, e.g. pyridyl groups for **II-III**, which results in intermolecular charge transfer towards the acceptor lone-pairs (LP*) of silver(I), giving rise to the stabilisation of the molecular system. Similarly, compounds **IV** and **V** contain donor lone-pairs (LP) of electrons on the halogens, i.e. Br and I, which donate charge towards the silver(I) acceptor lone-pairs, in turn stabilising the molecular system.

4.15 NBO analysis of NCIs in compound I

NBO calculations were utilised in order to study the orbital contributions of the major non-covalent interactions involved in the stabilisation of compound **I**. Focus was placed on the second-order perturbation energy $E^{(2)}$, which is an excellent analysis tool for these kinds of donor–acceptor interactions.[140] The results of the major donor−acceptor interaction energies for compound **I** both as a monomer and as a dimeric unit are summarised in Table 4.9 below. The two major non-covalent interactions present herein are $Ag^{I}\cdots Ag^{I}$ and $Ag^{I}\cdots\pi$ interactions. It should be worth noting that the $Ag^{I}\cdots Ag^{I}$ interaction was calculated on the intramolecular level within the monomer unit, while the $Ag^{I}\cdots\pi$ interactions were calculated intermolecularly within the dimeric unit.

The orbital interactions between the silver(I) lone-pair (LP_{Ag}) and an empty atomic orbital (LP^*_{Ag}) were found to significantly contribute to the $Ag^{I}\cdots Ag^{I}$ interaction, with $E^{(2)}$ ranging from 16.81 – 18.12 kcal/mol. Moreover, an energetically equivalent 'retro-donation' or 'back-donation' between the two silver(I) atoms was also observed. Therefore the total stabilisation energy due to donor–acceptor orbital interactions is between $E^{(2)}$ = 33.6 – 36.2 kcal/mol, which is in good agreement with other calculations involving Ag dimers.[141] Likewise, the results from the intermolecular $Ag^{I}\cdots\pi$ interactions also revealed a non-negligible amount of charge transfer from the bonding ($BD_{C\text{-}C}$) orbitals of the C-C donor atoms (π-system) to the empty atomic Ag^{I}-acceptor orbitals. Their corresponding $E^{(2)}$ range is from 0.94 – 1.32 kcal/mol. It is of particular note that the $E^{(2)}$ quantities for each interaction are not comparable to one another due to their differing levels of theory. Interestingly, the crystallographic alignment of the OBn π-system with the Ag^{I}-atom is such that the Ag^{I}-atom is positioned closer to the aromatic ring carbons (as opposed to the centroid), which seems to allow for the maximum molecular orbital overlap. This provides a stereo-electronic explanation for the $Ag^{I}\cdots\pi$ interaction while also explaining the sub-van der Waals Ag···C distance observed in the crystal structure. To better visualise the orbital contributions of the two major non-covalent interactions, the $BD_{C\text{-}C}$ and LP_{Ag} donor, and the LP^*_{Ag} acceptor orbitals involved in the formation of the $Ag^{I}\cdots Ag^{I}$ and $Ag^{I}\cdots\pi$ interactions studied, are illustrated in Figures 4.10 and 4.11 below.

Table 4.9. Results of NBO analysis of donor−acceptor interactions in compound **I**, estimated by second-order interaction energy, $E^{(2)}_{i\rightarrow j}$, at the B3LYP/aug-cc-PVTZ-PP (monomeric) and B3LYP/cc-PVTZ-PP (dimeric) levels of theory.

Donor NBO (i) [a]	Occu.	Acceptor NBO (j) [a]	Occu.	$E^{(2)}$ [b]	$E_{(j)} - E_{(i)}$ [c]	$F_{(i,j)}$ [c]
$LP(5)_{Ag}$	1.97e	$LP^*(6)_{Ag}$	0.26e	18.12	0.71	0.108
$LP(5)_{Ag}$	1.97e	$LP^*(8)_{Ag}$	0.04e	16.81	1.07	0.120
$BD(1)_{C\text{-}C}$	1.97e	$LP^*(9)_{Ag}$	0.02e	1.32	0.81	0.029
$BD(2)_{C\text{-}C}$	1.66e	$LP^*(6)_{Ag}$	0.29e	0.94	0.44	0.018
$BD(2)_{C\text{-}C}$	1.66e	$LP^*(9)_{Ag}$	0.02e	1.28	0.36	0.021

[a] BD, LP, and LP* represent the bonding, lone pair, and empty atomic orbital, respectively. [b] $E^{(2)}$ values are in kcal/mol. [c] $E_{(j)}$,$E_{(i)}$ and $F_{(i,j)}$ are given in standard atomic units (a.u.).

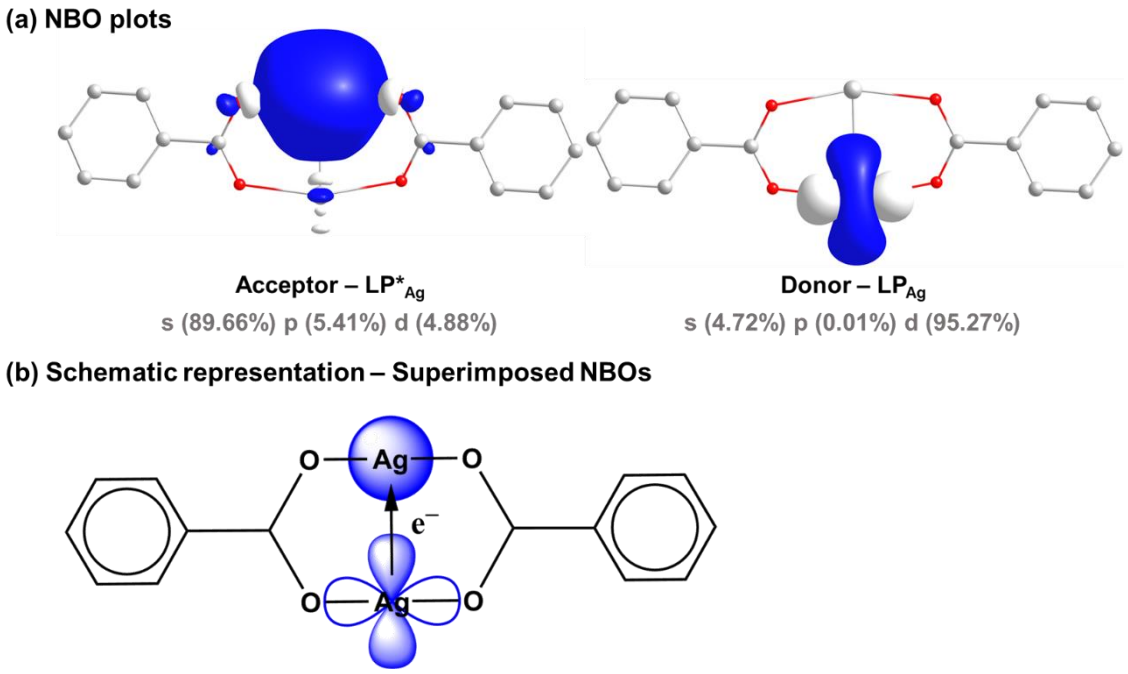

Figure 4.10. (a) NBO plots of the major donor (LP_{Ag}) and acceptor (LP^*_{Ag}) orbitals involved in the formation of $LP_{Ag} \rightarrow LP^*_{Ag}$ $Ag^I \cdots Ag^I$ interaction of compound **I**. (b) Schematic representation of the theoretical model used to compute the $Ag^I \cdots Ag^I$ interaction energies. Phase signs of the orbitals are shown in blue and white, charge transfer of the LP_{Ag} to the LP^*_{Ag} orbital is indicated with an arrow.

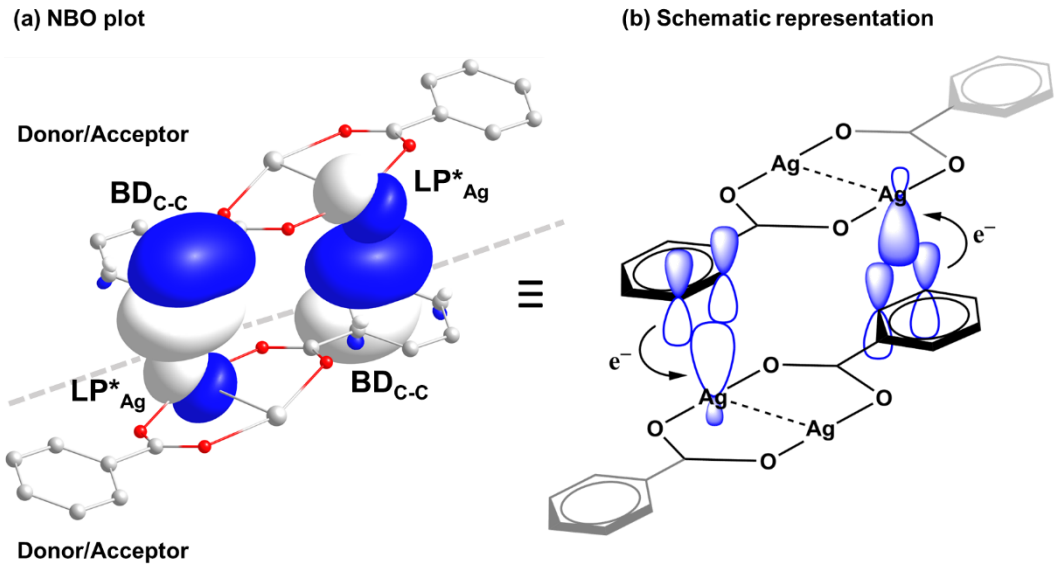

Figure 4.11. (a) Superimposed NBO plots of the donor ($BD_{C\text{-}C}$) and acceptor (LP^*_{Ag}) orbitals involved in the formation of $BD_{C\text{-}C} \rightarrow LP^*_{Ag}$ $Ag^{I}\cdots\pi$ interaction of the dimer of compound **I**. (b) Schematic representation of the theoretical model used to compute the $Ag^{I}\cdots\pi$ interaction energies. Phase signs of the orbitals are shown in blue and white, with the overlap of the $BD_{C\text{-}C}$ and LP^*_{Ag} orbitals being highlighted.

4.16 Molecular electrostatic potential (MEP) surface analysis of compound I

The MEP surface of compound **I** was computed in order to analyse the electron-rich and electron-poor regions of the molecule, as a means to rationalise some of the key interactions discussed in the previous section. The results estimate that the MEP minimum is present on the carboxylate oxygens of the benzoate substituents, with $V_{S,min}$ = –19.5 kcal/mol. The results also show moderate negative values at the centre of the two aryl rings, with V_S = –10.2 kcal/mol. In contrast, the MEP maximum is present at the silver(I) atoms, where $V_{S,max}$ = +17.6 kcal/mol. The results in Figure 4.12 below clearly demonstrate the potential for the occurrence of various π-interactions (i.e. $Ag^{I}\cdots\pi$ and $\pi\cdots\pi$) from an electrostatic perspective in the solid state of this compound, showing an extended negative π-surface, with the large positive region dominated by the silver(I) atoms.

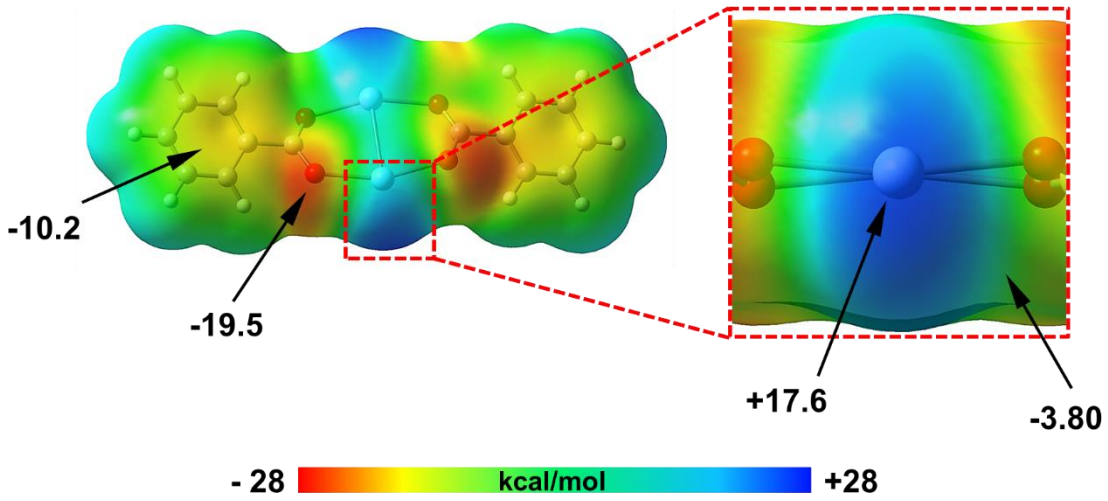

Figure 4.12. MEP surface of compound **I** at the B3LYP/cc-pVDZ-PP level of theory. Isosurface 0.001 a.u. The energies at selected points of the surface are given in kcal/mol.

4.17 NBO analysis of NCIs in compound II

The results of the major donor−acceptor interaction energies for compound **II** as a monomer and as a dimeric unit are summarised in Table 4.10 below. The two major non-covalent interactions present within compound **II**, much like **I**, are $Ag^{I}\cdots Ag^{I}$ and $Ag^{I}\cdots\pi$ interactions. The orbital interactions between the silver(I) lone-pair (LP_{Ag}) and the empty atomic orbitals (LP^{*}_{Ag}) were found to significantly contribute to the $Ag^{I}\cdots Ag^{I}$ interaction, with $E^{(2)}$ ranging from 27.54 – 31.58 kcal/mol. Moreover, an energetically equivalent 'retro-donation' or 'back-donation' between the two silver(I) atoms was also observed. Therefore the total stabilisation energy due to donor–acceptor orbital interactions is between $E^{(2)}$ = 55.1 – 63.2 kcal/mol. Likewise, the results from the $Ag^{I}\cdots\pi$ interactions reveal a nonnegligible amount of charge transfer from the bonding ($BD_{N\text{-}C}$) orbitals of the N-C donor atoms (π-system) to the empty atomic Ag^{I}-acceptor orbitals. The corresponding $E^{(2)}$ values range is from 1.07 – 5.55 kcal/mol. Interestingly, much like in **I**, the crystallographic alignment of the 2-Pic ligand (specifically the N-C double bond) with the silver(I) atom, is such that the silver(I) atom is positioned closer to the aromatic ring nitrogen and carbon atoms (as opposed to the centroid), which seems to allow for the maximum molecular orbital overlap. To better visualise the orbital contributions of the two major non-covalent interactions, the $BD_{N\text{-}C}$ and LP_{Ag} donor and the LP^{*}_{Ag} acceptor orbitals involved in the formation of the $Ag^{I}\cdots Ag^{I}$ and $Ag^{I}\cdots\pi$ interactions studied are illustrated in Figures 4.13 and 4.14 below.

Table 4.10. Results of NBO analysis of donor−acceptor interactions in compound **II**, estimated by second-order interaction energy, $E^{(2)}_{i\rightarrow j}$, at the B3LYP/aug-cc-PVTZ-PP (monomeric) and cc-PVTZ-PP (dimeric) levels of theory.

Donor NBO (i) [a]	Occu.	Acceptor NBO (j) [a]	Occu.	$E^{(2)}$ [b]	$E_{(j)} - E_{(i)}$ [c]	$F_{(i,j)}$ [c]
$LP(5)_{Ag}$	1.98e	$LP^*(6)_{Ag}$	0.25e	31.58	1.74	0.222
$LP(5)_{Ag}$	1.98e	$LP^*(7)_{Ag}$	0.07e	27.54	0.75	0.130
$BD(1)_{N-C}$	1.98e	$LP^*(7)_{Ag}$	0.11e	5.55	1.76	0.090
$BD(1)_{N-C}$	1.98e	$LP^*(9)_{Ag}$	0.06e	1.18	1.05	0.032
$BD(2)_{N-C}$	1.74e	$LP^*(7)_{Ag}$	0.11e	1.07	1.24	0.034

[a] BD and LP* represent the bonding and empty atomic orbital, respectively. [b] $E^{(2)}$ values are in kcal/mol. [c] $E_{(j)}$,$E_{(i)}$ and $F_{(i,j)}$ are given in standard atomic units (a.u.).

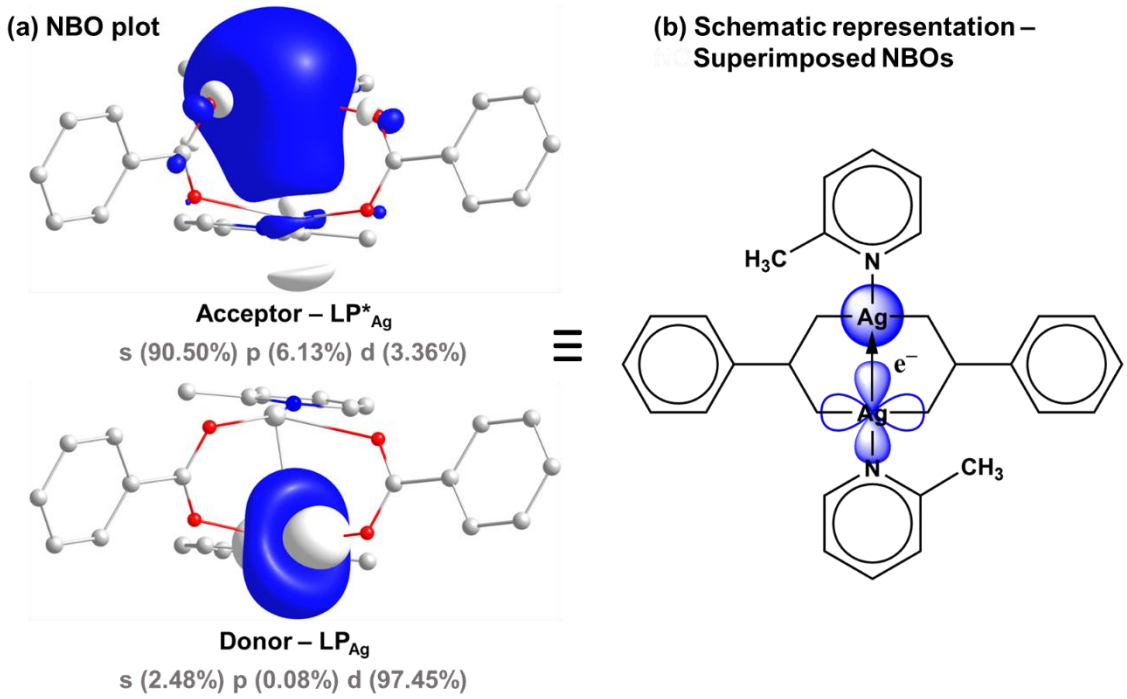

Figure 4.13. (a) NBO plots of the major donor (LP_{Ag}) and acceptor empty atomic (LP^*_{Ag}) orbitals involved in the formation of $LP_{Ag} \rightarrow LP^*_{Ag}$ $Ag^I\cdots Ag^I$ interaction of compound II. (b) Schematic representation of the theoretical model used to compute the $Ag^I\cdots Ag^I$ interaction energies. Phase signs of the orbitals are shown in blue and white, charge transfer of the LP_{Ag} to the LP^*_{Ag} orbital is indicated with an arrow.

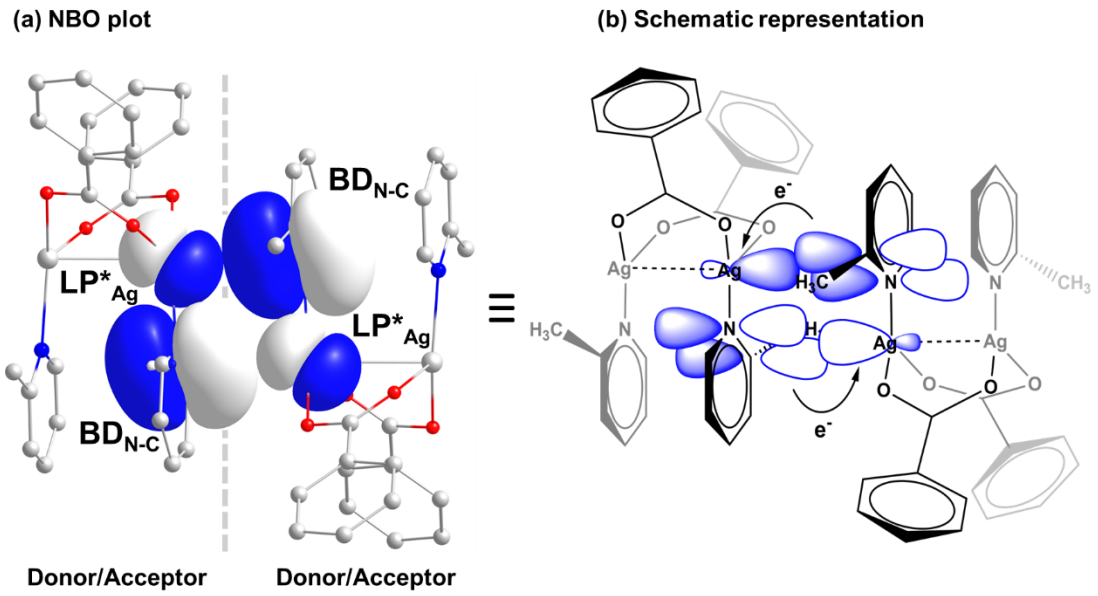

Figure 4.14. (a) NBO plots of the donor bonding (BD_{N-C}) and acceptor empty atomic (LP^*_{Ag}) orbitals involved in the formation of $BD_{N-C} \rightarrow LP^*_{Ag}$ $Ag^{I}\cdots\pi$ interaction of the dimer of compound II. (b) Schematic representation of the theoretical model used to compute the $Ag^{I}\cdots\pi$ interaction energies. Phase signs of the orbitals are shown in blue and white, with the overlap of the BD_{N-C} and LP^*_{Ag} orbitals being highlighted.

4.18 Molecular electrostatic potential surface analysis of compound II

The MEP minimum is present at the carboxyl oxygens of the benzoate substituents, with $V_{S,min}$ = -32.0 kcal/mol, as shown in Figure 4.15 below. The results also show relatively small negative values at the surface of the two silver(I) atoms, with V_S = –2.9 kcal/mol. In contrast, the MEP maximum is present at the aromatic H-atoms of the 2-Pic substituents, where $V_{S,max}$ = +25.1 kcal/mol. There also seems to be relatively small positive values at the centre of the 2-Pic rings, with V_S = +5.65 kcal/mol.

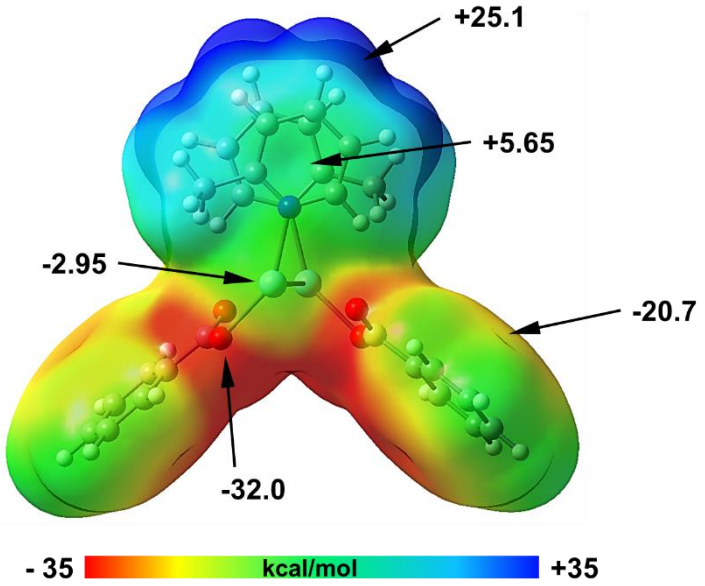

Figure 4.15. MEP surface of compound II at the B3LYP/cc-pVDZ-PP level of theory. Isosurface 0.001 a.u. The energies at selected points of the surface are given in kcal/mol.

4.19 NBO analysis of NCIs in compound III

The results of the major donor−acceptor interaction energies for compound **III** as a monomer and as a dimeric unit are summarised in Table 4.11 below. The two major non-covalent interactions present within compound **III**, again, much like that of **I** and **II**, are $Ag^{I}\cdots Ag^{I}$ and $Ag^{I}\cdots\pi$ interactions. It is interesting to note that the chlorine atoms do not form any contacts with other atoms, and consequently, they do not engage in any halogen-related interactions, such as halogen bonding. This observation may be attributed to the nature of the chlorine atom's orbitals, particularly their diffuseness or lack thereof. The orbital interactions between the silver(I) lone-pair (LP_{Ag}) and the empty atomic orbitals (LP^*_{Ag}) were found to significantly contribute to the $Ag^{I}\cdots Ag^{I}$ interaction, with $E^{(2)}$ ranging from 72.06 – 85.44 kcal/mol. Moreover, an energetically equivalent 'retro-donation' between the two silver(I) atoms was also observed. Therefore the total stabilization energy due to donor–acceptor orbital interactions is between $E^{(2)}$ = 144.12 – 170.9 kcal/mol. Likewise, the results from the $Ag^{I}\cdots\pi$ interactions also reveal nonnegligible amounts of charge transfer from the bonding ($BD_{C\text{-}C}$) orbitals of the C-C donor atoms (π-system) to the empty atomic Ag^{I}-acceptor orbitals. Their corresponding $E^{(2)}$ values range from 1.12 – 1.49 kcal/mol. Similar to **I** and **II**, the 3-Clpy ligand's (C-C double bond) crystallographic alignment with the silver(I) atom places it closer to the aromatic ring's nitrogen and carbon atoms. To better visualise the orbital contributions of the two major non-covalent interactions, the $BD_{C\text{-}C}$ and LP_{Ag} donor and the LP^*_{Ag} acceptor orbitals involved in the formation of the $Ag^{I}\cdots Ag^{I}$ and $Ag^{I}\cdots\pi$ interactions studied are illustrated in Figures 4.16 and 4.17 below.

Table 4.11. Results of NBO analysis of donor−acceptor interactions in compound **III**, estimated by second-order interaction energy, $E^{(2)}_{i\rightarrow j}$, at the B3LYP/aug-cc-PVTZ-PP (monomeric) and cc-PVTZ-PP (dimeric) levels of theory.

Donor NBO (i) [a]	Occu.	Acceptor NBO (j) [a]	Occu.	$E^{(2)}$ [b]	$E_{(j)} - E_{(i)}$ [c]	$F_{(i,j)}$ [c]
$LP(5)_{Ag}$	1.96e	$LP^*(6)_{Ag}$	0.27e	85.44	1.87	0.379
$LP(5)_{Ag}$	1.96e	$LP^*(7)_{Ag}$	0.08e	72.06	1.80	0.324
$BD(1)_{C\text{-}C}$	1.98e	$LP^*(9)_{Ag1}$	0.04e	1.37	0.96	0.032
$BD(2)_{C\text{-}C}$	1.61e	$LP^*(6)_{Ag2}$	0.28e	1.49	2.37	0.055
$BD(2)_{C\text{-}C}$	1.61e	$LP^*(9)_{Ag2}$	0.03e	1.12	0.43	0.022

[a] BD and LP* represent the bonding and empty atomic orbital, respectively. [b] $E^{(2)}$ values are in kcal/mol. [c] $E_{(j)}$,$E_{(i)}$ and $F_{(i,j)}$ are given in standard atomic units (a.u.).

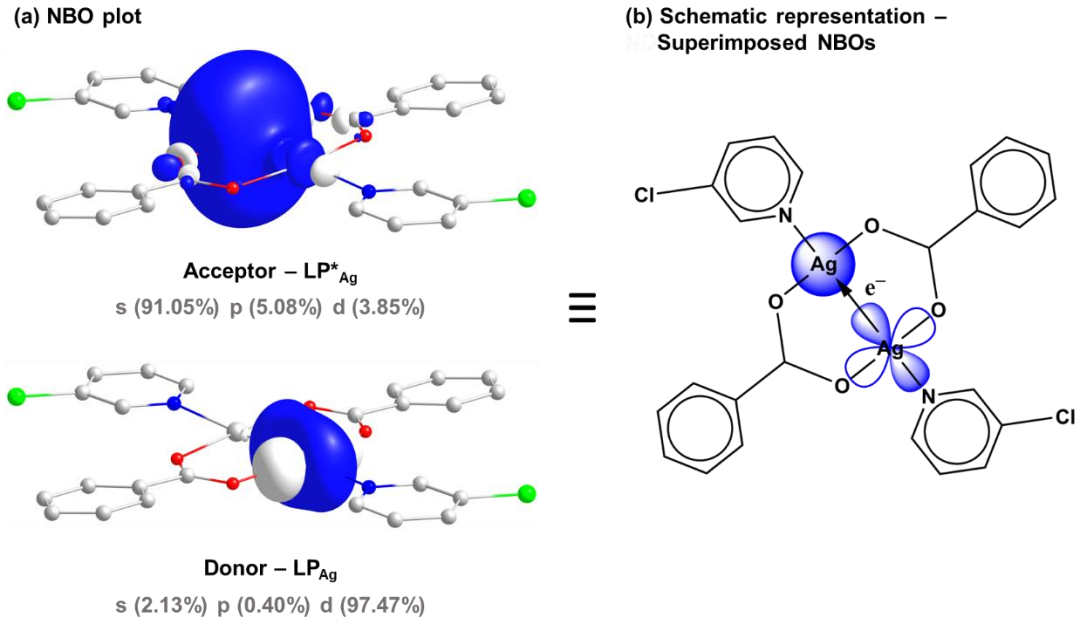

Figure 4.16. (a) NBO plots of the major donor (LP_{Ag}) and acceptor empty atomic (LP^*_{Ag}) orbitals involved in the formation of $LP_{Ag} \rightarrow LP^*_{Ag}$ $Ag^I\cdots Ag^I$ interaction of compound III. (b) Schematic representation of the theoretical model used to compute the $Ag^I\cdots Ag^I$ interaction energies. Phase signs of the orbitals are shown in blue and white, with the overlap of the LP_{Ag} and LP^*_{Ag} orbitals being highlighted.

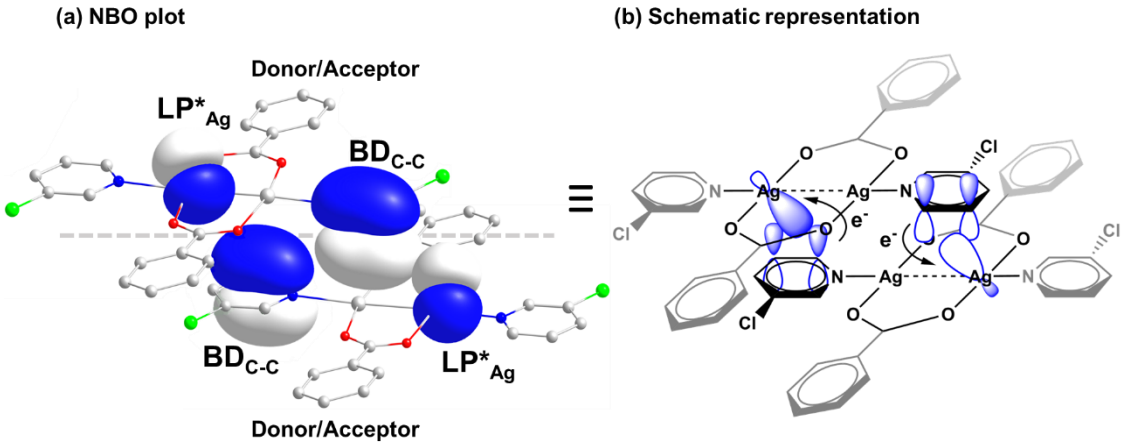

Figure 4.17. (a) NBO plots of the donor bonding (BD_{C-C}) and acceptor empty atomic (LP^*_{Ag}) orbitals involved in the formation of $BD_{C-C} \rightarrow LP^*_{Ag}$ $Ag^{I}\cdots\pi$ interaction of the dimer of compound III. (b) Schematic representation of the theoretical model used to compute the $Ag^{I}\cdots\pi$ interaction energies. Phase signs of the orbitals are shown in blue and white, with the overlap of the BD_{C-C} and LP^*_{Ag} orbitals being highlighted.

4.20 Molecular electrostatic potential surface analysis of compound III

The MEP minimum is present at the carboxyl oxygens of the benzoate substituents, with $V_{S,min}$ = -22.6 kcal/mol, as shown in Figure 4.18 below. The results also show relatively small negative values at the surface of the two silver atoms, with V_S = –5.0 kcal/mol. In contrast, the MEP maximum is present at the aromatic H-atoms of the 3-Clpy substituents, where $V_{S,max}$ = +21.3 kcal/mol. There also seems to be relatively small positive values at the centre of the 3-Clpy rings, with V_S = +4.40 kcal/mol.

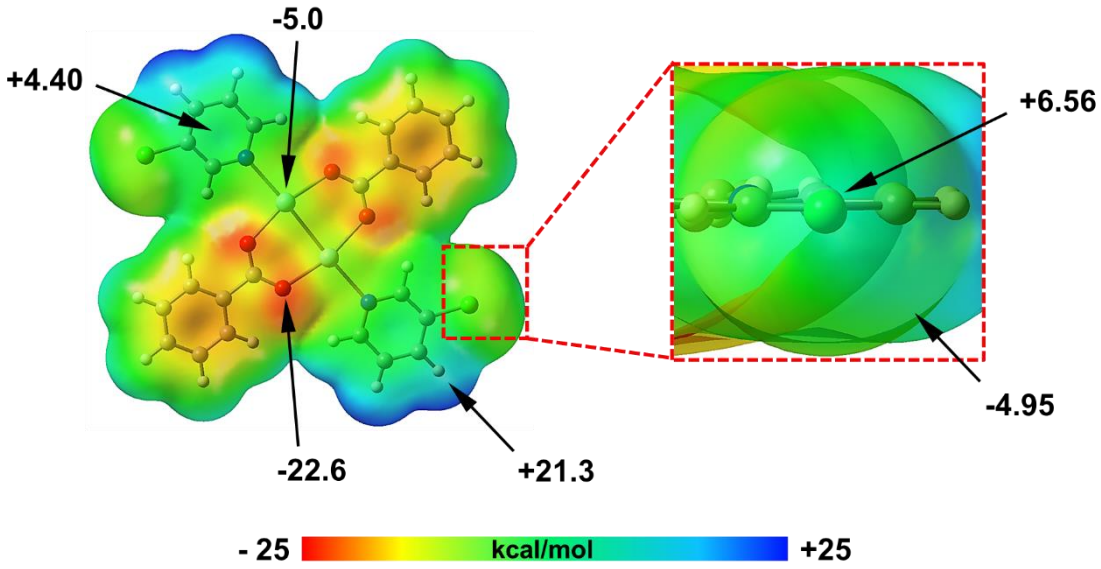

Figure 4.18. MEP surface of compound III at the B3LYP/cc-pVDZ-PP level of theory. Isosurface 0.001 a.u. The energies at selected points of the surface are given in kcal/mol.

4.21 NBO analysis of NCIs in compound IV

The results of the major donor−acceptor interaction energies for compound **IV** as a monomer and as a dimeric unit are summarised in Table 4.12 below. The two major non-covalent interactions present within compound **IV** are $Ag^{I}\cdots Ag^{I}$ and $Ag^{I}\cdots Br$ interactions. The orbital interactions between the silver(I) lone-pair (LP_{Ag}) and the empty atomic orbitals (LP^{*}_{Ag}) were found to significantly contribute to the $Ag^{I}\cdots Ag^{I}$ interaction, with $E^{(2)}$ ranging from 20.24 – 23.14 kcal/mol. Moreover, an energetically equivalent 'retro-donation' between the two silver(I) atoms is also observed. Therefore the total stabilisation energy due to donor–acceptor orbital interactions is between $E^{(2)}$ = 40.5 – 46.3 kcal/mol. Likewise, the results from the $Ag^{I}\cdots Br$ interactions also reveal moderate amounts of charge transfer from the lone pair (LP_{Br}) orbital of the Br donor atom to the empty atomic silver(I) acceptor orbital (LP^{*}_{Ag}). Their corresponding $E^{(2)}$ range from 1.05 – 10.6 kcal/mol. Interestingly, the crystallographic alignment of the 2-Brpy ligand with the silver(I) atom is such that the R_3C-Br atom is positioned ca. 80 ° to the silver(I) atom, as opposed to pointing ca. 180 ° This seems to allow for semi-maximum molecular orbital overlap, where the maximum would be 90 ° of the lone pair of the Br. To better visualise the orbital contributions of the two major non-covalent interactions, the LP_{Br} and LP_{Ag} donor and the LP^{*}_{Ag} acceptor orbitals involved in the formation of the $Ag^{I}\cdots Ag^{I}$ and $Ag^{I}\cdots Br$ interactions are illustrated in Figures 4.19 and 4.20 below.

Table 4.12. Results of NBO analysis of donor−acceptor interactions in compound **IV**, estimated by second-order interaction energy, $E^{(2)}_{i\rightarrow j}$, at the B3LYP/aug-cc-PVTZ-PP (monomeric) and cc-PVTZ-PP (dimeric) levels of theory.

Donor NBO (i) [a]	Occu.	Acceptor NBO (j) [a]	Occu.	$E^{(2)}$ [b]	$E_{(j)} - E_{(i)}$ [c]	$F_{(i,j)}$ [c]
$LP(5)_{Ag}$	1.98e	$LP^*(6)_{Ag}$	0.24e	23.14	1.74	0.190
$LP(5)_{Ag}$	1.98e	$LP^*(7)_{Ag}$	0.24e	20.29	0.75	0.112
$LP(5)_{Ag}$	1.98e	$LP^*(9)_{Ag}$	0.08e	20.24	0.74	0.109
$LP(1)_{Br}$	1.96e	$LP^*(7)_{Ag}$	0.13e	4.71	2.11	0.091
$LP(1)_{Br}$	1.96e	$LP^*(8)_{Ag}$	0.10e	7.08	0.83	0.070
$LP(1)_{Br}$	1.96e	$LP^*(9)_{Ag}$	0.07e	1.05	0.98	0.029
$LP(2)_{Br}$	1.92e	$LP^*(7)_{Ag}$	0.13e	3.43	1.97	0.074
$LP(2)_{Br}$	1.92e	$LP^*(8)_{Ag}$	0.24e	3.23	0.70	0.043
$LP(3)_{Br}$	1.88e	$LP^*(6)_{Ag}$	0.24e	1.93	1.81	0.053
$LP(3)_{Br}$	1.88e	$LP^*(7)_{Ag}$	0.13e	7.20	1.86	0.103
$LP(3)_{Br}$	1.88e	$LP^*(8)_{Ag}$	0.10e	10.60	0.56	0.071

[a] LP and LP* represent the lone pair and empty atomic orbital, respectively. [b] $E^{(2)}$ values are in kcal/mol. [c] $E_{(j)}$,$E_{(i)}$ and $F_{(i,j)}$ are given in standard atomic units (a.u.).

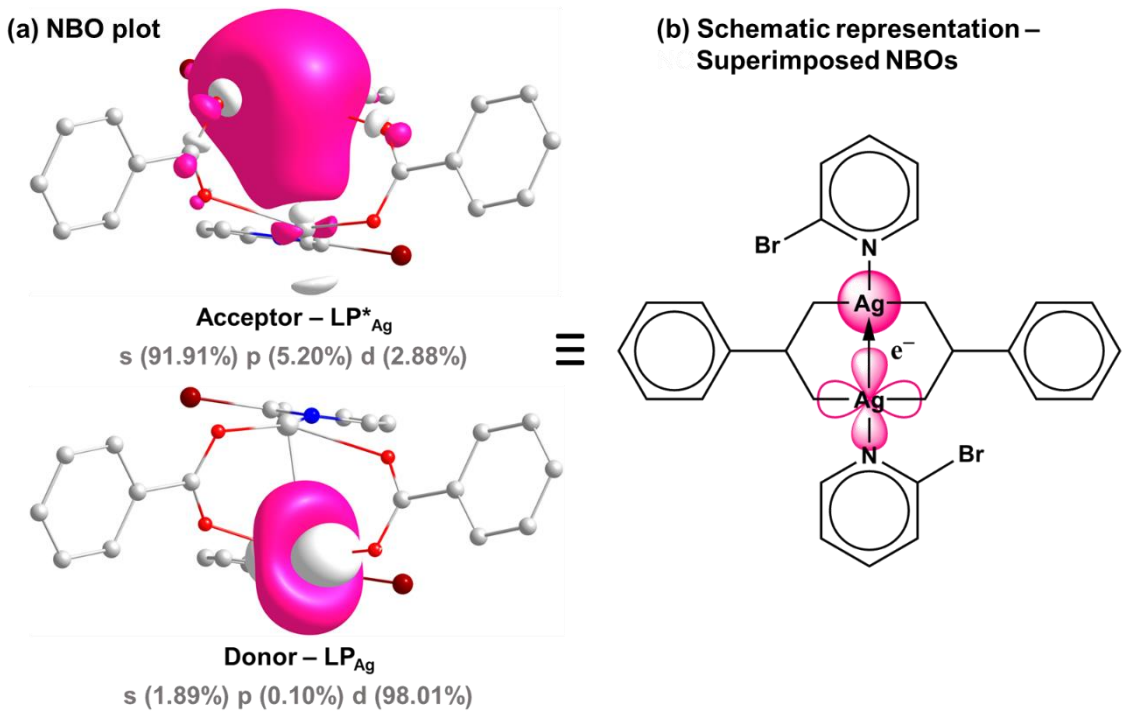

Figure 4.19. (a) NBO plots of the major donor (LP_{Ag}) and acceptor empty atomic (LP^*_{Ag}) orbitals involved in the formation of $LP_{Ag} \rightarrow LP^*_{Ag}$ $Ag^I \cdots Ag^I$ interaction of compound IV. (b) Schematic representation of the theoretical model used to compute the $Ag^I \cdots Ag^I$ interaction energies. Phase signs of the orbitals are shown in pink and white, charge transfer of the LP_{Ag} to the LP^*_{Ag} orbital is indicated with an arrow.

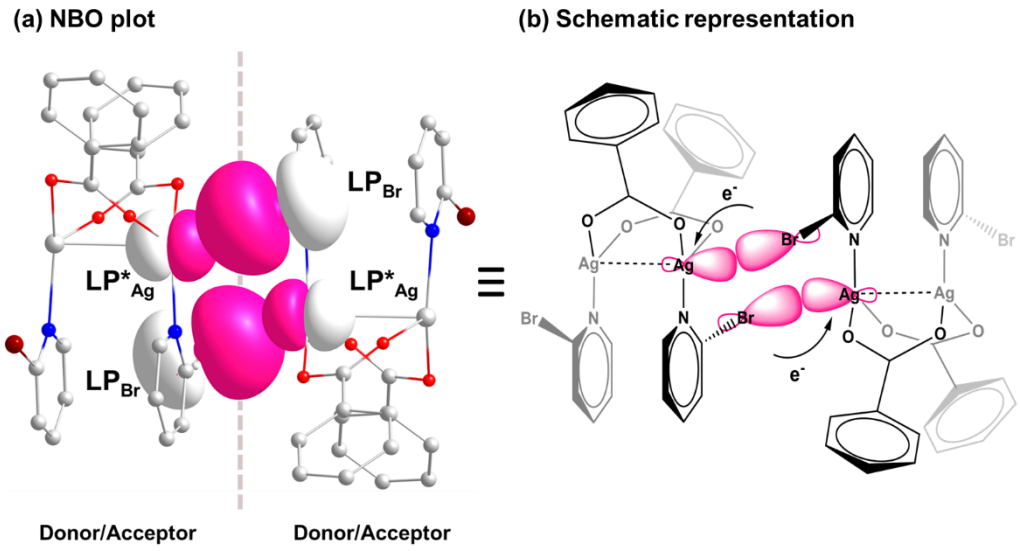

Figure 4.20. (a) NBO plots of the donor lone-pair (LP_{Br}) and acceptor empty atomic (LP^*_{Ag}) orbitals involved in the formation of $LP_{Br} \rightarrow LP^*_{Ag}$ semi-coordination interactions of a dimer of compound IV. (b) Schematic representation of the theoretical model used to compute the SCB interaction energies. Phase signs of the orbitals are shown in pink and white, with the overlap of the LP_{Br} and LP^*_{Ag} orbitals being highlighted in pink.

4.22 Molecular electrostatic potential surface analysis of compound IV

The MEP minimum on compound **V** is found at the carboxyl oxygens of the benzoate substituents, with $V_{S,min}$ = -36.4 kcal/mol, as shown in Figure 4.21 below. The results also show relatively small negative values at the surface of the two silver atoms, with V_S = –3.77 kcal/mol. In contrast, the MEP maximum is present at the aromatic H-atoms of the 2-Brpy substituents, where $V_{S,max}$ = +32.6 kcal/mol. There also seems to be positive values at the centre of the 2-Brpy rings and on the surface of the Br atom (σ-hole), with V_S = +12.2 and +12.6 kcal/mol, respectively. These results demonstrate the potential for the occurrence of the semi-coordination (i.e. $Ag^I \cdots Br$) interactions in the solid state of this compound. This is due to the extended negative π-surface (including the $Ag^I \cdots Ag^I$ atoms) associating with the large positive region dominated by the 2-Brpy aromatic rings.

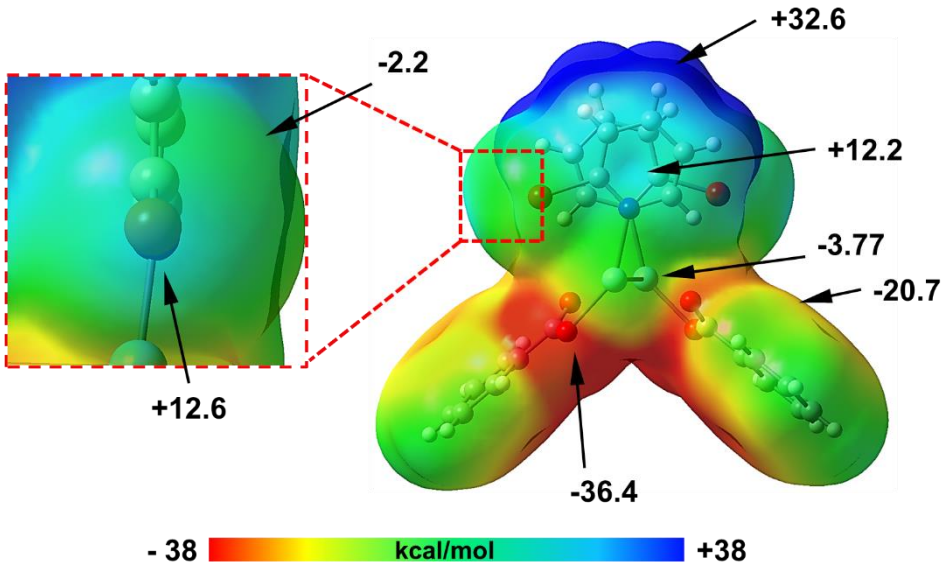

Figure 4.21. MEP surface of compound IV at the B3LYP/cc-pVDZ-PP level of theory. Isosurface 0.001 a.u. The energies at selected points of the surface are given in kcal/mol.

4.23 NBO analysis of NCIs in compound V

The results of the major donor−acceptor interaction energies for compound **V** as a monomer and as a dimeric unit are summarised in Table 4.13 below. The two major non-covalent interactions present within compound **V** are $Ag^{I}\cdots Ag^{I}$ and $Ag^{I}\cdots I$ interactions. The orbital interactions between the silver(I) lone-pair (LP_{Ag}) and the empty atomic orbitals (LP^{*}_{Ag}) were found to significantly contribute to the $Ag^{I}\cdots Ag^{I}$ interaction, with $E^{(2)}$ ranging from 21.15 – 22.26 kcal/mol. Moreover, an energetically equivalent 'retro-donation' between the two silver(I) atoms is also observed. Therefore the total stabilisation energy due to donor–acceptor orbital interactions is between $E^{(2)}$ = 42.3 – 44.6 kcal/mol. Likewise, the results from the $Ag^{I}\cdots I$ interactions reveal moderate amounts of charge transfer from the lone pair (LP_{I}) orbital of the I donor atom to the empty atomic silver(I) acceptor orbital (LP^{*}_{Ag}). Their corresponding $E^{(2)}$ range from 3.23 – 25.63 kcal/mol. The crystallographic alignment of the 2-Ipy ligand with the silver(I) atom is such that the I atom is positioned ca. 87 ° to the silver(I) atom, as opposed to pointing ca. 180 ° This seems to allow for maximum molecular orbital overlap of the lone pair of the iodine atom. To better visualise the orbital contributions of the two major non-covalent interactions, the LP_{I} and LP_{Ag} donor and the LP^{*}_{Ag} acceptor orbitals involved in the formation of the $Ag^{I}\cdots Ag^{I}$ and $Ag^{I}\cdots I$ interactions are illustrated in Figures 4.22 and 4.23 below.

Table 4.13. Results of NBO analysis of donor−acceptor interactions in compound **V**, estimated by second-order interaction energy, $E^{(2)}_{i\rightarrow j}$, at the B3LYP/aug-cc-PVTZ-PP (monomeric) and cc-PVTZ-PP (dimeric) levels of theory.

Donor NBO (i) [a]	Occu.	Acceptor NBO (j) [a]	Occu.	$E^{(2)}$ [b]	$E_{(j)} - E_{(i)}$ [c]	$F_{(i,j)}$ [c]
$LP(5)_{Ag}$	1.98e	$LP^*(6)_{Ag}$	0.24e	22.26	1.77	0.189
$LP(5)_{Ag}$	1.98e	$LP^*(7)_{Ag}$	0.24e	21.55	0.76	0.116
$LP(5)_{Ag}$	1.98e	$LP^*(9)_{Ag}$	0.08e	21.15	0.71	0.110
$LP(1)_{I}$	1.97e	$LP^*(7)_{Ag}$	0.15e	11.20	1.92	0.135
$LP(1)_{I}$	1.97e	$LP^*(8)_{Ag}$	0.11e	3.23	0.85	0.048
$LP(1)_{I}$	1.97e	$LP^*(9)_{Ag}$	0.08e	1.17	0.85	0.029
$LP(2)_{I}$	1.91e	$LP^*(7)_{Ag}$	0.15e	3.96	1.73	0.075
$LP(3)_{I}$	1.84e	$LP^*(6)_{Ag}$	0.26e	8.69	1.76	0.113
$LP(3)_{I}$	1.84e	$LP^*(7)_{Ag}$	0.15e	25.63	1.78	0.191
$LP(3)_{I}$	1.84e	$LP^*(8)_{Ag}$	0.11e	4.23	0.71	0.050

[a] LP and LP* represent the lone pair and empty atomic orbital, respectively. [b] $E^{(2)}$ values are in kcal/mol. [c] $E_{(j)}$,$E_{(i)}$ and $F_{(i,j)}$ are given in standard atomic units (a.u.).

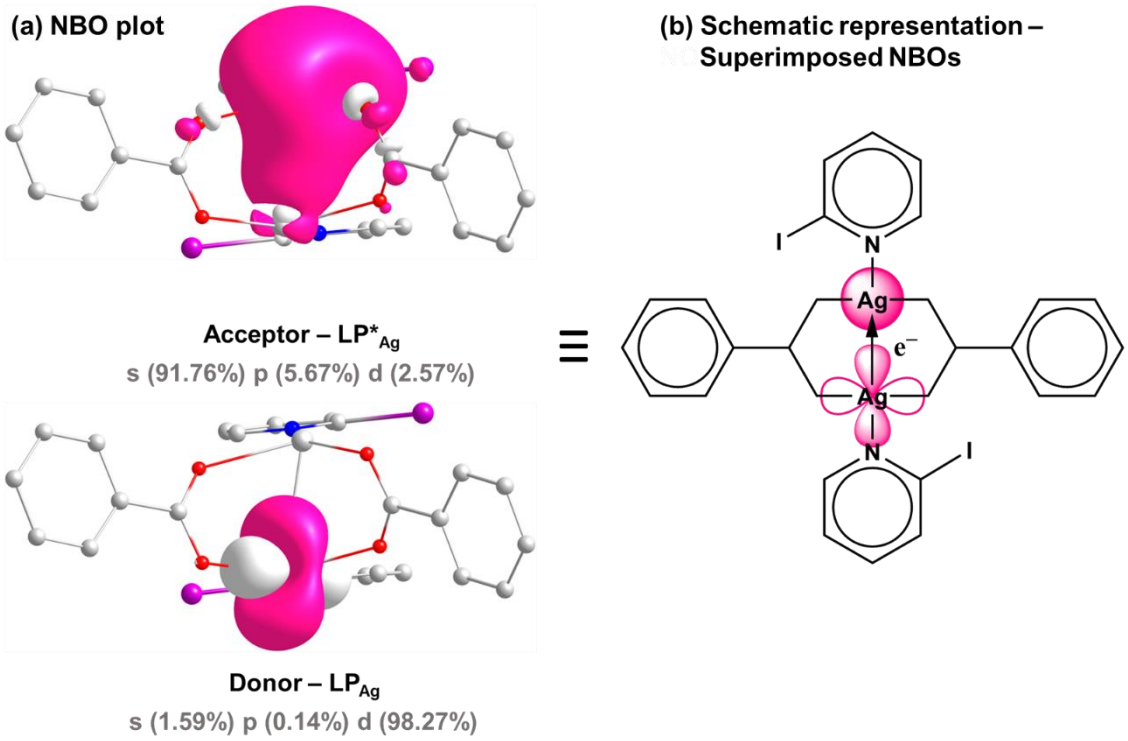

Figure 4.22. (a) NBO plots of the major donor (LP_{Ag}) and acceptor empty atomic (LP^*_{Ag}) orbitals involved in the formation of $LP_{Ag} \rightarrow LP^*_{Ag}$ $Ag^I\cdots Ag^I$ interaction of compound V. (b) Schematic representation of the theoretical model used to compute the $Ag^I\cdots Ag^I$ interaction energies. Phase signs of the orbitals are shown in pink and white, charge transfer of the LP_{Ag} to the LP^*_{Ag} orbital is indicated with an arrow.

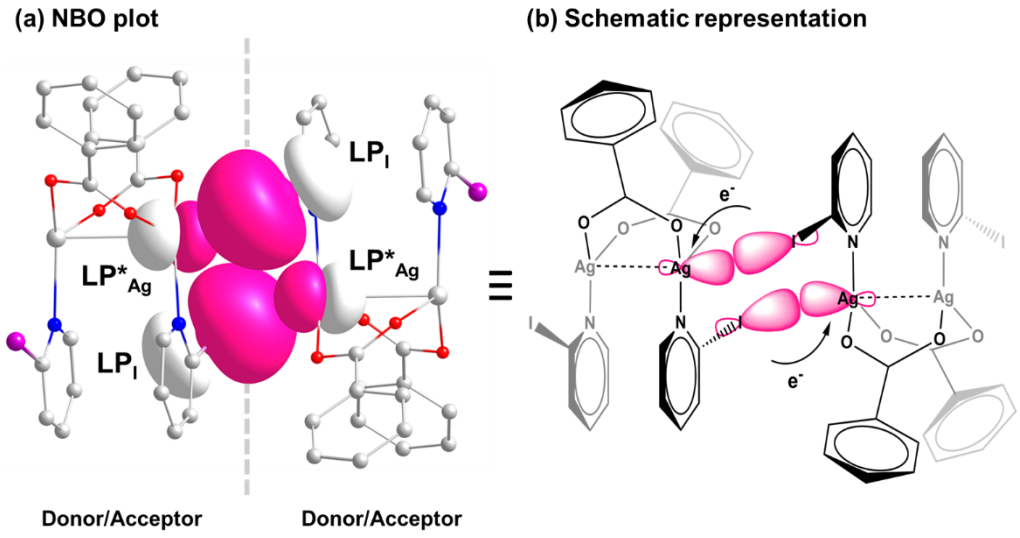

Figure 4.23. (a) NBO plots of the donor lone-pair (LP_{Br}) and acceptor empty atomic (LP^*_{Ag}) orbitals involved in the formation of $LP_{Br} \rightarrow LP^*_{Ag}$ semi-coordination interactions of a dimer of compound V. (b) Schematic representation of the theoretical model used to compute the SCB interaction energies. Phase signs of the orbitals are shown in pink and white, with the overlap of the LP_{Br} and LP^*_{Ag} orbitals highlighted in pink.

4.24 Molecular electrostatic potential (MEP) surface analysis of compound V

The MEP minimum on compound **V** is present at the carboxyl oxygens of the benzoate substituents, with $V_{S,min}$ = -36.4 kcal/mol, as shown in Figure 4.24 below. Interesting, the results also show relatively small negative values at the surface of the two silver atoms, with V_S = –5.77 kcal/mol. In contrast, the MEP maximum is present at the aromatic H-atoms of the 2-Ipy substituents, where $V_{S,max}$ = +31.2 kcal/mol. There also seems to be positive values at the centre of the 2-Ipy rings and on the surface of the I atom (σ-hole), with V_S = +10.2 and +18.8 kcal/mol, respectively.

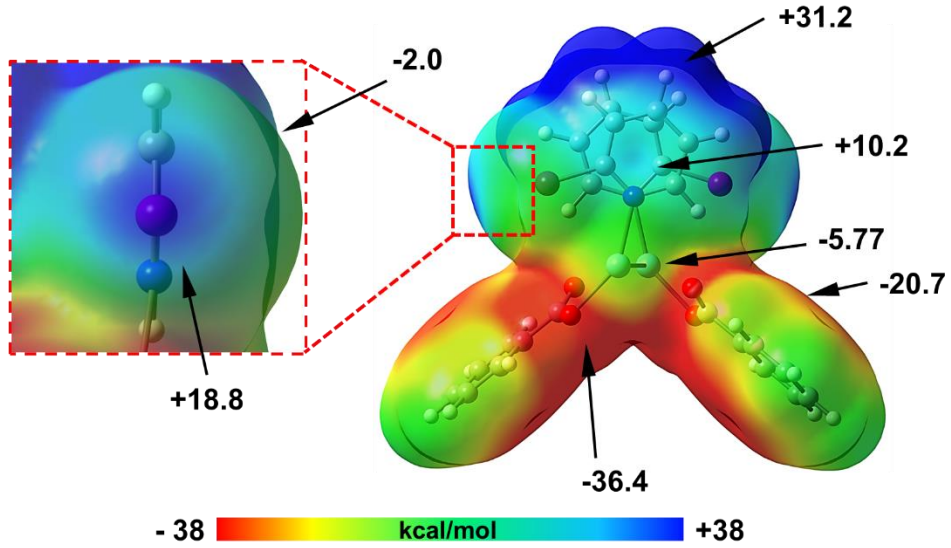

Figure 4.24. MEP surface of compound **V** at the B3LYP/cc-pVDZ-PP level of theory. Isosurface 0.001 a.u. The energies at selected points of the surface are given in kcal/mol.

4.25 Summary of theoretical studies of non-covalent interactions: NBO results

The current NBO study utilizing second-order perturbation analysis was conducted to see whether orbital contributions are of importance for explaining the $Ag^{I}\cdots Ag^{I}$ argentophilic interaction. The dimerisation and/or association of the silver(I) atoms in compounds **I-V**, leading to the $Ag^{I}\cdots Ag^{I}$ argentophilic interactions, has been shown to display moderate amounts of charge transfer between the two silver(I) atoms. The magnitude of the donor-acceptor orbital stabilisation energies $E^{(2)}$ were determined by DFT calculations and the NBO 3.0 program available through the Gaussian16 program suite.

The $E^{(2)}$ values of the intramolecular $Ag^{I}\cdots Ag^{I}$ interactions for each compound are listed in Table 4.14 below. The data indicate that compound **III**, with $E^{(2)}$ = 85.44 kcal/mol and excluding 'retro-donation', has the highest $Ag^{I}\cdots Ag^{I}$ donor-acceptor orbital stabilisation, as compared to compounds **I**, **II**, **IV**, and **V**. This is presumably due to the difference in geometry, where **III** exhibits a more planar structure, as compared to the 'bent' structures of compounds **II**, **IV**, and **V**. In opposition to the highest stabilisation energy, compound **I** exhibits the weakest $Ag^{I}\cdots Ag^{I}$ charge-transfer interaction, where $E^{(2)}$ = 18.12 kcal/mol, also excluding 'retro-donation'. This may be due to **I** not possessing a coordinated pyridyl ligand that could influence the silver(I)'s electrostatic contribution. Undertaking an energy decomposition analysis (EDA) may shed some light on the reason for this, but doing so falls outside the scope of this study. Interestingly, the NBO results are in agreement with the results obtained from the QTAIM analysis. A polynomial regression (n^{th} deg. = 2, R^2 = 0.978) shows a relationship between the stabilisation interaction energies, $E^{(2)}$, as a function of the $Ag^{I}\cdots Ag^{I}$ interaction distances displayed in Figure 4.25 below. This graph illustrates a general trend: as $Ag^{I}\cdots Ag^{I}$ interaction distance increases, the stabilisation interaction energy (in kcal/mol) decreases. The $E^{(2)}$ values range from 18.12 kcal/mol to 85.44 kcal/mol, which is considered to be moderate in terms of their strength.[134]

The values of donor-acceptor orbital stabilisation energies for the semi-coordination $Ag^{I}\cdots Br$ and $Ag^{I}\cdots I$ contacts in compounds **IV** and **V**, respectively, are indicated in Table 4.14 below. The results of $E^{(2)}$ (10.6 kcal/mol) between $Ag^{I}\cdots Br$ in **IV** is substantially smaller than that of $E^{(2)}$ (25.6 kcal/mol) between $Ag^{I}\cdots I$ in **V**, thus indicating **V** as having the stronger semi-coordination interaction. This result is in agreement with

the polarisability of iodine over bromine (I > Br), allowing R_3C-I to optimally position itself at ca. 87 ° to the silver(I) while the R_3C-Br atom sits at ca. 80 ° Interestingly, the MESP appears to contradict the latter reasoning: analysis of the surfaces of compounds **IV** and **V** clearly shows that the surfaces on both the silver(I) and halogen atoms are negative. One would expect there to be more of a repulsion between the two atoms. This may support the importance of the charge-transfer interaction from the halogen atoms to the silver(I) atoms. A method that could utilised to substantiate this claim would be to undertake an energy decomposition analysis, which, again, falls outside the scope of the current study.

Table 4.14. Results of NBO analysis of donor−acceptor interactions in compounds **I-V**, estimated by second-order interaction energy, $E^{(2)}_{i\rightarrow j}$, at the B3LYP/aug-cc-PVTZ-PP (monomer) level of theory.

Donor NBO (i) [a]	Occu.	Acceptor NBO (j) [a]	Occu.	$E^{(2)}$ [b]	$E_{(j)} - E_{(i)}$ [c]	$F_{(i,j)}$ [c]
$LP(5)_{Ag}$	1.97e	$LP^*(6)_{Ag}$	0.26e	18.12	0.71	0.108
$LP(5)_{Ag}$	1.98e	$LP^*(7)_{Ag}$	0.25e	31.58	1.74	0.222
$LP(5)_{Ag}$	1.96e	$LP^*(9)_{Ag}$	0.27e	85.44	1.87	0.379
$LP(5)_{Ag}$	1.98e	$LP^*(7)_{Ag}$	0.24e	23.14	1.74	0.190
$LP(5)_{Ag}$	1.98e	$LP^*(9)_{Ag}$	0.24e	22.26	1.77	0.189
$LP(3)_{Br}$	1.88e	$LP^*(8)_{Ag}$	0.10e	10.60	0.56	0.071
$LP(3)_{I}$	1.84e	$LP^*(7)_{Ag}$	0.15e	25.63	1.78	0.191

[a] LP and LP* represent the lone pair and empty atomic orbital, respectively. [b] $E^{(2)}$ values are in kcal/mol. [c] $E_{(j)}$,$E_{(i)}$ and $F_{(i,j)}$ are given in standard atomic units (a.u.).

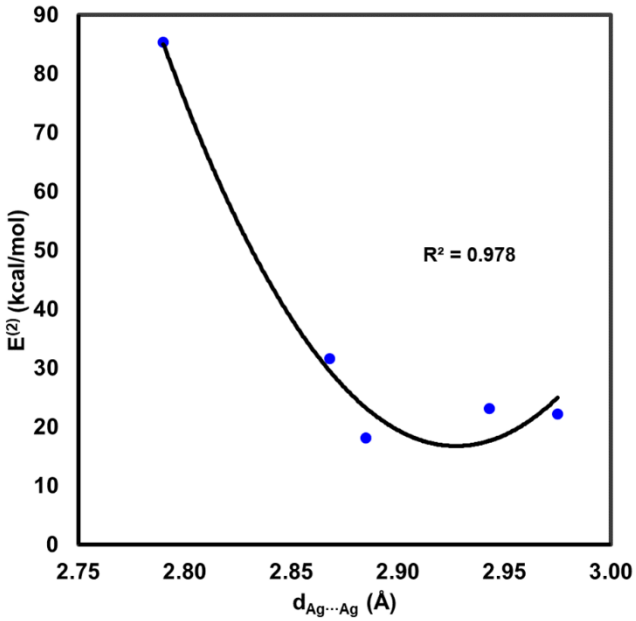

Figure 4.25. Correlation between the NBO donor-acceptor orbital stabilisation energy $E^{(2)}$ and the $Ag^{I}\cdots Ag^{I}$ distance (Å) of compounds **I-V**.

4.26 Conclusion

The structures of the solid species **I** through **V** were examined using XRD, topological analysis of the electron density distribution in accordance with Bader's QTAIM theory, natural bonding orbital (NBO), and molecular electrostatic surface potential (MESP) analysis at the B3LYP-D2/cc-pVTZ-PP or cc-pVDZ-PP level of theory.

Three different types of metal-involved interactions were identified as a result of the theoretical calculations: $Ag^{I}\cdots Ag^{I}$ argentophilic interactions between silver(I) centres were seen in all of the compounds (**I-V**), whereas $Ag^{I}\cdots X$ semi-coordination of the electrophilic silver(I) centre with electron belt of I or Br was seen in compounds **IV** and **V**. In compounds **I**, **II**, and **III**, silver(I) interactions between nucleophilic bonding orbitals of the pyridyl rings and empty atomic orbitals of silver(I) centres were theoretically observed.

The nature and energy of all recognized categories of non-covalent interactions involving metals in the synthesised compounds were theoretically investigated. These noncovalent interactions with metals have estimated strengths ranging from 4.1 to 11.0 kcal/mol (QTAIM) and from 11.0 to 85.4 kcal/mol (NBO). The emphasis on the electrophilic–nucleophilic dualism of the silver(I) metal centre toward noncovalent interactions is presented in this current study.

Chapter 5
Crystal Structures of Silver(I) Pyridyl Compounds

The present chapter includes a detailed structural analysis of various silver(I) compounds (**VI**-**VIII**). These compounds did not belong in the main series (**I**-**V**), as previously included in Chapter 3, as they did not correspond to the formulaic criteria, i.e. $[Ag_2(OBn)_2]$ or $[Ag_2(OBn)_2(Xpy)_2]$, of the series **I**-**V**. Nevertheless, compounds **VI**-**VIII** were still chosen to be discussed in this separate section, however, since all their structures exhibit prominent non-covalent interactions (NCIs) that govern their crystal packing. The latter is important in the context of the current study.

5.1 X-ray structure determination

X-ray diffraction data of compounds **VI**, **VII**, and **VIII** were collected with a Bruker DUO APEX II diffractometer with Mo Kα radiation (λ = 0.71073 Å) at 100 K. The structure was solved using direct methods via SHELXT 2014/5[101] and refined by full-matrix least-squares procedures on F^2 using the program SHELXL 2018.[102] All non-hydrogen atoms were refined anisotropically. Crystallographic data and details of the data collection and structure refinement are summarised in Table 5.1 below.

Table 5.1. Crystallographic information for compounds **VI**-**VIII**.

Compound	**VI**	**VII**	**VIII**
Chemical formula	$C_{24}H_{21}AgN_2O_4$	$C_{26}H_{30}Ag_2N_5O_5$	$C_{10}H_8AgI_2N_3O_3$
M_r	509.30	708.29	579.87
Space group	C2/c	$P2_1/c$	$P2_1/n$
Temperature (K)	100.15	100	100
a (Å)	11.9411(4)	11.3298(4)	21.0658(12)
b (Å)	16.6494(5)	19.3437(7)	18.7498(10)
c (Å)	10.7019(3)	13.8208(5)	26.3353(15)
α (°)	90	90	90
β (°)	91.0390(10)	113.1800(10)	97.582(2)
γ (°)	90	90	90
V (Å^3)	2127.32(11)	2784.45(17)	10311.0(10)
Z	4	4	28
$D_{calc.}$ (g cm^{-3})	1.590	1.690	2.615
μ (mm^{-1})	0.981	1.451	5.565
Crystal size (mm)	0.11 × 0.06 × 0.05	0.2 × 0.14 × 0.12	0.29 × 0.18 × 0.12
Radiation type	Mo Kα (λ = 0.71073)	Mo Kα (λ = 0.71073)	Mo Kα (λ = 0.71073)
2Θ range for data collection (°)	4.198 to 56.632	3.836 to 61.098	3.8 to 59.4
Index ranges	-15 ≤ h ≤ 15, -22 ≤ k ≤ 22, -14 ≤ l ≤ 14	-16 ≤ h ≤ 16, -27 ≤ k ≤ 27, -19 ≤ l ≤ 19	-29 ≤ h ≤ 29, -26 ≤ k ≤ 26, -36 ≤ l ≤ 36
Reflections collected	52541	240506	578872
Independent reflections	2648 [R_{int} = 0.0557, R_{sigma} = 0.0184]	8505 [R_{int} = 0.0497, R_{sigma} = 0.0151]	29054 [R_{int} = 0.0987, R_{sigma} = 0.0389]
Data/restraints/parameters	2648/104/184	8505/10/348	29054/0/1198
Goodness-of-fit on F^2	1.300	1.082	1.072
Final R indexes [I>=2σ (I)]	R_1 = 0.0406, wR_2 = 0.1065	R_1 = 0.0614, wR_2 = 0.1914	R_1 = 0.0496, wR_2 = 0.1128
Final R indexes [all data]	R_1 = 0.0438, wR_2 = 0.1077	R_1 = 0.0718, wR_2 = 0.2017	R_1 = 0.0875, wR_2 = 0.1332
$\Delta\rho_{max}/\Delta\rho_{min}$ (e Å^{-3})	0.82/-0.69	5.09/-2.72	5.96/-3.14

5.2 Single-crystal X-ray diffraction (SCXRD) analysis of compound VI

Figure 5.1 below represents the molecular structure of compound **VI**. Selected bond distances and angles are summarised in Table 5.2 below, with standard deviations given in parentheses. Compound **VI**, $[Ag(OBn)(py)_2](HOBn)$, crystallises in the monoclinic space group C2/c (no. 15) with a = 11.941(4), b = 16.649(5), c = 10.702(3) Å, β = 91.039(10)°, and Z = 4. The asymmetric unit (ASU) in Figure 5.1(a) consists of one silver(I) metal centre, one-half of a benzoate ligand (OBn), one pyridine (py) ligand, and one 'host' benzoic acid (HOBn). The molecular structure shown in Figure 5.1(b) illustrates how the silver(I) centre adopts a distorted tetrahedral (T_d) coordination geometry. This shape is formed by the two pyridyl nitrogen atoms and the two carboxylate donor oxygen atoms, where d(Ag1—N1) = 2.239(3) Å and d(Ag1—O1) = 2.504(3) Å, respectively. The OBn ligand coordinates to the silver(I)-metal cation through a bidentate (η^2-mode) chelation. Interestingly, the Ag—O coordination bond distances are shorter than the sum of Bondi's vdW radii ($R_{vdW}(Ag) + R_{vdW}(O)$ = 3.24 Å).[105,106] The $[AgO_2N_2]$ coordination geometry, at the silver(I) atom, are defined by four subtended angles: 52.58(13), 115.36(11), 108.06(11), and 131.37(17)° (see Table 5.2), which constitute the distorted tetrahedron. It is worth mentioning that compound **VI** is the first of the compounds synthesised for this study (**I**-**VIII**) that does not contain any $Ag^{I}\cdots Ag^{I}$ contacts.

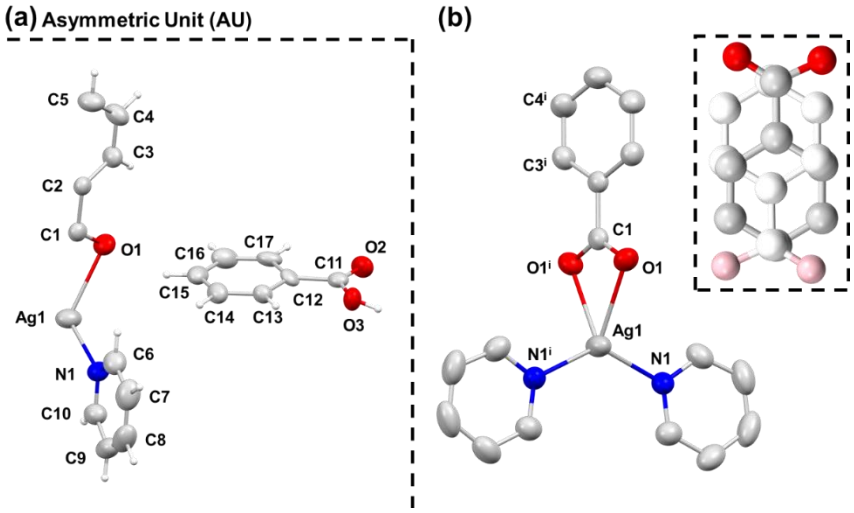

Figure 5.1. Molecular diagrams of compound VI determined by single crystal X-ray diffraction methods. The structure of the (a) asymmetric unit and of the (b) dimeric $[Ag_2(OBn)(py)_2](HOBn)$ compound with atomic labeling is given. The disordered benzoic acid across the two-fold symmetry axis (part 2) is shown in white superimposed over part 1. Hydrogen atoms are omitted in (b) for clarity; anisotropic displacement ellipsoids of non-hydrogen atoms are given with a 50% probability. Symmetry code: (i) 1−x, 1−y, 2−z.

Table 5.2. Selected bond lengths, *d* (Å), and bond angles, ∠ (°) in **VI**.

Bond/Contact	*d*	Bonds	∠
Ag1—O1	2.502(3)	O1—Ag1—O1^{i}	52.58(13)
Ag1—O1^{i}	2.502(3)	O1—Ag1—N1	115.36(11)
Ag1—N1	2.239(3)	O1^{i}—Ag1—N1^{i}	115.36(11)
Ag1—N1^{i}	2.239(3)	O1^{i}—Ag1—N1	108.06(11)
C1—O1	1.265(4)	O1—Ag1—N1^{i}	108.06(11)
C1—O1^{i}	1.265(4)	N1^{i}— Ag1—N1	131.37(17)
C11—O2	1.210(15)	C1—O1—Ag1	92.5(3)
C11—O3	1.327(16)	C1—O1^{i}—Ag1	92.5(3)

Symmetry code: (i) 2-x, +y, 3/2-z.

5.2.1 Molecular disorder: structure description

Analysis of the crystal structure obtained from the crystallisation of silver(I) benzoate and pyridine from dichloromethane (DCM), reveal that the structure contains a disordered benzoic acid 'guest' group. The benzoic acid is disordered between two different orientations, part 1 and part 2, described herein as a head-to-tail disorder as seen in Figure 5.2 below. The occupancies of the two molecular orientations are reported as being 0.5 each, due to the presence of a two-fold rotation axis (symmetry operator: -x, y, ½-z) with direction [0,1,0] at 0, y, ¼. Interestingly, the carboxylic (CO_2^-) acid group of the benzoate interacts with the carboxylic group (COOH) of adjacent silver(I) compounds via O—H···O hydrogen bonds, forming inversion dimers.

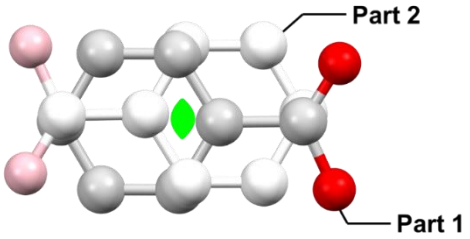

Figure 5.2. The HOBn molecule generated by the two-fold rotational axis (shown in green) symmetry operator (-x, y, ½-z) is shown in a muted CPK (Corey–Pauling–Koltun) colour scheme (labelled as 'Part 2'), while the acted-upon benzoic acid (present within the asymmetric unit) is in true CPK colours labelled as 'Part 1'. Hydrogen atoms are omitted for clarity.

5.2.2 Crystallographic evaluation of short contacts

Compound **VI** involves two identical intermolecular hydrogen bonds, where the second is a result of the symmetrically-generated HOBn molecule (see in Figure 5.3 below). These H-bonds characteristically both contain an -OH group as the H-bond donor. While the acceptors of the H-bonds are the deprotonated OBn groups of the silver(I) compounds. The intermolecular hydrogen bond distances, d(O1···H1) = 1.659(3) Å, in compound **VI** are shorter than the sum of Bondi's vdW radii of oxygen and hydrogen atoms (R_{vdW}(O) + R_{vdW}(H) = 2.72 Å).[105,106] The hydrogen bond angles between HOBn donors and OBn acceptors are 161.77°, which deviates slightly from the ideal 180°.

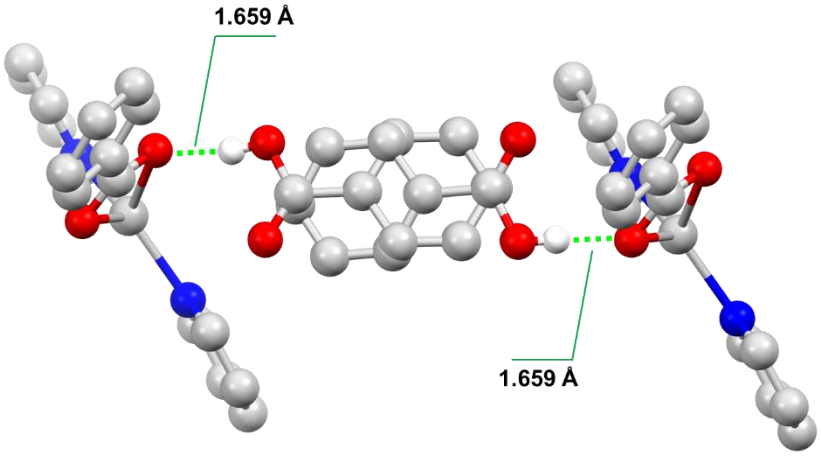

Figure 5.3. Selected part of the three-dimensional (3D) network of **VI** in the solid state. Hydrogen bonds are indicated by the dotted green lines, where the distances of interacting hydrogen bond donor/acceptors are given. Hydrogen atoms are omitted in for clarity, except for those participating in hydrogen bonding.

5.2.3 Non-covalent interactions analysis

The crystallographic packing of compound **VI**, much like that of compounds **I-III**, seems to contain prominent $Ag^{I}\cdots\pi$ interactions, but differing from the other compounds by having prominent D-H···A interactions. These interactions occur between the silver(I) transition-metal centre and the pyridine's aromatic ring (π-system) of a neighbouring molecule. The distance between the silver(I) metal and centroid (Cg) of the aromatic ring is d(Ag1···Cg) = 3.777 Å. Furthermore, the angle of the normal to the aromatic ring plane, ∠(Ag1···Cg), with the vector between the centre of the aromatic ring is 56.74°. Interestingly, compound **VI** packs such that the silver(I) atoms are positioned toward the C2 and C3 double bond (C=C) on the π-face of the adjacent aromatic ring (see Figure 5.4 below). The short contacts between the pyridine ring plane and silver(I) ion, the nearest aromatic atom (C2), the most prominent contact, $d(Ag^{I}\cdots C_{aromatic})$ = 3.341(3)Å, are smaller than the sum of Bondi's vdW radii ($R_{vdW}(Ag) + R_{vdW}(C)$ = 3.42 Å). The bond distance of the second contact, Ag1–C3^{i}, is also smaller than the sum of Bondi's vdW radii, where d = 3.354 Å.[105,106] As previously mentioned in Section 3.5.1, sub-vdWs distances are indicative of molecular orbital-based (covalent-like) effects, where the metal cation/π interactions exhibit substantial covalent character (η^1-, η^2-, or η^3-interactions), in addition to electrostatic effects.[119]

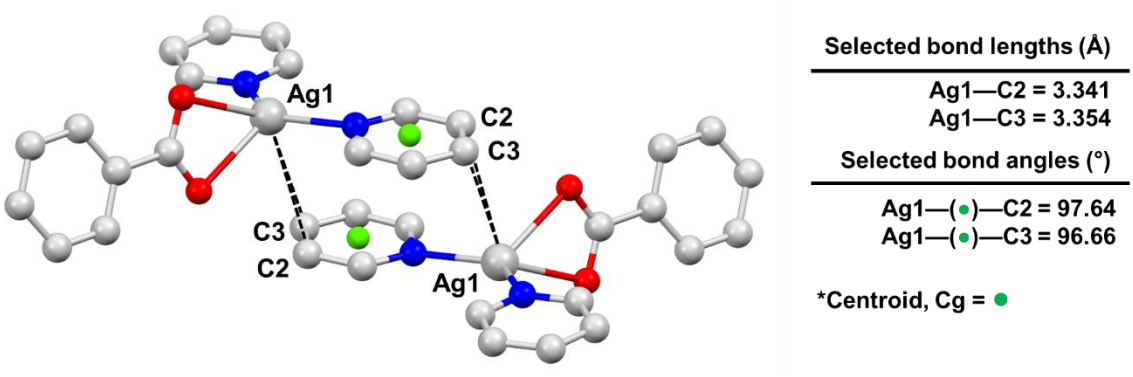

Figure 5.4. Crystal packing of **VI** showing the dimer interaction of two molecules of **VI** via $Ag^{I}\cdots\pi$ interactions. Hydrogen atoms are omitted for clarity. Distance (Å) and angle (°) parameters are shown (right).

5.2.4 Powder X-ray diffraction analysis

The PXRD pattern of the synthesised compound **VI** is depicted in Figure 5.5 below and was collected at room temperature and ambient pressure. The bulk material was analysed as is, without any further purification. The trace obtained for compound **VI** (light blue) is consistent with the calculated pattern (dark blue) from the single-crystal data. The agreement of the experimental with the calculated pattern proves the phase purity of the bulk material.

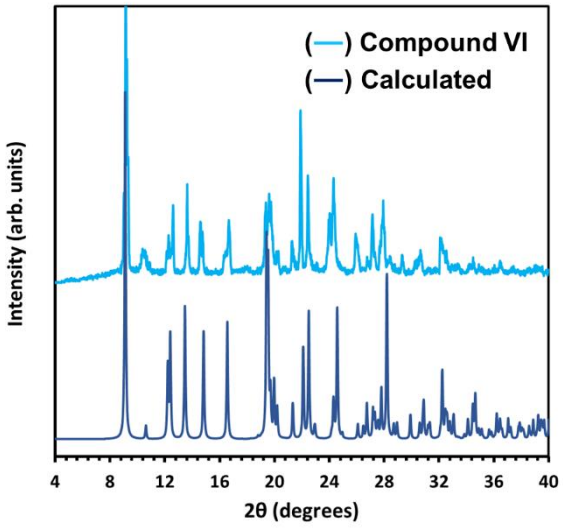

Figure 5.5. Comparison of the experimental powder X-ray diffraction pattern of compound **VI** (light blue) and the calculated one (dark blue) from single-crystal data.

5.3 Single-crystal X-ray diffraction analysis of compound VII

Figure 5.6 below represents the molecular structure of compound **VII**. Selected bond distances and angles are summarised in Table 5.3 below, where standard deviations are given in parentheses. The asymmetric unit consists of two silver(I) metal ions, four 4-picoline (4-Pic) ligands, a nitrate ion/water pair, and two (2 × 0.5) disordered ethoxide (EtO^-) counter ions. The author notes that charge balance requires either the disordered ethanol or water to be ionised. They have chosen to model the ethanol as ionised. Each silver(I) atom is coordinated by two neutral 4-Pic molecules through the N atoms [Ag1—N = 2.141(4) and 2.152(4) Å] and [Ag2—N = 2.138(4) and 2.1215(4) Å], with both Ag—N coordinations show a linear geometry with an [N—Ag—N] angle of 172.01(15) and 173.90(14)°, for Ag1 and Ag2 respectively. The short Ag—O distances of the nitrate (NO_3^-) and ethoxide ions indicate that they remain uncoordinated to the silver(I) cations, existing within the crystal structure by means of balancing the compound's 2+ charge, i.e. $[Ag_2(4\text{-}Pic)_4]^{2+}$. A 'guest' water molecule present in the crystal structure also does not seem to coordinate with any of the silver(I) cations, but rather forms a hydrogen bond to one of the O-atoms from the NO_3^- group, which acts as an acceptor. Furthermore, two $[Ag(4\text{-}Pic)_2]$ units are linked by an $Ag^I \cdots Ag^I$ argentophilic interaction, forming a centrosymmetric dimeric $[Ag_2(4\text{-}Pic)_4]^{2+}$ cation.

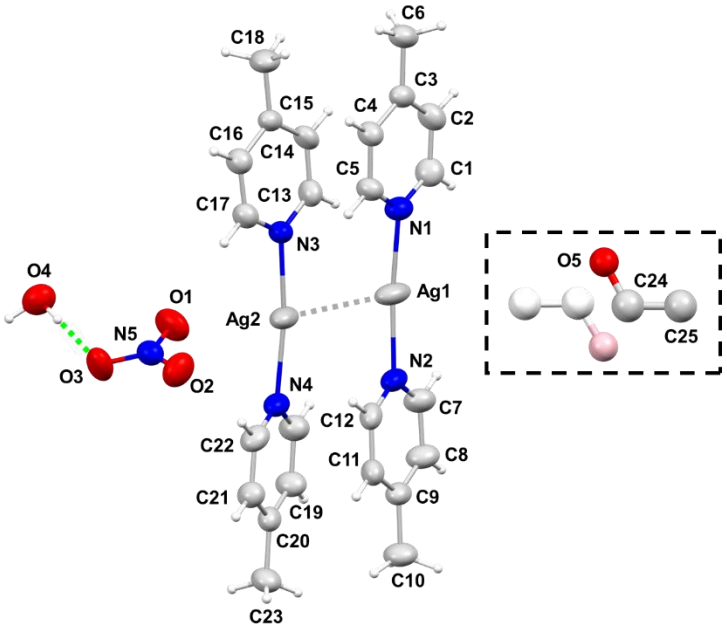

Figure 5.6. Molecular diagram of compound VII determined by single crystal X-ray diffraction methods. The structure of the asymmetric unit $[Ag_2(4\text{-}Pic)_2](OEt)(NO_3)(H_2O)$ with atomic labelling is given. The disordered ethoxide (across the two-fold symmetry axis) is shown in muted CPK colouring. Hydrogen atoms are omitted in (b) for clarity; anisotropic displacement ellipsoids of non-hydrogen atoms are given with a 50% probability.

Table 5.3. Selected bond lengths, *d* (Å), and bond angles, ∠ (°) in **VII**.

Bond/Contacts	*d*	Bonds	∠
Ag1—N1	2.141(4)	N1—Ag1—N2	172.01(15)
Ag1—N2	2.152(4)		
Ag2—N3	2.138(4)	N4—Ag3—N3	173.90(11)
Ag2—N4	2.125(4)		
N5—O4	1.244(5)	O4—N5—O2	120.3(4)
N5—O2	1.255(5)	O4—N5—O3	120.6(4)
N5—O3	1.255(5)	O2—N5—O3	119.1(4)
Ag1···Ag2	3.2338(5)		

Note: the disordered EtOH molecule is omitted.

5.3.1 Molecular disorder: structure description

The EtO^- is disordered over two different orientations, i.e. 'Part 1' and 'Part 2', described herein as a head-to-tail disorder (see Figure 5.7 below). The occupancies of the two molecular orientations are reported as being 0.5 (or 50%) each, due to the presence of a two-fold screw axis (sym. op. -x, ½+y, ½-z) with direction [0,1,0] at 0, y, ¼ with screw component [0, ½, 0].

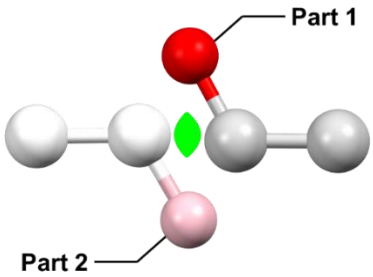

Figure 5.7. The EtO^- molecule generated by the two-fold rotational axis (coordinates: -x, ½+y, ½-z) is shown in green and is labelled as 'Part 2', while the EtO^- in the asymmetric unit is in CPK (Corey–Pauling–Koltun) colouring, labelled as 'Part 1'.

5.3.2 Solid-state network: packing

The asymmetric unit of **VII** consists of one 'host' molecule, two counter ions, and a 'guest' water molecule. The two counter ions (EtO^- and NO_3^-) and the water molecule reside within a 'zig-zag' boundary formed by the packing motif of $[Ag_2(4\text{-Pic})_4]^{2+}$ units (see Figure 5.8 below). The two counter ions seem to interact with the silver(I) atoms in a monodentate mode through seemingly weak $Ag^I\cdots O$ interactions [$Ag1\cdots ONO_2$ = 2.988 and Ag2···OEt = 2.962 Å]. Interestingly, the aromatic rings of the 4-Pic ligands seem to display a slight eclipsed conformation, presumably evidence of π···π stacking, with an average centroid–centroid distance of 3.548 Å.

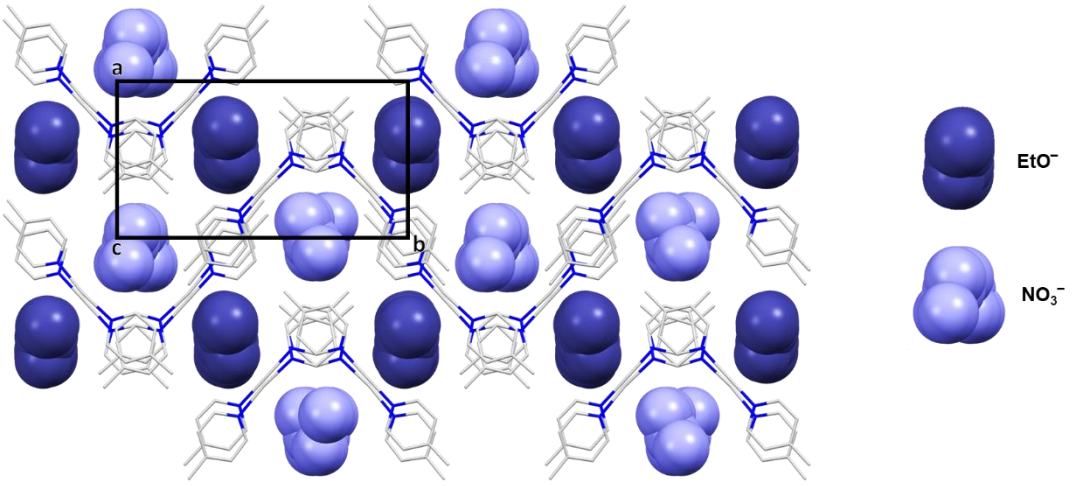

Figure 5.8. Packing diagram of compound **VII**. Counter ions are drawn in the space-fill style: EtO^- (dark blue) and NO_3^- (light blue).

5.3.3 Non-covalent interaction analysis

The crystallographic packing of compound **VII** contains prominent π···π stacking interactions, differing from compounds **I-VI**, which feature other more prominent non-covalent interactions (NCIs), such as: C-H···π, Ag^I···π, and C-X···Ag^I NCIs. These π···π stacking interactions occur between the 4-pyridyl aromatic (π-system) rings of neighbouring molecules. The distance between the centroids (Cg) of the aromatic rings is d(Cg1···Cg2) = 3.532 Å and d(Cg3···Cg4) = 3.563 Å (see Figure 5.9 below). Furthermore, the angle between the two plane normals, ∠(Cg1···Cg2), with the vector between the centre of the aromatic rings is 6.617° and ∠(Cg2···Cg3) is 7.970°. Interestingly, compound **VII** packs such that the π-faces of adjacent aromatic rings nearly eclipse one another, i.e. they exhibit a slight staggered conformation. Analysis of the short contacts between the 4-picoline ring planes, considering the nearest aromatic atom (N3), the most prominent contact, d(N3···$C_{aromatic}$) = 3.240 Å, shows them to be slightly smaller than the sum of Bondi's vdW radii (R_{vdW}(N) + R_{vdW}(C) = 3.25 Å). All remaining C···C contact bond distances are slightly larger than the sum of Bondi's vdW radii (R_{vdW}(C) + R_{vdW}(C) = 3.40 Å), the exception being C7···C20, where d = 3.338 Å. Lastly, the NO_3^- ion and H_2O molecule are linked by a O···H-O hydrogen bond, where d(O···H) = 2.050 Å, which is significantly shorter than the sum of Bondi's vdW radii (R_{vdW}(O) + R_{vdW}(H) = 2.72 Å).[105,106]

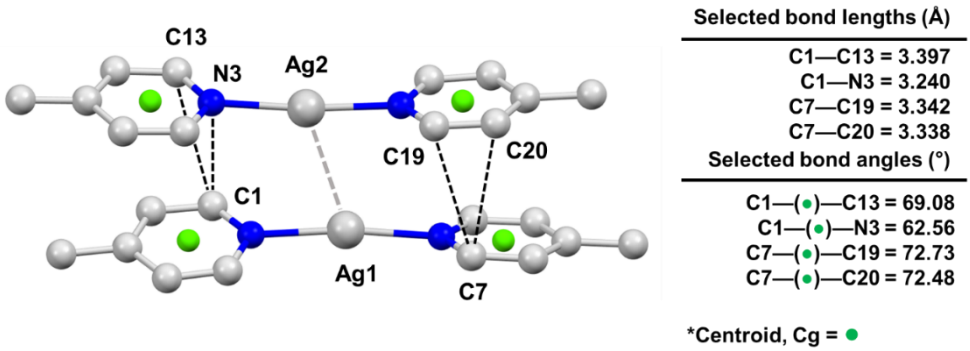

Figure 5.9. Crystal packing of **VII** showing the dimeric structure within the ASU, in which dimerization seems to be brought about by $Ag^{I}\cdots Ag^{I}$ and π···π stacking interactions. Hydrogen atoms are omitted for clarity. Distance (Å) and angle (°) parameters are shown (right).

5.3.4 Powder X-ray diffraction analysis

The PXRD pattern of the synthesised compound **VII** is depicted in Figure 5.10 below and was collected at room temperature and ambient pressure. The bulk material was analysed as is, without any further purification. The trace obtained for compound **VII** (light blue) is consistent with the calculated pattern (dark blue) from the single-crystal data. The agreement between the experimental and the calculated pattern proves the phase purity of the bulk material.

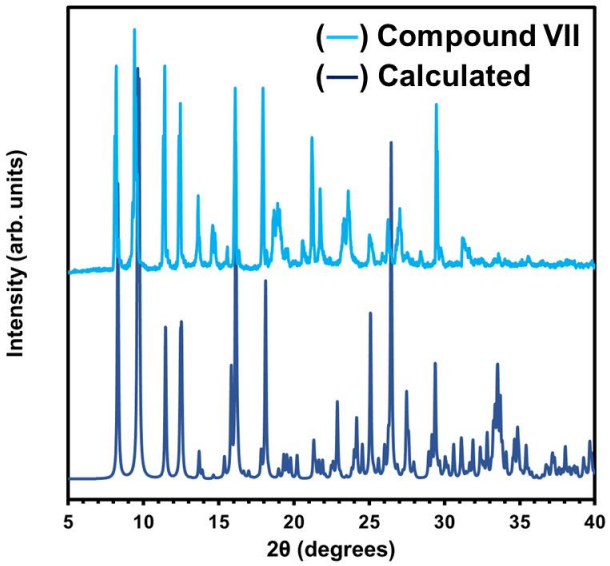

Figure 5.10. Comparison of the experimental powder X-ray diffraction pattern of compound **VII** (light blue) and the calculated one (dark blue) from single-crystal data.

5.4 Single-crystal X-ray diffraction analysis of compound VIII

Figure 5.11 below represents the generalized molecular unit of compound **VIII**. Selected bond distances and angles are summarized in Table 5.4 below, where standard deviations are given in parentheses. The generalized structure of compound **VIII** consists of one silver(I) metal ion, two 3-iodopyridine (3-Ipy) ligands, and a nitrate (NO_3^-) counter ion. In the crystal structure of **VIII** the silver(I) atoms display four different coordination environments, termed: AgI_A, AgII_B, AgIII_C, and AgIV_D. Although the presence of four compounds within the asymmetric unit (ASU) is rather rare, it is be no means exceptional, and it can be speculated that this is phenonenon is brought about by close-packing between said compounds.

Within the environments mentioned above, all silver(I) atoms are coordinated by at least two 3-Ipy ligands through their nitrogen atoms, and at least one NO_3^- counter ion, while other contacts such as $Ag^I\cdots Ag^I$ and $Ag^I\cdots I$ are present in some of them. The Ag–N bond distances are the shortest ones within the [O–Ag–N_2] coordination environments, where the Ag–N bond distances range from 2.182 - 2.191 Å. The [N-Ag-N] coordination environments all exhibit a slight bent geometry (< 180°), where the angles at the silver(I) atoms average ca. 160.01°, with the smallest angle being 145.52° and the largest being 172.82°. Bond lengths to the nitrate oxygen atoms from the silver(I) ions are all similar in length, where $d_{avg}(Ag\cdots O)$ = 2.697 Å, and where the largest Ag···O distance is 2.784 Å, which is still smaller than the sum of Bondi's vdW radii ($R_{vdW}(Ag) + R_{vdW}(O)$ = 3.24 Å). Interestingly, within the unit cell there are 3 out of 4 (or 75%) instances of two [Ag(3-Ipy)$_2$] units being linked by $Ag^I\cdots Ag^I$ argentophilic interactions, forming centrosymmetric $[Ag_2(I\text{-}py)_4]^{2+}$ dimeric cations. The average distance for the $Ag^I\cdots Ag^I$ interactions is given to be 2.994 Å, with the largest distance measuring 3.040 Å, which is smaller than the sum of Bondi's vdW radii ($R_{vdW}(Ag) + R_{vdW}(Ag)$ = 3.44 Å).[105,106]

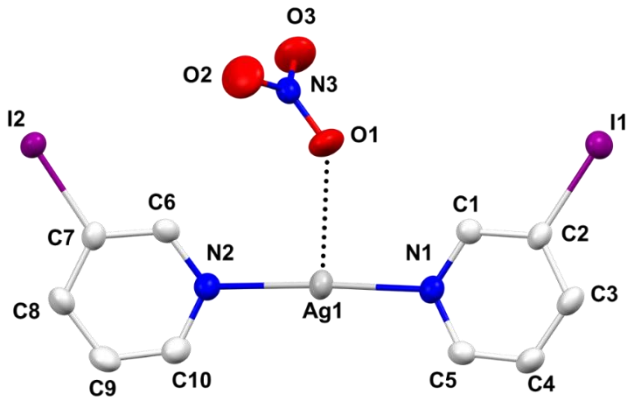

Figure 5.11. Molecular diagram of compound VIII determined by single crystal X-ray diffraction methods. The structure of the basic molecular unit [Ag(3-Ipy)$_2$]NO_3 with atomic labelling is given. All hydrogen atoms are omitted in for clarity; anisotropic displacement ellipsoids of non-hydrogen atoms are given with a 50% probability.

Table 5.4. Selected bond lengths, *d* (Å), and bond angles, ∠ (°) in **VIII**.

Bond/Contacts	*d*	Bonds	∠
Ag1—N1	2.190(6)	N1—Ag1—N2	168.9(2)
Ag1—N2	2.181(6)	N4—Ag2—N3	166.8(2)
Ag2—N3	2.202(6)	N5—Ag3—N6	148.6(2)
Ag2—N4	2.203(5)	N7—Ag4—N8	145.47(19)
Ag3—N5	2.166(6)	N9—Ag5—N10	172.5(2)
Ag3—N6	2.164(6)	N11—Ag6—N12	172.8(2)
Ag4—N7	2.212(5)	N14—Ag7—N13	146.5(2)
Ag4—N8	2.215(5)		
Ag5—N9	2.172(6)		
Ag5—N10	2.168(6)		
Ag6—N11	2.165(5)		
Ag6—N12	2.170(5)		
Ag7—N13	2.206(6)		
Ag7—N14	2.209(6)		
Ag1···Ag1^{i}	3.3250(11)		
Ag2···Ag3	3.0268(9)		
Ag4···Ag5	2.9822(7)		
Ag6···Ag7	2.9737(8)		

Symmetry code: (i) = 1-X,2-Y,1-Z

5.4.1 Non-covalent interaction analysis

The creation of weak connections both intra- and intermolecularly can be better understood by analysing the X-ray crystal structures of compound **VIII**. The crystal structure of **VIII** is composed of a complex three-dimensional (3D) network as can be seen in Figure 5.12 & 5.13 below. Within this 3D network, compounds are linked to one another via several types of non-covalent interactions (NCIs) such as pi-pi (π···π), argentophilic ($Ag^{I}\cdots Ag^{I}$), and intermediate metal···halogen ($R_3C\text{-}X\cdots Ag^{I}$) interactions.

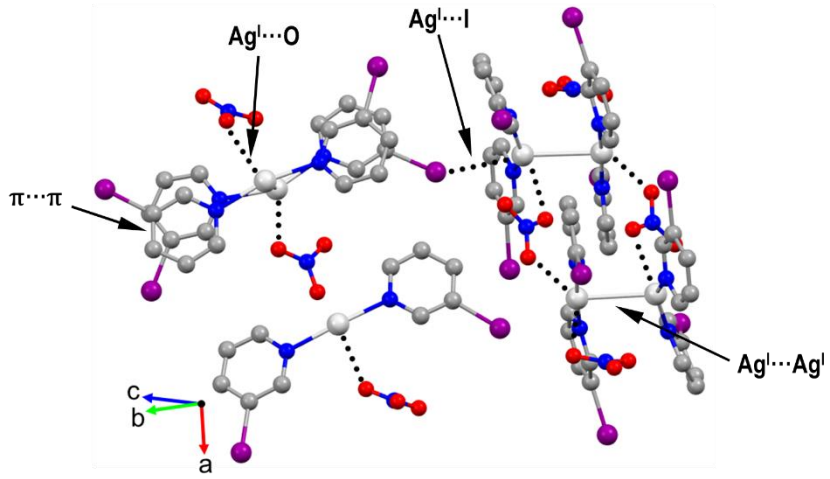

Figure 5.12. Packing diagram of compound **VII**. Counter ions are drawn in the space-fill style: EtO^{-} (dark blue) and NO_3^{-} (light blue).

5.4.2 Intermediate metal···halogen interactions

The most intriguing feature of the structure is the presence of intermediate metal···halogen interactions (between semi-coordination and halogen bonding XB). What defines an intermediate metal···halogen interaction in metal-containing systems is that the interaction between the metal and the halogen needs to be non-polar. This is to say that there aren't clear assignable roles, i.e. either electrophiles or nucleophiles, given to the interacting atoms. These non-covalent interactions are identified between the silver(I) centres, Ag(I), and iodine atoms of the 3-Ipy ligands, with interaction parameters in the range; d = 3.390-3.435 Å, and ∠Ag···I-CR_3 = 118.5 - 138.4°. The distances of the Ag^{I}···I contacts are significantly shorter than the sums of Bondi's vdW radii (R_{vdW}(I) + R_{vdW}(Ag) = 3.70 Å), thus favour the existence of the intermediate metal···halogen interactions. These Ag^{I}···I−CR_3 contacts could not be unambiguously attributed either to semi-coordination Ag^{I}···I bonds or to metal−iodine halogen bonds (XBs).

5.4.3 π-stacking interactions

In **VIII**, π-stacking interactions occur between 3-Ipy aromatic (or π-system) rings of neighbouring molecules. These interactions take place in environments AgII_B, AgIII_C, and AgIV_D. The distances between the centroids (Cg) of the aromatic ring pairs in each environment are given to be: d(Cg1···Cg2) = 4.042 Å and d(Cg3···Cg4) = 4.070 Å for AgII_B, d(Cg5···Cg6) = 4.007 Å and d(Cg7···Cg8) = 4.028 Å for AgIII_C, and d(Cg9···Cg10) = 3.892 Å and d(Cg11···Cg12) = 4.093 Å for AgIV_D. These values average a Cg···Cg distance of about 4.022 Å per ring, which falls within the range possible for π···π interactions to occur. Interestingly, compound **VII** packs such that the π-faces of adjacent aromatic rings do not eclipse one another, i.e. staggered conformations (see Figure 5.12 above).

5.4.4 Argentophilic (Ag^{I}···Ag^{I}) interactions

In compound **VIII** the metal···metal distances, within the range of 2.974(8)-3.027(9) Å, are significantly shorter than the sums of Bondi's vdW radii (RvdW(Ag) + RvdW(Ag) = 3.44 Å). It may be noted here, however, that the Ag···Ag distances are slightly longer than the conventional Ag···Ag separation within metallic silver, 2.889 Å. However, these close contacts are still suspected of d^{10}-d^{10} argentophilic interactions, as per the results discussed in Section 4.2. The N–Ag–N angles lie in a relatively broad interval spanning from 145.52(3)-172.82(3)°, which deviates slightly from ideal linear geometry. Interestingly, of the four environments previously defined, only one such environment (AgI_A) exists as a monomer, forming no Ag^{I}···Ag^{I} contact. It is clear from the observation that a preference towards the formation of argentophilic interactions, i.e. dimerisation, in comparison to compounds existing as singular entities, is favoured.

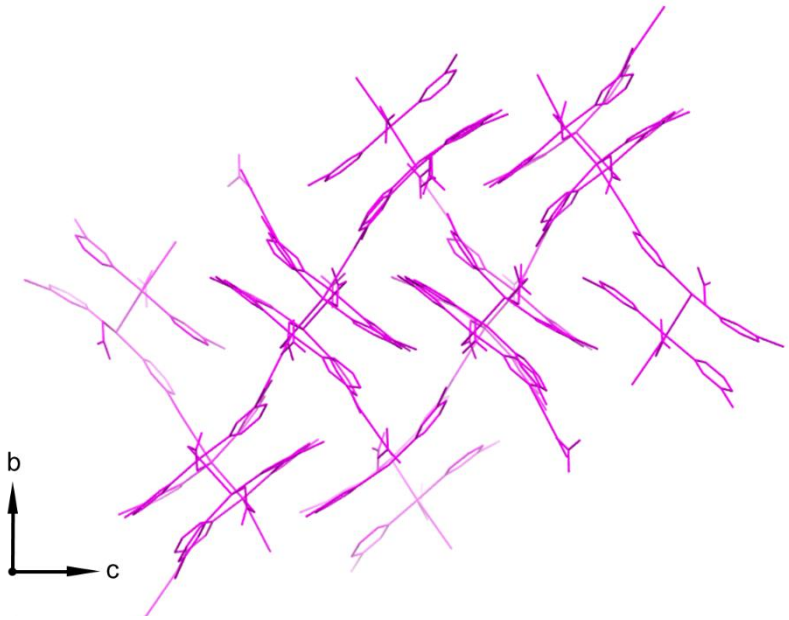

Figure 5.13. Packing diagram of compound **VIII** which illustrates the complex three-dimensional (3D) structure.

5.3.5 Powder X-ray diffraction analysis

The PXRD pattern of the synthesised compound **VIII** is depicted in Figure 5.14 below and was collected at room temperature and ambient pressure. The bulk material was analysed as is, without any further purification. The trace obtained for compound **VIII** (light blue) is consistent with the calculated pattern (dark blue) from the single-crystal data. The agreement between the experimental and the calculated pattern proves the phase purity of the bulk material.

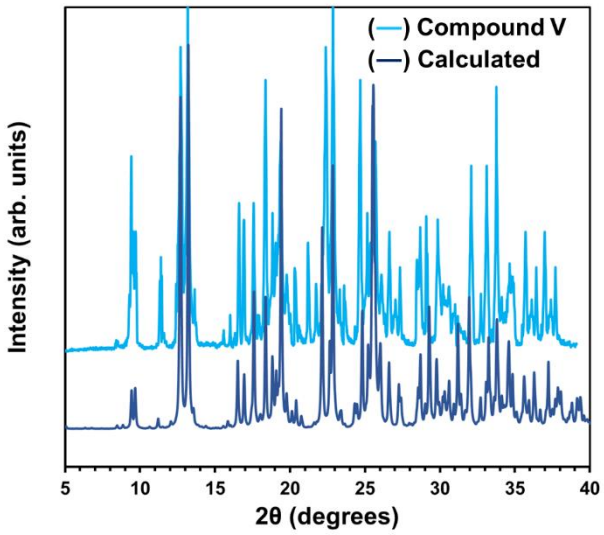

Figure 5.14. Comparison of the experimental powder X-ray diffraction pattern of compound **VII** (light blue) and the calculated one (dark blue) from single-crystal data.

5.5 Conclusion

In this chapter, a variety of silver(I) compounds (**VI**-**VIII**) have been successfully synthesized and described utilising single-crystal X-ray diffraction and powder X-ray diffraction. The current researcher found that of the compounds displayed unique sets of NCIs that govern their packing arrangements. SCXRD analysis revealed four major types of NCIs present within the aforementioned compounds. These have been described herein as: $Ag^{I}\cdots Ag^{I}$, intermediate $Ag^{I}\cdots X$, $Ag^{I}\cdots\pi$, and $\pi\cdots\pi$ interactions. Quantum chemical aspects of the non-covalently bonded compounds were discussed while referencing Chapter 4. These findings demonstrate the complexity of NCIs in silver(I) compounds and their involvement in determining the stability and structure of their structural packing.

Conclusion and Outlook
Chapter 6

The current dissertation has focused on a series of silver(I) coordination compounds involving pyridyl and benzoate ligands, which have been isolated and characterised by a single crystal X-ray diffraction, computational analysis, and thermogravimetric analysis. A total of eight crystal structures were obtained during the course of the study. The crystal structure analysis of compounds **I**, **II**, and **III** reveals the presence of uncommon $Ag^{I}\cdots\pi$(benzyl) (in **I**) and $Ag^{I}\cdots\pi$(pyridyl) (in **II** and **III**) non-covalent interactions (NCIs) between molecular units. Additionally, close contacts in compounds **IV** and **V** suggest the presence of uncommon $X\cdots M^{+}$ semi-coordination bonds (SCBs) that appear to play a crucial role in directing crystal packing in combination with weaker non-covalent interactions (i.e. $\pi\cdots\pi$) in combination with SCBs. The Hirshfeld surface analysis corroborates the importance of the SCBs in the solid state, which appear to make larger contributions to crystal packing than the $Ag^{I}\cdots\pi$ interactions. Interestingly, all compounds exhibit the same association mode, forming $Ag^{I}\cdots Ag^{I}$ argentophilic interactions in the solid state. Although the $Ag^{I}\cdots Ag^{I}$ interactions play a role in stabilising the molecular units, other intermolecular interactions are evidently more involved in the crystal packing. The influence of the latter interactions is thought to be the cause of the relative conformations in the crystal structures. This further highlights the necessity of incorporating multiple interactions into the design of supramolecular systems that utilise $Ag\cdots\pi$/$Ag\cdots X$ interactions.

QTAIM and NBO analyses of the experimentally obtained structures of compounds **I**-**V**, revealed the non-covalent nature of the $Ag\cdots X$ SCB and $Ag^{I}\cdots Ag^{I}$ argentophilic interactions. In summary, the prominent non-covalent interactions for **I**-**V** that seem to govern the formation of the crystal structures are metal-involving. In compounds **I**-**III**, these interactions have been identified primarily as $Ag^{I}\cdots\pi$ and $Ag^{I}\cdots Ag^{I}$, where the $Ag^{I}\cdots\pi$ interactions are thought to be the major structure-directing factors.

Computational calculations for compounds **I**-**V** reveal the existence of metallophilic interactions, which is supported by QTAIM analysis, as the findings reveal BCPs between the silver(I) metal centres (ca. -6 to -11 kcal/mol). For all compounds, the NBO analysis reveals charge transfer contributions to donor/acceptor orbitals (ca. 20−85 kcal/mol), as well as delocalisation of electrons, which can be largely attributed to a metallophilic interaction. Both the QTAIM and NBO analyses suggest that the strength of the metallophilic interaction in **I**-**V** decreases as the distance between the metal centres is increased (**III** > **II** > **I** > **VI** > **V**). Interestingly, the structure-directing interactions from **I**-**III** onwards seem to change from predominantly $Ag^{I}\cdots\pi$ interactions to more indicative of halogen-metal $X\cdots M^{+}$ interactions in compounds **IV** and **V**. Compounds **IV** and **V** were provided heavier halogen atoms, i.e. X = Br or I. This $X\cdots M^{+}$ interaction is brought about through a charge transfer from the lone pair (LP_X) on the halogen atom, which generally exhibits prominent p-orbital character (situated ∼80-90 ° relative to the M^{+} atom), and the empty atomic orbital (LP^{*}_{Ag}) of the Ag^{I}-atom. This is in line with the criteria for the classification of a halogen/metal interaction.

The nature of halogen/metal interactions has been debated for many years, namely whether such interactions involve electrostatic, covalent, or charge transfer characteristics. Speaking to this debate, the present study argues that the charge-transfer aspect of $X\cdots M^{+}$ interaction plays a significant role in the packing structures formed. NBO analysis confirms that the electron-donating ability of the lone-pair LP_X orbitals of the halogen follows the same pattern as the increasing polarisability of said halogen atom (responsible for electrostatic interactions), namely I > Br. The $R—I\cdots M^{+}$ interactions better represent a semi-coordination bond in comparison to the $R—Br\cdots M^{+}$ interactions, showing a significant increase in $LP_I\rightarrow LP^{*}_{M^{+}}$ CT (up to $\Delta\Delta E^{(2)} \cong 20$ kcal/mol). The QTAIM study reveals that the $Ag^{I}\cdots\pi$ and $Ag^{I}\cdots X$ interactions have comparable strengths, but are very different regarding their physical natures. Finally, this study suggests that SCBs involving silver(I) metal could be used in crystal engineering, supramolecular

chemistry, and molecular recognition. Furthermore, one may argue that the R—X···M interactions could be the major structure-directing force of supramolecular aggregation/assembly (from $\Delta E^{(2)} \cong 10$ to 30 kcal/mol) in compounds such as those studied here.

Recommended future studies, that may expand the findings of the current dissertation, or which fell outside the scope thereof (but which are still pertinent) are listed below:

• Calculations: a continuation

Given the time constraints and computational costs, calculations pertaining to the dimeric structures were calculated at a cc-pVDZ or cc-pVTZ-PP level of theory. This could be improved by the addition of the AUG diffuse function, especially where NCIs are concerned. Moreover, calculations could be performed regarding the exchange energies, especially with the aim of determining the repulsive contribution to the total interaction energy, and to calculate the polarisation energy in order to quantify its contribution to the total interaction energy.

• Medical applications: antimicrobial and anticancer properties

Numerous silver salts and complexes, particularly silver nitrate and silver sulfadiazine, have been utilized in the treatment of burn and wound infections since they contain antibacterial and antifungal properties.[141-143] However, silver complexes' cytotoxic effect are less studied. Since cisplatin has a similar anti-proliferative effect, numerous research groups have concentrated on comparing the in vitro anti-proliferative activity of new silver-based complexes to it.[144-148] Recent investigations have shown that the *in vitro* cytotoxic activity of silver(I) complexes against ovarian,[144] breast,[145] colorectal,[146] and lung cancers[147] is superior to that of cisplatin. To evaluate the *in vitro* anti-proliferative activity of these silver(I) complexes against human breast cancer cells, which are thought to account for 15% of all cancer-related deaths in women, the synthesis and characterisation of novel silver(I) complexes with picoline derivative ligands is recommended.

• Carbonyl hypoiodites: crystal engineering

Carbonyl hypoiodites and aromatic organic bases can be used to prepare neutral halogen-bonded [O-I-N] complexes. The iodine atom in carbonyl hypoiodites is more highly polarized and has a larger σ-hole than any other uncharged halogen bond donor currently known to researchers.[149] Studies regarding the latter are recommended in order to probe the nature of said carbonyl hypoiodites as potential new motifs of halogen bond donors. Halogen bonding has been effectively used to regulate the synthesis of functional materials (porous, magnetic, phosphorescent, liquid crystals) as well as the self-assembly of a wide range of host-guest systems (ion-pair recognition, biomolecular/chemical separations).[22,88] Halogen bonding utility was identified through crystal engineering,[22,88,150-152] which also established the directionality and specificity that led to complex structures with appealing topologies. Hollow capsular molecular assemblies that are completely based on halogen bonding have only recently been prepared due to the necessity for extremely precise design principles.

The production of iodine(I) salts (such as carbonyl hypoiodites) is achieved by reacting silver(I) carboxylates and iodine in the presence of pyridine, 2-picoline, or 4-picoline as the stabilising ligand, a technique originally described by Kleinberg, Zingaro, and colleagues.[97,153-155] This relatively simple one-pot method for the general synthesis of carbonyl hypoiodites includes a mechanism that involves silver(I) intermediates that is not completely understood.[97] This is in contrast to the analogous formation of the [O-I-N] complexes, where the silver(I) precursors and intermediates are practically insoluble in the solvents employed. In order to research these species and include other scaffolds in their design, it is necessary to have a better understanding of the silver(I) intermediates involved in the creation of carbonyl hypoiodites. The latter is therefore a recommended area for further research.

References

[1] Schmeck Jr, H. M. (1987). Chemistry and Physics Nobels hail discoveries on life and superconductors; Three share prize for synthesis of vital enzymes. New York Times, 15.

[2] Biedermann, F., & Schneider, H. J. (2016). Experimental binding energies in supramolecular complexes. Chemical reviews, 116(9), 5216-5300.

[3] Lehn, J. M. (1993). Supramolecular chemistry. Science, 260(5115), 1762-1763.

[4] Berry, D. J., & Steed, J. W. (2017). Pharmaceutical cocrystals, salts and multicomponent systems; intermolecular interactions and property-based design. Advanced drug delivery reviews, 117, 3-24.

[5] (a) Davey, R. J. (2002). Polymorphism in Molecular Crystals Joel Bernstein. Oxford University Press, New York, 2002. ISBN 0198506058; (b) Seddon, K. R., & Zaworotko, M. (Eds.). (1999). Crystal engineering: the design and application of functional solids (Vol. 539). Springer Science & Business Media; (c) Aitipamula, S., Chow, P. S., & Tan, R. B. (2014). Polymorphism in cocrystals: a review and assessment of its significance. CrystEngComm, 16(17), 3451-3465; (d) Bernstein, J. (2011). Polymorphism− a perspective. Crystal Growth & Design, 11(3), 632-650; (e) Brog, J. P., Chanez, C. L., Crochet, A., & Fromm, K. M. (2013). Polymorphism, what it is and how to identify it: a systematic review. Rsc Advances, 3(38), 16905-16931; (f) Tao, J., Wei, R. J., Huang, R. B., & Zheng, L. S. (2012). Polymorphism in spin-crossover systems. Chemical Society Reviews, 41(2), 703-737.

[6] (a) Karmakar, A., Sarma, R. J., & Baruah, J. B. (2007). Polymorphism in an Aqua-Bridged, Dinuclear 2-Nitrobenzoate Complex of Cobalt (II); (b) Karmakar, A., & Baruah, J. B. (2008). Polymorphism and symmetry non-equivalence in (3-carboxymethoxy-naphthalen-2-yloxy) acetic acid. Journal of Molecular Structure, 888(1-3), 197-203; (c) Chai, W., Hong, M., Song, L., Jia, G., Shi, H., Guo, J., ... & Chen, X. (2015). Three reversible polymorphic copper (I) complexes triggered by ligand conformation: insights into polymorphic crystal habit and luminescent properties. Inorganic Chemistry, 54(9), 4200-4207; (d) Šalitroš, I., Fuhr, O., & Ruben, M. (2016). Solvent-Induced Polymorphism of Iron (II) Spin Crossover Complexes. Materials, 9(7), 585; (e) Deacon, G. B., Harika, R., Junk, P. C., Skelton, B. W., Werner, D., & White, A. H. (2014). The Synthesis, Structures and Polymorphism of the Dimeric Trivalent Rare-Earth 3, 5-Dimethylpyrazolate Complexes [Ln (Me2pz) 3 (thf)] 2. European Journal of Inorganic Chemistry, 2014(14), 2412-2419; (f) Meundaeng, N., Rujiwatra, A., & Prior, T. J. (2016). Polymorphism in metal complexes of thiazole-4-carboxylic acid. Transition Metal Chemistry, 41(7), 783-793.

[7] (a) Fang, H. C., Ge, Y. Y., Jia, H. Y., Li, S. S., Sun, F., Zhang, L. G., & Cai, Y. P. (2011). Construction of three high-dimensional supramolecular networks from temperature-driven conformational isomers. CrystEngComm, 13(1), 67-71; (b) Kersten, K., Kaur, R., & Matzger, A. (2018). Survey and analysis of crystal polymorphism in organic structures. IUCrJ, 5(2), 124-129.

[8] (a) Mishra, M. K., Ramamurty, U., & Desiraju, G. R. (2016). Mechanical property design of molecular solids. Current Opinion in Solid State and Materials Science, 20(6), 361-370; (b) Steed, K. M., & Steed, J. W. (2015). Packing problems: high Z' crystal structures and their relationship to cocrystals, inclusion compounds, and polymorphism. Chemical Reviews, 115(8), 2895-2933; (c) Surov, A. O., Manin, A. N., Voronin, A. P., Churakov, A. V., Perlovich, G. L., & Vener, M. V. (2017). Weak interactions cause packing polymorphism in pharmaceutical two-component crystals. The case study of the salicylamide cocrystal. Crystal Growth & Design, 17(3), 1425-1437; (d) Ferreira, H., Conradie, M. M., Van Rooyen, P. H., & Conradie, J. (2017). Packing polymorphism of dicarbonyl-[2-(phenylamino) pent-3-en-4-onato] rhodium (I). Journal of Organometallic Chemistry, 851, 235-247.

[9] Braga, D. (2003). Crystal engineering, Where from? Where to? Chemical communications, (22), 2751-2754.

[10] Desiraju, G. R., & Parshall, G. W. (1989). Crystal engineering: the design of organic solids. Materials science monographs, 54.

[11] Mahmudov, K. T., Kopylovich, M. N., da Silva, M. F. C. G., & Pombeiro, A. J. (2017). Non-covalent interactions in the synthesis of coordination compounds: Recent advances. Coordination Chemistry Reviews, 345, 54-72.

[12] Maharramov, A. M., Mahmudov, K. T., Kopylovich, M. N., & Pombeiro, A. J. (Eds.). (2016). Non-covalent interactions in the synthesis and design of new compounds. John Wiley & Sons.

[13] Schmidt, G. M. J. (1971). Photodimerization in the solid state. Pure and Applied Chemistry, 27(4), 647-678.
[14] Desiraju, G. R. (2013). Crystal engineering: from molecule to crystal. Journal of the American Chemical Society, 135(27), 9952-9967.
[15] Lodish H, Berk A, Zipursky SL, Matsudaira P, Baltimore D, Darnell J (2000). "Glossary". Molecular Cell Biology (4th ed.). New York: W.H. Freeman. ISBN 978-0-7167-3136-8.
[16] Lodish H, Berk A, Zipursky SL, Matsudaira P, Baltimore D, Darnell J (2000). "Non-covalent bonds". Molecular Cell Biology (4th ed.). New York: W.H. Freeman. ISBN 978-0-7167-3136-8.
[17] Anslyn E (2004). Modern Physical Organic Chemistry. Sausalito, CA: University Science. ISBN 978-1-891389-31-3.
[18] Minkin, V. I. (1999). Glossary of terms used in theoretical organic chemistry. Pure and Applied Chemistry, 71(10), 1919-1981.
[19] Scholfield, M. R., Zanden, C. M. V., Carter, M., & Ho, P. S. (2013). Halogen bonding (X-bonding): A biological perspective. Protein Science, 22(2), 139-152.
[20] Voth, A. R., Khuu, P., Oishi, K., & Ho, P. S. (2009). Halogen bonds as orthogonal molecular interactions to hydrogen bonds. Nature chemistry, 1(1), 74-79.
[21] Sedlak, R., Kolář, M. H., & Hobza, P. (2015). Polar Flattening and the Strength of Halogen Bonding. Journal of Chemical Theory and Computation, 11(10), 4727–4732.
[22] Cavallo, G., Metrangolo, P., Milani, R., Pilati, T., Priimagi, A., Resnati, G., & Terraneo, G. (2016). The halogen bond. Chemical reviews, 116(4), 2478-2601.
[23] Metrangolo, P., & Resnati, G. (Eds.). (2015). Halogen Bonding I: Impact on Materials Chemistry and Life Sciences (Vol. 358). Springer.
[24] Desiraju, G. R., Ho, P. S., Kloo, L., Legon, A. C., Marquardt, R., Metrangolo, P., ... & Rissanen, K. (2013). Definition of the halogen bond (IUPAC Recommendations 2013). Pure and applied chemistry, 85(8), 1711-1713.
[25] Clark, T., Hennemann, M., Murray, J. S., & Politzer, P. (2007). Halogen bonding: the σ-hole. Journal of molecular modeling, 13(2), 291-296.
[26] Bikbaeva, Z. M., Ivanov, D. M., Novikov, A. S., Ananyev, I. V., Bokach, N. A., & Kukushkin, V. Y. (2017). Electrophilic–nucleophilic dualism of nickel (II) toward Ni··· I noncovalent interactions: semicoordination of iodine centers via electron belt and halogen bonding via σ-hole. Inorganic Chemistry, 56(21), 13562-13578.
[27] Efimenko, Z. M., Novikov, A. S., Ivanov, D. M., Piskunov, A. V., Vereshchagin, A. A., Levin, O. V., ... & Kukushkin, V. Y. (2020). The (Dioximate) NiII/I2 System: Ligand Oxidation and Binding Modes of Triiodide Species. Inorganic Chemistry, 59(4), 2316-2327.
[28] Huber, S. M., Scanlon, J. D., Jimenez-Izal, E., Ugalde, J. M., & Infante, I. (2013). On the directionality of halogen bonding. Physical Chemistry Chemical Physics, 15(25), 10350-10357.
[29] Riley, K. E., Murray, J. S., Fanfrlík, J., Řezáč, J., Solá, R. J., Concha, M. C., ... & Politzer, P. (2011). Halogen bond tunability I: the effects of aromatic fluorine substitution on the strengths of halogen-bonding interactions involving chlorine, bromine, and iodine. Journal of molecular modeling, 17(12), 3309-3318.
[30] Ivanov, D. M., Novikov, A. S., Ananyev, I. V., Kirina, Y. V., & Kukushkin, V. Y. (2016). Halogen bonding between metal centers and halocarbons. Chemical Communications, 52(32), 5565-5568.
[31] Brammer, L. (2003). Metals and hydrogen bonds. Dalton Transactions, (16), 3145-3157.
[32] Zelenkov, L. E., Ivanov, D. M., Sadykov, E. K., Bokach, N. A., Galmés, B., Frontera, A., & Kukushkin, V. Y. (2020). Semicoordination Bond Breaking and Halogen Bond Making Change the Supramolecular Architecture of Metal-Containing Aggregates. Crystal Growth & Design, 20(10), 6956-6965.
[33] Mahadevi, A. S., & Sastry, G. N. (2013). Cation− π interaction: Its role and relevance in chemistry, biology, and material science. Chemical reviews, 113(3), 2100-2138.
[34] Demircan, C. A., & Bozkaya, U. (2017). Transition metal cation− π interactions: complexes formed by Fe2+, Co2+, Ni2+, Cu2+, and Zn2+ binding with benzene molecules. The Journal of Physical Chemistry A, 121(34), 6500-6509.
[35] (a) Lindeman, S. V., Rathore, R., & Kochi, J. K. (2000). Silver(I) Complexation of (Poly)aromatic Ligands. Structural Criteria for Depth Penetration intocis-Stilbenoid Cavities. Inorganic Chemistry, 39(25),

5707–5716. (b) Bongoza, U., Zamisa, S. J., Munzeiwa, W. A., & Omondi, B. (2022). Silver (I) complexes of N, N'-diarylformamidine ligands: Synthesis, crystal structures, and in vitro antibacterial studies. Applied Organometallic Chemistry, e6726.
[36] Raju, S., Singh, H. B., & Butcher, R. J. (2020). Metallophilic interactions: observations of the shortest metallophilicinteractions between closed shell (d10···d10, d10···d8, d8···d8) metal ions [M··· M' M= Hg (ii) and Pd (ii) and M'= Cu (i), Ag (i), Au (i), and Pd (ii)]. Dalton Transactions, 49(26), 9099-9117.
[37] Sculfort, S., & Braunstein, P. (2011). Intramolecular d10–d10 interactions in heterometallic clusters of the transition metals. Chemical Society Reviews, 40(5), 2741-2760.
[38] Petrović, P., Djukic, J. P., Hansen, A., Bannwarth, C., & Grimme, S. (2016). Non-covalent stabilization in transition metal coordination and organometallic complexes. Non-covalent Interactions in the Synthesis and Design of New Compounds, 115-143.
[39] Saha, S., & Sastry, G. N. (2015). Cooperative or anticooperative: how noncovalent interactions influence each other. The Journal of Physical Chemistry B, 119(34), 11121-11135.
[40] Mahadevi, A. S., & Sastry, G. N. (2016). Cooperativity in noncovalent interactions. Chemical reviews, 116(5), 2775-2825.
[41] a) Schmidbaur, H., & Schier, A. (2015). Argentophilic interactions. Angewandte Chemie International Edition, 54(3), 746-784; b) Cebollada, A., Vellé, A., Iglesias, M., Fullmer, L. B., Goberna-Ferrón, S., Nyman, M., & Sanz Miguel, P. J. (2015). Direct X-Ray Scattering Evidence for Metal–Metal Interactions in Solution at the Molecular Level. Angewandte Chemie, 127(43), 12953-12957; c) Schmidbaur, H., & Schier, A. (2012). Aurophilic interactions as a subject of current research: an up-date. Chemical Society Reviews, 41(1), 370-412; d) Balch, A. L. (2009). Dynamic Crystals: Visually Detected Mechanochemical Changes in the Luminescence of Gold and Other Transition-Metal Complexes. Angewandte Chemie International Edition, 48(15), 2641-2644; e) Pyykkö, P. (2008). Theoretical chemistry of gold. III. Chemical Society Reviews, 37(9), 1967-1997; f) Katz, M. J., Sakai, K., & Leznoff, D. B. (2008). The use of aurophilic and other metal–metal interactions as crystal engineering design elements to increase structural dimensionality. Chemical Society Reviews, 37(9), 1884-1895.
[42] a) Zheng, J., Yu, Y. D., Liu, F. F., Liu, B. Y., Wei, G., & Huang, X. C. (2014). Modulation of argentophilic interactions by bridging amine ligands: photoluminescence tuneable by excitation energy or temperature. Chemical Communications, 50(64), 9000-9002; b) Jin, J., Wang, W., Liu, Y., Hou, H., & Fan, Y. (2011). A precise hexagonal octadecanuclear Ag macrocycle with significant luminescent properties. Chemical Communications, 47(26), 7461-7463; c) Kriechbaum, M., Hölbling, J., Stammler, H. G., List, M., Berger, R. J., & Monkowius, U. (2013). Unprecedented Large Temperature Dependence of Silver (I)–Silver (I) Distances in Some N-Heterocyclic Carbene Silver (I) Complex Salts. Organometallics, 32(10), 2876-2884; d) Ray, L., Shaikh, M. M., & Ghosh, P. (2008). Shorter argentophilic interaction than aurophilic interaction in a pair of dimeric {(NHC) MCl} 2 (M= Ag, Au) complexes supported over a N/O-functionalized N-heterocyclic carbene (NHC) ligand. Inorganic chemistry, 47(1), 230-240; e) Reger, D. L., Semeniuc, R. F., Captain, B., & Smith, M. D. (2005). An Unprecedented Coordination Mode of the Tris (pyrazolyl) methane Donor Set in {[Ph2 (O) POCH2C (pz) 3Ag] 2 (THF) 2}(BF4) 2: κ2− κ1 Bimetallic, Nσ/Nπ Chelating. Inorganic chemistry, 44(9), 2995-2997; f) Zhang, J. P., Wang, Y. B., Huang, X. C., Lin, Y. Y., & Chen, X. M. (2005). Metallophilicity versus π–π Interactions: Ligand-Unsupported Argentophilicity/Cuprophilicity in Oligomers-of-Dimers [M2L2] n (M= CuI or AgI, L= tridentate ligand). Chemistry–A European Journal, 11(2), 552-561.
[43] (a) Cotton, F. A.; Wilkinson, G. (1988). Advanced Inorganic Chemistry (5th ed.). John Wiley. p. 1087–1091. ISBN 0-471-84997-9 (b) Liddle, S.T. and Mills, D.P. (2009) Dalton Trans., 5592. (c) Liddle, S. T. (Ed.). (2015). Molecular Metal-Metal Bonds: Compounds, synthesis, properties. Wiley-VCH. p. 1–17
[44] (a) Mehrotra, P. K., & Hoffmann, R. (1978). Copper (I)-copper (I) interactions. Bonding relationships in d10-d10 systems. Inorganic Chemistry, 17(8), 2187-2189; (b) Cotton, F. A., Feng, X., Matusz, M., & Poli, R. (1988). Experimental and theoretical studies of the copper (I) and silver (I) dinuclear N, N'-di-p-tolylformamidinato complexes. Journal of the American Chemical Society, 110(21), 7077-7083; (c) Cotton, F. A.; Wilkinson, G. (1972). Advanced Inorganic Chemistry (3rd ed.). John Wiley. p. 1046. ISBN 0-471-17560-9

[45] Brands, M. B., Nitsch, J., & Guerra, C. F. (2018). Relevance of Orbital Interactions and Pauli Repulsion in the Metal–Metal Bond of Coinage Metals. Inorganic Chemistry, 57(5), 2603–2608.
[46] Lower, S. (2009) Matter under the Microscope, States of matter: introduction. Available at: https://www.chem1.com/acad/webtext/states/states.html#SEC4 (Accessed: July 29, 2022).
[47] Ashcroft, N. M., & Mermin, N. D. (1976). Solid state physics. Cengage Learning.
[48] Inkson, B. J. (2016). Scanning electron microscopy (SEM) and transmission electron microscopy (TEM) for materials characterization. In Materials characterization using non-destructive evaluation (NDE) methods (pp. 17-43). Woodhead Publishing.
[49] Bragg, W. H.; Bragg, W. L. (1913). "The Reflexion of X-rays by Crystals". Proc. R. Soc. Lond. A. 88 (605): 428–38.
[50] Friedrich W, Knipping P, von Laue M (1912). "Interferenz-Erscheinungen bei Röntgenstrahlen". Sitzungsberichte der Mathematisch-Physikalischen Classe der Königlich-Bayerischen Akademie der Wissenschaften zu München. 1912: 303.
[51] Moore, P. (1968).: Elements of X-Ray Crystallography. Journal of Geology, 76(5), 611-612.
[52] Stout, G. H., & Jensen, L. H. (1968). X-ray structure determination: a practical guide (Vol. 2). New York: Macmillan.
[53] Spackman, M. A., & Byrom, P. G. (1997). A novel definition of a molecule in a crystal. Chemical physics letters, 267(3-4), 215-220.
[54] Spackman, M. A., & Jayatilaka, D. (2009). Hirshfeld surface analysis. CrystEngComm, 11(1), 19-32.
[55] Hirshfeld, F. L. (1977). Bonded-atom fragments for describing molecular charge densities. Theoretica chimica acta, 44(2), 129-138.
[56] Spackman, M. A., & McKinnon, J. J. (2002). Fingerprinting intermolecular interactions in molecular crystals. CrystEngComm, 4(66), 378-392.
[57] McKinnon, J. J., Jayatilaka, D., & Spackman, M. A. (2007). Towards quantitative analysis of intermolecular interactions with Hirshfeld surfaces. Chemical Communications, (37), 3814-3816.
[58] Cramer, C. J., & Bickelhaupt, F. M. (2003). Essentials of computational chemistry. ANGEWANDTE CHEMIE-INTERNATIONAL EDITION IN ENGLISH-, 42(4), 381-381.
[59] Lewars, E. (2011). Computational chemistry. Introduction to the theory and applications of molecular and quantum mechanics, 318.
[60] Szabo, A., & Ostlund, N. S. (2012). Modern quantum chemistry: introduction to advanced electronic structure theory. Courier Corporation.
[61] Hartree, D. R. (1928). "The Wave Mechanics of an Atom with a Non-Coulomb Central Field. Part I. Theory and Methods". Mathematical Proceedings of the Cambridge Philosophical Society. Vol. 24, no. 1. Cambridge University Press. pp. 89–110.
[62] Sherrill, C. D. (2008). Computations of noncovalent π interactions. Reviews in computational chemistry, 26, 1-38.
[63] Sholl, D. S., & Steckel, J. A. (2022). Density functional theory: a practical introduction. John Wiley & Sons.
[64] Cramer, C. J. (2013). Essentials of computational chemistry: theories and models. John Wiley & Sons.
[65] Riley, K. E., & Hobza, P. (2011). Noncovalent interactions in biochemistry. Wiley Interdisciplinary Reviews: Computational Molecular Science, 1(1), 3-17.
[66] von Barth, U. (2004). Basic density-functional theory—an overview. Physica Scripta, 2004(T109), 9.
[67] Grimme, S. (2006). Semiempirical hybrid density functional with perturbative second-order correlation. The Journal of chemical physics, 124(3), 034108.
[68] Boys, S. F., & Bernardi, F. J. M. P. (1970). The calculation of small molecular interactions by the differences of separate total energies. Some procedures with reduced errors. Molecular Physics, 19(4), 553-566.
[69] Errol G. L. (2003). Computational Chemistry: Introduction to the Theory and Applications of Molecular and Quantum Mechanics (1st ed.). Springer.
[70] Grimme, S. (2011). Density functional theory with London dispersion corrections. Wiley Interdisciplinary Reviews: Computational Molecular Science, 1(2), 211-228.

[71] Klimeš, J., & Michaelides, A. (2012). Perspective: Advances and challenges in treating van der Waals dispersion forces in density functional theory. The Journal of chemical physics, 137(12), 120901.
[72] Grimme, S., Antony, J., Ehrlich, S., & Krieg, H. (2010). A consistent and accurate ab initio parametrization of density functional dispersion correction (DFT-D) for the 94 elements H-Pu. The Journal of chemical physics, 132(15), 154104.
[73] Brinck, T., Murray, J. S., & Politzer, P. (1992). Surface electrostatic potentials of halogenated methanes as indicators of directional intermolecular interactions. International Journal of Quantum Chemistry, 44(S19), 57-64.
[74] Bader, R. F., Carroll, M. T., Cheeseman, J. R., & Chang, C. (1987). Properties of atoms in molecules: atomic volumes. Journal of the American Chemical Society, 109(26), 7968-7979.
[75] Bader, R. F. W. (1990). Atoms in Molecules: A Quantum Theory, Claren.
[76] Matta, C. F., & Boyd, R. J. (2007). An introduction to the quantum theory of atoms in molecules. The quantum theory of atoms in molecules: from solid state to DNA and drug design.
[77] Grabowski, S. J. (2011). What is the covalency of hydrogen bonding?. Chemical Reviews, 111(4), 2597-2625.
[78] Baur, A., Bustin, K. A., Aguilera, E., Petersen, J. L., & Hoover, J. M. (2017). Copper and silver benzoate and aryl complexes and their implications for oxidative decarboxylative coupling reactions. Organic Chemistry Frontiers, 4(4), 519–524.
[79] Santra, R., Banerjee, K., & Biradha, K. (2011). Weak Ag···Ag and Ag···π interactions in templating regioselective single and double [2+2] reactions of N,N'-bis(3-(4-pyridyl)acryloyl)–hydrazine: synthesis of an unprecedented tricyclohexadecane ring system. Chemical Communications, 47(38), 10740.
[80] (a) Burdușel, A. C., Gherasim, O., Grumezescu, A. M., Mogoantă, L., Ficai, A., & Andronescu, E. (2018). Biomedical applications of silver nanoparticles: an up-to-date overview. Nanomaterials, 8(9), 681; (b) Puyo, M., Lebon, E., Vendier, L., Kahn, M. L., Fau, P., Fajerwerg, K., & Lepetit, C. (2020). Topological Analysis of Ag–Ag and Ag–N Interactions in Silver Amidinate Precursor Complexes of Silver Nanoparticles. Inorganic Chemistry, 59(7), 4328-4339.
[81] Metrangolo, P., Neukirch, H., Pilati, T., & Resnati, G. (2005). Halogen bonding based recognition processes: a world parallel to hydrogen bonding. Accounts of chemical research, 38(5), 386-395.
[82] Gilday, L. C., Robinson, S. W., Barendt, T. A., Langton, M. J., Mullaney, B. R., & Beer, P. D. (2015). Halogen bonding in supramolecular chemistry. Chemical reviews, 115(15), 7118-7195.
[83] Metrangolo, P., & Resnati, G. (2001). Halogen bonding: a paradigm in supramolecular chemistry. Chemistry–a European journal, 7(12), 2511-2519.
[84] Auffinger, P., Hays, F. A., Westhof, E., & Ho, P. S. (2004). Halogen bonds in biological molecules. Proceedings of the National Academy of Sciences, 101(48), 16789-16794.
[85] You, Z. L., Zhu, H. L., & Liu, W. S. (2004). Bis (μ-4-chlorobenzoato-κ2O: O') bis [(2-aminopyridine-κN) silver (I)](Ag—Ag) monohydrate. Acta Crystallographica Section E: Structure Reports Online, 60(12), m1863-m1865.
[86] Harurluoglu, B., Altay, A., Caglar, S., Yeniceri, E. K. K., Caglar, B., & Şahin, Z. S. (2021). Binuclear silver (I) complexes with the non-steroidal anti-inflammatory drug tolfenamic acid: Synthesis, characterization, cytotoxic activity and evaluation of cellular mechanism of action. Polyhedron, 202, 115189.
[87] Altay, A., Caglar, S., Caglar, B., & Sahin, Z. S. (2019). Novel silver (I) complexes bearing mefenamic acid and pyridine derivatives: Synthesis, chemical characterization and in vitro anticancer evaluation. Inorganica Chimica Acta, 493, 61-71.
[88] Altay, A., Caglar, S., Caglar, B., & Sahin, O. (2018). Synthesis, structural, thermal elucidation and in vitro anticancer activity of novel silver (I) complexes with non-steroidal anti-inflammatory drugs diclofenac and mefenamic acid including picoline derivatives. Polyhedron, 151, 160-170.
[89] Singh, M. P., & Baruah, J. B. (2020). Photophysical properties of Ag, Zn and Cd-N-(4-pyridylmethyl)-1, 8-naphthalimide complexes: influences of π-stacking and C–H··· O interactions. CrystEngComm, 22(26), 4374-4385.

[90] Usubaliev, B. T., Movsumov, E. M., Amiraslanov, I. R., Akhmedov, A. I., Musaev, A. A., & Mamedov, K. S. (1981). Crystal structures of silver (I) benzoate and p-hydroxybenzoate. Journal of Structural Chemistry, 22(1), 73-77.
[91] Lodish H, Berk A, Zipursky SL, Matsudaira P, Baltimore D, Darnell J (2000). "Non-covalent bonds". Molecular Cell Biology (4th ed.). New York: W.H. Freeman. ISBN 978-0-7167-3136-8.
[92] Mahadevi, A. S., & Sastry, G. N. (2016). Cooperativity in Non-covalent Interactions. Chemical Reviews, 116(5), 2775–2825.
[93] Braga, D., & Grepioni, F. (2000). Intermolecular Interactions in Nonorganic Crystal Engineering. Accounts of Chemical Research, 33(9), 601–608.
[94] Hedrich, M., & Hartl, H. (1983). catena-Bis(μ-benzoato-O,O',μ-O)-bis(pyridine)-disilver(I), [Ag2(C5H5N)2-(C7H5O2)2]. Acta Crystallographica Section C, Crystal Structure Communications, 39(5), 533–536.
[95] You, Z.-L., Zhu, H.-L., & Liu, W.-S. (2004). Bis(μ-4-chlorobenzoato-κ2O:O')bis[(2-aminopyridine-κN)silver(I)](Ag—Ag) monohydrate. Acta Crystallographica Section E Structure Reports Online, 60(12), m1863–m1865.
[96] Harurluoglu, B., Altay, A., Caglar, S., Kubra Kagan Yeniceri, E., Caglar, B., & Sibel Şahin, Z. (2021). Binuclear silver(I) complexes with the non-steroidal anti-inflammatory drug tolfenamic acid: Synthesis, characterization, cytotoxic activity and evaluation of cellular mechanism of action. Polyhedron, 202, 115189.
[97] Ward, J. S., Martõnova, J., Wilson, L. M., Kramer, E., Aav, R., & Rissanen, K. (2022). Carbonyl hypoiodites from pivalic and trimesic acid and their silver (i) intermediates. Dalton Transactions, 51(38), 14646-14653.
[98] SAINT-Plus; Bruker AXS Inc.: Madison, Wisconsin, USA, 2012.
[99] Sheldrick, G. I. (1996). Program for empirical absorption correction of area detector data. Sadabs.
[100] XPREP, D. P. (2008). Reciprocal Space Group Exploration.
[101] Sheldrick, G. M. (2015). SHELXT–Integrated space-group and crystal-structure determination. Acta Crystallographica Section A: Foundations and Advances, 71(1), 3-8.
[102] Sheldrick, G. M. (2015). Crystal structure refinement with SHELXL. Acta Crystallographica Section C: Structural Chemistry, 71(1), 3-8.
[103] Dolomanov, O. V., Bourhis, L. J., Gildea, R. J., Howard, J. A., & Puschmann, H. (2009). OLEX2: a complete structure solution, refinement and analysis program. Journal of applied crystallography, 42(2), 339-341.
[104] Macrae, C. F., Sovago, I., Cottrell, S. J., Galek, P. T., McCabe, P., Pidcock, E., ... & Wood, P. A. (2020). Mercury 4.0: From visualization to analysis, design and prediction. Journal of applied crystallography, 53(1), 226-235.
[105] Troff, R. W., Mäkelä, T., Topić, F., Valkonen, A., Raatikainen, K., & Rissanen, K. (2013). Alternative motifs for halogen bonding. European Journal of Organic Chemistry, 2013(9), 1617-1637.
[106] Bondi, A. V. (1964). van der Waals volumes and radii. The Journal of physical chemistry, 68(3), 441-451.
[107] Microsoft Corporation. (2018). Microsoft Excel. Retrieved from https://office.microsoft.com/excel.
[108] M. J. Turner, J. J. McKinnon, S. K. Wolff, D. J. Grimwood, P. R. Spackman, D. Jayatilaka and M. A. Spackman, Crystal Explorer17 (2017). University of Western Australia.
[109] Frisch, M. E., Trucks, G. W., Schlegel, H. B., Scuseria, G. E., Robb, M. A., Cheeseman, J. R., ... & Fox, D. J. (2016). Gaussian 16.
[110] a) Becke, A. D. (1993). Becke's three parameter hybrid method using the LYP correlation functional. J. Chem. Phys, 98(492), 5648-5652; b) Lee, C., Yang, W., & Parr, R. G. (1988). Development of the Colle-Salvetti correlation-energy formula into a functional of the electron density. Physical review B, 37(2), 785; c) Vosko, S. H., Wilk, L., & Nusair, M. (1980). Accurate spin-dependent electron liquid correlation energies for local spin density calculations: a critical analysis. Canadian Journal of physics, 58(8), 1200-1211; d) Stephens, P. J., Devlin, F. J., Chabalowski, C. F., & Frisch, M. J. (1994). Ab initio calculation of vibrational absorption and circular dichroism spectra using density functional force fields. The Journal of physical chemistry, 98(45), 11623-11627.

[111] a) Kendall, R. A., Dunning Jr, T. H., & Harrison, R. J. (1992). Electron affinities of the first-row atoms revisited. Systematic basis sets and wave functions. The Journal of chemical physics, 96(9), 6796-6806; b) Figgen, D., Peterson, K. A., Dolg, M., & Stoll, H. (2009). Energy-consistent pseudopotentials and correlation consistent basis sets for the 5 d elements Hf–Pt. The Journal of chemical physics, 130(16), 164108.
[112] Van Duijneveldt, F. B., van Duijneveldt-van de Rijdt, J. G., & van Lenthe, J. H. (1994). State of the art in counterpoise theory. Chemical Reviews, 94(7), 1873-1885.
[113] Bader, R. F. (1985). Atoms in molecules. Accounts of Chemical Research, 18(1), 9-15.
[114] Bader, R. F. (1991). A quantum theory of molecular structure and its applications. Chemical Reviews, 91(5), 893-928.
[115] Glendening, E. D., Reed, A. E., Carpenter, J. E., & Weinhold, F. (1998). NBO Version 3.1. Google Scholar There is no corresponding record for this reference.
[116] Chemcraft - graphical software for visualization of quantum chemistry computations. https://www.chemcraftprog.com
[117] Olson, L. P., Whitcomb, D. R., Rajeswaran, M., Blanton, T. N., & Stwertka, B. J. (2006). The Simple Yet Elusive Crystal Structure of Silver Acetate and the Role of the Ag−Ag Bond in the Formation of Silver Nanoparticles during the Thermally Induced Reduction of Silver Carboxylates. Chemistry of Materials, 18(6), 1667–1674.
[118] Hu, M. L., Morsali, A., & Aboutorabi, L. (2011). Lead(II) carboxylate supramolecular compounds: Coordination modes, structures and nano-structures aspects. Coordination Chemistry Reviews, 255(23-24), 2821–2859.
[119] Liang, M. X., Ruan, C. Z., Sun, D., Kong, X. J., Ren, Y. P., Long, L. S., … Zheng, L. S. (2014). Solvothermal Synthesis of Four Polyoxometalate-Based Coordination Polymers Including Diverse Ag(I)···π Interactions. Inorganic Chemistry, 53(2), 897–902.
[120] Bikbaeva, Z.M. et al. (2017) "Electrophilic–nucleophilic dualism of nickel(ii) toward NI···I non-covalent interactions: Semi-coordination of iodine centers via electron belt and halogen bonding via σ-hole," Inorganic Chemistry, 56(21), pp. 13562–13578
[121] Lepetit, C., Fau, P., Fajerwerg, K., Kahn, M. L., & Silvi, B. (2017). Topological analysis of the metal-metal bond: A tutorial review. Coordination Chemistry Reviews, 345, 150-181.
[122] Gervasio, G., Bianchi, R., & Marabello, D. (2004). About the topological classification of the metal–metal bond. Chemical physics letters, 387(4-6), 481-484.
[123] Bianchi, R., Gervasio, G., & Marabello, D. (2000). Experimental electron density analysis of Mn2 (CO) 10: metal− metal and metal− Ligand bond characterization. Inorganic Chemistry, 39(11), 2360-2366.
[124] Espinosa, E., Alkorta, I., Elguero, J., & Molins, E. (2002). From weak to strong interactions: A comprehensive analysis of the topological and energetic properties of the electron density distribution involving X–H··· F–Y systems. The Journal of chemical physics, 117(12), 5529-5542.
[125] (a) Espinosa, E., Molins, E., & Lecomte, C. (1998). Hydrogen bond strengths revealed by topological analyses of experimentally observed electron densities. Chemical physics letters, 285(3-4), 170-173; (b) Espinosa, E., Alkorta, I., Rozas, I., Elguero, J., & Molins, E. (2001). About the evaluation of the local kinetic, potential and total energy densities in closed-shell interactions. Chemical physics letters, 336(5-6), 457-461. Eint = −1/2Vbcp and Eint (kcal/mol) = −313.754Vbcp (au).
[126] (a) Bader, R. F. W. (1990). Atoms in Molecules, Clarendon. (b) Bader, R. F., & Essén, H. (1984). The characterization of atomic interactions. The Journal of chemical physics, 80(5), 1943-1960.
[127] Outeiral, C., Vincent, M. A., Martín Pendás, Á., & Popelier, P. L. A. (2018). Revitalizing the concept of bond order through delocalization measures in real space. Chemical Science, 9(25), 5517–5529.
[128] Green, M. L. H. (1995). A new approach to the formal classification of covalent compounds of the elements. Journal of Organometallic Chemistry, 500(1-2), 127-148.
[129] a) Ivanov, D. M., Novikov, A. S., Starova, G. L., Haukka, M., & Kukushkin, V. Y. (2016). A family of heterotetrameric clusters of chloride species and halomethanes held by two halogen and two hydrogen bonds. CrystEngComm, 18(28), 5278-5286; b) Mikherdov, A. S., Kinzhalov, M. A., Novikov, A. S., Boyarskiy, V. P., Boyarskaya, I. A., Dar'in, D. V., ... & Kukushkin, V. Y. (2016). Difference in energy

between two distinct types of chalcogen bonds drives regioisomerization of binuclear (diaminocarbene) PdII complexes. Journal of the American Chemical Society, 138(42), 14129-14137; c) Serebryanskaya, T. V., Novikov, A. S., Gushchin, P. V., Haukka, M., Asfin, R. E., Tolstoy, P. M., & Kukushkin, V. Y. (2016). Identification and H (D)-bond energies of C–H (D)··· Cl interactions in chloride–haloalkane clusters: a combined X-ray crystallographic, spectroscopic, and theoretical study. Physical Chemistry Chemical Physics, 18(20), 14104-14112; d) Anisimova, T. B., Kinzhalov, M. A., da Silva, M. F. C. G., Novikov, A. S., Kukushkin, V. Y., Pombeiro, A. J., & Luzyanin, K. V. (2017). Addition of N-nucleophiles to gold (III)-bound isocyanides leading to short-lived gold (III) acyclic diaminocarbene complexes. New Journal of Chemistry, 41(9), 3246-3250; e) Ivanov, D. M., Kinzhalov, M. A., Novikov, A. S., Ananyev, I. V., Romanova, A. A., Boyarskiy, V. P., ... & Kukushkin, V. Y. (2017). H2C (X)–X··· X–(X= Cl, Br) Halogen Bonding of Dihalomethanes. Crystal Growth & Design, 17(3), 1353-1362.
[130] a) Ivanov, D. M., Kirina, Y. V., Novikov, A. S., Starova, G. L., & Kukushkin, V. Y. (2016). Efficient π-stacking with benzene provides 2D assembly of trans-[PtCl2 (p-CF3C6H4CN) 2]. Journal of Molecular Structure, 1104, 19-23; b) Kulish, K. I., Novikov, A. S., Tolstoy, P. M., Bolotin, D. S., Bokach, N. A., Zolotarev, A. A., & Kukushkin, V. Y. (2016). Solid state and dynamic solution structures of O-carbamidine amidoximes gives further insight into the mechanism of zinc (II)-mediated generation of 1, 2, 4-oxadiazoles. Journal of Molecular Structure, 1111, 142-150; c) Ding, X., Tuikka, M. J., Hirva, P., Kukushkin, V. Y., Novikov, A. S., & Haukka, M. (2016). Fine-tuning halogen bonding properties of diiodine through halogen–halogen charge transfer–extended [Ru (2, 2'-bipyridine)(CO) 2 X 2]· I 2 systems (X= Cl, Br, I). CrystEngComm, 18(11), 1987-1995; d) Novikov, A. S., Kuznetsov, M. L., & Pombeiro, A. J. (2013). Theory of the Formation and Decomposition of N-Heterocyclic Aminooxycarbenes through Metal-Assisted [2+ 3]-Dipolar Cycloaddition/Retro-Cycloaddition. Chemistry–A European Journal, 19(8), 2874-2888.
[131] Vener, M. V., Egorova, A. N., Churakov, A. V., & Tsirelson, V. G. (2012). Intermolecular hydrogen bond energies in crystals evaluated using electron density properties: DFT computations with periodic boundary conditions. Journal of computational chemistry, 33(29), 2303-2309.
[132] Bader, R.F.W. (1998). A bond path: A universal indicator of bonded interactions. J. Phys. Chem. A 102, 7314–7323.
[133] Ivanov, D.M. et al. (2021) “Metal Centers as nucleophiles: Oxymoron of halogen bond-involving crystal engineering,” Chemistry – A European Journal, 28(2).
[134] Glendening, E. D., Reed, A. E., Carpenter, J. E., & Weinhold, F. (2003). NBO, version 3.1, Gaussian. Inc.: Pittsburgh, PA.
[135] Schwenke, D. W., & Truhlar, D. G. (1985). Systematic study of basis set superposition errors in the calculated interaction energy of two HF molecules. The Journal of chemical physics, 82(5), 2418-2426.
[136] Gutowski, M., van Duijneveldt-van de Rijdt, J. G., van Lenthe, J. H., & van Duijneveldt, F. B. (1993). Accuracy of the Boys and Bernardi function counterpoise method. The Journal of chemical physics, 98(6), 4728-4737.
[137] Fang, J., Zhang, Y., Wang, Y., Li, Y., Li, H., & Li, C. (2020). The molecular design and experimental study on the catalytic cleavage of linkages in lignin with binuclear ionic liquid. Journal of Molecular Liquids, 308, 113128.
[138] Sharma, A., Verma, V. K., Singh, J. B., & Guin, M. (2022). Investigation of intramolecular hydrogen bonding in naphthoquinone derivatives by quantum chemical calculations. Journal of Physical Organic Chemistry, e4413.
[139] Weinhold, F., & Landis, C. R. (2005). Valency and bonding: a natural bond orbital donor-acceptor perspective. Cambridge University Press.
[140] Terro´ n, A., Moreno-Vachiano, B., Bauza´, A., Garcı´a-Raso, A., Fiol, J.J., Barcelo´ -Oliver, M., Molins, E., and Frontera, A. (2017). X-ray crystal structure of a metalled double-helix generated by infinite and consecutive C*-AgI-C* (C*:N1-hexylcytosine) base pairs through argentophilic and hydrogen bond interactions. Chemistry 23, 2103–2108.

[141] Silver, S., Phung, L. T., & Silver, G. (2006). Silver as biocides in burn and wound dressings and bacterial resistance to silver compounds. Journal of industrial microbiology and biotechnology, 33(7), 627-634.
[142] Lansdown, A. B. (2010). Silver in healthcare: its antimicrobial efficacy and safety in use. Royal Society of Chemistry.
[143] De Gracia, C. G. (2001). An open study comparing topical silver sulfadiazine and topical silver sulfadiazine–cerium nitrate in the treatment of moderate and severe burns. Burns, 27(1), 67-74.
[144] Martins, P., Marques, M., Coito, L., JL Pombeiro, A., Viana Baptista, P., & R Fernandes, A. (2014). Organometallic compounds in cancer therapy: past lessons and future directions. Anti-Cancer Agents in Medicinal Chemistry (Formerly Current Medicinal Chemistry-Anti-Cancer Agents), 14(9), 1199-1212.
[145] Haque, R. A., Budagumpi, S., Zulikha, H. Z., Hasanudin, N., Ahamed, M. B. K., & Majid, A. M. A. (2014). Silver (I)-N-heterocyclic carbene complexes of nitrile-functionalized imidazol-2-ylidene ligands as anticancer agents. Inorganic chemistry communications, 44, 128-133.
[146] Li, S., Zhang, S., Jin, X., Tan, X., Lou, J., Zhang, X., & Zhao, Y. (2014). Singly protonated dehydronorcantharidin silver coordination polymer induces apoptosis of lung cancer cells via reactive oxygen species-mediated mitochondrial pathway. European journal of medicinal chemistry, 86, 1-11.
[147] Rao, P., & Knaus, E. E. (2008). Evolution of nonsteroidal anti-inflammatory drugs (NSAIDs): cyclooxygenase (COX) inhibition and beyond. Journal of pharmacy & pharmaceutical sciences, 11(2), 81s-110s.
[148] Johnsen, J. I., Lindskog, M., Ponthan, F., Pettersen, I., Elfman, L., Orrego, A., ... & Kogner, P. (2005). NSAIDs in neuroblastoma therapy. Cancer letters, 228(1-2), 195-201.
[149] Yu, S., Ward, J. S., Truong, K. N., & Rissanen, K. (2021). Carbonyl hypoiodites as extremely strong halogen bond donors. Angewandte Chemie, 133(38), 20907-20911.
[150] Kolar, M. H., & Hobza, P. (2016). Computer modeling of halogen bonds and other σ-hole interactions. Chemical reviews, 116(9), 5155-5187.
[151] Wang, H., Wang, W., & Jin, W. J. (2016). σ-Hole bond vs π-hole bond: a comparison based on halogen bond. Chemical reviews, 116(9), 5072-5104.
[152] Rissanen, K. (2008). Halogen bonded supramolecular complexes and networks. CrystEngComm, 10(9), 1107-1113.
[153] Kleinberg, J., Novak, M., & Gerber, V. (1945). Antibacterial Properties of Some Positive Univalent Iodine Compounds. Proceedings of the Society for Experimental Biology and Medicine, 58(3), 238-239.
[154] Zingaro, R. A., Werf, C. A. V., & Kleinberg, J. (1950). Further Observations on the Preparation and Reactions of Positive Iodine Salts. Journal of the American Chemical Society, 72(11), 5341-5342.
[155] Colton, E. (1955). Quinoline Derivatives of Iodine (I). Journal of the American Chemical Society, 77(23), 6190-6191.

Appendix: Supplementary Information

S1. CIF and check CIF file details

S1.1 CIF and check CIF files for structures **I-VIII** are available at:

https://uctcloud-my.sharepoint.com/:f:/g/personal/thntri002_myuct_ac_za/Et-VmQTvx8lJrV38AHggpLkBFDBgYOaYZ564tVe6_uEm4Q?e=RCsfND

S2. Thermal analysis of compounds II-V (heating rate 10 °C/min)

Table S2: Thermogravimetry of compounds **II-V**.

Compound	Approx. Temp range (°C)	Experimental weight loss (%)	Interpretation of weight loss	Theoretical weight loss (%)
II				
Step 1	65-140	25.3	Loss of 2 x 2-pic	27.4
Step 2	250-325	31.1	Loss of 2 x OBn	36.0
III				
Step 1	75-155	29.7	Loss of 2 x 3-Clpy	31.5
Step 2	245-325	33.1	Loss of 2 x OBn	34.1
IV				
Step 1	65-160	37.7	Loss of 2 x 2-Brpy	39.1
Step 2	250-300	28.6	Loss of 2 x OBn	30.3
V				
Step 1	65-160	43.9	Loss of 2 x 2-Ipy	45.4
Step 2	250-290	25.1	Loss of 2 x OBn	27.5

S3. B3LYP-D2/aug-cc-pVTZ-PP or cc-pVTZ-PP optimised coordinates

S3.1 Compound I

S3.1.1 Monomer

Optimised Coordinates

47	5.696014000	5.855802000	12.419401000
8	5.429953000	4.157837000	11.014527000
8	3.327228000	4.686091000	10.384080000
6	4.371794000	3.989925000	10.335693000
6	4.368753000	2.843157000	9.313902000
6	3.533905000	2.906628000	8.227909000
1	2.864922000	3.750710000	8.134697000
6	3.546068000	1.921533000	7.287786000
1	2.888532000	1.984064000	6.430439000
6	4.387444000	0.856578000	7.431058000
1	4.395268000	0.071599000	6.685097000
6	5.224796000	0.775647000	8.508790000
1	5.890176000	-0.070828000	8.618320000
6	5.221308000	1.767928000	9.452218000
1	5.887560000	1.732507000	10.302877000
47	3.247186000	6.750198000	11.183999000
8	5.615972000	7.919909000	13.219320000
8	3.513247000	8.448163000	12.588873000
6	4.571406000	8.616075000	13.267707000

6	4.574447000	9.762843000	14.289498000
6	5.409295000	9.699372000	15.375491000
6	3.721892000	10.838072000	14.151182000
1	6.078278000	8.855290000	15.468703000
6	5.397132000	10.684467000	16.315614000
1	6.054668000	10.621936000	17.172961000
6	4.555756000	11.749422000	16.172342000
1	4.547932000	12.534401000	16.918303000
6	3.718404000	11.830353000	15.094610000
1	3.053024000	12.676828000	14.985080000
1	3.055640000	10.873493000	13.300523000

S3.1.2 Dimer

Optimised Coordinates

47	1.224386000	2.704302000	0.617691000
8	0.958692000	1.006592000	-0.785976000
8	-1.144704000	1.534781000	-1.418540000
6	-0.100186000	0.838290000	-1.465735000
6	-0.102842000	-0.308216000	-2.487758000
6	-0.937197000	-0.244535000	-3.573516000
1	-1.611707000	0.608710000	-3.662689000
6	-0.925588000	-1.229706000	-4.512901000
1	-1.591139000	-1.167524000	-5.377683000
6	-0.084065000	-2.294911000	-4.371277000
1	-0.079537000	-3.093129000	-5.118300000
6	0.752996000	-2.375626000	-3.292604000
1	1.411205000	-3.239228000	-3.169463000
6	0.749397000	-1.383593000	-2.348448000
1	1.419394000	-1.411475000	-1.486284000
47	-1.224386000	3.598698000	-0.617691000
8	1.144704000	4.768220000	1.418540000
8	-0.958690000	5.296411000	0.785980000
6	0.100168000	5.464705000	1.465741000
6	0.102844000	6.611217000	2.487762000
6	0.937219000	6.547551000	3.573499000
6	-0.749428000	7.686508000	2.348494000
1	1.610147000	5.692811000	3.664136000
6	0.925604000	7.532717000	4.512892000
1	1.590519000	7.469851000	5.378332000
6	0.084069000	8.597925000	4.371272000
1	0.076155000	9.390599000	5.124777000
6	-0.753001000	8.678598000	3.292622000
1	-1.424779000	9.533820000	3.182014000
1	-1.421027000	7.719430000	1.488684000
47	-1.224386000	-2.704302000	-0.617691000
8	-0.958692000	-1.006592000	0.785976000
8	1.144704000	-1.534781000	1.418540000
6	0.100186000	-0.838290000	1.465735000
6	0.102842000	0.308216000	2.487758000

6	0.937197000	0.244535000	3.573516000
1	1.611707000	-0.608710000	3.662689000
6	0.925588000	1.229706000	4.512901000
1	1.591139000	1.167524000	5.377683000
6	0.084065000	2.294911000	4.371277000
1	0.079537000	3.093129000	5.118300000
6	-0.752996000	2.375626000	3.292604000
1	-1.411205000	3.239228000	3.169463000
6	-0.749397000	1.383593000	2.348448000
1	-1.419394000	1.411475000	1.486284000
47	1.224386000	-3.598698000	0.617691000
8	-1.144704000	-4.768220000	-1.418540000
8	0.958690000	-5.296411000	-0.785980000
6	-0.100168000	-5.464705000	-1.465741000
6	-0.102844000	-6.611217000	-2.487762000
6	-0.937219000	-6.547551000	-3.573499000
6	0.749428000	-7.686508000	-2.348494000
1	-1.610147000	-5.692811000	-3.664136000
6	-0.925604000	-7.532717000	-4.512892000
1	-1.590519000	-7.469851000	-5.378332000
6	-0.084069000	-8.597925000	-4.371272000
1	-0.076155000	-9.390599000	-5.124777000
6	0.753001000	-8.678598000	-3.292622000
1	1.424779000	-9.533820000	-3.182014000
1	1.421027000	-7.719430000	-1.488684000

S3.2 Compound II

S3.2.1 Monomer

Optimised Coordinates

47	0.013006000	1.434047000	-0.042418000
8	1.587433000	1.418765000	-1.540330000
8	2.163545000	-0.611626000	-0.782319000
7	-0.558469000	1.585813000	2.089078000
6	4.401054000	-0.671663000	-2.478091000
1	4.185702000	-1.535305000	-1.865707000
6	3.548376000	0.430524000	-2.399974000
6	3.818765000	1.550770000	-3.182673000
1	3.156384000	2.401348000	-3.117130000
6	5.736645000	0.450086000	-4.135931000
1	6.578651000	0.453982000	-4.816040000
6	5.485342000	-0.661756000	-3.343952000
1	6.132801000	-1.527097000	-3.404752000
6	0.349142000	1.840427000	3.054950000
6	2.340373000	0.404916000	-1.495821000
6	-1.828194000	1.303670000	2.444071000
1	-2.499451000	1.103852000	1.618515000
6	4.905155000	1.557806000	-4.049435000
1	5.098892000	2.429560000	-4.661026000
6	-0.013006000	1.810190000	4.400143000

1	0.732016000	2.014503000	5.155625000
6	1.750078000	2.167081000	2.630579000
1	2.096031000	1.481260000	1.859709000
1	2.435927000	2.135097000	3.474969000
1	1.786633000	3.170880000	2.200898000
6	-2.249757000	1.266233000	3.755927000
1	-3.281139000	1.041586000	3.985992000
6	-1.320985000	1.528044000	4.754236000
1	-1.612493000	1.509928000	5.796122000
47	-0.013006000	-1.434047000	-0.042418000
8	-1.587433000	-1.418765000	-1.540330000
8	-2.163545000	0.611626000	-0.782319000
7	0.558469000	-1.585813000	2.089078000
6	-4.401054000	0.671663000	-2.478091000
1	-4.185702000	1.535305000	-1.865707000
6	-3.548376000	-0.430524000	-2.399974000
6	-3.818765000	-1.550770000	-3.182673000
1	-3.156384000	-2.401348000	-3.117130000
6	-5.736645000	-0.450086000	-4.135931000
1	-6.578651000	-0.453982000	-4.816040000
6	-5.485342000	0.661756000	-3.343952000
1	-6.132801000	1.527097000	-3.404752000
6	-0.349142000	-1.840427000	3.054950000
6	-2.340373000	-0.404916000	-1.495821000
6	1.828194000	-1.303670000	2.444071000
1	2.499451000	-1.103852000	1.618515000
6	-4.905155000	-1.557806000	-4.049435000
1	-5.098892000	-2.429560000	-4.661026000
6	0.013006000	-1.810190000	4.400143000
1	-0.732016000	-2.014503000	5.155625000
6	-1.750078000	-2.167081000	2.630579000
1	-2.096031000	-1.481260000	1.859709000
1	-2.435927000	-2.135097000	3.474969000
1	-1.786633000	-3.170880000	2.200898000
6	2.249757000	-1.266233000	3.755927000
1	3.281139000	-1.041586000	3.985992000
6	1.320985000	-1.528044000	4.754236000
1	1.612493000	-1.509928000	5.796122000

S3.2.2 Dimer

Optimised Coordinates

47	-2.063587000	0.123924000	0.120481000
8	-3.132067000	1.479237000	1.441190000
8	-4.491378000	1.940888000	-0.281595000
7	-0.696909000	-0.145578000	-1.597794000
6	-5.807574000	3.919742000	1.214218000
1	-6.153213000	3.696007000	0.203914000
6	-4.720584000	3.200666000	1.713593000
6	-4.259725000	3.478618000	2.998729000

1	-3.407733000	2.913009000	3.378393000
6	-5.984878000	5.133788000	3.284077000
1	-6.485075000	5.883849000	3.902358000
6	-6.436833000	4.876906000	1.997095000
1	-7.294117000	5.426342000	1.599110000
6	-0.106574000	0.901641000	-2.211394000
6	-4.064205000	2.124949000	0.883301000
6	-0.539754000	-1.379998000	-2.116583000
1	-1.063842000	-2.171359000	-1.574546000
6	-4.892054000	4.437276000	3.780605000
1	-4.528896000	4.640992000	4.791691000
6	0.651840000	0.717311000	-3.365498000
1	1.121641000	1.582573000	-3.834691000
6	-0.285329000	2.260797000	-1.602757000
1	-1.290858000	2.370352000	-1.168817000
1	-0.123479000	3.046195000	-2.356827000
1	0.467528000	2.404505000	-0.807546000
6	0.204464000	-1.627913000	-3.250786000
1	0.312643000	-2.648546000	-3.619648000
6	0.814787000	-0.554904000	-3.885923000
1	1.423656000	-0.710512000	-4.779153000
47	-4.430746000	-0.192210000	-1.467999000
8	-4.981008000	-1.939266000	-0.298458000
8	-2.802570000	-2.202781000	0.164196000
7	-3.493970000	0.634756000	-3.293230000
6	-3.318995000	-4.625074000	1.487615000
1	-2.297429000	-4.242249000	1.459524000
6	-4.321471000	-3.885544000	0.858224000
6	-5.628357000	-4.368249000	0.874592000
1	-6.404115000	-3.784801000	0.377404000
6	-4.932964000	-6.272638000	2.173398000
1	-5.173705000	-7.202864000	2.694744000
6	-3.625148000	-5.808623000	2.143749000
1	-2.833116000	-6.376218000	2.639894000
6	-3.040450000	-0.159823000	-4.285517000
6	-4.000778000	-2.573312000	0.185426000
6	-3.267813000	1.961954000	-3.364170000
1	-3.646909000	2.531737000	-2.511019000
6	-5.932121000	-5.553456000	1.532776000
1	-6.962790000	-5.917568000	1.547101000
6	-2.345393000	0.376285000	-5.367463000
1	-1.981911000	-0.291095000	-6.150236000
6	-3.320743000	-1.630099000	-4.187947000
1	-2.990064000	-2.013251000	-3.208991000
1	-2.815357000	-2.187945000	-4.989814000
1	-4.407720000	-1.811165000	-4.249262000
6	-2.593680000	2.553135000	-4.411923000
1	-2.437630000	3.632903000	-4.419530000
6	-2.125466000	1.741152000	-5.435985000
1	-1.582410000	2.169901000	-6.281747000
47	2.063587000	-0.123925000	-0.120481000
8	3.132067000	-1.479237000	-1.441190000

8	4.491378000	-1.940888000	0.281595000
7	0.696910000	0.145577000	1.597794000
6	5.807573000	-3.919742000	-1.214219000
1	6.153212000	-3.696007000	-0.203914000
6	4.720584000	-3.200666000	-1.713593000
6	4.259725000	-3.478617000	-2.998729000
1	3.407734000	-2.913009000	-3.378393000
6	5.984878000	-5.133788000	-3.284077000
1	6.485075000	-5.883848000	-3.902357000
6	6.436834000	-4.876905000	-1.997095000
1	7.294117000	-5.426341000	-1.599109000
6	0.106574000	-0.901642000	2.211394000
6	4.064205000	-2.124949000	-0.883301000
6	0.539754000	1.379998000	2.116583000
1	1.063842000	2.171359000	1.574546000
6	4.892055000	-4.437276000	-3.780605000
1	4.528896000	-4.640992000	-4.791691000
6	-0.651840000	-0.717311000	3.365498000
1	-1.121641000	-1.582573000	3.834691000
6	0.285328000	-2.260796000	1.602756000
1	1.290858000	-2.370352000	1.168818000
1	0.123477000	-3.046195000	2.356826000
1	-0.467528000	-2.404503000	0.807545000
6	-0.204465000	1.627913000	3.250785000
1	-0.312644000	2.648546000	3.619647000
6	-0.814787000	0.554905000	3.885924000
1	-1.423656000	0.710513000	4.779153000
47	4.430746000	0.192210000	1.467999000
8	4.981008000	1.939267000	0.298458000
8	2.802570000	2.202781000	-0.164196000
7	3.493970000	-0.634756000	3.293230000
6	3.318995000	4.625074000	-1.487615000
1	2.297429000	4.242248000	-1.459524000
6	4.321470000	3.885545000	-0.858224000
6	5.628356000	4.368249000	-0.874592000
1	6.404114000	3.784800000	-0.377405000
6	4.932964000	6.272638000	-2.173399000
1	5.173704000	7.202864000	-2.694745000
6	3.625147000	5.808622000	-2.143749000
1	2.833115000	6.376218000	-2.639894000
6	3.040451000	0.159824000	4.285517000
6	4.000778000	2.573312000	-0.185426000
6	3.267812000	-1.961954000	3.364169000
1	3.646908000	-2.531737000	2.511019000
6	5.932121000	5.553456000	-1.532776000
1	6.962790000	5.917568000	-1.547101000
6	2.345393000	-0.376286000	5.367463000
1	1.981911000	0.291095000	6.150237000
6	3.320743000	1.630099000	4.187947000
1	2.990062000	2.013251000	3.208992000
1	2.815359000	2.187944000	4.989815000
1	4.407720000	1.811165000	4.249259000

6	2.593680000	-2.553134000	4.411923000
1	2.437630000	-3.632903000	4.419530000
6	2.125466000	-1.741153000	5.435985000
1	1.582410000	-2.169902000	6.281747000

S3.3 Compound III

S3.3.1 Monomer

Optimised Coordinates

47	-0.676247000	1.169682000	0.347309000
17	-5.426151000	4.430496000	-0.412084000
8	1.924033000	-0.554113000	1.360280000
8	0.795971000	1.281176000	1.973406000
7	-2.006206000	3.007322000	0.957002000
6	2.806431000	0.771840000	3.096525000
6	2.779571000	1.970739000	3.814276000
1	2.007684000	2.692923000	3.593712000
6	4.746450000	0.085076000	4.358895000
1	5.511153000	-0.651509000	4.566785000
6	1.759561000	0.477433000	2.055942000
6	-3.966336000	4.261072000	0.509695000
6	-3.133855000	3.195384000	0.259997000
1	-3.357142000	2.466073000	-0.506918000
6	-3.658431000	5.170601000	1.499233000
1	-4.314048000	6.005071000	1.702549000
6	-1.693687000	3.886626000	1.912213000
1	-0.775239000	3.691550000	2.450118000
6	-2.489559000	4.976941000	2.213403000
1	-2.199892000	5.661362000	2.998129000
6	3.806037000	-0.153920000	3.365476000
1	3.827322000	-1.074819000	2.802034000
6	3.718569000	2.210855000	4.803964000
1	3.688021000	3.137269000	5.362536000
6	4.693451000	1.261586000	5.089184000
1	5.418104000	1.449138000	5.870881000
47	0.676247000	-1.169682000	-0.347309000
17	5.426151000	-4.430496000	0.412084000
8	-1.924033000	0.554113000	-1.360280000
8	-0.795971000	-1.281176000	-1.973406000
7	2.006206000	-3.007322000	-0.957002000
6	-2.806431000	-0.771840000	-3.096525000
6	-2.779571000	-1.970739000	-3.814276000
1	-2.007684000	-2.692923000	-3.593712000
6	-4.746450000	-0.085076000	-4.358895000
1	-5.511153000	0.651509000	-4.566785000
6	-1.759561000	-0.477433000	-2.055942000
6	3.966336000	-4.261072000	-0.509695000
6	3.133855000	-3.195384000	-0.259997000
1	3.357142000	-2.466073000	0.506918000
6	3.658431000	-5.170601000	-1.499233000

1	4.314048000	-6.005071000	-1.702549000
6	1.693687000	-3.886626000	-1.912213000
1	0.775239000	-3.691550000	-2.450118000
6	2.489559000	-4.976941000	-2.213403000
1	2.199892000	-5.661362000	-2.998129000
6	-3.806037000	0.153920000	-3.365476000
1	-3.827322000	1.074819000	-2.802034000
6	-3.718569000	-2.210855000	-4.803964000
1	-3.688021000	-3.137269000	-5.362536000
6	-4.693451000	-1.261586000	-5.089184000
1	-5.418104000	-1.449138000	-5.870881000

S3.3.1 Dimer

Optimised Coordinates

47	-3.840037000	-1.058272000	0.677470000
17	-8.894465000	1.630341000	-0.320174000
8	-1.154384000	-2.938030000	0.790651000
8	-3.329320000	-3.161581000	0.304217000
7	-6.110590000	-1.141741000	0.081426000
6	-1.996486000	-5.104756000	0.407480000
6	-3.102226000	-5.944359000	0.246392000
1	-4.097774000	-5.500893000	0.221197000
6	-0.546198000	-7.032084000	0.306473000
1	0.460881000	-7.454012000	0.336444000
6	-2.174678000	-3.613996000	0.513499000
6	-8.108977000	0.084790000	-0.259179000
6	-6.768375000	0.023772000	0.041824000
1	-6.184825000	0.920613000	0.263249000
6	-8.815754000	-1.066587000	-0.535469000
1	-9.877714000	-1.019769000	-0.780391000
6	-6.786781000	-2.264059000	-0.176331000
1	-6.205305000	-3.188754000	-0.131676000
6	-8.134232000	-2.269372000	-0.488207000
1	-8.646297000	-3.210766000	-0.695249000
6	-0.725523000	-5.663328000	0.454556000
1	0.131515000	-5.006903000	0.596163000
6	-2.923856000	-7.310300000	0.100522000
1	-3.791539000	-7.961530000	-0.033110000
6	-1.644865000	-7.854724000	0.114065000
1	-1.509261000	-8.932291000	-0.010177000
47	-1.111378000	-0.771152000	1.183766000
17	3.943050000	-3.459764000	2.181411000
8	-3.797031000	1.108607000	1.070585000
8	-1.622095000	1.332158000	1.557019000
7	1.159175000	-0.687682000	1.779809000
6	-2.954908000	3.275299000	1.453876000
6	-1.849062000	4.115106000	1.614592000
1	-0.853202000	3.672759000	1.630271000
6	-4.405165000	5.202791000	1.554565000

1	-5.412295000	5.626160000	1.529050000
6	-2.776733000	1.784576000	1.347696000
6	3.157562000	-1.914213000	2.120415000
6	1.816959000	-1.853195000	1.819411000
1	1.235781000	-2.749988000	1.597152000
6	3.864339000	-0.762835000	2.396705000
1	4.925803000	-0.809990000	2.641938000
6	1.835366000	0.434636000	2.037567000
1	1.257035000	1.360322000	1.995767000
6	3.182818000	0.439948000	2.349443000
1	3.689636000	1.383218000	2.557420000
6	-4.225702000	3.833931000	1.406265000
1	-5.083347000	3.175451000	1.270097000
6	-2.027492000	5.481019000	1.760364000
1	-1.159724000	6.128236000	1.899787000
6	-3.306543000	6.025261000	1.747251000
1	-3.443252000	7.102163000	1.876996000
47	1.111378000	0.771153000	-1.183771000
17	-3.943049000	3.459766000	-2.181415000
8	3.797032000	-1.108606000	-1.070590000
8	1.622096000	-1.332157000	-1.557024000
7	-1.159174000	0.687683000	-1.779815000
6	2.954912000	-3.275305000	-1.453879000
6	1.849141000	-4.115067000	-1.614698000
1	0.853248000	-3.672794000	-1.629946000
6	4.405168000	-5.202788000	-1.554580000
1	5.412298000	-5.626158000	-1.529055000
6	2.776734000	-1.784574000	-1.347703000
6	-3.157561000	1.914214000	-2.120420000
6	-1.816959000	1.853197000	-1.819417000
1	-1.235780000	2.749990000	-1.597157000
6	-3.864338000	0.762837000	-2.396709000
1	-4.925802000	0.809992000	-2.641943000
6	-1.835365000	-0.434635000	-2.037572000
1	-1.257033000	-1.360321000	-1.995778000
6	-3.182817000	-0.439947000	-2.349448000
1	-3.689635000	-1.383216000	-2.557427000
6	4.225701000	-3.833928000	-1.406264000
1	5.083340000	-3.175462000	-1.269997000
6	2.027377000	-5.480895000	-1.760268000
1	1.159555000	-6.128289000	-1.898228000
6	3.306530000	-6.025292000	-1.747234000
1	3.443170000	-7.102223000	-1.876765000
47	3.840038000	1.058273000	-0.677475000
17	8.894466000	-1.630340000	0.320170000
8	1.154385000	2.938031000	-0.790656000
8	3.329320000	3.161582000	-0.304222000
7	6.110590000	1.141742000	-0.081432000
6	1.996502000	5.104786000	-0.407504000
6	3.102225000	5.944361000	-0.246391000
1	4.097769000	5.500889000	-0.221181000
6	0.546115000	7.032047000	-0.306376000

1	-0.461019000	7.453827000	-0.336708000
6	2.174679000	3.613996000	-0.513499000
6	8.108978000	-0.084789000	0.259174000
6	6.768375000	-0.023770000	-0.041830000
1	6.184826000	-0.920611000	-0.263257000
6	8.815755000	1.066589000	0.535464000
1	9.877715000	1.019771000	0.780387000
6	6.786782000	2.264060000	0.176326000
1	6.205306000	3.188755000	0.131671000
6	8.134233000	2.269373000	0.488202000
1	8.646298000	3.210768000	0.695244000
6	0.725644000	5.663207000	-0.454671000
1	-0.131421000	5.006832000	-0.596395000
6	2.923857000	7.310301000	-0.100535000
1	3.791535000	7.961544000	0.033066000
6	1.644862000	7.854731000	-0.114068000
1	1.509269000	8.932305000	0.010156000

S3.4 Compound IV

S3.4.1 Monomer

Optimised Coordinates

47	0.352380000	0.396254000	1.428784000
35	2.564653000	-2.165449000	1.807002000
8	1.865651000	1.959911000	1.115628000
8	1.933790000	1.086442000	-0.952152000
7	-0.155812000	-1.766954000	1.688998000
6	0.756838000	-2.733331000	1.731746000
6	2.341021000	1.868361000	-0.054110000
6	-1.452903000	-2.138406000	1.662754000
1	-2.161797000	-1.323207000	1.603763000
6	3.936512000	2.865583000	-1.718961000
1	3.446804000	2.259976000	-2.467212000
6	0.469547000	-4.090667000	1.730693000
1	1.261098000	-4.822250000	1.757295000
6	3.492378000	2.785741000	-0.399591000
6	-1.848084000	-3.466163000	1.696201000
1	-2.899035000	-3.713896000	1.686100000
6	-0.870859000	-4.450958000	1.727323000
1	-1.146296000	-5.497162000	1.746990000
6	5.605259000	4.484677000	-1.083256000
1	6.422114000	5.144319000	-1.345703000
6	4.111732000	3.563849000	0.578431000
1	3.755233000	3.503901000	1.596459000
6	4.991928000	3.707838000	-2.059281000
1	5.326865000	3.763334000	-3.086898000
6	5.164797000	4.409643000	0.236144000
1	5.639493000	5.012225000	0.999514000
47	-0.352379000	0.396255000	-1.428783000
8	-1.933788000	1.086446000	0.952152000

8	-1.865646000	1.959914000	-1.115629000
7	0.155807000	-1.766955000	-1.688997000
35	-2.564658000	-2.165443000	-1.807002000
6	-0.756845000	-2.733330000	-1.731747000
6	1.452897000	-2.138409000	-1.662755000
6	-0.469558000	-4.090666000	-1.730694000
1	2.161793000	-1.323212000	-1.603764000
6	1.848075000	-3.466167000	-1.696200000
1	-1.261110000	-4.822247000	-1.757297000
6	0.870847000	-4.450960000	-1.727323000
1	2.899025000	-3.713903000	-1.686099000
1	1.146282000	-5.497165000	-1.746988000
6	-2.341016000	1.868367000	0.054109000
6	-3.492370000	2.785750000	0.399591000
6	-3.936505000	2.865594000	1.718961000
1	-3.446799000	2.259985000	2.467212000
6	-4.991920000	3.707851000	2.059282000
6	-4.111723000	3.563860000	-0.578431000
6	-5.605249000	4.484690000	1.083256000
1	-6.422102000	5.144334000	1.345702000
6	-5.164787000	4.409656000	-0.236145000
1	-3.755224000	3.503911000	-1.596460000
1	-5.326856000	3.763348000	3.086898000
1	-5.639482000	5.012239000	-0.999515000

S3.4.2 Dimer

Optimised Coordinates

47	1.364101000	-0.837997000	-4.466705000
35	3.579449000	1.723708000	-4.826446000
8	2.874713000	-2.401650000	-4.140931000
8	2.925643000	-1.528182000	-2.072655000
7	0.858101000	1.325234000	-4.731090000
6	1.771054000	2.291590000	-4.766226000
6	3.340329000	-2.310105000	-2.967277000
6	-0.439169000	1.696659000	-4.715638000
1	-1.152944000	0.870931000	-4.658783000
6	4.921906000	-3.307325000	-1.289201000
1	4.423563000	-2.688606000	-0.542841000
6	1.483807000	3.648946000	-4.767622000
1	2.282830000	4.387926000	-4.785081000
6	4.488778000	-3.227485000	-2.612226000
6	-0.834062000	3.024431000	-4.752363000
1	-1.895341000	3.274453000	-4.748288000
6	0.143397000	4.009201000	-4.775414000
1	-0.134486000	5.065836000	-4.794162000
6	6.595887000	-4.926424000	-1.911003000
1	7.420183000	-5.591016000	-1.639507000
6	5.116249000	-4.005584000	-3.585066000
1	4.762807000	-3.941356000	-4.614864000

6	5.974464000	-4.149578000	-0.940118000
1	6.307509000	-4.203205000	0.099807000
6	6.166418000	-4.851392000	-3.234020000
1	6.653747000	-5.458887000	-4.001053000
47	0.635589000	-0.837996000	-1.615033000
8	-0.925953000	-1.528182000	-4.009079000
8	-0.875023000	-2.401650000	-1.940803000
6	-1.340639000	-2.310106000	-3.114456000
6	-2.489078000	-3.227479000	-3.469499000
6	-2.922214000	-3.307332000	-4.792530000
1	-2.421284000	-2.690781000	-5.539302000
6	-3.974764000	-4.149590000	-5.141623000
6	-3.116624000	-4.005586000	-2.496638000
6	-4.596184000	-4.926434000	-4.170734000
1	-5.419677000	-5.591802000	-4.442387000
6	-4.166742000	-4.851377000	-2.847715000
1	-2.763945000	-3.936227000	-1.468146000
1	-4.305721000	-4.204960000	-6.181847000
1	-4.655902000	-5.459960000	-2.082212000
7	1.141590000	1.325231000	-1.350631000
35	1.579760000	-1.723708000	1.255299000
35	-1.579760000	1.723708000	-1.255299000
6	0.228673000	2.291582000	-1.315499000
6	2.438861000	1.696661000	-1.366099000
6	0.515836000	3.648988000	-1.314112000
1	3.152906000	0.871366000	-1.420912000
6	2.833741000	3.024425000	-1.329377000
1	-0.282746000	4.387742000	-1.280539000
6	1.856309000	4.009174000	-1.306321000
1	3.895294000	3.273393000	-1.328459000
1	2.132485000	5.066084000	-1.279687000
47	-0.635589000	0.837996000	1.615033000
6	-0.228673000	-2.291582000	1.315499000
7	-1.141590000	-1.325231000	1.350631000
6	-2.438861000	-1.696661000	1.366099000
6	-0.515836000	-3.648988000	1.314112000
1	-3.152906000	-0.871366000	1.420912000
6	-2.833741000	-3.024425000	1.329377000
1	0.282746000	-4.387742000	1.280539000
6	-1.856309000	-4.009174000	1.306321000
1	-3.895294000	-3.273393000	1.328459000
1	-2.132485000	-5.066084000	1.279687000
8	0.875023000	2.401650000	1.940803000
47	-1.364101000	0.837997000	4.466705000
8	-2.925643000	1.528182000	2.072655000
6	1.340639000	2.310106000	3.114456000
8	0.925953000	1.528182000	4.009079000
6	2.489078000	3.227479000	3.469499000
6	2.922214000	3.307332000	4.792530000
1	2.421284000	2.690781000	5.539302000
6	3.974764000	4.149590000	5.141623000
6	3.116624000	4.005586000	2.496638000

6	4.596184000	4.926434000	4.170734000
1	5.419677000	5.591802000	4.442387000
6	4.166742000	4.851377000	2.847715000
1	2.763945000	3.936227000	1.468146000
1	4.305721000	4.204960000	6.181847000
1	4.655902000	5.459960000	2.082212000
8	-2.874713000	2.401650000	4.140931000
6	-3.340329000	2.310105000	2.967277000
6	-4.488778000	3.227485000	2.612226000
6	-4.921906000	3.307325000	1.289201000
1	-4.423563000	2.688606000	0.542841000
6	-5.974464000	4.149578000	0.940118000
6	-5.116249000	4.005584000	3.585066000
6	-6.595887000	4.926424000	1.911003000
1	-7.420183000	5.591016000	1.639507000
6	-6.166418000	4.851392000	3.234020000
1	-4.762807000	3.941356000	4.614864000
1	-6.307509000	4.203205000	-0.099807000
1	-6.653747000	5.458887000	4.001053000
7	-0.858101000	-1.325234000	4.731090000
35	-3.579449000	-1.723708000	4.826446000
6	-1.771054000	-2.291590000	4.766226000
6	0.439169000	-1.696659000	4.715638000
6	-1.483807000	-3.648946000	4.767622000
1	1.152944000	-0.870931000	4.658783000
6	0.834062000	-3.024431000	4.752363000
1	-2.282830000	-4.387926000	4.785081000
6	-0.143397000	-4.009201000	4.775414000
1	1.895341000	-3.274453000	4.748288000
1	0.134486000	-5.065836000	4.794162000

S3.5 Compound V

S3.5.1 Monomer

Optimised Coordinates

47	0.479341000	0.587388000	1.391340000
53	2.716651000	-1.974314000	1.569239000
8	1.958351000	2.151045000	0.943472000
8	1.840409000	1.277576000	-1.122066000
7	-0.003413000	-1.575820000	1.696166000
6	0.909387000	-2.542197000	1.656732000
6	2.326689000	2.059496000	-0.264249000
6	-1.297614000	-1.947271000	1.786582000
1	-2.009717000	-1.117473000	1.778728000
6	3.766126000	3.056717000	-2.065732000
1	3.204821000	2.440704000	-2.769215000
6	0.623164000	-3.899533000	1.681499000
1	1.414228000	-4.645546000	1.628876000
6	3.442344000	2.976875000	-0.711791000
6	-1.688192000	-3.275028000	1.855403000

1	-2.746703000	-3.524761000	1.934128000
6	-0.712123000	-4.259824000	1.798589000
1	-0.991755000	-5.315785000	1.838174000
6	5.485246000	4.675812000	-1.582548000
1	6.283301000	5.342015000	-1.920664000
6	4.147076000	3.754983000	0.206621000
1	3.876485000	3.690633000	1.261447000
6	4.786693000	3.898973000	-2.499512000
1	5.030841000	3.954777000	-3.563632000
6	5.165124000	4.600777000	-0.228906000
1	5.712187000	5.209517000	0.495802000
47	-0.479340000	0.587389000	-1.391339000
8	-1.840407000	1.277581000	1.122066000
8	-1.958346000	2.151049000	-0.943474000
7	0.003408000	-1.575821000	-1.696165000
53	-2.716655000	-1.974308000	-1.569239000
6	-0.909393000	-2.542196000	-1.656734000
6	1.297609000	-1.947275000	-1.786582000
6	-0.623174000	-3.899532000	-1.681500000
1	2.009714000	-1.117479000	-1.778729000
6	1.688182000	-3.275033000	-1.855402000
1	-1.414240000	-4.645543000	-1.628877000
6	0.712111000	-4.259825000	-1.798587000
1	2.746693000	-3.524769000	-1.934127000
1	0.991742000	-5.315787000	-1.838172000
6	-2.326683000	2.059502000	0.264248000
6	-3.442336000	2.976884000	0.711790000
6	-3.766119000	3.056728000	2.065732000
1	-3.204815000	2.440713000	2.769215000
6	-4.786683000	3.898985000	2.499513000
6	-4.147065000	3.754994000	-0.206622000
6	-5.485235000	4.675824000	1.582547000
1	-6.283289000	5.342028000	1.920663000
6	-5.165112000	4.600790000	0.228905000
1	-3.876474000	3.690644000	-1.261448000
1	-5.030831000	3.954789000	3.563633000
1	-5.712175000	5.209530000	-0.495803000

S3.5.2 Dimer

Optimised Coordinates

53	-0.039754000	-1.240640000	2.288422000
47	-1.924200000	0.699275000	0.012578000
8	-1.415951000	2.526788000	1.159521000
8	-3.035315000	1.866007000	2.567924000
7	-1.850880000	-1.571643000	-0.005089000
6	-2.098211000	2.631058000	2.216336000
6	-1.206609000	-2.306190000	0.897703000
6	-1.778103000	3.800222000	3.128362000
6	-1.269533000	-3.691768000	0.972010000

1	-0.722620000	-4.232384000	1.742900000
6	-2.014640000	-4.351211000	0.006251000
1	-2.073397000	-5.442120000	0.013172000
6	-2.632030000	4.099858000	4.187847000
1	-3.502808000	3.463143000	4.347376000
6	-2.676515000	-3.609388000	-0.962020000
1	-3.277964000	-4.088203000	-1.735382000
6	-2.370501000	5.186048000	5.011341000
1	-3.049532000	5.418437000	5.835994000
6	-2.580963000	-2.232326000	-0.926012000
1	-3.112627000	-1.584977000	-1.628522000
6	-1.257688000	5.983173000	4.785563000
1	-1.056983000	6.840897000	5.432880000
6	-0.654594000	4.596112000	2.909581000
1	0.003757000	4.350213000	2.075164000
6	-0.397421000	5.683159000	3.742002000
1	0.484714000	6.305100000	3.565848000
53	0.039754000	1.240640000	-2.288422000
47	-4.663276000	0.764461000	1.172488000
47	1.924200000	-0.699275000	-0.012578000
8	-3.645276000	0.816024000	-1.671216000
8	-5.389937000	1.794558000	-0.650824000
7	-4.409468000	-1.244531000	2.203164000
6	-4.694186000	1.513762000	-1.665859000
6	-5.148005000	2.094036000	-2.991959000
6	-4.310508000	2.009370000	-4.102322000
6	-6.381184000	2.732983000	-3.112786000
1	-3.352228000	1.500895000	-3.990890000
6	-4.697468000	2.564228000	-5.314238000
1	-4.031791000	2.498476000	-6.179202000
6	-5.920483000	3.208924000	-5.429726000
1	-6.220652000	3.648892000	-6.384412000
6	-6.763650000	3.285249000	-4.333219000
1	-7.023660000	2.798471000	-2.233687000
1	-7.731008000	3.786958000	-4.420868000
53	-6.170177000	-2.235270000	0.065812000
6	-4.910154000	-2.388706000	1.745039000
6	-3.623696000	-1.312578000	3.296574000
6	-4.645914000	-3.636881000	2.294142000
1	-5.069244000	-4.538635000	1.854203000
6	-3.846989000	-3.681713000	3.426576000
1	-3.622647000	-4.640564000	3.899889000
6	-3.332179000	-2.499378000	3.939430000
1	-2.689716000	-2.491952000	4.820553000
1	-3.213460000	-0.351173000	3.617512000
47	4.663276000	-0.764461000	-1.172489000
8	5.389937000	-1.794558000	0.650823000
7	4.409469000	1.244531000	-2.203163000
8	3.035316000	-1.866007000	-2.567923000
6	1.206608000	2.306190000	-0.897703000
7	1.850879000	1.571643000	0.005090000
6	2.580963000	2.232326000	0.926012000

6	1.269533000	3.691768000	-0.972008000
1	0.722620000	4.232384000	-1.742899000
6	2.014640000	4.351213000	-0.006250000
1	2.073396000	5.442121000	-0.013171000
6	2.676514000	3.609388000	0.962020000
1	3.277964000	4.088202000	1.735383000
1	3.112627000	1.584977000	1.628521000
53	6.170177000	2.235270000	-0.065812000
6	4.910154000	2.388706000	-1.745039000
6	3.623696000	1.312578000	-3.296574000
6	4.645914000	3.636881000	-2.294142000
1	5.069245000	4.538635000	-1.854202000
6	3.846989000	3.681714000	-3.426577000
1	3.622647000	4.640565000	-3.899890000
6	3.332179000	2.499379000	-3.939429000
1	2.689715000	2.491952000	-4.820552000
1	3.213461000	0.351172000	-3.617512000
8	1.415951000	-2.526788000	-1.159521000
6	2.098212000	-2.631058000	-2.216336000
6	1.778103000	-3.800223000	-3.128362000
6	2.632030000	-4.099858000	-4.187846000
6	0.654594000	-4.596112000	-2.909581000
1	3.502807000	-3.463143000	-4.347376000
6	2.370501000	-5.186048000	-5.011341000
1	3.049532000	-5.418437000	-5.835995000
6	1.257687000	-5.983173000	-4.785563000
1	1.056982000	-6.840898000	-5.432879000
6	0.397421000	-5.683158000	-3.742001000
1	-0.003757000	-4.350213000	-2.075164000
1	-0.484714000	-6.305100000	-3.565847000
6	4.694186000	-1.513762000	1.665858000
8	3.645276000	-0.816023000	1.671217000
6	5.148005000	-2.094036000	2.991958000
6	4.310508000	-2.009370000	4.102323000
6	6.381184000	-2.732983000	3.112785000
1	3.352228000	-1.500894000	3.990891000
6	4.697469000	-2.564228000	5.314238000
1	4.031792000	-2.498476000	6.179203000
6	5.920483000	-3.208924000	5.429726000
1	6.220651000	-3.648892000	6.384412000
6	6.763650000	-3.285250000	4.333219000
1	7.023660000	-2.798471000	2.233687000
1	7.731008000	-3.786958000	4.420868000